Stress Corrosion Cracking and Crack Tip Characterization of Alloy X-750 in Light Water Reactor Environments

by

Jonathan Paul Gibbs

B.S. Marine Engineering Systems (2005)
United States Merchant Marine Academy

M.S. Nuclear Science and Engineering (2008)
Massachusetts Institute of Technology

M.S. Materials Science and Engineering (2010)
Massachusetts Institute of Technology

SUBMITTED TO THE DEPARTMENT OF NUCLEAR SCIENCE
AND ENGINEERING
IN PARTIAL FULFILLMENT OF THE REQUIREMENTS FOR THE DEGREE OF

DOCTOR OF PHILOSOPHY IN NUCLEAR SCIENCE AND ENGINEERING
AT THE
MASSACHUSETTS INSTITUTE OF TECHNOLOGY

JUNE 2011

Signature of Author: _____
Department of Nuclear Science and Engineering
May 20, 2011

Certified by: _____
Ronald G. Ballinger
Professor of Nuclear Science and Engineering, Materials Science and Engineering
Thesis Supervisor

Certified by: _____
John H. Jackson
Research Scientist, Idaho National Laboratory
Thesis Supervisor

Certified by: _____
Bilge Yildiz
Assistant Professor of Nuclear Science and Engineering
Thesis Reader

Accepted by: _____
Mijid S. Kazimi
TEPCO Professor of Nuclear Engineering
Chair, Department Committee on Graduate Students

This page intentionally left blank

To my parents:

Thank you for your continuous support and encouragement.

This page intentionally left blank

Stress Corrosion Cracking and Crack Tip Characterization of Alloy X-750 in Light Water Reactor Environments

by

Jonathan Paul Gibbs

Submitted to the Department of Nuclear Science & Engineering
on May 20, 2011 in Partial Fulfillment of the
Requirements for the Degree of Doctor of Philosophy in
Nuclear Science and Engineering

Abstract

Stress corrosion cracking (SCC) susceptibility of Inconel Alloy X-750 in the HTH condition has been evaluated in high purity water at 93 and 288 °C under Boiling Water Reactor Normal Water Chemistry (NWC) and Hydrogen Water Chemistry (HWC) conditions. SCC crack growth rates of approximately 1.1×10^{-7} mm/s (K=28 MPa$\sqrt{m}$) under NWC conditions and 1.4×10^{-8} mm/s (K=28 MPa$\sqrt{m}$) under HWC in high purity water at 288 °C were observed. The environmental conditions were changed from NWC to HWC during constant K loading, and the crack growth rate immediately slowed down by approximately one order of magnitude. The alloy was also tested in HWC at 93 °C. No SCC crack growth was observed at K= 35 MPa$\sqrt{m}$ for the length of time tested at 93 °C. The fracture mode transitioned from predominantly transgranular cracking under fatigue conditions to a mixture of intergranular, pseudo-intergranular, and a small amount of transgranular fracture in constant stress intensity SCC. Pseudo-intergranular cracking is when a crack propagates directly adjacent to the grain boundary carbides and not actually on the grain boundary.

The SCC crack tips were characterized with scanning electron microscopy (SEM) and 3D Atom Probe Tomography (APT). The SEM analysis was focused on the fractographic analysis and crack-propagation mode. The crack was observed to propagate adjacent to grain boundary carbides (pseudo-intergranular) and along a boundary with high coherency where no carbides were present (intergranular). The small and localized areas of transgranular cracking were occasionally seen between two regions of intergranular cracking.

The APT reconstructions of the crack tips and crack wall identified several key features contributing to the SCC process: 1) Preferential oxygen transport occurs in either a finger-like or crystallographic morphology extending from the crack tip region. These regions are enriched in both oxygen and oxide with the oxide being a chromium-nickel spinel. 2) The matrix ahead of each finger-like "tunnel" is enriched in oxygen and predominantly chromium oxide. This indicates that oxygen is diffusing ahead of the crack tip into the bulk material. 3) The oxygen that penetrates directly into the base material from the crack walls in an ordered manner suggests that it is controlled by crystallographic features. 4) The main SCC crack tip is full of predominantly oxide phase and, to a lesser extent, metal atoms. The very crack tip forms a spinel of chromium and nickel oxides. Iron oxide begins to contribute to the oxide spinel approximately 25-30 nm from the actual tip. 5) The γ' precipitates that are directly adjacent to

each crack tip and crack wall were deficient in aluminum content. The aluminum content in the bulk γ' was approximately 6.6 at% and the near-crack γ' aluminum content ranged from 2.5-3.5 at%. The range of affected γ' was approximately 100 nm wide.

Thesis Supervisor: Ronald G. Ballinger
Title: Professor of Nuclear Science and Engineering, Material Science and Engineering

Thesis Supervisor: John H. Jackson
Title: Research Scientist, Idaho National Laboratory

Acknowledgements

First and foremost, I would like to express my deepest gratitude to my two advisors: Professor Ronald Ballinger and Dr. John Jackson. Professor Ballinger's expertise in materials science and engineering, careful scrutiny of my technical work, and patience have been instrumental to my success at MIT. Dr. Jackson's vast, practical knowledge in materials science and expertise in material fracture have helped me immensely. I am also appreciative for Dr. Jackson's mentoring throughout this research project and during my summer internships at Idaho National Laboratory.

Professor Hannu Hänninen and Tapio Saukkonen from Aalto University made significant contributions to this work. Professor Hänninen spent countless hours mentoring and instructing me in fractography and his input has been instrumental in helping me to understand many of the technical details of material failure and environmental degradation. Mr. Saukkonen provided many of the electron micrograph images in this work and I am very appreciative for his hard work.

I am very appreciative to Dr. Dieter Isheim from Northwest University's Center for Atom Probe Tomography (NUCAPT). Dr. Isheim was instrumental in teaching me about atom probe tomography and in manufacturing and running the atom probe tips in this work. Additionally, Dr. Isheim's passion for atom probe microscopy is contagious and I look forward to future collaboration.

I would like to thank Tim Lucas and Mike Short. I am truly fortunate to have Tim and Mike as co-workers and friends. Their assistance with scientific work has been instrumental to by success, and I will enjoy their friendship for years to come.

I would like to express my appreciation to Professor Bilge Yildiz. Professor Yildiz has been a wonderful mentor and her scientific knowledge and high standards have enabled me to surpass my expectations and become a better scientist.

I would like to thank Pete Stahle for his help in the laboratory with my environmental degradation tests.

Finally, I would like to thank the exceptional people at Idaho National Laboratory. Specifically, I would like to thank Mr. Todd Morris and Mr. Randy Lloyd. Mr. Morris provided much of the materials preparation for microstructural characterization, and Mr. Lloyd provided considerable assistance in fracture toughness testing.

Table of Contents

Table of Figures

Chapter 1 – Introduction and Overview

1.1 Introduction

The phenomena of crack nucleation and growth in structural materials due to effects of environmental degradation, stress, and a material's microstructure have been recognized and studied for many years. Alloys used in environments containing corrosive species, such as chlorides or phosphates, and localized environments with gradients in temperature and electrochemical potential have received special attention in materials research. However, cracks can initiate in environments with ultra-high purity water for both static and cyclic loading. Cracking susceptibility is generally lower in pure water than in concentrated environments, but is sufficient to cause concern when plants are operated longer than initially designed. This is most prevalent in the power generation industry and especially for light water nuclear reactors, especially if corrosion issues have had to be mitigated earlier in the plant's life.

These issues are further exacerbated in the nuclear industry due to an incomplete data base and classification of corrosion issues in federal regulation. As a result, the current life prediction models and the effect on life prediction for environmentally assisted cracking of materials in high-temperature water usually represent the upper bounds of the data. Lack of complete understanding of environmental degradation, especially with regard to crack initiation and growth, has burdened specific industries with excessive constraints for continued operation or plant lifetime extensions, most notably being the nuclear power generation industry. Much of the constraints are due to the difficulty associated with long term environmental degradation experiments to better understand the long term corrosion mechanisms. Previous experimental work has resulted in considerable data scatter between different testing techniques as well as the same tests from different institutions, which make the development of a life prediction model for a single environment excessively difficult and a life prediction model for multiple environments unfeasible. Furthermore, many of the plants' operations have evolved to be different from the initial design making their initial life prediction less accurate or even invalid in some cases.

While there is uncertainty in many cases, the outlook is not as gloomy as it may seem. The lack of understanding and classification of corrosion mechanisms in real world applications is partially offset by the increase in mechanistic understanding of environmentally assisted cracking. The knowledge base and comprehension have quickly accelerated in the past fifteen

years because of the development and refinement of experimental and analytical techniques which allow quantification and validation of various cracking hypotheses. The difficulty with developing a universal model is that it will be a function of the specific material, environment, and stress conditions. To more completely portray how quickly this model becomes excessively complicated many of the variables for each category are listed in Figure 1-1. It is important to mention here that this list is not complete, and it will be further complicated with the interplay between the three categories and is still further exacerbated when one accounts for plant operation history, which includes perturbations from normal/nominal conditions.

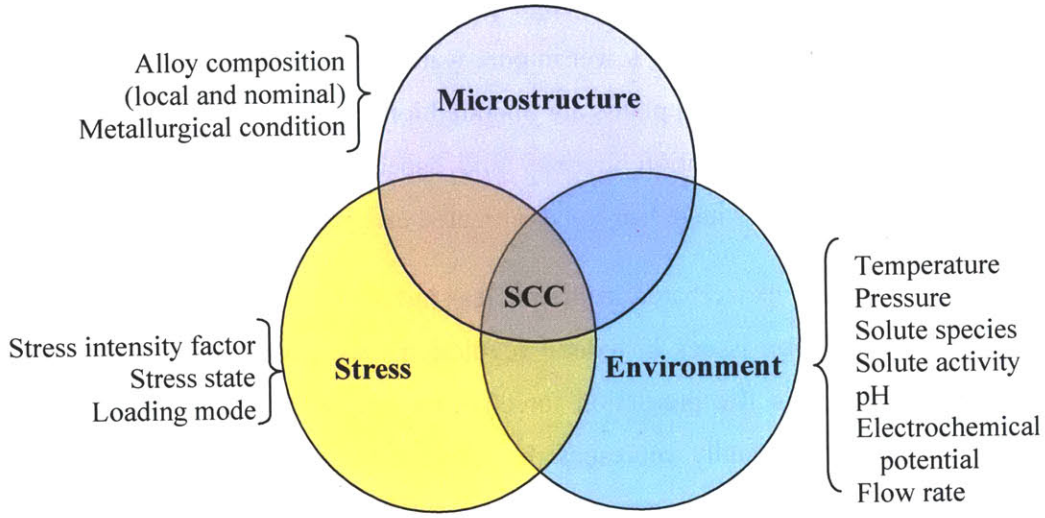

Figure 1-1: Factors contributing to environmental cracking

In addition to the other low or medium strength alloys, three main high-strength materials are used in nuclear reactor internals: Alloy X-750, Alloy 718, and Alloy A-286.[1] Both alloys X-750 and 718 are nickel-based superalloys and alloy A-286 is a stainless steel. These alloys were chosen because they exhibit good corrosion resistance, favorable mechanical properties, and load relaxation resistance. Components constructed from alloy X-750 have suffered from various failures, of which stress corrosion cracking (SCC) has been identified as a reason for many failures. As a result, alloy X-750 has undergone extensive research and development in order to make the material less susceptible to SCC in light water reactor environments. The majority of the work done to lessen the extent of SCC has included alloying and heat treatment modification. Great strides have been made to improve the resistance to environmental degradation. A considerable amount of testing has been accomplished and continues to be performed to better

understand the behavior of various alloys under particular environments, such as varying the amount of dissolved hydrogen or oxygen to characterize ongoing corrosion mechanisms. Many efforts have been made to characterize the SCC and fatigue crack propagation rate as a function of mechanical, environmental, and material parameters, but no accurate models have been developed to accurately predict crack growth behavior.

Alloy X-750 is a high strength, precipitation-hardened, nickel-based superalloy used in light water nuclear reactors. Alloy X-750 was initially developed for use in the aircraft industry because of its high temperature strength and excellent corrosion properties. Later, alloy X-750 was adopted by the nuclear industry to be used in structural components requiring high strength and corrosion resistance. Typical uses in nuclear reactors include bolts, pins, springs, and hold down beams. Generally, alloy X-750 performs well in aqueous environments, but can be susceptible to localized forms of attack such as corrosion fatigue, stress corrosion cracking, and hydrogen-assisted cracking.[2] Although only a limited number of failures have been observed for alloy X-750 components, these are typically strategically placed and result in costly unplanned shutdowns. For example, jet pump beam failures and fuel assembly finger springs have failed in boiling water reactors (BWR) and fuel assembly bolts, fuel assembly holddown springs, and guide tube support pins have failed in pressurized water reactors (PWR).[3]

The effect of irradiation damage on crack growth rates of alloy X-750 remains to be quantified, but previous work has shown that radiation effects are minor for fatigue cracking.[4-5] Representative nuclear environment testing is still required to determine more accurate crack growth rate dependence on irradiation and enable more reliable life expectancy predictions for affected components. The alloy X-750 components used in BWRs are located in low neutron flux regions and are not expected to become irradiation embrittled in their operating lifetime. However, the secondary effects of radiation, namely the radiolysis of water and its effect on water chemistry, can greatly affect crack growth rates. Radiation damage causes alloy X-750 to undergo significant strengthening and ductility loss associated with the formation of cavities and dislocation loops; however, significant radiation induced segregation has not been observed of alloying or trace elements.[6]

Thermal processing has been shown to have the largest effect on the susceptibility of alloy X-750 to stress corrosion cracking.[7] The heat treatments initially used by the aircraft industry have proven to be highly susceptible to localized corrosion in nuclear reactor environments.

Considerable work has gone into optimizing the heat treatment for corrosion resistance in nuclear reactor environments. This will be discussed in greater detail in the next chapter.

The purpose of this thesis is to explore and understand the fundamental mechanism(s) of stress corrosion crack growth in alloy X-750. Furthermore, this work is intended to establish baseline crack growth rate behavior in both oxygen and hydrogen rich aqueous environments. BWRs operate with dissolved oxygen water chemistry but can have localized deaerated environments in areas such as pits, crevices, cracks, and other areas where access is restricted. It has been previously shown on multiple occasions that hydrogen water chemistry (HWC) and dissolved hydrogen in the metal can have a large effect on crack growth rates.[8-12] Moreover, hydrogen embrittlement of materials is not only a problem in hydrogen water chemistry; hydrogen can be formed at or near the crack tip as a corrosion product. Currently no data exist that document the fundamental mechanisms of stress corrosion crack growth in alloy X-750 for in situ or long-term aqueous testing for light water reactor conditions. This is not to imply that little work has been completed for this alloy but that the work to date has only provided limited understanding. Much work has been done to show the correlation of hydrogen and oxygen content on the crack growth rates, in addition to other additives such as sulfates, but a detailed analysis of the microstructure at and ahead of the crack tip remains to be performed. Moreover, much of the work to determine the susceptibility of alloy X-750 to SCC has been focused on crack initiation and not crack growth. In order to more fully understand the root mechanism(s) a thorough analysis at the nano-level is necessary.

1.2 Motivation

It has been estimated that the economic effects of environmental degradation are more than $200 billion dollars annually.[13] Much of this is attributed to general corrosion such as rust on bridges or the bottom of an automobile, and these are easily fixable. Immediate effects of corrosion damage can be in the form of component failure in a power plant leading to an unplanned or immediate and costly shutdown. Mitigating environmental degradation of components and materials is of utmost importance to enable the smooth and reliable operation of engineering systems. Moreover, better understanding of materials further enhances economic optimization of operations as it enables engineers to perform only necessary planned maintenance and not replace unnecessary components.

Stress corrosion cracking (SCC) remains a formidable challenge to the power generation industries. Most notably, the nuclear industry is highly susceptible because of the added environmental degradation variable of radiation fields and their secondary effects. Materials development for nuclear applications is further challenged by the verification and validation step of model development to predict material behavior. Achieving comparable environments as those within a nuclear reactor is extremely difficult and expensive. The alloys used in nuclear reactors are mostly mature materials, meaning that their behavior should be well understood. However, the legacy nuclear fleet has added another dimension to the materials challenge due to the effects of aging, most notably in welds.

The first reported cases of SCC and irradiation-assisted stress corrosion cracking (IASCC) were intergranular cracking of stainless steel fuel cladding in the early 1960s.[14-16] IASCC instances have been increasing in stainless steel and nickel alloy core components. Neutron source holders were reported to fail in 1976 and control rod absorber tubes in 1978.[17] Instrument dry tubes and control blade handles and sheaths, which are subject to low stress were also reported to crack, but these were located in regions of higher fluences.[18] A large number of IASCC failures has been reported since the early 1990s, most of these have occurred in BWR core shrouds and PWR baffle bolts, as outlined in Table 1-1. A more detailed discussion of SCC experimental results is provided in Chapter 2.

Table 1-1: IASCC service experience [19-20]

Component	Alloy	Reactor Type	Possible sources of stress
Fuel cladding	304 SS	BWR	Fuel swelling
Fuel cladding	304 SS	PWR	Fuel swelling
Fuel cladding*	20%Cr/25%Ni/Nb	AGR†	Fuel swelling
Fuel cladding ferrules	20%Cr/25%Ni/Nb	SGHWR‡	Fabrication
Neutron source holders	304 SS	BWR	Welding and Be swelling
Instrument dry tubes	304 SS	BWR	Fabrication
Control rod absorber tubes	304/304L/316L SS	BWR	B_4C swelling
Fuel bundle cap screws	304 SS	BWR	Fabrication
Control rod follower rivets	304 SS	BWR	Fabrication
Control blade handle	304 SS	BWR	Low stress
Control blade sheath	304 SS	BWR	Low stress
Control blades	304 SS	PWR	Low stress
Plate type control blade	304 SS	BWR	Low stress
Various bolts**	A-286	PWR & BWR	Service
Steam separator dryer bolts**	A-286	BWR	Service
Shroud head bolts**	600	BWR	Service
Various bolts	X-750	BWR & PWR	Service
Guide tube support pin	X-750	PWR	Service
Jet pump beams	X-750	BWR	Service
Various springs	X-750	BWR & PWR	Service
Various springs	718	PWR	Service
Baffle former bolts	316 SS Cold-Work	PWR	Torque, differential swelling
Core shroud	304/315/347/ L SS	BWR	Weld residual stress
Top guide	304 SS	BWR	Low stress (bending)

*Cracking in AGR fuel occurred during storage in spent fuel pool

** Cracking of core internals occurred away from high neutron and gamma fluxes

†Advanced gas reactor

‡Steam generating heavy water reactor

1.3 SCC Overview

Environmentally Induced Cracking (EIC) is a general term for low ductility mechanical failures that result from a synergism between tensile stress and a corrosive environment.[21] EIC can result in failures at stresses below the yield stress. EIC includes SCC, corrosion fatigue cracking (CFC), and hydrogen embrittlement or hydrogen induced cracking (HIC). All three forms of EIC are prevalent in nuclear environments, but the focus here is primarily on SCC. In any given situation, more than one of these three forms of EIC may be operative, which further complicates failure analyses. Liquid metal embrittlement and solid metal embrittlement can also contribute to SCC, but this discussion is focused on those systems most pertinent to the nuclear power environment.

Instances of EIC have increased rapidly in recent years as new and higher-performance alloys are developed to meet the demand for materials that can extend the operation temperature range. Modern alloys of high strength are often more susceptible to EIC. SCC, CFC, and HIC are perhaps the most pernicious forms of corrosion due to their elusive mechanisms and prediction difficulties. Several SCC models have been proposed to describe SCC processes, but no universal model exists. The most widely accepted models are hydrogen embrittlement, adsorption induced cleavage, atomic surface mobility, film rupture (or slip-step dissolution), film induced cleavage, internal oxidation, corrosion-deformation interaction, vacancy-creep, and localized surface plasticity. The models most pertinent to this work are addressed and described in the results section as they relate to the cracking in alloy X-750.

1.3.1 Stress Corrosion Cracking

SCC is the low ductility failure at relatively low constant tensile stress (or constant stress intensity) of a susceptible alloy exposed to a corrosive environment.[21] SCC was first reported as the so-called season cracking of brass in ammonia-bearing environments in the early twentieth century and was a serious problem in the failure of cartridge casings for firearms in India during the monsoon season.[22] Caustic cracking resulted in explosions of carbon-steel steam-engine boilers and became a serious and dangerous problem in the 1920s.[21]

Three conditions must be present simultaneously to produce SCC: Susceptible alloy, critical environment, and some component of tensile stress, as previously shown in Figure 1-1. The susceptible alloy and critical environment are tied together in that environmental species are

often specific to the alloy system and may not have an effect on other alloys. For example, hot aqueous chloride solutions readily attack stainless steels, but do not have the same effect on carbon steels, aluminum, or other nonferrous alloys.[23] Although many engineering systems are initially designed to prevent the three factors necessary to SCC to be present simultaneously, time and service conditions may conspire to change the alloy and or system, which results in SCC. For example, nuclear reactor environments are known to sensitize* some stainless steels. While these steels may have initially had high resistance to SCC, after sensitization they may readily crack.

Controlling SCC requires removing one of the necessary conditions. However, this is more complex than it may seem because in practice engineering systems are composed of many alloys that operate in different environments in the same overall system.

Metallurgical Effects

Examining the fracture surface of failed component or sample (either intentionally in the lab or unintentionally as the result of a failed component examination) may reveal features that provide insight to the failure mode and process. Intergranular failure mode suggests some inhomogeneity at the grain boundaries. Sulfur and phosphorous segregation at the grain boundaries is a prime example of grain boundary inhomogeneity. An example more pertinent to the nickel base alloy and stainless steel inhomogeneities is grain boundary sensitization, either manifested through poor heat treatment, microstructural changes as a result of operating conditions and time, or a combination of both. Moreover, intergranular SCC (IGSCC) may be the result of stress-assisted IG corrosion since most failed components exhibit at least weak evidence of IG corrosion without stress.[24]

Electrochemical Effects

Electrochemical potential (ECP) plays a critical role in SCC. ECP can determine the thermodynamic stability of a protective oxide or base metal. A typical polarization curve for an active-passive alloy is shown in Figure 1-2.[21] The ideal operating locations for the alloy represented by the curve in Figure 1-2 would be at the intermediate potentials corresponding to

* Grain boundary sensitization is a phenomenon where chromium content is depleted at the grain boundary. This is caused by carbon diffusing faster to the grain boundary than chromium. With a sufficiently long aging time chromium can become desensitized. In stainless steels, and some nickel-base alloys, this increases corrosion susceptibility.

the vertical line (passive or stable oxide zone) or at very low potentials near an metal oxide/metal equilibrium potential (most notable in this work is NiO/Ni equilibrium). One important concept to note is that the corrosion current is never zero, although it may approach zero. A passive alloy or protective oxide is one that reduces the corrosion current to a minimum value. A passive film is an apparent prerequisite for SCC, but the zones of susceptibility appear at the potential boundaries where the passive film is less stable. Transitioning from the active to the passive potential is a region of oxide and electrochemical instability. Very small changes in potential can result in many orders of magnitude changes in current density. Many times the alloy dissolution is localized and the high current density in a concentrated region is very deleterious. The passive to transpassive transition results in oxide breakdown and can lead to pitting. Metal dissolution can be manifested in a pit or localized region. The regions in which an alloy is most susceptible to cracking are first the transition between the active to the passive range and then the transition between the passive and transpassive regions. The common example of zone 1 SCC is austenitic stainless steel in hot $MgCl_2$ solutions.[25] SCC may initiate at pits due to stress intensification but are not necessarily a prerequisite for SCC, even in zone 1. In zone 2, far from the pitting potential* range, SCC occurs where the passive film becomes weak and at active potentials barely adequate to form the film. An example of zone 2 SCC is typified by carbon steel in hot carbonate/bicarbonate solutions and alloy X-750 SCC in this thesis. [26] Line 1 in Figure 1-2 indicates the region of immunity on a Pourbaix Diagram for many nickel-alloys. In this region a stable and protective oxide forms. Line 2 points to the location where the NiO begins to become unstable and where alloy X-750 and other nickel-based alloys are susceptible to SCC. [27]

Although an active-passive alloy may behave similar to the polarization curve in Figure 1-2, this does not necessarily mean it is susceptible to SCC. A nonsusceptible alloy-environment combination will not crack even if held in one of the transient potential zones described. Thus, temperature and solution composition (including pH and dissolved oxidizers, aggressive ions, and inhibitors or passivators) can modify the anodic polarization behavior to permit or reduce SCC. Hence, alone, the anodic polarization curve cannot predict susceptibility to SCC. However, crack growth rates have been shown to be proportional to anodic dissolution currents

* The pitting potential is typically a high potential that marks the upper limit on film stabiligy. At this potential, the specific film will begin to become unstable and results in localized pitting corrosion.

at straining electrode surfaces.[28] Imposing a potential on a system, especially an aqueous system, either too low or too high to reduce the current density is not necessarily a solution. The water stability lines are shown as the dashed-lines in Figure 1-2. A system (or local) potential either below or above the water stability lines will result in either hydrogen or oxygen evolution, respectively. The severity of evolving either of these two species is system dependent but may be harmful as in the case of hydrogen embrittlement of high strength steels.

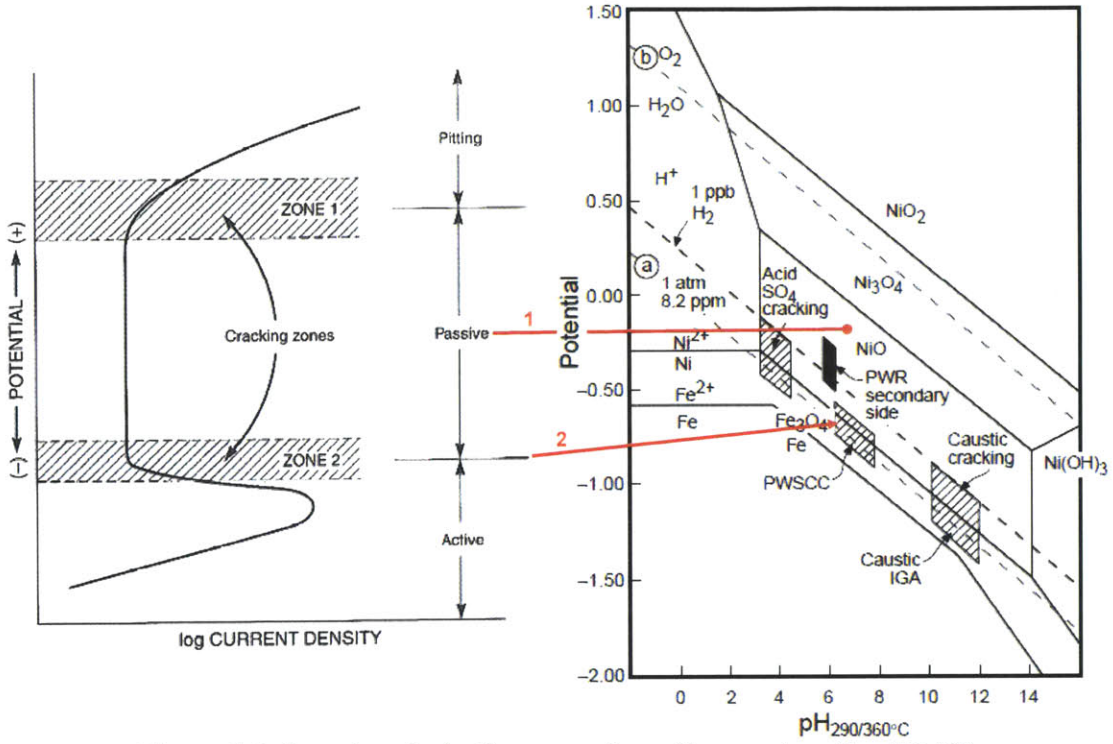

Figure 1-2: Sample polarization curve for active-passive alloy [21,29]

1.3.2 Hydrogen-Induced Cracking

HIC is the brittle mechanical fracture as a result of atomic hydrogen penetration and diffusion into the crystal structure of an alloy. Hydrogen may be present from reduction of water or acid by:

$$H_2O + e^- \rightarrow H + OH^- \qquad (1)$$

and

$$H^+ + e^- \rightarrow H, \qquad (2)$$

in neutral and acidic solutions, respectively.[21] Hydrogen can also be present as a result of the corrosion process. Before H_2 molecule can be formed, there is a significant residence time of the nascent H atom on the surface. This time is dependent upon the particular external conditions and alloy composition. Resident time of atomic hydrogen atoms on the surface is increased if cathodic poisons such as S^{2-} and As^{3+} are present to delay the recombination reaction,

$$H + H \rightarrow H_2 \qquad (3)$$

Sulfur and phosphorus are the two hydrogen recombination poisons pertinent to this work. If atomic hydrogen does not recombine, it can then enter the lattice and begin the HIC process. The presence of hydrogen is increased and reactions (1) and (2) are further accelerated. The danger of HIC further increases during cathodic protection and electroplating.[21] Atomic hydrogen can also be provided by dissociation of hydrogen gas on the surface during exposure at elevated temperatures, but those conditions are outside the scope of the work presented here. The hydrogen surfaces reactions and absorption process is illustrated in Figure 1-3.

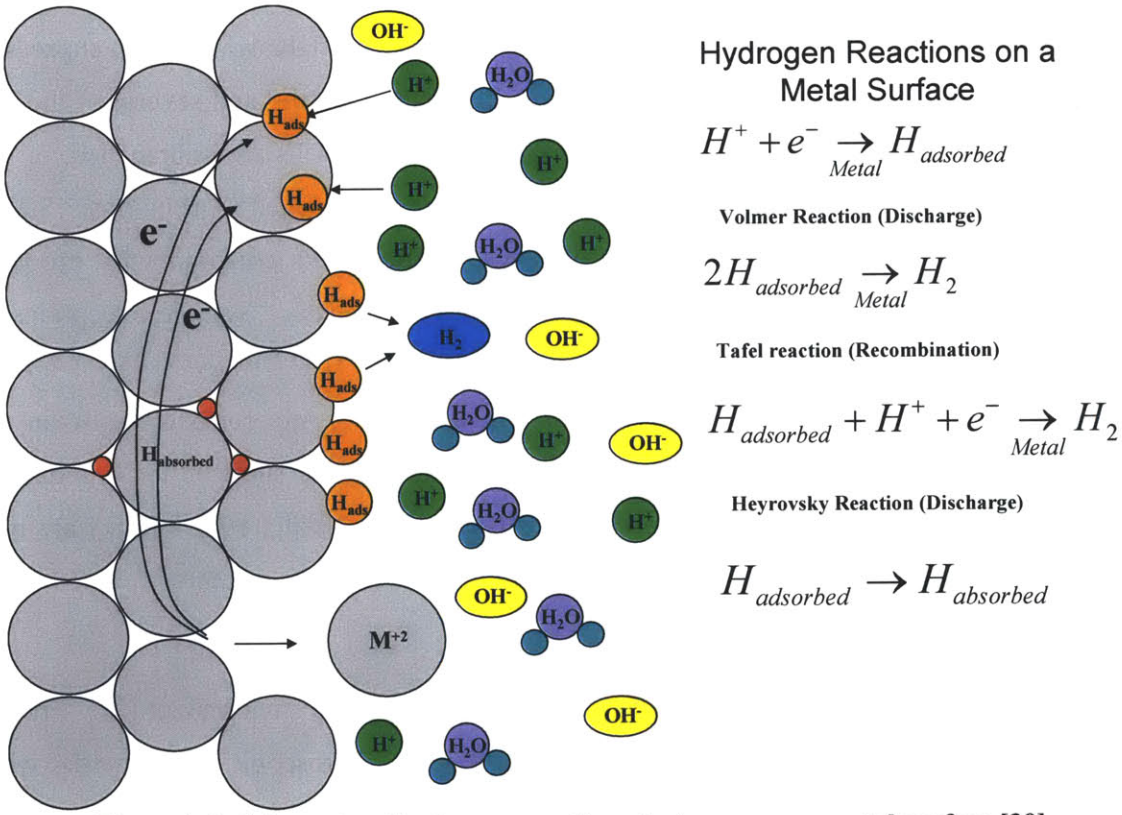

Figure 1-3: Schematic of hydrogen reactions that occur on a metal surface [30]

HIC requires an incubation time in which sufficient hydrogen is absorbed into the metal to a deleterious amount. Hydrogen is known to accumulate in the triaxial stress region in front of a crack tip, in vacancies, grain boundaries, and other imperfections such as dislocations. The incubation time decreases with increasing applied stress. This also implies that there is a minimum stress below which HIC will not occur. Increasing hardness or tensile strength of steel also decreases the incubation time and minimum stress for HIC.

HIC is especially prevalent in iron alloys because of the restricted slip capabilities in the predominantly body-centered cubic (BCC) structure and is generally limited to steels having a hardness of 22 or greater on the Rockwell C scale.[31] The face-centered cubic (FCC) alloys are more resistant because of their inherent high ductility and lower diffusivity for hydrogen, but all can become susceptible if highly cold worked.[32] Hydrogen embrittlement is a temperature dependent phenomenon occurs only over specific temperature ranges.

Comparison with SCC

HIC is similar to SCC in that brittle failure occurs in corrosive environments under constant tensile stress. However, cathodic polarization initiates or enhances HIC while it can suppress or stop SCC. The notable differences between HIC and SCC are plentiful and several of the most noteworthy are briefly discussed. With internal HIC and CFC, cracks are unbranched, or only slightly branched, while a clear feature of SCC cracks is their branched morphology. Surface cracks are often similar between HIC, CFC and SCC. HIC cracks predominantly propagate transgranular and at higher rates than the intergranular SCC cracks*. Notable exceptions are many cold-worked nickel alloys, which crack intergranularly by HIC. Alloy X-750 is a prime example of an alloy that undergoes intergranular HIC and SCC. Any corrosive solution may produce HIC in a susceptible alloy, if hydrogen is liberated on the surface. SCC requires a specific and usually different dissolved species for each alloy. Lastly, HIC failures are more predominant at lower temperatures while SCC is more likely at high temperatures.

1.3.3 Corrosion Fatigue

CFC is failure of an alloy caused by fluctuating stress in a corrosive environment.[21] Fracture surfaces from CFC, as well as from air fatigue, can exhibit macroscopic beach marks where corrosion products accumulate at step-wise crack-advance fronts. Striations are often evident

* This is usually the case; however, it will be shown in this work that this is not always the case.

where each cycle produces a discontinuous crack advance, albeit this occurs on the microscopic scale. Two loading parameters are known to affect the degree of CFC: Frequency and load ratio. Fatigue loading frequency has an important role in CFC as lower frequency can lead to increased crack propagation per cycle, while high frequencies can eliminate the effect of the corrosive environment. Generally, an increase in the load ratio*, R, results in an increase in fatigue-crack propagation rate at a given applied cyclic stress intensity, ΔK.[34-36] The effect of R is much lower in noncorrosive environments at ambient temperature. The R-ratio can also have an effect at higher temperature when creep is possible, but this is beyond the scope of the experimental conditions presented in this work. The effects of R and loading frequency on crack growth rate are explored in this work.

Stress risers, such as notches and grooves, have a greater effect on the fatigue life than does corrosion alone. Corrosion effects have been known to manifest in regions of higher stress, which are common at localized stress risers. Cracks have often been observed to initiate from corrosion pits, which also serve as stress concentrators.[37]

Many alloys exhibit an endurance limit in air or inert environment fatigue for a stress, below which, cracks do not initiate. This, however, is eliminated in a corrosive environment as corrosion shortens the number of cycles and reduces the stress amplitude before failure. Thus, an unnoticed low-frequency and/or low-amplitude stress can cause failures where it was originally thought to be constant stress conditions.

Comparison with SCC

CFC is similar to SCC in that failure by which very low ductility and much lower stresses than would be required otherwise in a normally ductile alloy can occur. CFC is also similar to SCC in as much as some portion of the stress must be tensile and that the cracks propagate normal to the principle tensile stress. Unlike SCC, CFC does not require a specific corrodent. Simply changing the conditions from vacuum to moist, or even dry, air can reduce the fatigue life.[38-39] Moreover, pure metals are not as resistant to CFC as they are to SCC. Other notable differences between CFC and SCC include crack morphology and potential initiation sites. CFC

* The load ratio, R, is defined under fatigue loading conditions as the minimum load divided by the maximum load.

fractures are predominantly transgranular and can initiate and grow from areas of localized slip within grains exposed to the surface.

1.3.4 SCC and Nickel Alloys

It has been well documented that increasing the nickel content above 8% has improved effects on SCC resistance of austenitic alloys in hot chloride solutions, as illustrated in Figure 1-4. Thus, high-nickel content alloys are often chosen for fossil- and nuclear-fueled power plants if chlorides could be present. Nickel alloys draw many parallels with stainless steels with respect to SCC susceptibility. However, nickel typically requires higher concentrations and temperatures to become susceptible.[40] Nickel alloys are susceptible to hydrogen damage in both aqueous and gaseous hydrogen environments [41], and the susceptibility of nickel alloys is governed by the same factors that affect ferrous alloy susceptibility to hydrogen embrittlement. Hydrogen damage in nickel alloys may cause intergranular, transgranular, or quasi-cleavage cracking. Although the fracture surface may appear to have undergone brittle fracture, on a microscopic scale there may be a high-degree of local plasticity, which suggests that hydrogen can enhance plastic flow at the crack tip in some cases.

The most well-known example of SCC in nickel alloys in the nuclear industry is with alloy 600 (Ni-Cr-Fe alloy), which was widely deployed as a heat-exchanger material in steam generators. Alloy 600 has been systematically replaced with alloy 690 due to its susceptibility to IGSCC in pressurized water at operating temperatures. Alloy 690 has experienced instances of SCC in laboratory testing but not in steam generator service and is much less susceptible than alloy 600. However, it has been suggested that alloy 690 will be susceptible to Pb-induced cracking after sufficient operational time.[42]

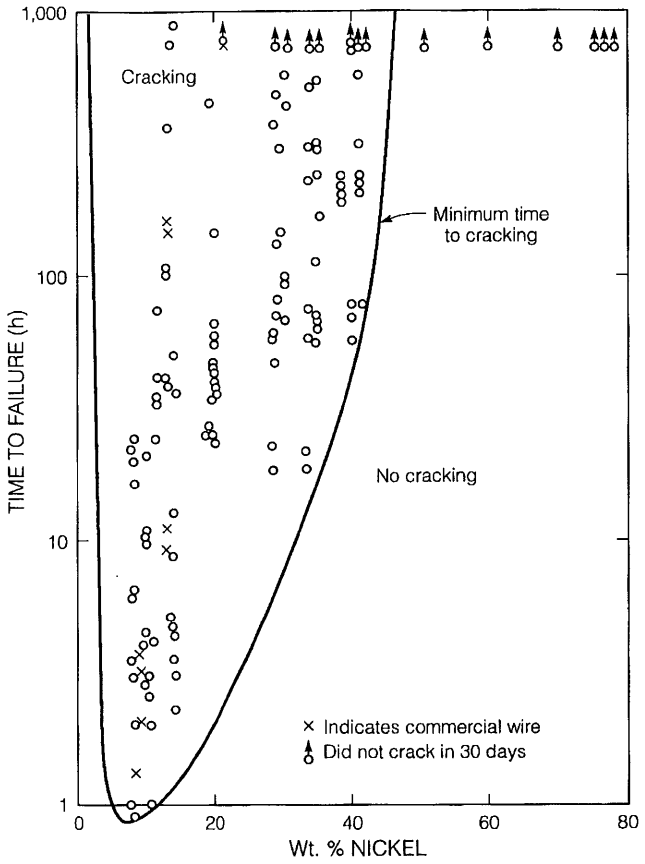

Figure 1-4: Effect of nickel content on SCC for Fe-Cr-Ni alloys [43]

1.4 Challenges

Challenges related to environmental degradation in high strength alloys, such as alloy X-750, fall into two classes: (1) a proper rationalization/understanding of the interplay between criteria such as temperature, other environmental variables (corrosion potential), mechanical variables (stress intensity factor and strain rate), and microstructure-through heat treatment and their effect on crack growth response, and (2) the conduct of proper experiments with the control and measurement of all important variables.

Understanding of Environmentally Assisted Cracking: The complex interplay between hydrogen (cathodically driven) effects and "classical" stress corrosion cracking (SCC) (anodically driven) have not been systematically explored. Indeed, much work has been done in regimes where one or the other has been dominant, but these efforts have largely been separate effects tests. This work is one of the first to conduct an investigation where both regimes are explored in the same set of experiments using the same sample. In this type of test, the heat treatment and mechanical

variables can be kept the same while the environment can be varied. The challenge associated with this work were to perform proper tests over the continual duration of 6000+ hours where both temperature and mechanical variables can be controlled (and varied) using the same material (single specimen). The effect of crack length, important for access of the environment to the crack tip, can also be explored. However, the difficulties to testing a single specimen in multiple environments is mostly reflected in the post-test analyses. Ideally, the crack tip analysis would be conducted on the main SCC tip, but by varying the environment the main crack tip can only be explored for the final water chemistry, which makes it necessary to run several tests, each with different final water chemistries to enable characterization of various crack tips in those environments most pertinent to real world operations.

Experimental and Mechanical Control: High accuracy corrosion (static and cyclic crack growth) testing remains a formidable challenge. Maintaining the system conditions over a long period of time where crack growth rates can be as low as 10^{-9} mm/s requires extreme attention to detail. Furthermore, crack length measurement techniques, mainly direct current potential drop (DCPD), sometimes have limited success in determining the crack length accurately, while producing data with a clear trend and minimal scatter for low growth rates (small crack length increments). Post-test analyses are also challenging to determine the dominant crack mechanism or combination of multiple mechanisms. The system corrosion potential, temperature, pressure, and dissolved hydrogen/oxygen are important criteria for crack propagation analysis, but the overall solution is a challenging, multivariable problem.

Post-Test Analyses: Most of the analysis techniques used in this thesis employ well established techniques such as scanning electron microscopy, electron backscatter detection, and orientation image mapping; however, employing atom probe tomography to investigate the **crack tip region** is a new challenge that few researchers have attempted and been successful with.

1.5 Goals and Objectives

The goals of this thesis were to understand the fundamental mechanisms of crack growth for nickel-based superalloy X-750 in high temperature aqueous systems and to understand the interplay between hydrogen embrittlement and SCC. A detailed exploration of the electrochemical and mechanical behavior of alloy X-750 was conducted. More specifically, understanding the crack propagation process required a detailed analysis of the processes occurring at the front of the crack tip and in the surrounding matrix. This was accomplished

during the post-test analyses. Complete characterization of the microstructure around the crack enabled a more fundamental understanding of the mechanisms that contribute to crack growth.

The work was completed in three main subareas: experiment construction, crack growth rate tests, and post-test analyses.

1.6 Idaho National Laboratory Collaboration

The project was conducted as collaboration between the Idaho National Laboratory (INL) and Massachusetts Institute of Technology (MIT). The experimental program was conducted both at MIT and the INL. A separate, but essential objective/requirement of this project was validation of the testing method for measurement of crack length over long periods of time as well as to control environmental and mechanical variables. The INL is in the process of developing hardware and test methods for conducting crack growth rate testing in LWR-prototypic environments with MIT collaboration. The H. H. Uhlig Corrosion Laboratory at MIT has a long history and much experience in this area and the transfer of this experience to the INL was and is critical part of this effort. Success in this area provides a solid foundation for future and longer term crack growth rate experiments in irradiative and non-irradiative PWR and BWR simulated environments at the INL. Furthermore, the location of the experimental work was split between the H.H. Ulhig corrosion laboratory at MIT and the Center for Advanced Energy Studies (CAES) testing facility at the INL.

1.7 Original Contributions

The original contributions in this thesis represent a significant contribution to the understanding of the fundamental SCC process at the crack tip in alloy X-750. The results from the crack growth rate response analysis allow prediction of component lifetime for specific conditions. The crack tip characterization has provided unique insight to the processes occurring at and ahead of the crack tip, which was accomplished through high-resolution reconstruction and elemental analysis. This thesis was the first successful attempt to complete an atom probe reconstruction of a crack tip and established the methodology and procedures for atom probe abalysis of crack tips. This achievement will spurn additional attention to this characterization technique for further SCC analyses. Together these contributions will facilitate a greater undertstnading of the SCC processes and facilitate mitigation processes. The original contributions in this work are as follows:

- Determination and analyses of crack growth rates of alloy X-750 in 200 ppb dissolved oxygen at 288 °C.
- Determination and analyses of crack growth rates of alloy X-750 in 5-30 cc/kg hydrogen water chemistry at 93 and 288 °C.
- Determination of the crack path and role of grain structure in controlling environmental fracture.
- Critical analyses of crack tip properties by three dimensional crack tip reconstruction with atom probe tomography.
    - Determined crack tip and ahead of crack tip chemistry
- Substantially advanced the knowledge of fundamental SCC mechanisms active in alloy X-750 for NWC and HWC.

1.8 Thesis Organization

This work is organized in seven chapters. This chapter served as an introduction and overview of the project. The remaining chapters are as follows:

Chapter 2: Alloy background, evolution, and characterization

Chapter 3: Stress Corrosion Cracking Experiment and Crack Growth Results

Chapter 4: Fractographic Analysis

Chapter 5: Crack Tip Characterization

Chapter 6: Integration and Discussion

Chapter 7: Summary, Conclusions, and Future Work

The results of the work are covered in detail in chapters 4 and 5 and are the main contributions.

1.9 References

1. R. McIlree, "Degradation of high strength austenitic alloys X-750, 718, and A-286 in nuclear power systems", Proceedings of the International Symposium on Environmental Degradation of Materials in Nuclear Power Systems – Water Reactors, NACE, pp. 838-850, 1984.

2. R.G. Ballinger, C.K. Elliott and I.S. Hwang, "Corrosion fatigue of alloy X-750 in aqueous environments", International Conference on Environment-Induced Cracking of Metals, Kohler, Wisconsin, pp. 241-249, 1988.

3. G.L. Garner and J.L. Smith, "Identification and characterization of commercial nuclear power plant components fabricated from age-hardenable alloys X-750, A-286, and 718", EPRI Report RP-2058-4, 1984.

4. A. Jenssen, P. Efsing and J. Sandberg, "Influence of heat treatment, aging, and neutron irradiation on the fracture toughness and crack growth rate in BWR environments of alloy X-750", Proceedings of the 12th International Conference on Environmental Degradation of Materials in Nuclear Power Systems – Water Reactors, pp. 73-85, 2005.

5. L.A. James, "Effect of fast neutron irradiation on fatigue crack growth behavior of three nickel-base alloys", Nuclear Technology, Vol. 53, pp. 64-68, 1981.

6. R. Bajaj, W.J. Mills, M.R. Lebo, B.Z. Hyatt and M.G. Burke, "Irradiation-assisted stress corrosion cracking of HTH alloy X-750 and alloy 625", Meeting of the International Collaborative Group on Irradiation-Assisted Stress Corrosion Cracking (ICGIASCC), 32 p., 1994.

7. C.K. Elliott, "Effect of Thermal Treatment on the Fracture Properties of Alloy X-750 in Aqueous Environments", Ph.D. Thesis, Massachusetts Institute of Technology, 1985.

8. W.J. Mills, M.R. Lebo and J.J. Kearns, "Hydrogen embrittlement, grain boundary segregation, and stress corrosion cracking of alloy X-750 in low- and high-temperature water", Metallurgical and Materials Transactions A, Vol. 30, pp. 1579-96, 1999.

9. D.S. Morton, S.A. Attanasio, E. Richey and G.A. Young, "In search of the true temperature and stress intensity factor dependencies for PWSCC," Proceedings from the Tweltfh International Conference on Environmental Degradation of Materials in Nuclear Power System – Water Reactors, TMS, pp. 977-988, 2005.

10. D.S. Morton, J. Fish, M.K. Schurman and S.A. Attanasio, "The influence of dissolved hydrogen on nickel alloy SCC in high temperature water," Corrosion/99, Paper 99447, 1999.

11. M.M. Hall, Jr., .M. Symons and J.J. Kearns, "Strain energy density – initiation of hydrogen-induced cracking of alloy X-750," Proceedings of the Parkins Symposium on Fundamental Aspects of Stress Corrosion Cracking, TMS, pp. 231-244, 1992.

12. D.M. Symons, "Hydrogen embrittlement of Ni-Cr-Fe alloys," Metallurgical and Materials Transactions A, Vol. 28, No. 3, pp. 655-663, 1997.

13. Class notes, Corrosion: The Environmental Degradation of Materials (3.54), Spring 2008.

14. P.L. Andresen, F.P. Ford, S.M Murphy, and J.M. Perks, "State of knowledge of radiation effects on environmental cracking in light water reactor core materials," Proceedings of the 4th International Symposium on Environmental Degradation of Materials in Nuclear Power Systems - Water Reactors, NACE, pp. 83-121, 1990.

15. F.P. Ford and P.L. Andresen, in *Corrosion Mechanisms in Theory and Practice*, Ed P. Marcus and J. Oudar, Marcel Dekker, New York, pp. 501-546, 2002.

16. P.L. Andresen, in *Stress Corrosion Cracking: Materials Performance and Evaluation*, Ed. R.H. Jones, ASM International, Materials Park, OH, pp. 181-210, 1992.

17. P.L. Andresen, F.P. Ford, S.M Murphy, and J.M. Perks, "State of knowledge of radiation effects on environmental cracking in light water reactor core materials," Proceedings of the 4th International Symposium on Environmental Degradation of Materials in Nuclear Power Systems - Water Reactors, NACE, pp. 83-121, 1990.

18. G.S. Was, J.T. Busby and P.L. Andresen, "Effect of irradiation on stress corrosion cracking and corrosion in light water reactors: corrosion in the nuclear industry," In: *Corrosion: Environments and Industries*, ASM Handbook, ASM International, Metals Park, OH, Vol. 13c., pp. 386-414, 2006.

19. R.L. Jones, "Critical Corrosion Issues and Mitigation Strategies Impacting the Operability of LWR's", Corrosion 96, Paper No. 103.

20. G.S. Was and P.L. Andresen, "Stress corrosion cracking behavior of alloys in aggressive nuclear reactor core environments," Corrosion, Vol. 63. No. 1, pp. 19-45, 2007.

21. D.A. Jones, *Principles and Prevention of Corrosion, 2nd Ed.*, Prentice Hall, Upper Saddle River, NJ, 1996.

22. H. Moore, S. Beckinsale and C.E. Mallinson, "The Season Cracking of Brass and other Copper Alloys", *Journal of the Institute of Metals* XXV: pp. 59-125, 1921.

23. R.J. Jones, ed., *Stress Corrosion Cracking, Materials Performance and Evaluations*, ASM International, Materials Park, Ohio, 1992.

24. R.N. Parkins, in *Environment-Induced Cracking of Metals*, Eds. R.P. Gangloff and M.B. Ives, NACE, Houston, TX, 1990.

25. R.W. Staehle, in *Stress Corrosion Cracking and Hydrogen Embrittlement of Iron Base Alloys*, Eds. R.W. Staehle et al., NACE, Houston, 1977.

26. R.N. Parkins, "Controlling parameters in stress-corrosion cracking", Proceedings from the Fifth Symposium on Line Pipe Research, Houston, Texas, pp. U-1 – U-40, 1974.

27. D.S. Morton, S.A. Attanasio, J.S. Fish and M.K. Schurman, "Influence of dissolved hydrogen on nicekal alloy SCC in high temperature water", Corrosion/99, Paper 99447, NACE, 1999.

28. R.N. Parkins, "Environment sensitive fracture and its prevention", British Corrosion Journal, Vol. 14, Issue 1, pp. 5-14, 1979.

29. P.M. Scott, P. Combrade, "On the mechanisms of secondary-side PWR steam generator tube cracking," Proceedings from the Eighth International Symposium on Environmental Degradation of Materials in Nuclear Power Systems – Water Reactors, ANS, pp. 65-73, 1997.

30. R.G. Ballinger, personal communication, May 2011

31. G. Korbin, *Metals Handbook*, Vol. 13, *Corrosion,* 9th *ed.*, ASM International, Metals Park, OH, pp. 329-31, 1987.

32. B.D. Craig, *Metals Handbook*, Vol. 13, *Corrosion*, 9th ed., ASM International, Metals Park, OH, p. 1132, 1987.

33. H.H. Uhlig and R.W. Revie, *Corrosion and Corrosion Control: An Introduction to Corrosion Science and Engineering, 3rd Ed.*, John Wiley and Sons, New York, 1985.

34. R.A. Schmidt and P.C. Paris, "Threshold for fatigue crack propagation and the effects of load ratio and frequency" Progress in Flow Growth and Fracture Toughness Testing, ASTM PT 536, ASTM, Philadelphia, pp. 79-94, 1973.

35. R.O. Ritchie, "Near-threshold fatigue crack propagation in ultra-high strength steel: influence of load ratio and cyclic strength." Journal of Engineering Material Technology, SME Series H, pp. 99:195-204, 1977.

36. P.K. Liaw, T.R. Lea and W.A. Logsdon, "Near-threshold fatigue crack growth behavior in metals," Acta Metallurgica, Vol. 31, Issue 10, pp. 1581-1587, 1983.

37. S.I. Rokhlin, J.Y. Kim, H. Nagy and B. Zoofan, "Effect of pitting corrosion on fatigue crack initiation and fatigue life," Engineering Fracture Mechanics, Vol. 62, Issues 4-5, pp. 425-444, 1999.

38. D.O. Sprowls, *Metals Handbook, Corrosion*, 9th ed., ASM International, Metals Park, OH, Vol. 13, p. 296, 1987.

39. W. Glaeser and I.G. Wright, *Metals Handbook, Corrosion*, 9th ed., ASM International, Metals Park, OH, Vol. 13, p. 142, 1987.

40. J. Kolts, *Metals Handbook, Corrosion*, 9th ed., ASM International, Metals Park, OH, Vol. 13, p. 647, 1987.

41. S.D. Cramer and B.S Covino, Jr. Eds, *Corrosion: Fundamentals, Testing, and* Protection, ASM Handbook, Vol. 13A, 2003.

42. R.W. Staehle, "Critical analysis of "tight cracks"", Corrosion Reviews, Vol. 28, Nos. 1 and 2, pp. 1-103, 2010.

43. H.R. Copson, *Physical Metallurgy of Stress Corrosion Fracture*, T.N. Rhodin, ed., Interscience, p. 247, 1959.

Chapter 2 – Alloy Background, Evolution, and Characterization

2.1 Introduction

Inconel® alloy X-750 is a precipitation-hardenable, austenitic, nickel-based superalloy. The nominal composition is listed in Table 2-1. This alloy is used due to its corrosion and oxidation resistance and high strength up to 700°C and excellent properties down to cryogenic temperatures.[1] Alloy X-750 was initially developed for the aircraft industry due to its creep resistance at high temperatures. In gas turbines, it is used for blades and discs, bolts, as well as other structural members. Alloy X-750 is also used extensively in rocket engine thrust chambers. This alloy was adopted by the nuclear industry and is used for components such as nuts, bolts, springs, and jet pump hold-down beams where high temperature strength and corrosion resistance are required.[2] However, the initial deployment of alloy X-750 used the same heat treatment as the aircraft industry, which resulted in several incidences of stress corrosion cracking (SCC). The heat treatments were reevaluated and it was determined that those used for the high-strength, high-temperature aircraft applications were less than ideal for aqueous environments in light water nuclear reactors. Considerable research has been conducted to understand and document the behavior and properties for the uses in the aircraft industry, but the amount of research devoted to the behavior of this alloy in aqueous environments is substantially less. Moreover, the aqueous work completed has been focused on heat treatments that have been largely phased out of the nuclear industry and are no longer pertinent to light water reactors. The background and evolution of the research devoted to understanding alloy X-750 is presented in this chapter along with the characterization of microstructure for the alloy's heat treatment used in this work. This review does not represent an exhaustive list of work performed on this alloy, but it is a relatively complete record of the pertinent published research to the focus of this thesis.

Table 2-1: Alloy X-750 nominal composition [3]

Element	Content (wt %)
Ni	70.00 min
Cr	14.0-17.0
Fe	5.0-9.0
Ti	2.25-2.75
Nb	0.7-1.2
Al	0.4-1.0
Mn	1.00 max
Cu	0.50 max
Si	0.50 max
C	0.08 max
S	0.01 max

2.2 Heat Treatments

The effect microstructure has on corrosion resistance is one of the largest controllable factors for alloy X-750. Much work has gone into determining the best heat treatment to control the grain boundary carbides to yield the most desirable microstructure for a combination of strength and corrosion resistance. However, many conflicting suggestions have been presented as the "best" heat treatment to prevent corrosion. Many of the conflicting opinions stem from researchers using different corrosion tests, such as the Huey test [4] vs. an aqueous corrosion test, and different evaluation metrics to determine the corrosion resistance.

Alloy X-750 is an alloy consisting of a γ face-centered cubic matrix hardened by the γ' [$Ni_3(Ti,Al)$] intermetallic precipitation, homogeneous and coherent with the γ matrix.[2] Titanium can substitute for aluminum in the γ' phase up to a critical atomic concentration of 60%, above which η phase, Ni_3Ti (HCP), is formed, which is undesirable. Typical heat treatments and alloy compositions avoid the formation of the η phase due to its poor corrosion and fracture properties. Alloy X-750 also forms both MC and $M_{23}C_6$ carbides. M represents the metallic constituent, titanium or niobium for the MC carbides, and predominantly chromium for the $M_{23}C_6$ carbides. The MC carbides have little or no direct effect on the corrosion resistance or mechanical properties. However, the MC carbides can indirectly affect the corrosion resistance by reducing the availability of carbon to precipitate the $M_{23}C_6$ carbides. The optimum IGSCC resistance has been correlated with the presence of continuous grain boundary $M_{23}C_6$ carbides.[5] The MC carbides form at very high temperatures and the $M_{23}C_6$ form at lower temperatures. Annealing temperatures higher than 1066 °C can dissolve a large fraction of the

MC carbide, which, on cooling and age hardening, provide carbon for the precipitation of $M_{23}C_6$. Annealing temperature greatly influences the amount of MC carbides present, the ratio of $M_{23}C_6$ to MC, and the SCC resistance of the alloy.[6] This process is illustrated with a Time-Temperature-Transformation diagram in Figure 2-1 and the common commercial heat treatments are in Table 2-2.

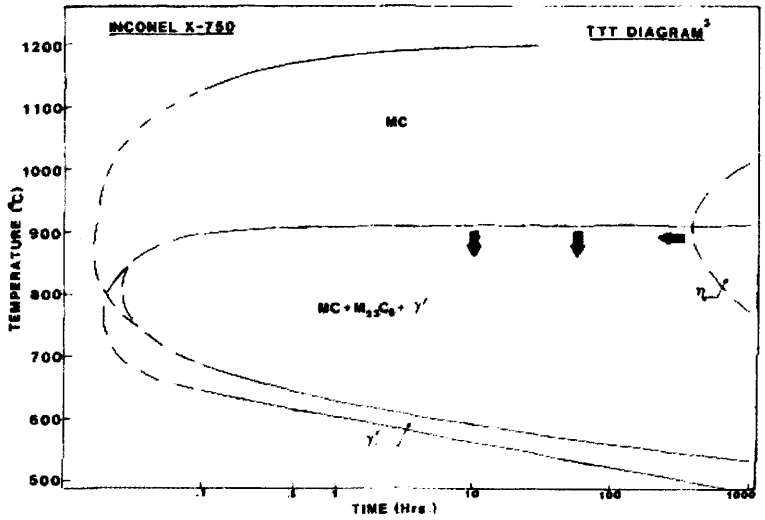

Figure 2-1: Alloy X-750 Time-Temperature-Transformation (TTT) diagram [1]

Table 2-2: Common Alloy X-750 Heat Treatments [7-8]

Treatment	Anneal	Intermediate	Age
SA	1093 °C/1 h/ wq[a]/ oq[b]		
AH		885 °C/24 h/ ac[c]	704 °C/ 20 h/ ac
HTH	1093 °C/1 h/ wq/ oq/ ac		704 °C/ 20 h/ ac
AHTH	1093 °C/1 h/ wq/ oq	885 °C/24 h/ ac[c]	704 °C/ 20 h/ ac
HOA	1093 °C/1 h/ wq/ oq		760 °C/ 100 h/ ac
BH			704 °C/ 20 h/ ac

[a]wq; water quench
[b]oq; oil quench
[c]ac; air cool

The nomenclature for the heat treatments listed in Table 2-2 are as follows:

SA:	solution annealed
AH:	equalized and aged
HTH:	solution annealed and aged
AHTH:	solution annealed, equalized, and aged
HOA:	solution annealed and over aged
BH:	hot worked and aged (no anneal or equalizing step)

The heat treatments basically consist of a high temperature solution annealing step, and/or aging, followed by a precipitation step.*

Several important processes occur during the heat treatment of alloy X-750 at temperatures between 650 °C and 850 °C: Chromium carbides in the form of MC or $M_{23}C_6$ precipitate at grain boundaries, which are accompanied by chromium depletion in the surrounding matrix. The higher diffusivity of carbon compared to chromium (carbon diffuses as an interstitial) enables formation of chromium carbides with an accompanying chromium depleted region immediately adjacent to the carbide. Carbon content greatly affects the degree of sensitization because it acts as the limiting constituent for chromium carbide precipitation. Once the initial chromium carbides have formed and sensitization has occurred for any temperature and as aging time increases, chromium desensitization, or recovery, of the grain boundary occurs. Naturally, the kinetics follows Arrhenius behavior and temperature greatly influences the desensitization time. For long aging times the chromium depleted zone bordering the carbides will have desensitized, the carbides can restructure to form more discrete precipitates, and further aging will cause chromium carbide precipitation to occur intragranularly.

As mentioned above, when carbides nucleate and grow they act as sinks for neighboring chromium resulting in a chromium denuded zone in close proximity to the carbides. The result is the formation of a sensitized microstructure in the same manner as for austenitic stainless steels. The growth rate decreases with the decreasing availability of carbon. Since chromium diffuses at a much slower rate than the interstitial carbon it requires ample time to diffuse to the sensitized regions and homogenize the local chemistry. Aging at 700°C will take nearly 100 hours for desensitization to occur and will take substantially longer at lower temperatures. This was illustrated by Was in Figure 2-2 which shows the effect of grain boundary sensitization as a function of time for a 700°C age of alloy 600.[9] This aging temperature is representative to the aging temperature of the commercial heat treatment (HTH) for alloy X-750. The notable differences between alloys X-750 and 600 are the γ' and other intragranular precipitates, (Ti,Nb)C, in alloy X-750, but the grain boundary carbide precipitation, growth, and structure are representative. Hence, alloy X-750 is essentially a precipitation hardened version of alloy 600. Alloy X-750 has approximately 3x the strength at elevated temperatures than alloy 600. The precipitation of $Cr_{23}C_6$ results in a temporary depletion of chromium from the region adjacent to

* Except for the BH condition.

the grain boundary. However, the 704°C, 20-h aging provides ample time for chromium to diffuse back into the depleted zone.[10] The grain boundary carbide formation, in both alloy 600 and X-750, can either enhance or substantially degrade the corrosion characteristics. Latanision noted that low temperature aging studies on Inconel alloy 600 have been shown to not undergo chromium depletion for aging times up to 15,000 hours at 300 °C.[11] However, Ljungberg showed that 304 stainless steel can undergo low temperature chromium depletion (300 °C) if a carbide "seeds" are initiated, but not grown, at a higher temperature age.[12] While Ljungberg's studies were for 304 stainless steel and not a nickel-based alloy, this is exceptionally important because this implies that a poor heat treatment can ultimately render structural components susceptible to grain boundary sensitization at light water reactor operating temperatures.

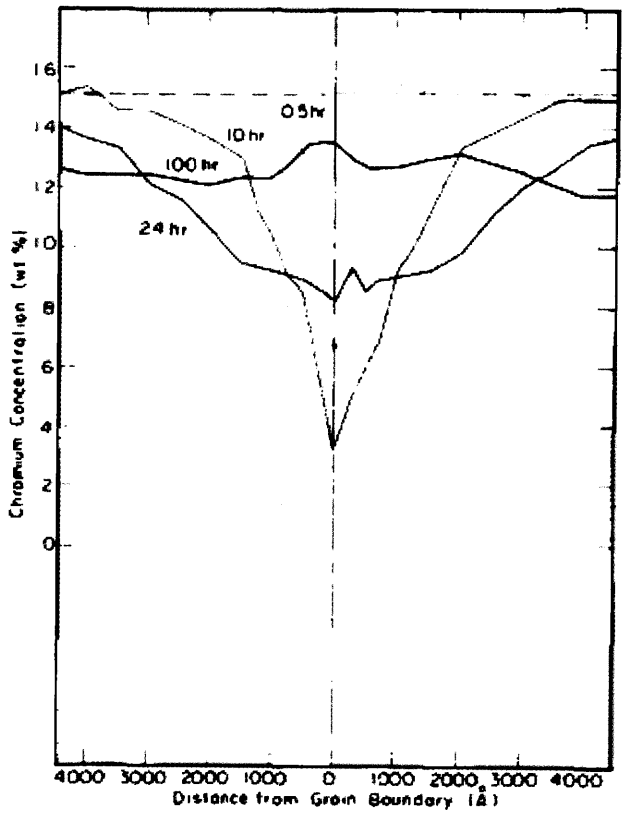

Figure 2-2: Grain boundary chromium depletion in alloy 600 [9]

The earliest reports of using thermal treatments to control the microstructure of alloy X-750 are from the 1940s, when the material was first developed.[13] The early work was focused on improving creep and stress rupture performance. Much of the early research to optimize the X-750 microstructure was performed by Raymond in the 1960s.[8] The two heat treatments

Raymond focused on are outlined in Table 2-2 , and are the triple-heat (AH) and direct-aged (HTH) treatments. The AH heat treatment employs a high temperature solution anneal followed by a 24 h aging at 885 °C and then a secondary aging for 20 h at 704 °C. This triple-heat heat treatment was designed to produce grain boundaries characterized by a predominance of γ' precipitates. The AH microstructure is shown in Figure 2-3. The HTH heat treatment utilized the same solution anneal time and temperature as AH, but only undergoes a 20 h aging at 704 °C. This direct-age heat treatment was designed to produce a predominance of $Cr_{23}C_6$ grain-boundary precipitations. The AH heat treatment is known for its high temperature strength, which is derived from both the γ' intragranular precipitates and the small grain size. However, AH exhibits poor resistance to SCC in light water reactor environments. The AH and HTH treatments represent the primary commercial heat treatments of alloy X-750. With respect to light water reactor environments, AH is classified as "highly susceptible" and HTH is "less susceptible" to environmental assisted corrosion.[10]

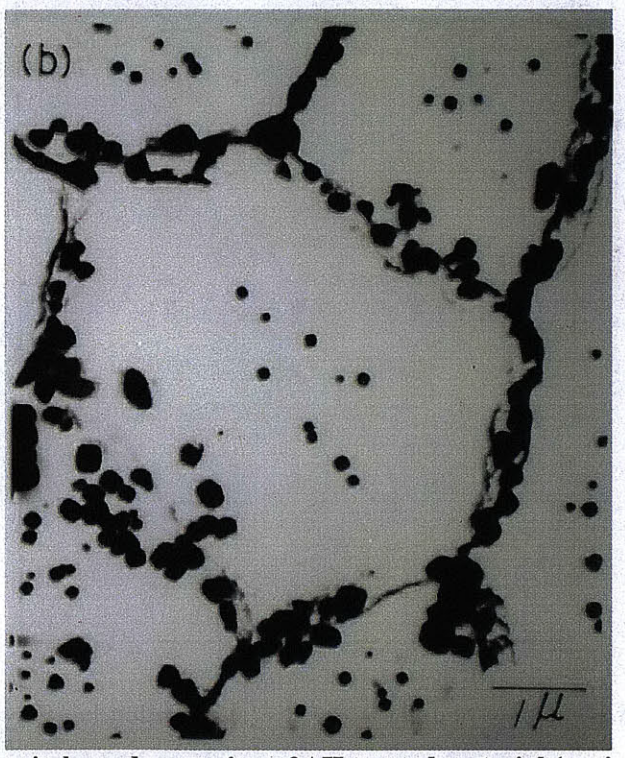

Figure 2-3: Typical grain boundary region of AH treated material (grain boundary γ' has an average diameter of 0.3 μm)[14]

Using electron diffraction patterns Raymond was able to show that the primary strengthening mechanism, γ' phase, was isomorphous with Ni_3Al, FCC ordered, and coherent with the matrix.

Raymond also noted the precipitation of chromium-rich $M_{23}C_6$ carbides on the grain boundaries when alloy X-750 was aged at 704°C. Adjacent to the $M_{23}C_6$ carbides was a γ' denuded zone resulting from chromium diffusion towards the carbides creating a chromium depleted zone and increasing the solubility of γ' within the matrix. Furthermore, Raymond was able to show that if alloy X-750 was given a 24 h age at 843°C between the solution anneal and the 704°C age the microstructure was able to desensitize and eliminate the γ' denuded zone. Microstructure comparison between the 843 °C and 704 °C aging resulted in course intragranular γ' particles and intergranular $M_{23}C_6$ carbides. The $M_{23}C_6$ carbides grew in a blocky shape along the grain boundaries. The final 704 °C, 20 h aging transformed the course γ' into a finer precipitate and removed the denuded zone along the grain boundaries. A schematic of the microstructure of the HTH treatment is shown in Figure 2-4.

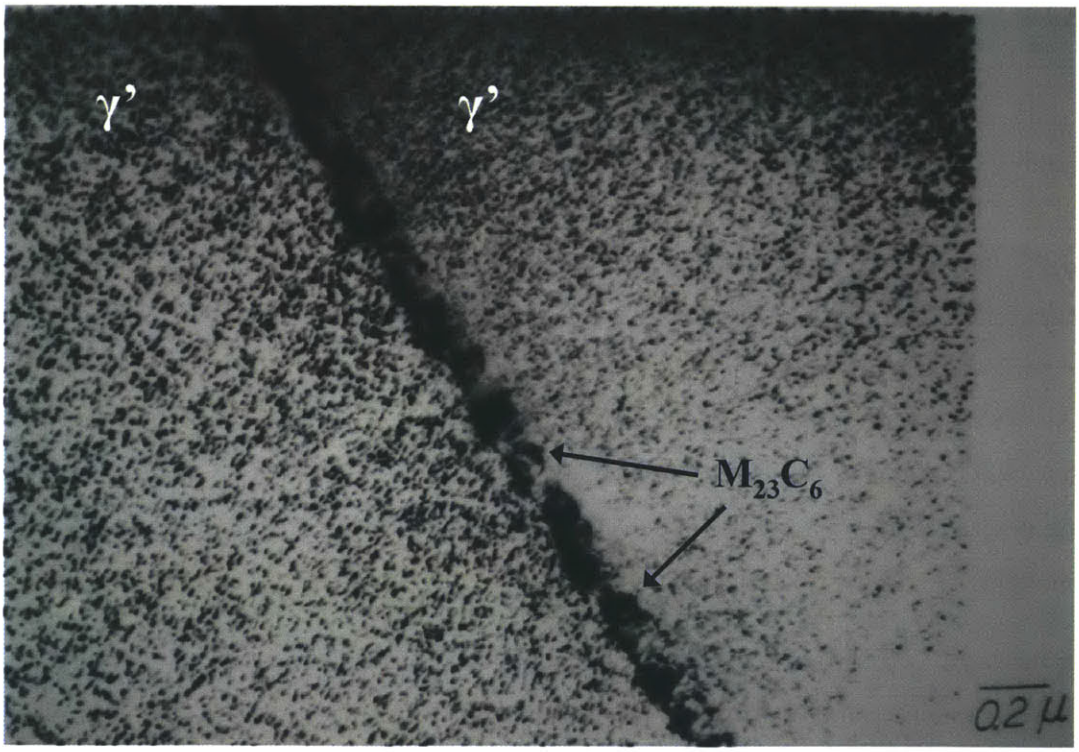

Figure 2-4: TEM micrograph of alloy X-750 HTH microstructure showing intragranular γ and grain boundary $M_{23}C_6$ carbides [14]

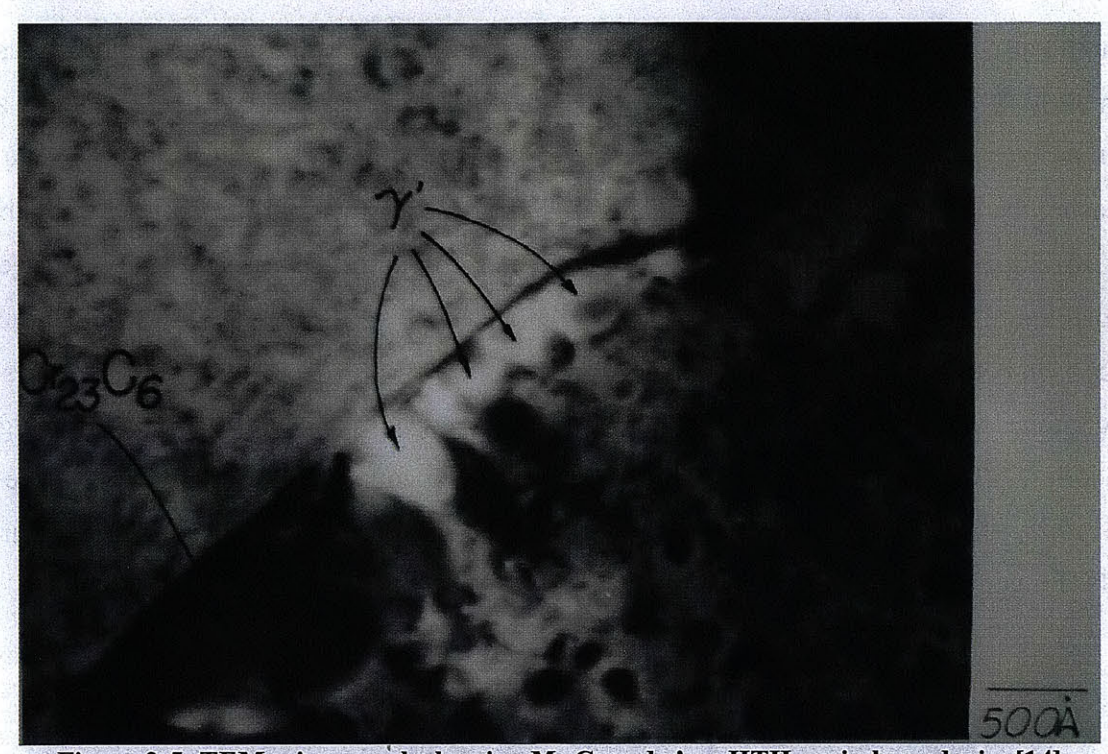

Figure 2-5: TEM micrograph showing $M_{23}C_6$ and γ' on HTH grain boundaries [14]

Using a direct age at 704 °C immediately following the solution anneal instead of the three-step heat process Raymond was able to evolve a different $M_{23}C_6$ morphology at the grain boundaries. The $M_{23}C_6$ carbides of the direct age treatment precipitated and grew primarily perpendicular to the grain boundary and formed a cellular type structure with a γ' denuded zone between the larger carbides. Conversely, the AH heat treatment resulted in the $M_{23}C_6$ carbides growing primarily in the grain boundary plane and did not have a γ' denuded zone between the larger carbides. Raymond also compared the Huey Test results between the two heat treatments. The HTH treatment resulted in approximately 10x higher corrosion rate than the AH treatment, which is attributed to the higher degree of sensitization.

During the late 1970s, Mills reported on the same triple-heat treatment as Raymond.[15] Mills highlighted the intragranular, duplex γ' structure with the coarse γ' precipitates appearing after an 843 °C intermediate age, followed by fine γ' precipitates after the final 704 °C age. Mills agreed with Raymond that the sensitization of the grain boundaries depleted the coarse γ' phase because the lower chromium content increased the solubility of γ'. However, more importantly, Mills reported that by lowering the aging temperature the solubility of titanium and aluminum was sufficiently reduced so that fine γ' particles precipitated in the chromium denuded zone.

During the 1980s, Floreen used the same heat treatments as Raymond (Table 2-2) to study the effects on carbon content.[16] Floreen's results largely agree with Raymond's, with the following exceptions: the triple-heat treatment resulted in discrete, blocky $M_{23}C_6$ grain boundary carbides with a size of approximately 3 μm, and the γ' precipitates consisting of a bimodal morphology of 14.5 and 180 nm cuboidal particles. Furthermore, Floreen did not report any γ' denuded zone from the direct-age treatment.

The first reporting of (Ti,Nb)C carbides along the grain boundary, in addition to the $M_{23}C_6$ carbides, was by Miglin in 1984.[7] Miglin was also the first to report the η phase (Ni_3Ti) in the AH treated material, which was surrounded with narrow γ' denuded zones. For the HTH treatment, Miglin reported on irregular, globular $M_{23}C_6$ morphologies and the grain boundary (Ti,Nb)C carbides having equal amounts of titanium and niobium and a uniform and continuous intragranular γ' precipitation phase up to the grain boundaries. In this work, Miglin introduced a third heat treatment, which was labeled HOA, and is outlined in Table 2-2. The HOA treatment is a direct-age treatment, similar to the HTH treatment, but with the 20 h age at 760 °C instead of 704 °C. The microstructure after the HOA is shown in Figure 2-6. The HOA treatment produces a microstructure with a narrow γ' denuded zones near the grain boundaries and carbides. The γ' denuded zone is dependent upon the adjacent carbide and is greater for the MC carbides. The $M_{23}C_6$ carbides produce a γ' denuded zone approximately 10-50 nm. Small γ' is present within the denuded zone, but not large γ'.

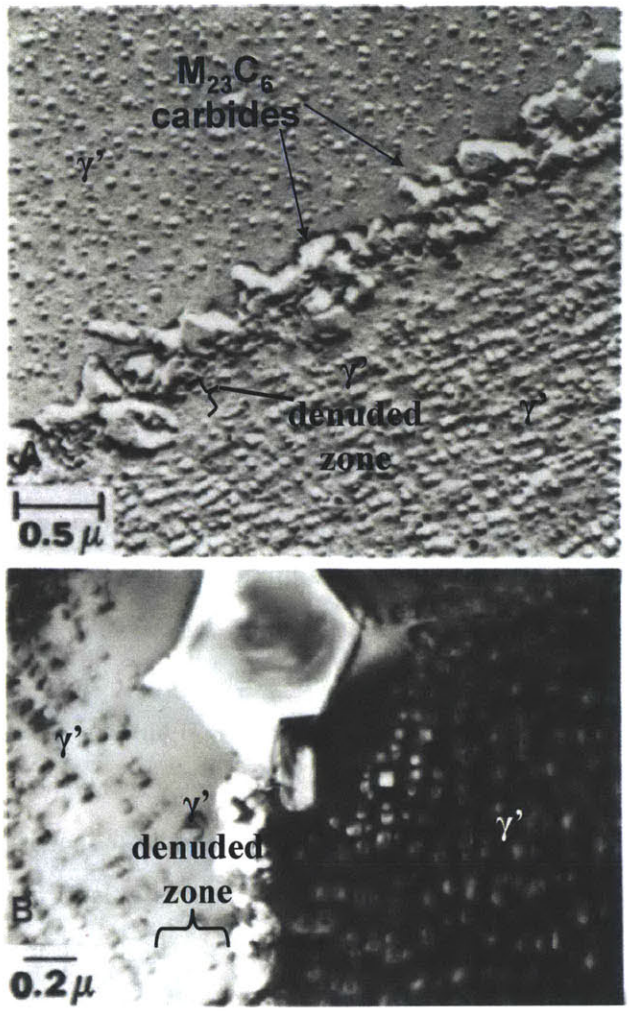

Figure 2-6: Grain boundary microstructure of Alloy X-750 in the HOA condition (γ' denuded zone contains fine γ' compared to the coarse γ' in the bulk) [17]

Also in 1984, Grove and Petzold used TEM and SEM analyses to further investigate the grain boundary microstructure of the AH and HTH treatments.[18] The findings were two distinct types of carbides on the grain boundaries, MC and $M_{23}C_6$. The MC carbides were blocky, ranging in size from 0.1 to 0.6 μm and were predominantly comprised of titanium. The $M_{23}C_6$ carbides resembled a plate-like shape comprised predominantly of chromium.

In 1985, Mishra reported more results on the effect of single aging on the microstructure and impact energy of alloy X-750.[19] Instead of comparing the AH and HTH heat treatments, Mishra focused on optimizing the aging temperature for the solution annealed and single age treatment. Essentially, Mishra performed parametric studies on the already established HTH treatment. The samples were solution annealed 1075 °C for two hours followed by a water

quench. The aging temperatures used were 704 °C, 760 °C, and 871 °C, with aging times varying between 2 and 200 h, followed by air cooling. Mishra noted that aging at 871°C for 2 h, followed by furnace cooling, initiated dissolution of the $M_{23}C_6$ carbides. It was noted that the carbides were completely dissolved after aging for 100 h and reappeared after aging 200 h. Using a Huey test to determine intergranular corrosion susceptibility, Mishra reported that aging a 871 °C for 100 h followed by furnace cooling yielded the lowest corrosion rate, while aging at 704 °C for 100 h gave the highest corrosion rate. Mishra concluded that alloy X-750, aged for 200 h at 871 °C, followed by air cooling, or aged for 50 to 100 h at 871 °C, followed by furnace cooling, may provide a solution to SCC. Although these tests may have performed well in a Huey test, when tested in a more representative environment to light water reactors, it is known that the heat treatment suggested by Mishra is not an adequate solution to SCC and is more susceptible than the HTH treatment.[14]

In the 1990s, Ferreño [5] further optimized the previously mentioned heat treatments, but with the focus on IGSCC resistance for BWR water conditions. Ferreño concluded that the HTH and HOA treatments guarantee, at any temperature, the absence of intergranular attack because they are able to obtain a suitable grain size combined with consistent grain boundary $M_{23}C_6$ carbide distribution, which are responsible for the favorable IGSCC characteristics. Furthermore, from a mechanical point of view, the HTH and HOA treatments are equivalent, and clearly superior to the other listed treatments, because they also avoid intergranular corrosion mechanisms. Ferreño concluded, from an economical perspective, HTH is superior to HOA because it requires a shorter aging time at a lower temperature.

2.3 Microstructure of As-Tested Alloy X-750

The alloy tested in this work was treated in the HTH condition. The methods employed to analyze the microstructure were light microscopy, scanning electron microscopy (SEM), and three-dimension atom probe tomography (APT). The samples for the analysis methods were dispersion polished on a ChemoMet cloth with 0.04 μm colloidal silica suspension solution and then immersion etched with a 2% bromine balance methanol solution. The bromine-methanol attacks the austenitic matrix leaving the carbides and other precipitates unaffected. This procedure allows the examination of the distribution and morphology of grain boundary and matrix precipitates and other inclusions. In addition to the polishing, the APT specimens were

prepared by focused ion beam (FIB) milling for site specific analyses. The light microscopy and SEM analyses were used to determine the grain size and distribution of carbides. APT analysis was used to determine the distribution and composition of γ' precipitates. The focus in this work is on and around the grain boundary carbides as the intermetallic γ' provides strengthening, but does not affect the corrosion behavior.

The microstructure of alloy X-750 after the HTH treatment is shown in Figure 2-7. The 1093 °C anneal and 20 h aging at 704 °C results in a recrystallized microstructure with an equiaxed grain size of 130 μm. The numbers in Figure 2-7 correspond to prominent features in the microstructure, which are the grain boundaries with continuous or semi-continuous chains of discrete cuboidal shaped $M_{23}C_6$ carbides [6] (most visible at this magnification), numerous twin boundaries, sparse inter- and intragranular MC carbides (1), sparse distribution of intragranular MC carbides (2) with an average spacing of approximately 10-20 μm, and sparse Ti(C,N) phase (3). The γ' phase is not apparent in Figure 2-7 as it has an average size of 10-12 nm, but is discussed below.

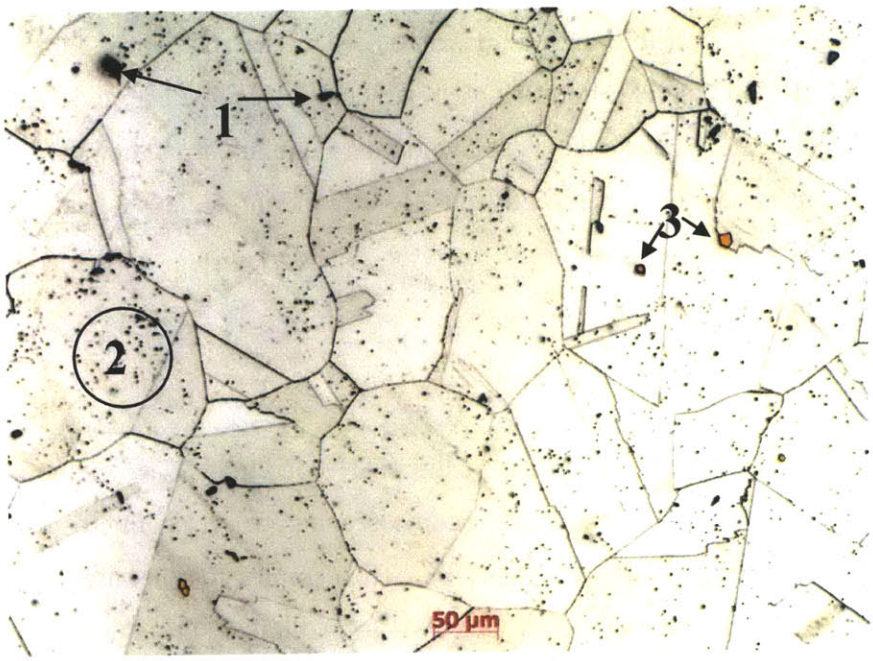

Figure 2-7 Alloy X-750 HTH microstructure

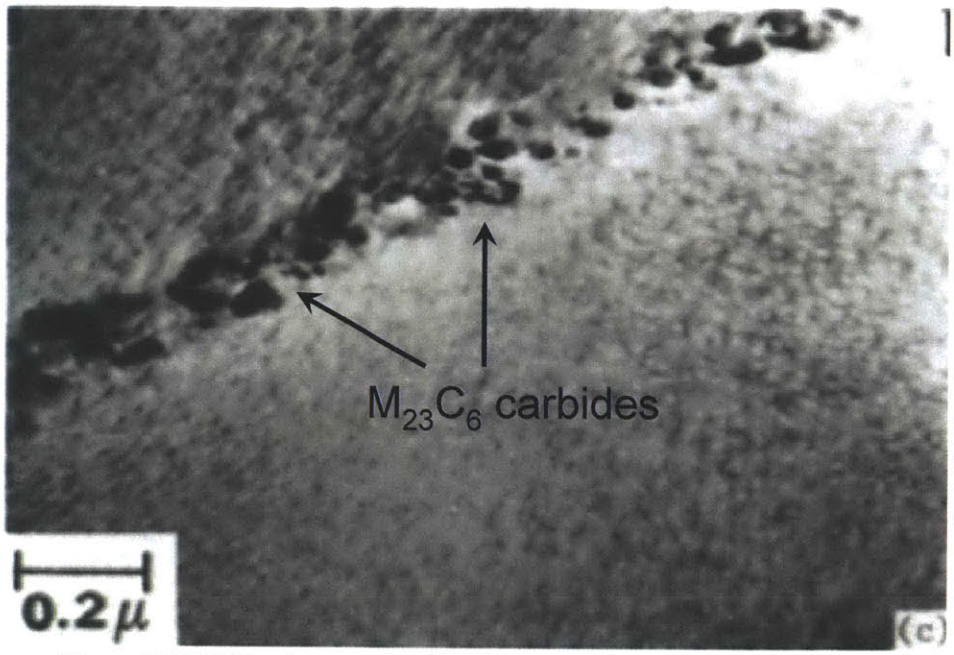

Figure 2-8 TEM micrograph of HTH grain boundary microstructure ($M_{23}C_6$ carbides on grain boundary)[14]

Discontinuous precipitation of $M_{23}C_6$ is also observed in the microstructure. These precipitates can nucleate and grow into widely spaced rod and pear shapes. The second type of $M_{23}C_6$ precipitate remains small and roughly spherical. The smaller $M_{23}C_6$ precipitates are semi-coherent (aligned with the matrix, but not in a one-to-one correspondence of crystal structure).[20] Large MC particles are sparsely distributed and have been reported to include a high dislocation density.[6] The MC carbides have a hexagonal shape and are predominantly Nb and Ti carbides. MC carbides were documented by Elliott [14] as a titanium-niobium mix (≈71% Ti, 18% Nb) and the $M_{23}C_6$ carbides were, on average, 90% chromium, with the balance elements being nickel and iron. It was further noted that it is thermodynamically feasible for Al, Ti, and Nb to alloy with carbon to form $M_{23}C_6$ carbides, but this is unlikely because they are minor alloying elements.

The γ' phase precipitates intragranularly with a semi-uniform distribution. These precipitates have an average diameter of 10-12 nm and are too small to be seen in Figure 2-7. The size and distribution of γ' within the bulk of alloy X-750 is shown in Figure 2-9, which is an APT reconstruction. This APT is part of the metal characterization in this thesis and a more detailed discussion of APT theory is presented in Chapter 5. The image on the right side of Figure 2-9 shows all γ' precipitates and the image on the left has the γ' that intersects the exterior surface

removed to further elucidate the size and distribution. The γ' precipitates are a $Ni_3(Ti,Al)$ ordered phase. The γ' phase precipitates and grows semi-uniformly in the microstructure. The intragranular γ' is distributed uniformly, but there is a narrow γ' denuded zone directly adjacent to the grain boundary that contains fine γ'. The γ' phase has also been documented on grain boundaries, but slightly larger than the intragranular phase, with an average size of 0.04 μm. The grain boundary γ' precipitates are typically found on grains containing small, discontinuous $M_{23}C_6$ carbides. [14]

The composition of intragranular γ' is presented with a series of proxigrams* [21] in Figure 2-10 through Figure 2-12. The same proxigrams, with error bars, are provided in Appendix B. The vertical dotted lines indicate the approximate interface between γ' and matrix. A proxigram determines the compositional changes at an interface between two phases. The proxigram analyses here show that other elements also contribute to the γ' phase composition. The γ' proxigram analysis is divided into three scales to highlight various elemental trends and concentrations. The full scale concentration profiles are presented in Figure 2-10. Elemental concentrations of up to 10 at% are highlighted in Figure 2-11, and elemental contributions less than 1.0 at% are the focus in Figure 2-12. Elements not shown in each proxigram do not undergo any noticeable compositional profile changes across the γ'/matrix interface. Base elemental composition information for the analysis volume is provided in Table 2-3. It is important to note here that the bulk composition does not discriminate between the γ' phase and matrix. For each of the proxigrams, point 0.0 on the x-axis corresponds to the physical interface between the γ' phase and matrix. Positive x-values are within the γ' phase and the negative x-values correspond to distance within the matrix and moving away from the γ' interface. The interface is further

Table 2-3: Bulk Composition

Element	Comp (at %)
Al	1.208
Ti	2.712
Cr	17.243
Mn	0.281
Fe	7.715
Ni	69.725
Si	0.359
C	0.037
V	0.030
P	0.014
Nb	0.354
O	0.005
B	0.016
Co	0.187
Mo	0.058
Cu	0.011
W	0.007
As	0.002

* A proxigram is an analysis technique to analyze interfaces. A proxigram presents a plot of concentration versus distance. This is analogous to a liner concentration profile. The distance is measured as the proximity of each point to a reference surface, which is user defined. The surface can be any shape, orientation, and complexity as long as it is closed and continuous. The surfaces are user defined and are generated by calculating the isosurface of a scalar 3D field. Positive and negative proximities correspond to the point of space being on the outside and inside of the user established isosurface, respectively.

identified by a dotted line. It is important to note here that the interface is identified in the analysis software via a statistical method and may not be the absolute interface. This is further complicated in that the concentration profiles are averaged over all γ' precipitates within the analysis volume shown in Figure 2-10. The interface between the γ' precipitates and matrix will also be dependent upon individual precipitates. However, several clear elemental trends can be identified.

As previously noted, the γ' phase is predominantly a nickel-aluminum-titanium phase. The nickel concentration immediately surrounding the averaged γ' phase is approximately 69.0 at%, while the nickel content within γ' is 74 at%. No sharp transition is present between the two phases and the transition is through a shallow compositional gradient. The bulk nickel composition is 69.7 at%, which indicates that a very small Ni depletion is present in the immediate periphery of γ'.

Chromium and iron undergo substantial elemental depletion in γ', as evident in Figure 2-11 and Figure 2-12. Chromium is the major depleted element in the γ' phase. The nominal Cr composition in the periphery of γ' is approximately 19.5 at%, compared to 17.2 at% bulk. The Cr concentration has a high gradient across the γ'/matrix interface is very steep, as it decreases by a factor of six over a 3 nm distance. Fe is depleted to approximately 2.75 at% in γ' from periphery and bulk values of 8.3 and 7.7 at%, respectively.

Titanium and aluminum are the major enriched elements within γ'. In alloy X-750, the bulk Al and Ti compositions are 1.2 and 2.7 at%, respectively. Within γ', Al and Ti are as about five times higher at 6.6 and 12.5 at%, respectively. Both Al and Ti undergo approximately a 5x increase in concentration within a distance less than 3 nm from the γ' periphery.

The other notable elemental changes in and around γ' are Nb, Si, Mn, and B. Nb experiences a fairly severe gradient in the vicinity of the γ' interface as it increases from a bulk concentration of 0.30 at% to approximately 0.75 at% in less than 3 nm. Si and Mn increases from approximately 0.35 and 0.25 at% to 0.45 and 0.35 at%, respectively. Boron undergoes a 3X enrichment within γ' as it increase from 0.015 to 0.04 at%. Previously B has been known to segregate to grain boundaries and contribute to intergranular cracking.[22] However, these results indicate that γ' phase acts as a B trap during processing. Furthermore, although not shown on any of the above proxigrams, P, which is also a known contributor to intergranular

cracking increases from 0.01 to 0.03 at% within γ', further indicating that γ' serves to trap some of the harmful constituents.

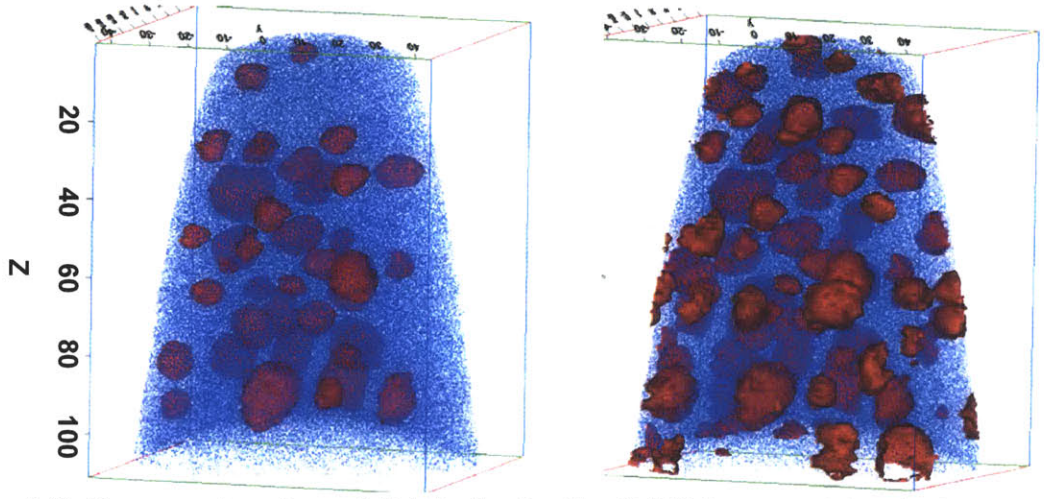

Figure 2-9: Gamma prime size and distribution in alloy X-750, image on left only shows complete γ' precipitates and image on right includes γ' that intersects APT reconstruction surface, dimensions in nm

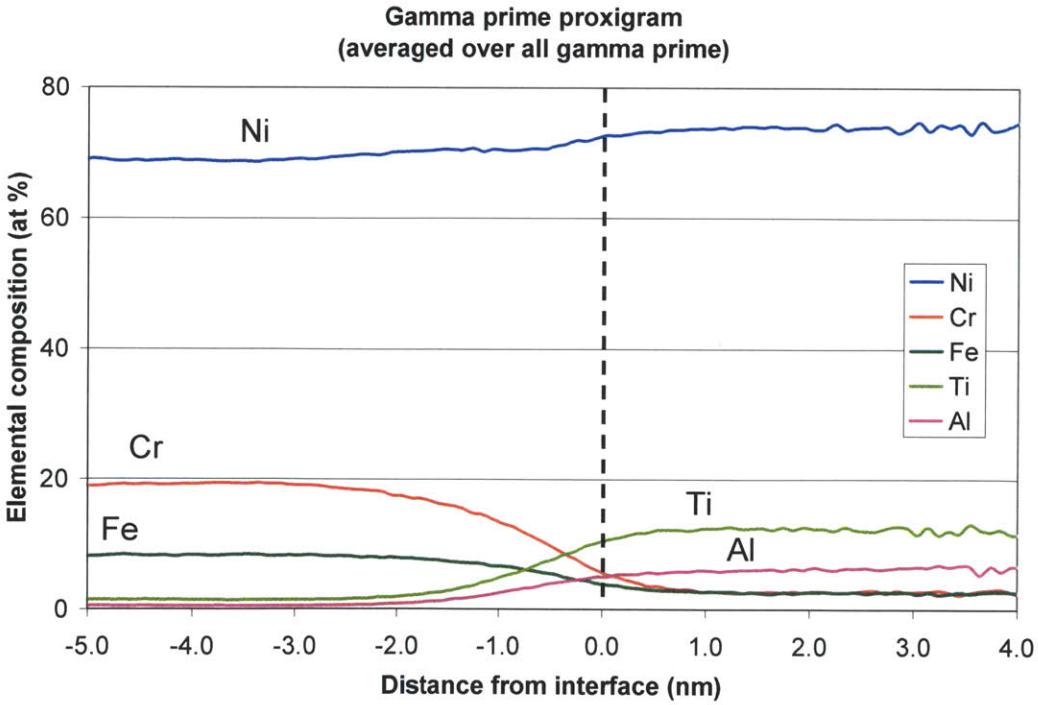

Figure 2-10: Compositional profiles in γ'

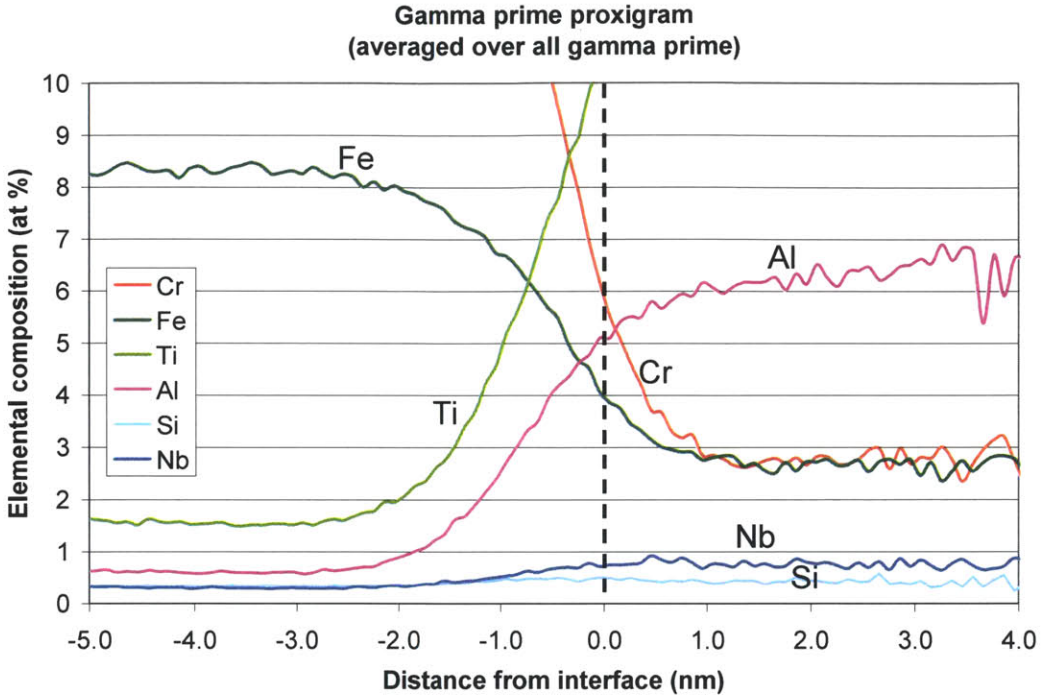

Figure 2-11: Compositional profiles in γ' (focused on 0-10 at% range)

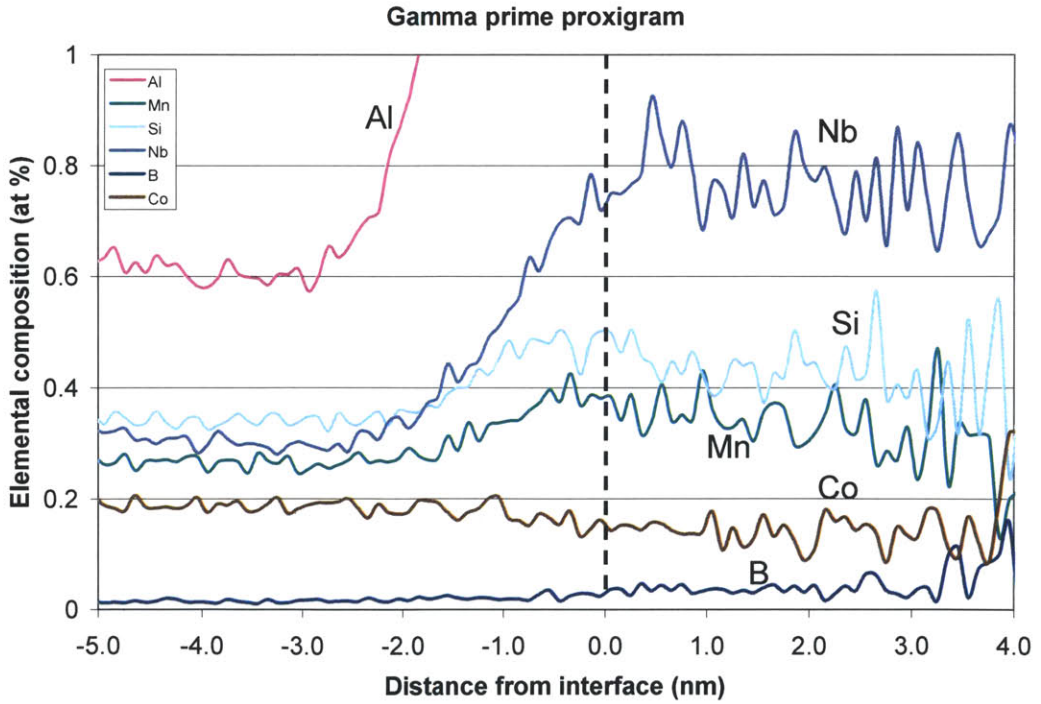

Figure 2-12: Compositional profiles in γ' (focused on 0-1 at% range)

It is important to make a note here about the resolution of the APT technique and how it affects the composition profiles across the γ/γ' interface. The atom probe has a sub-nanometer resolution, but the method employed to average the elemental positions can affect the perceived profiles. A good reference and discussion on the method employed by APT for assigning atomic locations and their respective local elemental enrichment is provided in [23]. This technique uses a Gaussian distribution to "smear" the elemental location in the localized reconstruction and may have an effect on the perceived elemental gradients in the above three figures. The actual elemental composition profile across a precipitate/matrix interface should be sharper due to the presence of a phase boundary. For example, Figure 2-13 the γ/γ' interface was analyzed on AM1 alloy and clearly shows a sharp transition between the two phases.[24] The $L1_2$ Ni_3Al phase is rich in Ni, Al, and to a lesser degree Ti. The transition between the chromium-rich matrix and the Al-rich γ' occurs on a {002} plane. The plane on the γ' side of the interface is rich in Al.

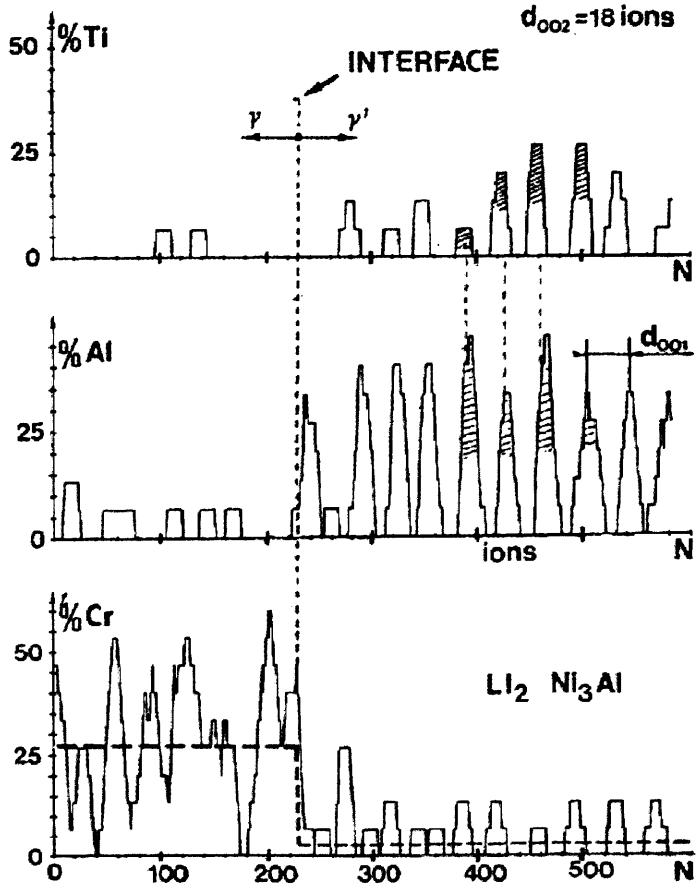

Figure 2-13: Atom microprobe depth concentration profile that shows the sharp transition between the γ matrix and γ' precipitate, (x-axis is ion count, y-axis is composition in at %)[24]

2.3 Mechanical Properties

Various tests were performed to document the mechanical properties of alloy X-750. Although alloy X-750 is a mature material and the properties are well documented, properties can vary for an alloy between heat treatments and also for the same heat treatment but different heats. The mechanical properties for alloy X-750 used in this work were determined with tensile and fracture toughness tests. The published values for various room-temperature tensile properties in the HTH condition pertinent to this work are provided in Table 2-4 and the fracture properties are presented in Table 2-5.

Table 2-4: Alloy X-750 tensile properties [25]

Temperature (°C)	Young's Modulus, E GPa (Msi)	Yield Strength MPa (ksi)	Ultimate Tensile Strength MPa (ksi)
25	213.7 (31.0)	841.2 (122.0)	1241.1 (180.0)
288	196.5 (28.5)	670.8 (101.5)	1033.5 (149.9)

Table 2-5: Alloy X-750 air fracture toughness properties[25]

Temperature (°C)	Fracture Toughness, K_{IC} MPa$\sqrt{m}$ (ksi$\sqrt{in}$)
25	145 (132)
288	155 (141)

2.3.2 Mechanical and Fracture Properties

The mechanical properties of alloy X-750 have been reported extensively, and a brief overview is provided here.

Raymond compared the fracture properties of the AH and HTH treated materials and noted that removing the γ' denuded zone in the AH also increases ductility.[8] Using a TEM to better understand the fracture behavior Raymond found that the HTH treated material contains a high density of dislocations near the grain boundaries, while the AH treated specimens have a random distribution of dislocations, which explains the increase in ductility in the AH materials.

In 1979, Mills reported the effect of temperature on tensile fracture properties and in 1981 he reported on the fracture toughness for the AH treated.[15,26] Mills reported that the yield strength decreased slightly from 640 to 610 MPa and the ultimate tensile strength decreased from 1040 to 1010 MPa, when the temperature was raised from 24 °C to 316 °C, respectively. The J_{IC}

fracture toughness increased from 102 to 130 kJ/m^2 when the temperature was raised from 24 °C to 427 °C.

The γ' phase in alloy X-750 is the primary strengthening mechanism. Decker [27] discussed the interaction differences between dislocations and γ' for the AH and HTH heat treatments. Recall that the γ' precipitates in AH are coarse due to the intermediate aging at 885 °C and the HTH contains a distribution of fine γ' precipitates. Overall, the fine γ' strengthen alloy X-750 more than the coarse γ' precipitates. During deformation the dislocations cut through the fine γ', while the coarse γ' precipitates require a dislocation to either pass via a climb or looping mechanism. Decker found that, during γ' cutting, dislocations with **b** = a/2<110> were found to glide in pairs. It was postulated that the dislocation pairs form because the glide motion of the leading dislocation is impeded as it must create antiphase boundary, while the motion of the second dislocation is assisted because it annihilates the antiphase boundary. Also, the coherency strains contribute to the strengthening because they essentially make the γ' precipitate appear larger, increasing the difficulty for both the bypass and cutting mechanisms.

The fracture behavior reported by Mills [15] is consistent with the theory presented by Decker. At room temperature the dislocation network was uniformly distributed, but dislocations existed as singles, not pairs, which is a result of dislocation pinning on γ' precipitates. Therefore, the grain boundary carbide-matrix interface will experience a stress buildup and lead to intergranular fracture because the stresses cannot be relieved in the bulk matrix. At elevated temperatures the dislocations are able to cut through the γ' precipitates and appear as pairs. This results in a transition from intergranular to transgranular fracture because now the dislocation movement serves as method to relieve grain boundary stresses in the bulk.

Miglin reported the effect of heat treatment on the impact properties of alloy X-750 by performing Charpy V-Notch tests.[17] The variability of impact toughness is a function of carbide presence on the grain boundary. The maximum hardness was achieved with coherent, intermetallic γ' precipitates, which corresponded to the 100 h aging at 704°C. The formation and growth of incoherent intermetallic precipitates result in a reduction in the hardness values.

In 2004 Ferreño reported the effect of heat treatment on the yield and ultimate tensile strength. The heat treatments investigated are listed in

Table **2-2** and the results are presented in Figure 2-14. The $M_{23}C_6$ carbides are responsible for the hardening. The SA heat treatment exhibits lower hardness values because the heat treatment consists of only an annealing step (no hardening). Thus, the grain boundary $M_{23}C_6$ carbides are not permitted to form. The other heat treatments all undergo an aging step, which is the source of their similar hardness properties.

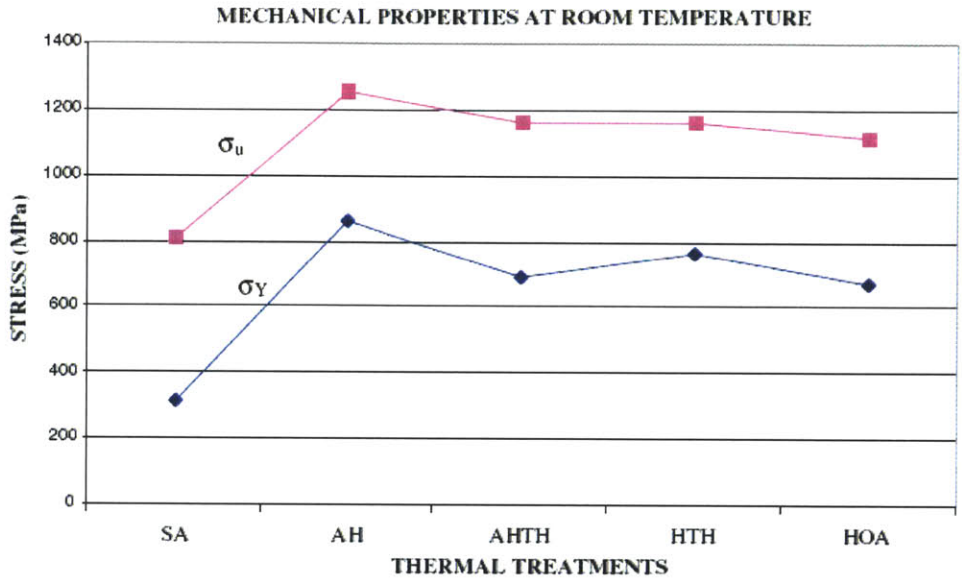

Figure 2-14: Effect of heat treatment on strength of Alloy X-750 [5]

2.3.3 Fracture Toughness Review

The fracture toughness of alloy X-750 has been evaluated by various researchers in various environments.[15, 26, 28-31] This review is focused on the fracture variables pertinent to light water reactors that are known to change fracture properties in nickel alloys, such as effects of hydrogen and neutron irradiation. These effects are compared to fracture toughness values in air at room and high temperature.

Symons and Thompson investigated the effect of hydrogen on fracture toughness at room temperature [28], and later Symons reported on the effect of hydrogen on fracture toughness at elevated temperatures.[29] The fracture toughness testing was performed using compact tension and notch bend specimens in the HTH condition. Each specimen was charged in an autoclave with hydrogen to saturate with dissolved hydrogen. The resulting fracture toughness of the

hydrogen charged specimens was as low as 42 MPa$\sqrt{m}$ and corresponded to 65 ppm dissolved hydrogen. The fracture toughness when tested in air was reported as 147 MPa$\sqrt{m}$. Previous work using plateau etching* showed that voids initiated around grain boundary carbides and then grew by plastic deformation. The remarkable decrease in fracture toughness is attributed to hydrogen causing a reduced strain required to initiate defects at the grain boundary carbides by reducing the strength of the interface or increasing the rate of void growth by increasing the local stress due to localized hydrogen pressure.[30] Hydrogen embrittlement can involve crack initiation and growth of microvoids ahead of the crack. Hydrogen may diffuse to the dislocation stress fields and be transported along the dislocation to the grain boundary. It was also noted that both critical stress and critical strain were necessary for fracture, with this case the critical strain being the limiting factor and controlled the fracture process for the onset of crack growth. Previous work on uniaxial specimens showed that plasticity is required in the presence of hydrogen for embrittlement of alloy X-750 to occur.[31] This is further confirmed with the fracture morphology transitioning from a mixture of transgranular dimples and fine intergranular dimples to a predominantly intergranular dimpled surface.

It was postulated that hydrogen would not affect the fracture behavior of alloy X-750 at temperatures representative of light water reactor operating conditions.[32] However, while hydrogen embrittlement of the nickel-base alloy is not commonly reported at elevated temperatures, Symons showed that embrittlement is possible under conditions where hydrogen levels are typical of those developed in the corrosion reactions during SCC.[31] Symons reported that alloy X-750 in the HTH condition was severely embrittled in hydrogen gas environments, for testing temperatures of 260 °C and 338 °C. At 260 °C, K_{Jc} was reduced from 220 to 68 MPa$\sqrt{m}$, while at 338 °C K_{Jc} was reduced from 230 to 87 MPa$\sqrt{m}$. The change in fracture toughness for elevated temperature testing was similar to the room temperature testing with the morphology changing from a predominantly transgranular ductile dimple surface to an intergranular dimpled surface.

In 1980, Mills reported that fracture is a mechanism of microvoid coalescence along the grain boundary denuded zone for alloy X-750 in the AH condition.[15] The microvoids are initiated at the $M_{23}C_6$ carbides, and coalesce within the denuded zone. The denuded zone is a narrow region

* Plateau etching is a method in which the plane normal to the fracture surface is etched to reveal the underlying microstructure.

directly adjacent to the grain boundary that is denude of normal (intragranular) γ', but contains fine γ'. In 1983, Mills investigated the effect of neutron irradiation on fracture toughness.[33] The test specimens were subjected to exposures ranging from 3 to 16 displacements per atom (dpa) and found that the fracture toughness, at these exposures, was independent of irradiation damage. The fracture toughness* decreased from an unirradiated condition of 130 kJ/m^2 to a saturated value of 76 kJ/m^2. The fracture toughness appeared to saturate at an exposure less than 3 dpa, but the exact value was not pinpointed. Mills noted that 3 dpa resulted in small faulted dislocation loops through the material and increasing the exposure to 16 dpa caused an overlapping of the dislocation stress fields resulting in the dislocations unfaulting into dislocation tangles. The yield strength increased from approximately 570 to 975 MPa at 3 dpa, but decreased with increasing dose to approximately 900 MPa at 16 dpa. The fracture surface exhibited nearly complete intergranular dimple rupture, which is attributed to the stress concentrations at the grain boundaries causing decohesion between the carbides and matrix. The coalescence of microvoids produced the dimpled rupture texture. Mills concluded that the inferior J_{IC} fracture toughness and tearing resistance after irradiation was due to the strengthened matrix coupled with severe dislocation channeling. The material exposed to 16 dpa also exhibited a high density of voids, but did not influence fracture behavior.

2.4 Crack Growth Testing in High Temperature Water

Considerable work has been performed on the susceptibility of alloy X-750 to stress corrosion cracking behavior for a variety of heat treatments.[14, 18, 34] The two most common heat treatments for light water reactor applications are the AH and HTH treatments. However, the most researched heat treatment, with respect to SCC behavior, is the AH treatment. The AH treatment is more susceptible to SCC, and is being replaced by, HTH treated components. However, little work has been focused on the HTH treatment and the cracking behavior is not well understood. Moreover, it is important to note here that of the research performed on the HTH condition, none have measured in situ crack growth rates. Moreover, much of the SCC testing has been conducted in environments not representative of LWR condition. During the 1970s, a number of researchers published data on stress corrosion cracking properties of alloy X-750, but little work was focused on the corrosion fatigue properties. A considerable amount of

* Note, the results were reported in terms of toughness (G_{IC}) and not fracture toughness (K_{IC})

research has been devoted to the corrosive properties in room and high temperature air testing, but little testing has been completed for aqueous environments. Furthermore, the research focused on aqueous environment testing has been relatively crude, using specimen geometries such as the U-bend test, which is practically incapable of providing crack growth results and is more often used as a screening test for susceptibility. Virtually no long term crack growth rate testing has been performed for the HTH heat treatment in representative aqueous environments. Moreover, much of the environmental degradation work has been focused on crack initiation and not growth.[35-39]

Test techniques that have been popular to document the effect of SCC include the rising load test, inclusions analysis, intergranular attack, potentiodynamic anodic polarization test, and raised grain boundary examinations. These techniques can determine the degree of intergranular attack in various environments, such as boiling acid (Huey test), but are not representative of LWR environments and have yielded conflicting results. Many of these tests are used due to their experimental ease, but their results need to be used with caution.

2.4.1 Fatigue Crack Growth

During the mid-1980s, Elliott investigated the susceptibility of various heat treatments of alloy X-750 to fatigue cracking.[14] Testing involved fatigue loading at various stress intensity levels in an inert helium environment and in air-saturated and deaerated high purity water at various temperatures. The crack growth rates were reported in terms of da/dN versus ΔK. In the helium environment, the HTH treatment did not exhibit any cracking dependence on loading frequency and experienced lower crack growth rates than the AH treatment. However, in deaerated 93 °C water, the HTH material exhibited a frequency dependence on cracking, but the AH material did not. The fracture path in the HTH material followed a highly crystallographic path and experienced extensive slip deformation in the grains immediately above and below the crack plane. A small frequency dependence was reported for fatigue crack growth in aqueous environments (93 and 288 °C and air-saturated and deaerated). The 0.1 Hz frequency loading patterns exhibited slightly lower fatigue crack growth rates than the 10 Hz. The fracture surfaces from the aqueous testing exhibited a transgranular appearance at 10 Hz and the 0.1 Hz fracture surface was characterized with less crystallographic nature than the higher frequency and also contained many fine secondary cracks. Fatigue cracks propagated faster in aqueous environments than in inert helium.[40]

2.4.2 Stress Corrosion Cracking

Ballinger, et al. performed SCC tests on multiple alloy X-750 heat treatments in PWR, deaerated, and hydrogen water chemistry.[6] Bolt-loaded 1TCT specimens were used and operated under a falling K profile. These tests were divided into crack initiation and propagation. In deaerated water at 288 °C the HTH treatment resulted in a peak crack growth rate of 7.5×10^{-8} mm/s with a final K=38.4 MPa$\sqrt{m}$. Similarly, crack growth rates of 8.8×10^{-8} and 4.4×10^{-8} mm/s were recorded for PWR and hydrogenated water chemistries, respectively. It is important to note here that these crack growth rates were measured by recording the final length and represent the average rates and did not take into account any form of inhomogeneous growth, such as with a branched crack front.

In the 1990s, Shen explored the susceptibility to SCC of alloys 600 and X-750 in high-temperature (380°C), deaerated water and steam.[41] Shen used U-bend specimens heat treated in the AH and HTH conditions. The analysis of SCC susceptibility when using U-bend specimens has its merit in the post mortem analysis because the crack growth rate is merely recorded as the time required to crack through and break the specimen. The reported values of crack growth rate for the AH and HTH samples were 3×10^{-6} mm/s and 3×10^{-7} mm/s, respectively. The crack growth rates are consistent with previous results which showed higher susceptibility of the AH treatment. Shen concluded that the IGSCC occurred through the nucleation, growth, and linkup of grain boundary voids, rather than by grain boundary dissolution. The crack growth rate was strongly affected by the heat treatment, namely the effect of controlling the carbon. The HTH treated material has much of the carbon in grain boundary $M_{23}C_6$ carbide form and not available for reaction with hydrogen. This phenomena is more deleterious to the AH treated material because it does not form grain boundary carbides. A higher crack growth rate would occur if the carbon was kept in solution rather than being allowed to precipitate as grain boundary carbides. If carbon was allowed to precipitate into stable grain boundary carbides, less carbon was available to react with hydrogen and form high pressure methane, which can agglomerate at grain boundary voids and increases decohesion between grains. The nucleation of methane bubbles only occurred near the source of hydrogen and the high pressure assisted in void growth. The grain boundary voids initiated via slip impingement and were spaced at approximately 0.2 μm. It was estimated that the equilibrium methane pressure in a freshly quenched material is approximately three times the flow stress of the material.[42] However, the methane effect is most applicable for temperatures higher than those tested in this work. The

thermodynamics for hydrogen and carbon to react and form methane is favorable at temperatures greater than 400 °C, which would correspond to high-temperature steam cracking. It should be noted here that the methane theory for bubble-assisted grain boundary decohesion is unlikely because the experimental testing by Shen was performed at 380 °C, which is too low to favor the thermodynamics of methane formation. The presence of methane was suggested, not measured.

It was further noted that the precipitation of carbide at the grain boundary would decrease the carbon activity in the matrix near the boundary by a factor of 30.[43] This drastically retards the IGSCC growth, but does not completely stop it.

In the late 1990s Mills *et al.* [44] researched hydrogen embrittlement, grain boundary segregation, and SCC of alloy X-750 in low- and high-temperature water for AH, BH, and HTH heat treatments. The high-temperature stress corrosion cracking (HTSCC) tests were performed between 288 °C and 360 °C on bolt-loaded CT specimens. The objectives were to study the time required to initiate SCC from a notch, time required to initiate SCC from a fatigue precrack, and crack growth rates. The results and conclusions from Mills' work are as follows:

1. All heat treatments covered were susceptible to rapid low-temperature crack propagation (LTCP), with growth rates as high as 7 mm/min (for the BH condition).* The LTCP is due to hydrogen embrittlement of the grain boundaries. Mills argued that hydrogen diffuses to the triaxial stress region ahead of the crack, which lowers the energy barrier to crack extension.
2. Variability in LTCP resistance is correlated with the degree of phosphorus segregation to grain boundaries. HTH was superior to AH and BH conditions due to its reduced phosphorus segregation to the grain boundaries. This is due to the high temperature anneal of HTH, which allows grain coarsening, and, subsequently produces a grain boundary structure that decreases phosphorus content at grain boundaries during the 704 °C aging. In addition, the superior performance of HTH is attributed to a reduced intragranular γ', large grain size, and high density of intergranular $M_{23}C_6$ carbides, rather than niobium- and titanium-rich MC carbides.
3. Rapid cracking does not occur above 150 °C because the degree of hydrogen enrichment decreases dramatically and the fracture resistance of the grain boundaries increases.

* The BH treated material is not used due to its high susceptibility to SCC.

HTSCC exhibits growth rates approximately one order of magnitude lower than LTCP. HTSCC requires high activation energy for growth: 33.7 and 41.4 kcal/mol for AH and HTH treated materials, respectively. This indicates that the controlling mechanism is a thermally activated slip process.

4. The HTSCC initiation time was one to three orders of magnitude longer for HTH than AH, and the crack growth rate was one to two orders of magnitude lower.
5. The failure scenario for alloy X-750 involves crack initiation and growth by HTSCC for fatigue, followed by LTCP, when a critical flaw size is reached.

Andresen reported on the stress corrosion crack growth rate response of AH and HTH alloy X-750 in high temperature water as a function of loading, corrosion potential, and water purity.[45] Andresen tested 0.5TCT specimens in an autoclave arrangement similar to the testing in this thesis. It was reported that AH and HTH treatments underwent similar crack growth rates at high corrosion potential, but HTH consistently exhibited lower rates at low potential. It is important to note here that Andresen used 2000 ppb dissolved oxygen to raise the electrochemical potential and H_2SO_4 to raise the conductivity. These conditions are not representative of current LWR water chemistries. Ultimately, Andresen concluded that a more controlled evaluation of the HTH condition is necessary.

Irradiation Effects on SCC

Bajaj performed in reactor SCC tests of HTH alloy X-750 using bolt-loaded CT specimens.[22] At fluences above 10^{19} n/cm^2 the SCC resistance of HTH was significantly reduced. At low fluences (10^{14} to 10^{18} n/cm^2) only a slight degradation in SCC resistance occurred, and was attributed to radiolysis effects. Bajaj also noted that the presence of boron (a trace element) can increase the susceptibility to irradiation assisted SCC by promoting grain boundary helium embrittlement via transmutation of $B^{10}(n,\alpha)Li^7$ reaction. Irradiation only caused a slight depletion (2-2.5% by weight) of chromium at the grain and phase boundaries. It was postulated that the chromium depletion was not severe enough to significantly change the SCC resistance.

2.7 Summary

A detailed discussion was presented in this chapter regarding the performance of alloy X-750 with regard to high-purity aqueous environments. The mechanical properties of alloy X-750 were documented in this chapter along with characterization of the heat of X-750 used in this

work. Much work has been completed on improving the engineering properties and the microstructure through various heat treatments to increase the SCC resistance. Also, background and history as to the previous SCC and corrosion fatigue studies was presented here. Although conflicting results have been produced documenting the "best" heat treatment to resist SCC, the general consensus is that the HTH condition is best suited for light water reactor environments, and further analyses are necessary to understand the fundamental mechanisms active in crack propagation.

2.8 References

1. INCONEL Alloy X-750, 4th ed., Huntington Alloys, Inc., 1979.
2. A.A. Stein and M.S. Gennaro, "Material Specification for alloy X-750 for use in LWR internal components, revision 1", EPRI NP-7032 RP-2181-4; 1990.
3. World wide web: www.specialmetals.com, accessed 1 May 2011.
4. Intergranular Corrosion Test (IGC), per ASTM A262, Practice C.
5. D. Ferreño, I. Gorrochategui, L. Sanchez and F. Guitierrez-Solana, "Optimization of heat treatment for improvement of IGSCC properties of an X-750 alloy", Engineering Failure Analysis 11, pp. 799-810, 2004.
6. R.G. Ballinger, C.S. Elliott, S. Hwang and J. Prybylowksy, "The effect of thermal treatment on the fracture properties of alloy X-750 in aqueous environments", EPRI Report CR-102-437; 1993.
7. M. Miglin and H.A. Domain, "Metallurgical characterization of Ni-Cr-Fe alloys as related to stress corrosion cracking in light water reactors," Proceedings from the International Conference on the Corrosion of Nickel Base Alloys, ASM, Cincinnati, OH, 1984.
8. E.L. Raymond, "Effect of grain boundary denudation of gamma prime on notch-rupture ductility of Inconel nickel-chromium alloys X-750 and 718", Transactions of the Metallurgical Society of AIME, Vol. 239, pp.1415-1422, 1967.
9. G.S. Was, H.H. Tischner and R.M. Latanison, "The influence of thermal treatment on the chemistry and structure of grain boundaries in Inconel 600," Metallurgical and Materials Transactions A, Vol. 12, No. 8, pp. 1397-1408, 1981.

10. A. Turnbull, R.G. Ballinger, I.S. Hwang, M.M. Morra, M. Psaila-Dombrowski and R.M. Gates, "Hydrogen transport in nickel-base alloys," Metallurgical and Materials Transactions A, Vol. 23, pp. 3231-3244, 1992.

11. R.M. Latanision, "Physical metallurgy of nickel-base alloys as it relates to corrosion", Journal of Materials Engineering, Vol. 10, pp. 143-162, 1988.

12. L. Ljungberg, EPRI International Workshop on Low Temperature Sensitization, Paper No. 5, 1982.

13. S. Floreen and J.L. Nelson, "The effects of heat treatment and composition on the stress corrosion cracking resistance of Inconel alloy X-750," Metallurgical and Materials Transactions A, Vol. 14, pp. 133-139, 1983.

14. C.K. Elliott, "Effect of Thermal Treatment on the Fracture Properties of Alloy X-750 in Aqueous Environments", Ph.D. Thesis, Massachusetts Institute of Technology, 1985.

15. W.J. Mills, "The deformation and fracture characteristics of Inconel X-750 at room temperature and elevated temperatures", Metallurgical and Materials Transactions A, Vol. 11, No. 6, pp. 1039-1047, 1980.

16. S. Floreen, "Microstructural and environmental effects during creep crack growth in a superalloy", Elastic-Plastic Fracture, Vol. 1, pp. 708-720, 1983.

17. M.T. Miglin and H.A. Domain, "Microstructure and stress corrosion resistance of alloys X750, 718, and A286 in light water reactor environments", Journal of Materials Engineering, Vol. 9, No. 2, pp. 113-132, 1987.

18. C.A. Grove and L.D. Petzold, "Mechanism of stress corrosion cracking of Alloy X-750 in high purity water", Journal of Materials for Energy Systems, Vol. 7 No. 2, pp. 147-162, 1985.

19. B. Mishra, A.K. Sinha and J.J. Moore, J.J., "Effect of Single Aging on Microstructure and Impact Property of Inconel X-750", Metallurgical Transactions A, Volume 16. pp. 821-829, 1985.

20. J.W. Edington, *Interpretation of Transmission Electron Micrographs*, University Press, Belfast, 1975.

21. O. Hellman, J. Vandenbroucke, J. Blatz du Rivage and D. N. Seidman, "Application Software for data analysis for three-dimensional atom probe microscopy", Materials Science and Engineering, A327, pp. 29-33, 2002.

22. R. Bajaj, W.J. Mills, M.R. Lebo, B.Z. Hyatt and M.G. Burke, "Irradiation-assisted stress corrosion cracking of HTH alloy X-750 and alloy 625", Meeting of the International Collaborative Group on Irradiation-Assisted Stress Corrosion Cracking (ICGIASCC), 32 p., 1994.

23. O.C. Hellman, J.B. du Ravage and D.N. Seidman, "Efficient sampling for three-dimensional atom probe microscopy data", Ultramicroscopy, Vol. 95, pp. 199-205, 2003.

24. M. Durand-Charre, *The Microstructure of Superalloys*, CRC Press, London, p. 84, 1997.

25. World Wide Web: http://www.specialmetals.com/documents/Inconel% 20alloy%20X-750.pdf, Accessed 13 May 2011.

26. W.J. Mills "Effect of temperature on the fracture toughness behavior of Inconel X-750", *Fractography and Materials Science*, Eds. L.N. Gilbertson and R.D. Zipp ASTM STP 733, pp. 98-114, 1981.

27. R.F. Decker, "Strengthening mechanisms in nickel-base superalloys", Strengthening Mechanisms in Nickel-Base Superalloys, Intl. Nickel Co., pp. 275-298, 1969.

28. D. Symons and A.W. Thompson, "The effect of hydrogen on the fracture toughness of alloy X-750", Metallurgical and Materials Transactions A, Volume 28, pp. 817-823, 1997.

29. D. Symons, "The effect of hydrogen on the fracture toughness of alloy X-750 at elevated temperatures," Journal of Nuclear Materials, Vol. 265, pp. 225-231, 1999.

30. R.O. Ritchie, W.L. Server and R.A. Wullaert, "Critical fracture stress and fracture strain models for the prediction of lower and upper shelf toughness in nuclear pressure vessel steels," Metallurgical and Materials Transactions A, Vol. 10, pp. 1557-1570, 1979.

31. D.M. Symons and A.W. Thompson, "The effect of hydrogen on the fracture toughness of alloy X-750," Metallurgical and Materials Transactions A, Vol. 27, pp. 101-110, 1996.

32. P.L. Andresen and T.M. Angeliu, "Evaluation of the role of hydrogen in SCC hot water", Corrosion/97, NACE, paper 195, 1997.

33. W.J. Mills, "Postirradiation fracture toughness of Inconel X-750", Engineering Fracture Mechanics, Vol. 18, No. 3, pp. 601-607, 1983.

34. T. Kekkonen and H. Hänninen, "The effect of heat treatment on the microstructure and corrosion resistance of Inconel X-750 alloy," Corrosion Science, Vol. 25, Issues 8-9, pp. 789-803, 1985.

35. M. Yamamoto, J. Kuniya and S. Uchida, "Threshold for stress corrosion cracking initiation of alloy X750 under long term uniaxial constant load test in high-temperature water", Corrosion, Vol. 60, Issue 3, pp. 229-236, 2004.

36. M. Coucault and C. Benhamou, "Influence of the surface condition on the susceptibility of alloy X-750 to crack initiation in PWR primary water", Proceedings from the Sixth International Symposium on Environmental Degradation of Materials – Nuclear Power Systems - Water Reactors, pp. 791-798, 1993.

37. M.M. Hall and D.M. Symons, "Strain energy density-distance criterion for the initiation of stress corrosion cracking of alloy X-750", ASTM Special Technical Publication, v. 1298, p. 167-181, 1997.

38. E. Richey, D.S. Morton and M.K. Schurman, "SCC initiation testing of nickel-based alloys using *in-situ* monitored uniaxial tensile specimens," Proceedings from the Twelfth International Symposium on Environmental Degradation of Materials – Nuclear Power Systems - Water Reactors, pp. 947-958, 2005.

39. D.J. Morrison and J.C. Moosbrugger, "Effect of grain size on cyclic plasticity and fatigue crack initiation in nickel", International Journal of Fatigue, Vol. 19, No. 1, pp. S51-S59, 1997.

40. C.K. Sheeks, R.G. Ballinger and R.M. Latanison, "Fatigue crack growth of Inconel alloy X-750 in simulated BWR environments," Proceedings – International Congress on Metallic Corrosion, p. 310-316, 1984.

41. Y. Shen and P.G. Shewmon, "Intergranular stress corrosion cracking of alloy 600 and X-750 in high-temperature deaerated water/steam", Metallurgical and Materials Transactions A, Vol. 22, pp. 1857-1864, 1991.

42. C.H. Shen and P.G. Shewmon, "A mechanism for hydrogen-induced intergranular stress corrosion cracking in alloy 600," Metallurgical and Material Transactions A, Vol. 21, No. 5, pp. 1261-71, 1990.

43. K. Natesan and T.F. Kassner, *Metall. Trans.*, 1973, vol. 4, pp. 2557-66.

44. W.J. Mills, M.R. Lebo and J.J. Kearns, "Hydrogen embrittlement, grain boundary segregation, and stress corrosion cracking of alloy X-750 in low- and high-temperature water", Metallurgical and Materials Transactions A, Vol. 30, pp. 1579-96, 1999.

45. P.L. Andresen, P.W. Emigh and R.M Horn, "Stress corrosion crack growth rate response of AH & HTH alloy X-750 in high temperature water", Corrosion/03, Paper No. 03660, 2003.

Chapter 3 – Stress Corrosion Cracking Results

3.1 Introduction

Stress corrosion cracking tests were performed in dissolved oxygen and dissolved hydrogen chemistries of pure BWR water at 93 and 288 °C. The purpose of these tests was to understand the influence of various factors, such as stress intensity and water chemistry, on crack growth rate, both in fatigue and constant K loading. Testing was performed in both normal water chemistry (NWC) and hydrogen water chemistry (HWC).

3.2 Experimental Method

The experimental part is divided into two sections: The first being the in-situ stress corrosion crack growth rate measurements and the second being the post-test microstructural and fracture surface documentation. The description for the SCC testing is presented here.

3.2.1 Sample Preparation

The 1T compact tension (CT) specimens were machined in the R-C orientation (crack growing in radial direction) from an 8.9 cm (3.5 in) round bar of alloy X-750 in the commercial HTH heat treatment. The fatigue starter notch was electro discharge machined (EDM) to a length of 0.8 in (0.4 a/W)*. Samples were machined with 10% semicircular side grooves on each side to reduce crack tunneling and to control the SCC propagation direction. One compression cycle to P_{max} (K=25 MPa$\sqrt{m}$) was conducted to facilitate fatigue crack initiation. Fatigue crack extension from the starter notch to approximately 0.44 a/W was performed in room-temperature air at a maximum stress intensity of 25 MPa$\sqrt{m}$ and 20 Hz at a load ratio (P_{min}/P_{max}) R=0.1. The fatigue crack was further extended in the oxygen containing aqueous test conditions within the autoclave. The in-autoclave fatigue process utilized an increasing load ratio and decreasing cycle frequency sequence to transition the crack morphology and plastic zone from fatigue crack extension to stress corrosion crack growth. A representative crack-conditioning test plan ending in an SCC step is recorded in Table 3-1.

* The 'a/W' unit is a standard unit to express crack length in a compact tension specimen. The variable 'a' is the crack length and 'W' is the total length of the specimen. An a/W value of 0.5 indicates that the crack has propagated half the total possible specimen length.

Table 3-1: Crack-conditioning test plan

Step	Frequency (Hz)	Wave Form	K_{max} (MPa$\sqrt{m}$)	R-ratio
1	1	Sine	25.0	0.5
2	1	Sine	26.5	0.5
3	1	Sine	28	0.6
4	1	Sine	28	0.7
5	0.1	Sine	28	0.7
6	0.01	Sine	28	0.7
7	0.001	Sine	28	0.7
8	-	Constant	28	-

3.2.2 Experimental Test Loop

The test loop schematic is shown in Figure 3-1, and the DCPD measurement schematic is shown in Figure 3-2. The water for the test loop was supplied in the demineralized and deionized condition. This water was processed through a second demineralizer (Barnstead Model D4511) and Barnstead Model D3750 0.2 μm filter before flowing into a 6.4 cm diameter by 183 cm long glass water column. The water was circulated through the test loop by a Pulsafeeder model 7120 hydraulically-actuated diaphragm pump. A low pressure pump was used to provide positive pressure to the Pulsafeeder pump and circulate excess water through the glass column. System pressure was controlled with a back-pressure regulator then measured for conductivity and dissolved oxygen using a Thornton 770Max multi-channel analyzer. The conductivity probes were Thornton conductivity sensors Model 230-211, and the dissolved oxygen sensor was an AC Tech MC Series M1105SBH. Dissolved gas concentration was controlled by bubbling a gas mixture (either 5% oxygen balance argon or 5% hydrogen balance argon) into the glass water make-up column. The tests were performed in a 4 L titanium autoclave at 9.65 MPa (1400 psi) and 288 °C for 200 ppb dissolved oxygen and 288 °C and 93 °C for dissolved hydrogen water chemistry. The flow rate was maintained at approximately 3.86 L (1 gallon) per hour. NWC corresponds to 200 ppb dissolved oxygen and HWC corresponds to a dissolved hydrogen overpressure. Hydrogen or oxygen overpressure is controlled on the water column using a pack pressure regulator; the amount of overpressure must be determined for each case to ensure the correct amount of dissolved oxygen or hydrogen for given conditions. The technical information for the reference electrode used in this thesis is included in Appendix D.

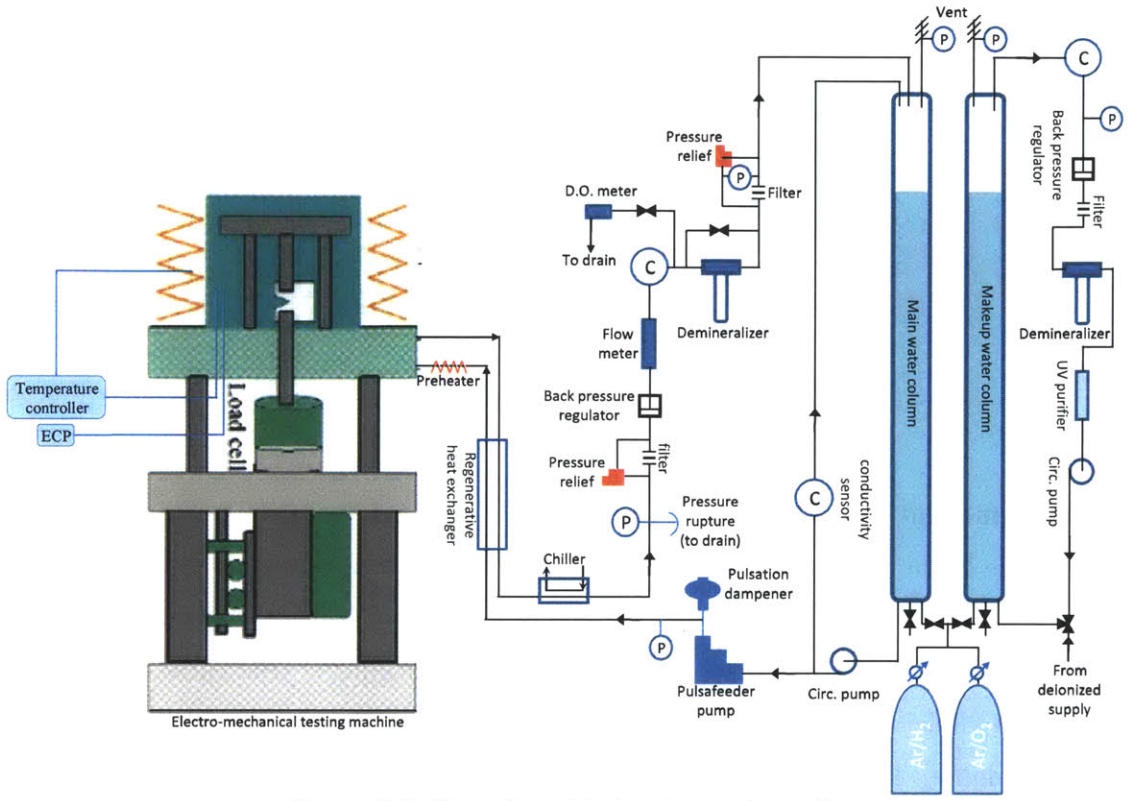

Figure 3-1: Experiment test system schematic

The CT specimens were instrumented with platinum current and potential probe leads for direct current potential drop (DCPD) measurements of crack length. The voltage probes used 0.5 mm (0.02 in) diameter wire and the current probes used 0.81 mm (0.032 in) wire. With high-resolution voltmeters the DCPD technique is known for accurately measuring small crack extensions in-situ. The DCPD arrangement used in this work is shown in Figure 3-2, and the voltage and current probe placement is shown in Figure 3-3. Additional DCPD discussion and information is provided in Appendix C which includes the voltage/crack length relationship and the sampling process. The DCPD technique passes current through the CT specimen and measures the voltage drop. As the crack propagates through the sample the voltage drop increases as less ligament was available to pass current.* The polarity of the applied current was switched every cycle as a means of reducing scatter in measurements. Moreover, a null reading was taken at the beginning of each DCPD cycle to measure a baseline voltage reading. The change in polarity combined with the null reading was used to reduce measurement error associated with thermocouple effects and amplifier offsets. An Agilent nanovolt meter was used

* DCPD essentially relates the measured voltage to an uncracked ligament, and then one can calculate crack length.

to measure the voltage across the sample. The specimen was also instrumented with a 0.81 mm platinum wire to measure the sample electrochemical potential (ECP). Parameters measured and recorded by the computer control included DCPD voltage, time/date, test step, temperature, pressure, inlet and outlet fluid conductivity, specimen load, specimen electrochemical potential, and potential of a platinum reference probe. The specimen and platinum probes were measured with to a Cu/Cu_2O reference probe, which has a +253 mV potential with respect to standard hydrogen electrode. Additional information about the reference electrode, calibration curves, and how it compares to similar environmental conditions in literature is provided in Appendix D.

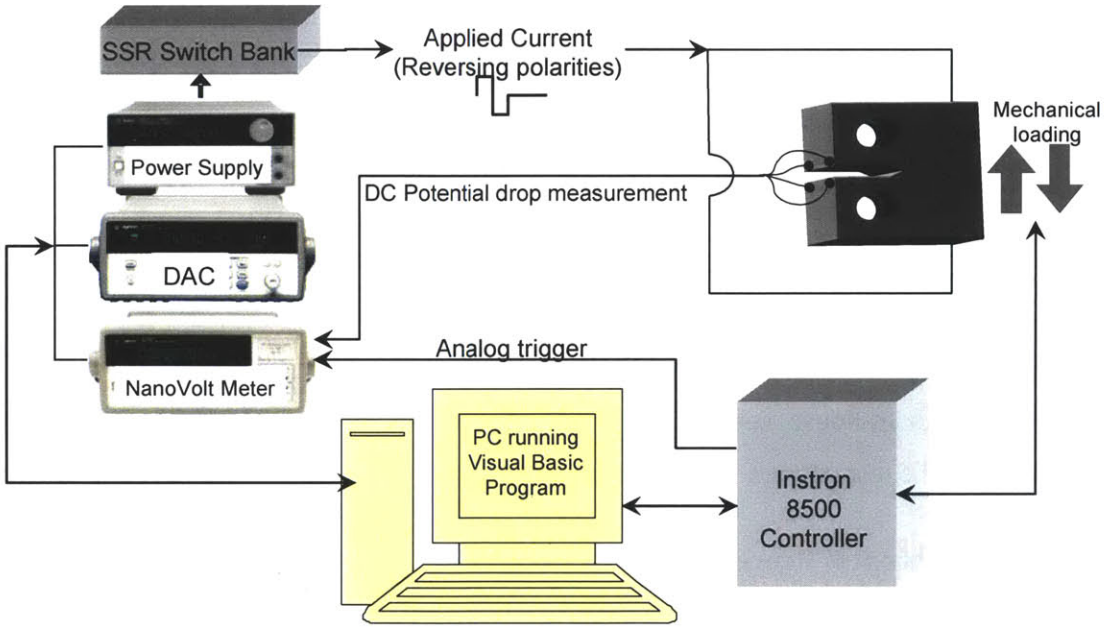

Figure 3-2: DCPD crack measurement system

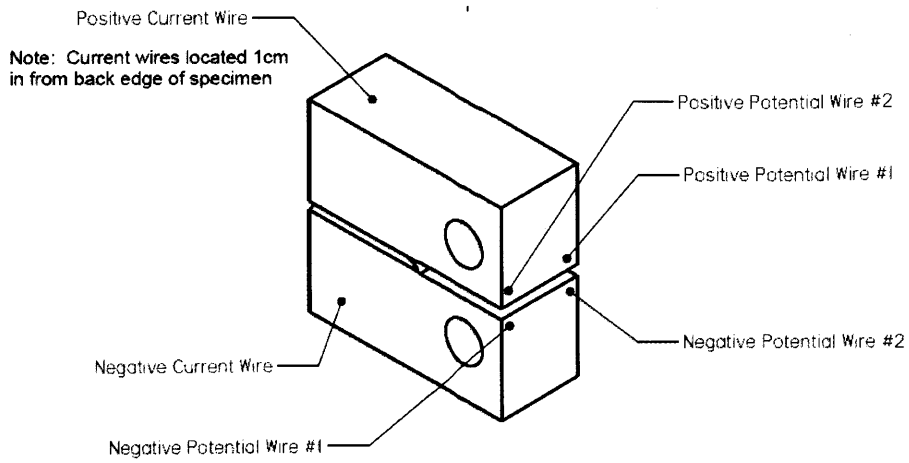

Figure 3-3: DCPD wire placement

The CT specimen was electrically insulated from the autoclave by using zirconia sleeves on the loading pins. Furthermore, the upper pull rod was electrically insulated from the internal load frame by a zirconia washer, and the lower pull rod was electrically isolated from the autoclave using an Omniseal pressure seal. Platinum voltage and current leads were electrically isolated from each other within the autoclave with Teflon insulation and from the autoclave with a Conax pressure fitting with Teflon internals.

Testing was performed using an electro-mechanical testing machine with Instron Model 8560 digital controls. An in-house visual basic program was used to interface with the Instron to control and record the testing parameters and DCPD.

3.2.3 SCC Experimental Procedure

Before placing the CT specimen into the aqueous testing loop, it was ultrasonically cleaned in an ethanol bath. The specimens were then placed in the autoclave and the DCPD and ECP leads were attached by spot welding. Next, the system was sealed, purged with an inert gas, filled with high-purity water, and then pressurized. The loop was run for approximately 24 h at test pressure, but at room temperature, to inspect the system for leaks.

Next, heaters were turned on and the system was brought up to temperature. Nitrogen gas was bubbled into the main water column to deaerated the water and further stabilize the water chemistry. Next, the system was run through a conditioning procedure to remove contamination

from the sample and any that may have been introduced into the test loop while it was open to the atmosphere. The conditioning procedure was as follows:

- Bubble in N_2 to eliminate the effect of chromate on the outlet conductivity. This step was run until the outlet conductivity reached ≈0.06 μS/cm.
- Switch to 100% O_2 gas to burn off chromates.
- Once the outlet conductivity had stabilized to 0.12 μS/cm or better, switch to a gas more representative of the testing conditions (5% O_2 or 5% H_2 balanced with an inert gas).

When the outlet conductivity of the last step reached the target conditions the test was engaged. The shakedown procedure has a variable length and is controlled by the water chemistry. Each step could take as little as a few days to as long as several weeks.

Each test started with fatigue loading to condition the crack from the air-fatigue precracking to one that is more representative of a stress corrosion crack. Each test was run continuously until sufficient data in each test condition was obtained.

3.3 Stress Corrosion Cracking Results

The SCC testing completed in this work focused on exploring the effects of the anodic and cathodic driven SCC processes, at various temperatures, on the same specimen. The duration of the complete test was determined predominantly by the crack growth rate. It was important to allow the test to run sufficiently long for several reasons: Long crack growth provides more mature crack growth rates, provides additional fracture surface for post-test examination, and reduces error associated with comparing the measured crack growth rates (with DCPD) to the actual fracture length. The difference in predicted crack growth extension (with DCPD measurements) and measured crack length (with SEM macrographs) was approximately 4%.

The final step in each test plan was especially important because it determined the end state and conditions of the crack tip. The test was concluded by simply reducing the load to a minimal value (2-3 MPa$\sqrt{m}$) while the system cooled down. No post-test "beachmark" fatigue step was performed while the specimen was in the autoclave. Upon test cooldown, the specimen was removed from the autoclave and sectioned into several pieces, as shown in Figure 3-4, to preserve crack tips for characterization with atom probe tomography and electron microscopy.

One mid-section was subjected to a post-fatigue and fracture step (in air) to delineate the end of the SCC crack and to provide an accessible fracture surface for further examination.

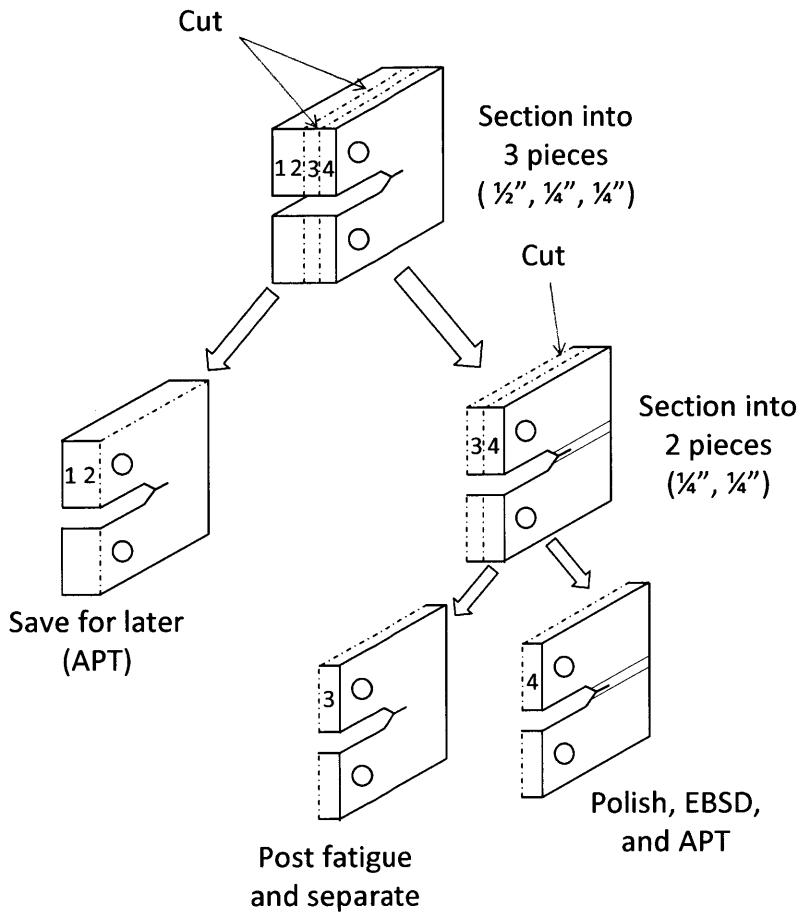

Figure 3-4: Post SCC test specimen sectioning plan

3.3.1 Crack Growth Rate

The fatigue crack growth measurement was performed in air on a servo-hydraulic load frame instrumented with Instron Model 8560 digital controls. The air fatigue crack served as the starter crack for the in-autoclave crack conditioning sequence. The 1TCT specimen was precracked with K_{max}< 25 MPa$\sqrt{m}$ at a rate not exceeding 20 Hz. The fatigue precrack was extended in air with decreasing K_{max} to its final length (target final length was approximately 0.45 a/W) with a final K_{max} approximately 22 MPa$\sqrt{m}$. The sample was placed in the autoclave, and once the water chemistry reached specification and the ECP was stabilized, further crack conditioning was resumed. The measured crack growth rate and loading parameters for the crack conditioning sequence are recorded in Table 3-2. Figure 3-5 shows the crack growth rate plot

during the conditioning sequence. The air-fatigued crack was transitioned from transgranular fatigue to ultimately intergranular SCC propagation by shifting the precrack conditions to lower frequency and higher K_{max} and load ratio (R) with time. The growth rate displayed distinct, well-behaved transitions when the loading conditions were changed. Steps 2-4 exhibited similar crack growth rates, which show that the (mid-range) R-ratio only plays a weak role in crack behavior. The crack growth rates for steps 5-7 are very similar, which shows that frequency only plays a weak role in low-frequency crack growth. Previous work by Elliott showed similar results for low-frequency cracking. [1]

Table 3-2: Test Plan and Crack Growth Rate for Crack Tip Conditioning

Step	Crack Growth Rate (mm/s)	Frequency (Hz)	Wave Form	Hold Time (s)	K_{max} (MPa$\sqrt{m}$)	R-ratio	Temp. (°C)	Water Chemistry†
1	$7.5x10^{-6}$	1	sine	-	27.0	0.5	288	NWC
2	$6.5x10^{-6}$	1	sine	-	25.83	0.5	288	NWC
3	$4.5x10^{-6}$	1	sine	-	27.67	0.6	288	NWC
4	$1.5x10^{-6}$	1	sine	-	27.67	0.7	288	NWC
5	$1.0x10^{-7}$	0.1	sine	-	27.67	0.7	288	NWC
6	$1.25x10^{-7}$	0.01	sine	-	27.67	0.7	288	NWC
7	$7.5x10^{-8}$	0.001	sine	-	27.67	0.7	288	NWC

†NWC = 200 ppb dissolved oxygen water chemistry

In NWC conditions the specimen maintained an electrochemical potential (ECP) of approximately 0.44 V (≈ 190-200 mV_{SHE}) with respect to a Cu/Cu_2O reference electrode. The inlet and outlet water conductivities were approximately 0.07 and 0.14 μS/cm, respectively. The inlet water conductivity was held between 0.06 and 0.07 μS/cm over the duration of the crack growth rate testing in NWC. The outlet water conductivity exhibited a slowly decreasing conductivity over the course of the test beginning with 0.21 μS/cm and ending with 0.115 μS/cm. The small perturbations in the specimen ECP and inlet and outlet water conductivities are attributed to refilling the main water column from the makeup water column. These small conductivity and ECP spikes were settled out of the system within 2-3 h and had no discernable effect on the SCC growth rate.

The precracking response on initial testing in 288 °C water at 27.67 MPa$\sqrt{m}$ with continuous cycling is shown in Figure 3-5. The growth rate in the beginning of the aqueous testing started very high and decayed rapidly once the frequency was reduced to less than 1 Hz. The growth

rate behavior for the 1 Hz cycling is approximately 1 order of magnitude higher than the lower frequency cycling. The gaps in the crack growth plot in Figure 3-5 are due to the autoclave heaters tripping offline. When the test temperature changes by more than a preset amount (typically 5-6 °C) the test disengaged itself from computer control and maintained constant load as a preventative measure against changing test parameters. Temperature changes affect the metal resistivity: the DCPD monitoring program does not automatically update its temperature-dependent calibration and would have resulted in incorrect crack length measurements during temperature perturbations if the test were to have been continued.

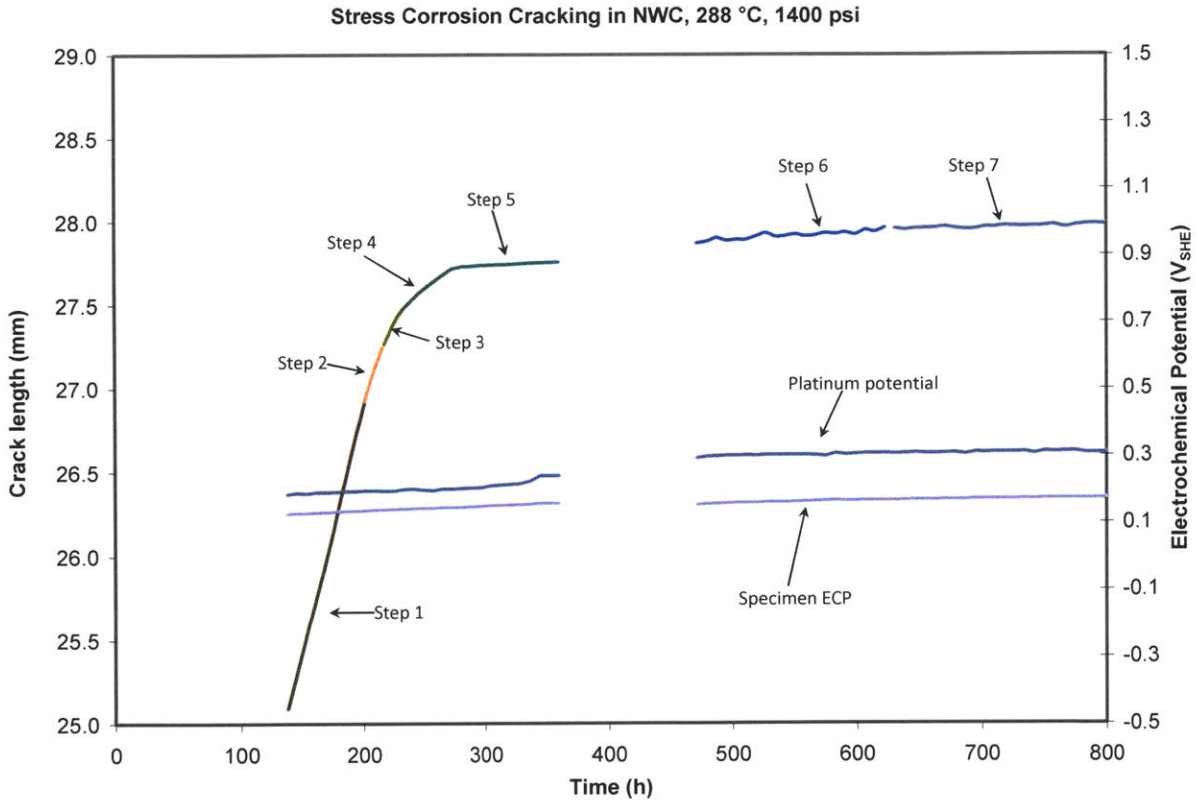

Figure 3-5: Fatigue crack tip conditioning in NWC

The transition from the final crack tip conditioning step to the constant load (constant K) step is shown in Figure 3-6. The test plan and crack growth rates are recorded in Table 3-3. Switching the loading conditions from cyclic loading at 0.001 Hz and R=0.7 to constant load produced a clear change in crack growth rate. The constant load crack grew at a constant rate of approximately 1.2×10^{-7} mm/s over the entire step. At test time 2826 h the test was transitioned to a trapezoidal loading pattern (R=0.7, f=0.001 Hz) with a 9000 s hold time at K_{max}. This step

was introduced to ensure the test was in active SCC growth. Figure 3-6 shows the crack growth plot transitioning from constant K to trapezoidal at test time 2826 h back to constant K loading at test time 2976 h with clear changes in crack growth rates. The crack growth rate increases from $1.1x10^{-7}$ mm/s to $7.5x10^{-7}$ mm/s and back down to $1.2x10^{-7}$ mm/s for the constant K, trapezoidal, constant K loading parameters, respectively. The clear distinction between the constant K and trapezoidal unloading parameters indicates that the crack was in fully active SCC mode. Transitioning back to near reproducible crack growth rates after the trapezoidal unloading step further indicates that the crack returned to active SCC growth. The SCC growth maintained a near constant growth rate over the duration of step 10.

Table 3-3: Test plan and crack growth rates for NWC

Step	Crack Growth Rate (mm/s)	Frequency (Hz)	Wave Form	Hold Time (s)	K max (MPa√m)	R-ratio	Temp (°C)	Water Chemistry†
8	$1.1x10^{-7}$	-	constant	-	27.67	-	288	NWC
9	$2.0x10^{-7}$	0.001	trapezoidal	9000	27.67	0.7	288	NWC
10	$1.2x10^{-7}$	-	constant	-	27.67	-	288	NWC

†NWC=200 ppb dissolved oxygen water chemistry

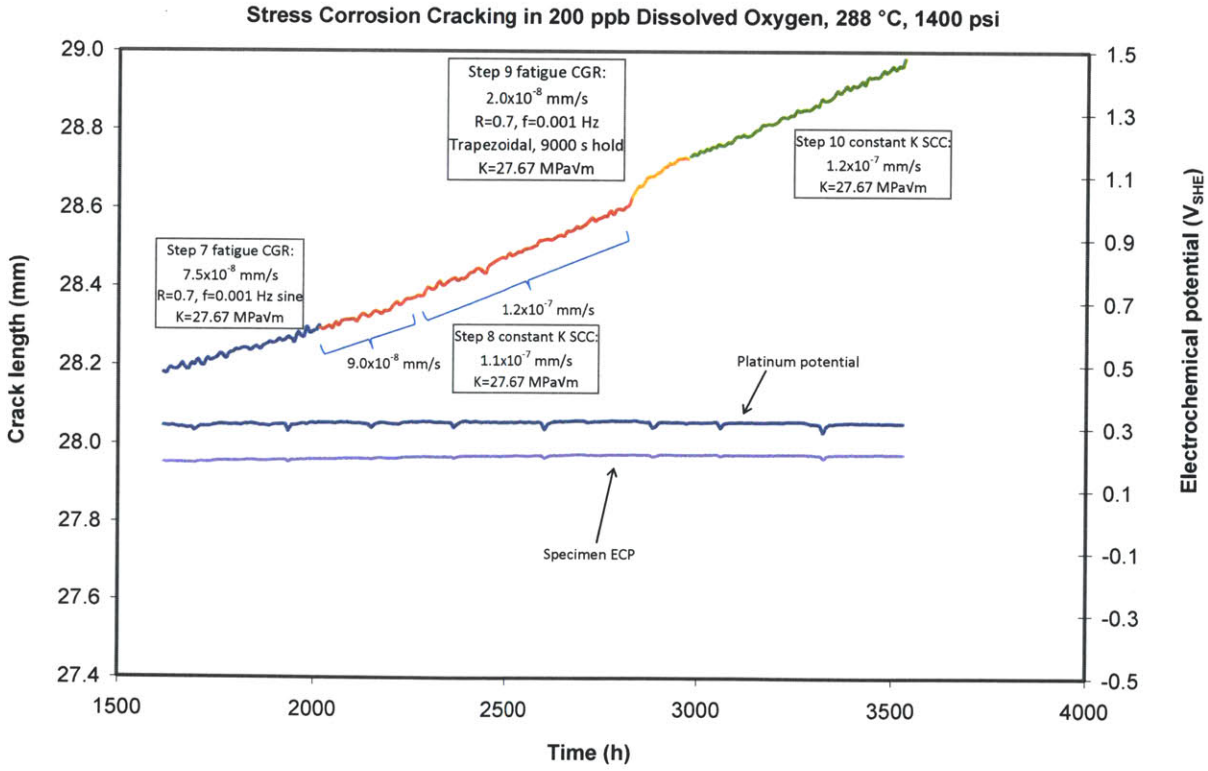

Figure 3-6: Constant stress intensity SCC in NWC

At the end of step 10 the water chemistry was changed from NWC to HWC to determine the effect of potential on crack growth rate. The test plan and crack growth rate for the HWC SCC testing are recorded in Table 3-4. Figure 3-7 shows the crack growth rate vs. time plot and clearly shows the step change in growth rate as the water chemistry was changed from NWC to HWC at test time 3536 h. The crack growth rate decreased nearly one order of magnitude from $1.2x10^{-7}$ mm/s to $1.4x10^{-8}$ mm/s and continued to grow at a constant rate over the duration of the 288 °C hydrogen water chemistry step (step 11). Approximately 185 h before switching to hydrogen water chemistry the data acquisition system did not record the data from the crack growth rate test; however, the test continued to operate in steady state with no parameter perturbations, which accounts for the discontinuity in data in Figure 3-7. The dotted lines between the gaps in test data in Figure 3-7 show the observed crack growth rate and electrochemical potential behavior. The perturbation in electrochemical potential at 3820 h is attributed to refilling the primary water column; no discernible change in crack growth rate was evident with the brief water chemistry fluctuation. The outlet conductivity dropped from 0.115 to 0.08 μS/cm when the environment was switched from NWC to HWC.

Table 3-4: Test plan and crack growth rates for HWC

Step	Crack Growth Rate (mm/s)	Frequency (Hz)	Wave Form	Hold Time (s)	K_{max} (MPa$\sqrt{m}$)	R-ratio	Temp. (°C)	Water Chemistry†
11	$1.4x10^{-8}$	-	constant	-	27.67	-	288	HWC
12	$-1.1x10^{-9}$	-	constant	-	30.0	-	93	HWC
13	***7.5x10^{-6}**	0.01	sine	-	35.0	0.7	93	HWC
14	$1.2x10^{-8}$	0.001	sine	-	35.0	0.7	93	HWC
15	$-1.6x10^{-9}$	0.001	trapezoidal	3600	35.0	0.7	93	HWC
16	$1.5x10^{-8}$	0.001	trapezoidal	9000	35.0	0.7	93	HWC
17	$2.3x10^{-8}$	0.001	trapezoidal	9000	35.0	0.7	288	HWC
18	$7.1x10^{-9}$	-	Constant	-	35.0	-	288	HWC

*Step average, †HWC = dissolved hydrogen water chemistry

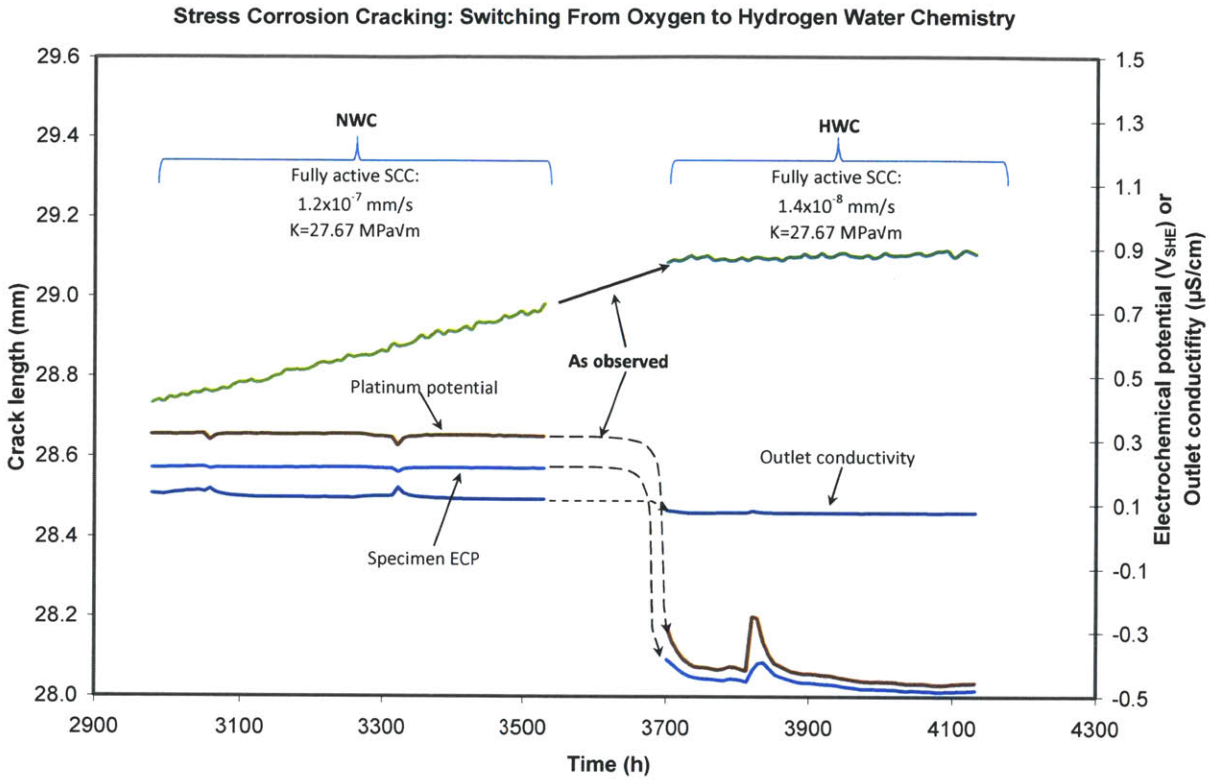

Figure 3-7: Effect of potential on crack growth rate, transitioning from NWC to HWC

Pourbaix diagrams are shown in Figure 3-8 for a Ni-Cr-H_2O system and Figure 3-9 for a Cr-Ni-H_2O system to show the thermodynamically stable oxide phases for the test environment. The Pourbaix diagrams were generated with HSC Chemistry software.[2] The potential measurements were measured on the surface of the specimen. The nickel (NiO), chromium (Cr_2O_3), and iron (Fe_2O_3) oxides are all stable in the aqueous conditions between NWC and HWC, but the potential at the crack tip is close to the NiO stability limit. Figure 3-10 shows a partial Pourbaix diagram of a Ni-Cr-Fe-H_2O system at 288 °C shows the thermodynamic effects of changing from NWC to HWC. Switching from NWC to HWC results in approximately a 0.75 V decrease in the corrosion potential (at the sample surface). The potential at the crack tip is approximately -0.65 V_{SHE} and is very close to the Ni/NiO equilibrium line. The potential at the specimen surface does not result in any substantial thermodynamic changes, with respect to known SCC susceptibility regions. The outlet water conductivity dropped from 0.115 in NWC to 0.08 µS/cm in HWC.

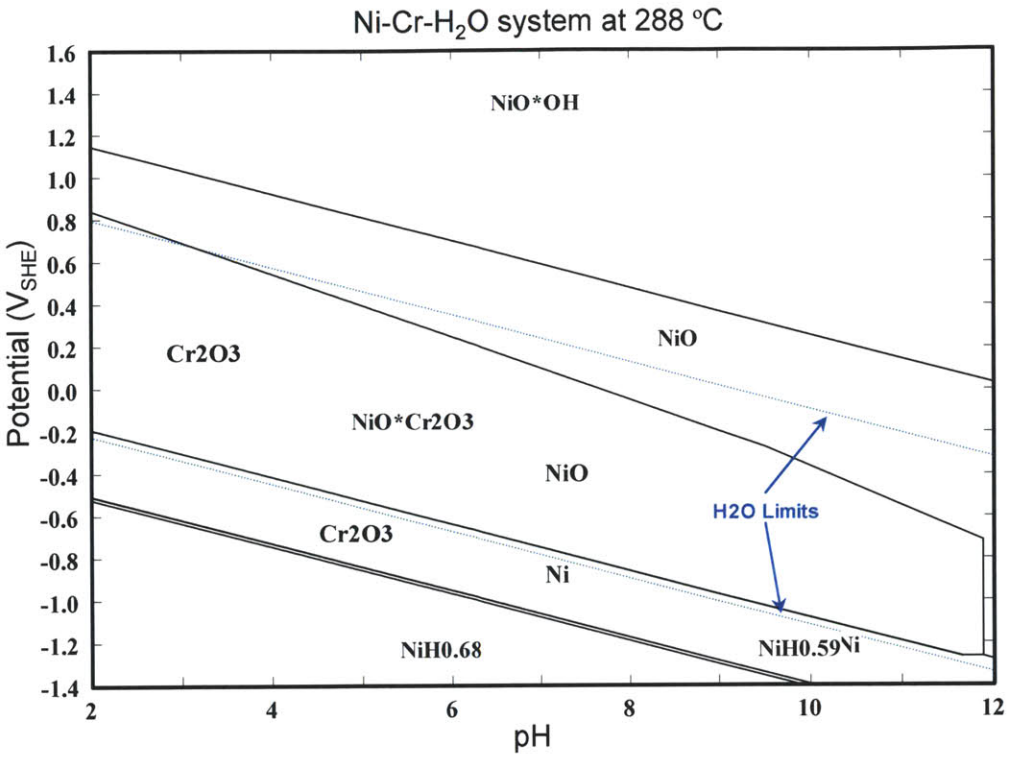

Figure 3-8: Pourbaix diagram of Ni-Cr-H_2O system at 288 °C

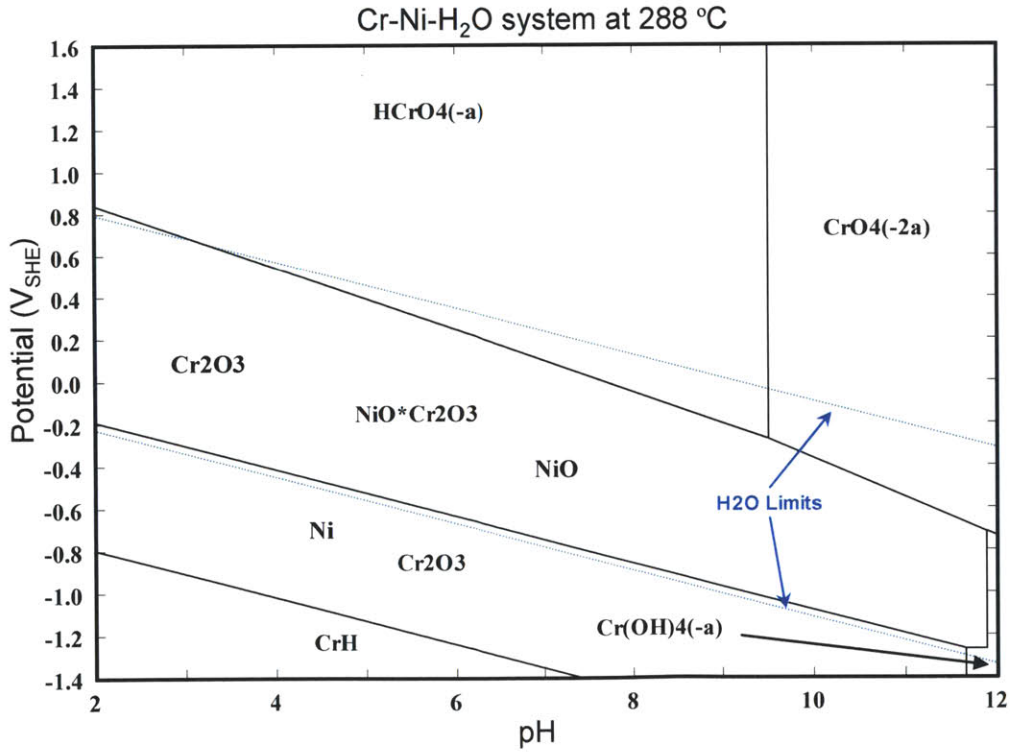

Figure 3-9: Pourbaix diagram of Cr-Ni-H_2O system at 288 °C

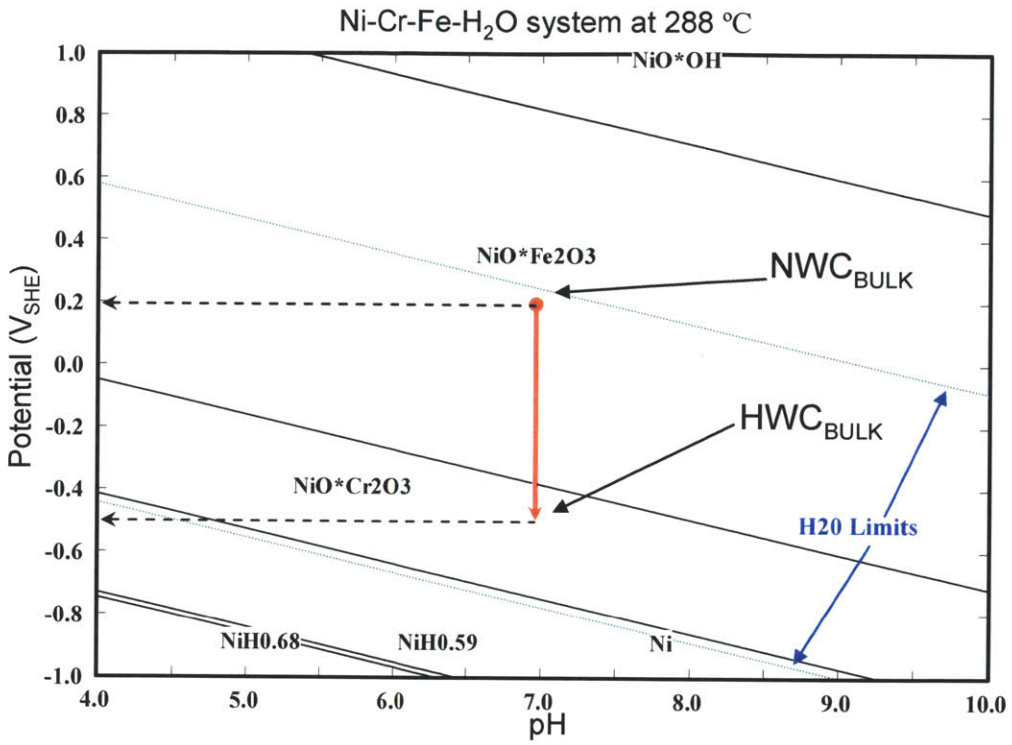

Figure 3-10: Pourbaix diagram outlining potential change, electrochemical potential is measured on the sample surface

Between steps 11 and 12 the test temperature was lowered from 288 to 93 °C and the stress intensity was increased from 27.7 to 30.0 MPa√m, which is shown in the crack growth rate plot in Figure 3-11. The lower test temperature was set at 93 °C as it is a common test temperature for nickel-based alloys susceptible to low temperature crack propagation in HWC.[1] Figure 3-12 shows the Pourbaix diagram outlining the thermodynamics effects of the temperature reduction. Once the temperature of the system was stabilized at 93 °C the DCPD was recalibrated to the new temperature and the test was resumed at constant stress intensity. Despite the higher stress intensity, the temperature change resulted in a distinct drop in crack growth rate from 1.4×10^{-8} to -1.1×10^{-9} mm/s. The temperature reduction to 93 °C affects the stability of NiO, which is clearly manifested in the crack growth rate. The measured negative crack growth rate is an artifact related most likely to a transition in oxide morphology near the crack tip. It has been reported that the indicated negative crack growth rate for nickel alloys in hydrogen water chemistry is consistent with the transition from nickel oxide (NiO) stability to nickel metal stability.[3] Dissolution of the NiO produces a shorting path in the wake of the crack, resulting

in a lower voltage drop in DCPD measurements, and a shorter indicated crack, which is manifested as an electrical effect.[4]

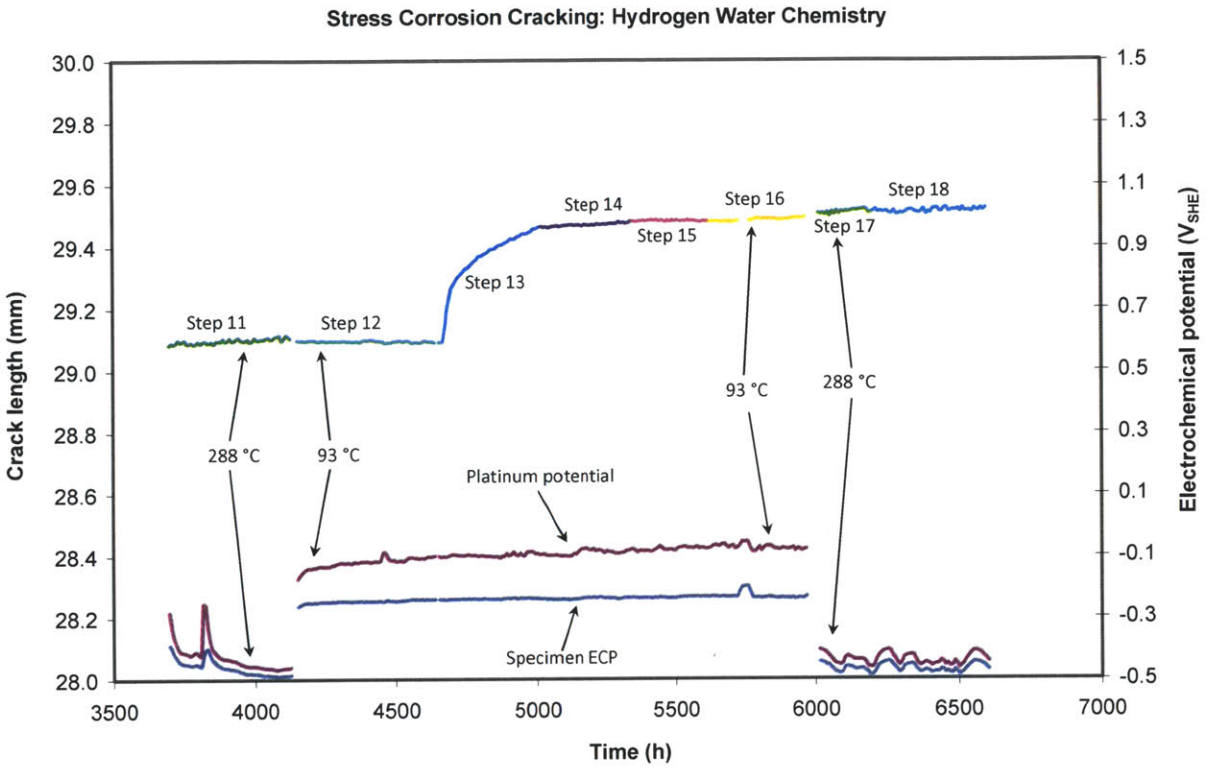

Figure 3-11: SCC and corrosion fatigue cracking in HWC

Step 12 was continued for approximately 525 h before switching the loading parameters to a crack-tip resharpening procedure. The loading parameters were changed to sine wave loading with R=0.7, f=0.01 Hz, and K_{max}=35.0 MPa$\sqrt{m}$. Figure 3-13 is focused on the transition between the constant K crack growth in step 12 and the fatigue crack growth in step 13. The initial fatigue crack growth rate is $1.5x10^{-6}$ mm/s and decays approximately one order of magnitude to $1.3x10^{-7}$ mm/s before transitioning to the next loading step. The large crack growth rate at the beginning of the resharpening step is most likely due to specimen ligament cracking, which is a fatigue-fracture driven event. Figure 3-14 shows a schematic of a crack with excessive tunneling and a large uncracked ligament (part A) and a crack with minimal tunneling (part B). The large crack ligament (part A) contributes to an underestimation in crack length. If excessive SCC tunneling occurs, fatigue loading fractures the ligament and results in a straighter crack front. This results in the DCPD registering an increase in growth rate despite the tip of the crack front is experiencing little or no extension.

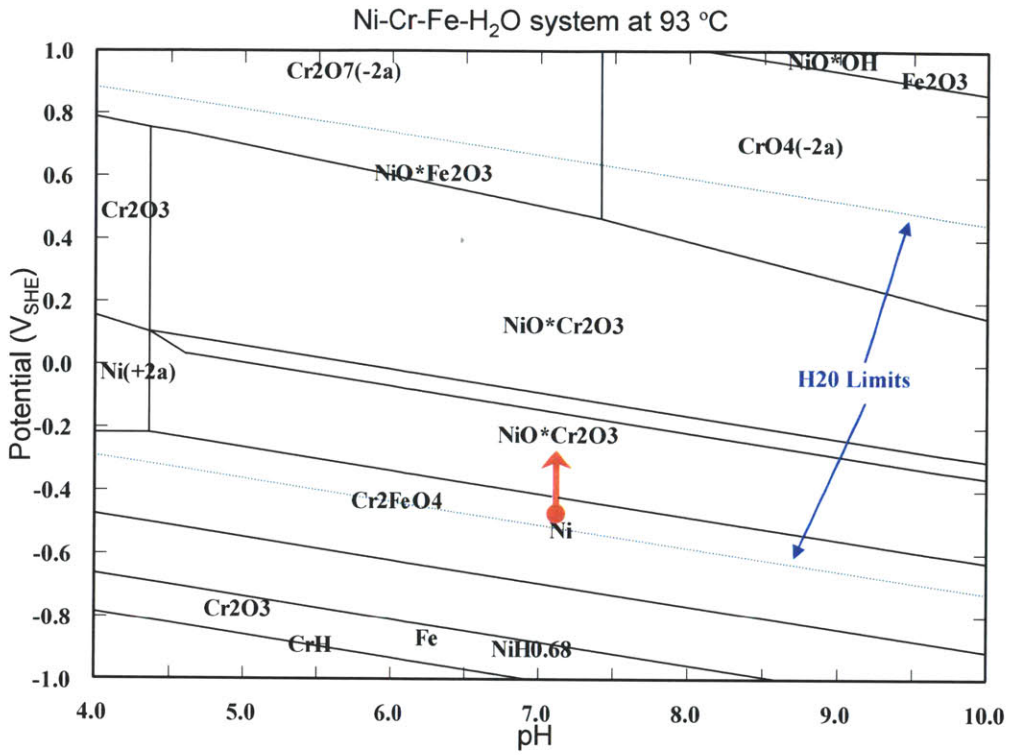

Figure 3-12: Thermodynamics for lowering temperature from 288 to 93 °C

A distinct change in fatigue crack growth rate to $1.2x10^{-8}$ mm/s is evident when the frequency is reduced from 0.01 to 0.001 Hz between steps 13 and 14. Figure 3-15 shows the final steps in the crack growth rate test. Steps 15-17 are the final steps in crack tip-reconditioning procedure with transition to SCC growth. Step 15 exhibits a measured, but not real, crack growth rate of negative $1.6x10^{-9}$ mm/s ($-1.6x10^{-9}$ mm/s) as the loading parameters are changed to trapezoidal loading with a 3600 s hold time at K_{max}. The NiO stability is attributed to the "negative" crack growth measurements as previously discussed. Step 16 increases the trapezoidal hold time to 9000 seconds at K_{max} and exhibits a crack growth rate of $1.5x10^{-8}$ mm/s. Between hours 5715-5772 a small (4 °C) temperature perturbation occurred and is evident by the simultaneous increase in both the specimen and platinum potential. Moreover, the crack growth rate data is not shown during that perturbation because the temperature change resulted in an incorrect crack growth profile (due to temperature driven resistivity changes). Between test times 5973 to 6015 h the test temperature was raised from 93 °C and stabilized at 288 °C. During this controlled system change the specimen was held in constant load. Step 17 has the same loading parameters as step 16. Raising the temperature to 288 °C showed a clear change in crack growth rate to

$2.3x10^{-8}$ mm/s. The previous 288 °C step in HWC recorded a CGR of $1.4x10^{-8}$ mm/s and was at lower stress intensity (27.7 vs. 35 MPa√m). The test transitioned to constant K crack growth in step 18. A clear change occurs in crack behavior after transition from trapezoidal fatigue to constant K loading. The crack growth rate in step 18 was $7.1x10^{-9}$ mm/s, which is approximately 50% lower than the previous 288 °C step in hydrogen water chemistry despite a 26% increase in stress intensity. The crack growth rate test ended at hour 6641.

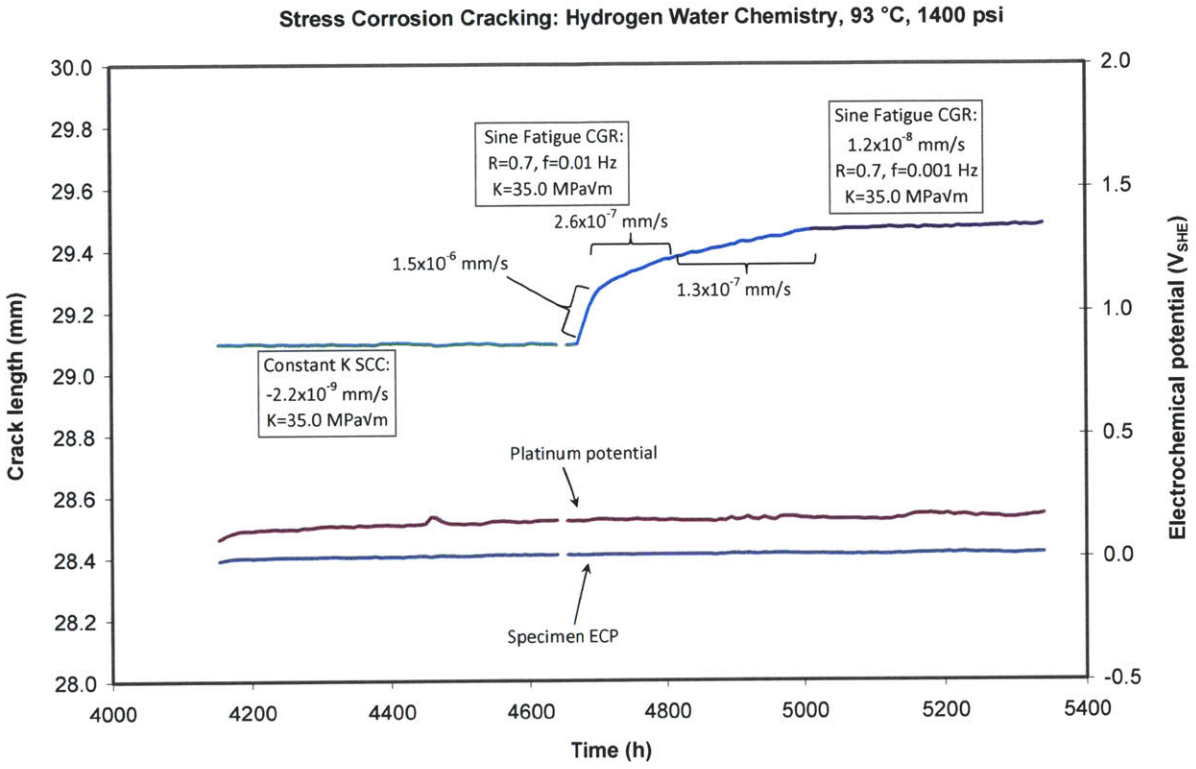

Figure 3-13: SCC in 93 °C HWC

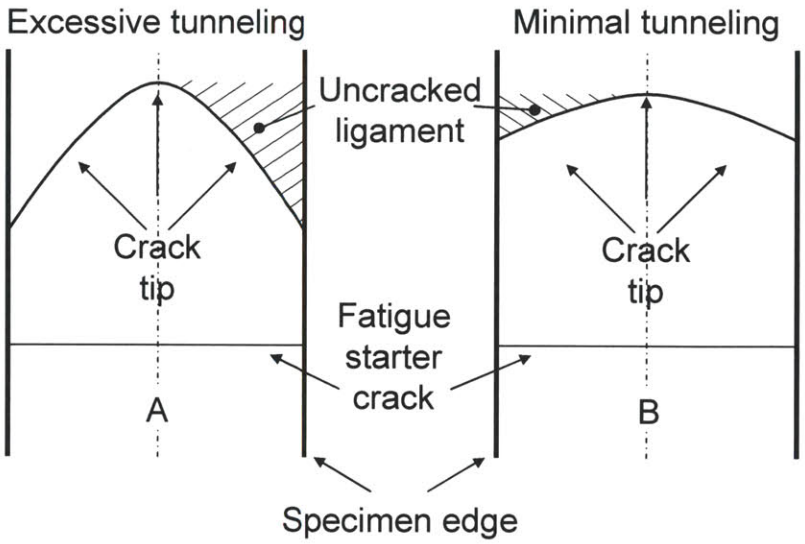

Figure 3-14: SCC crack tunneling schematic

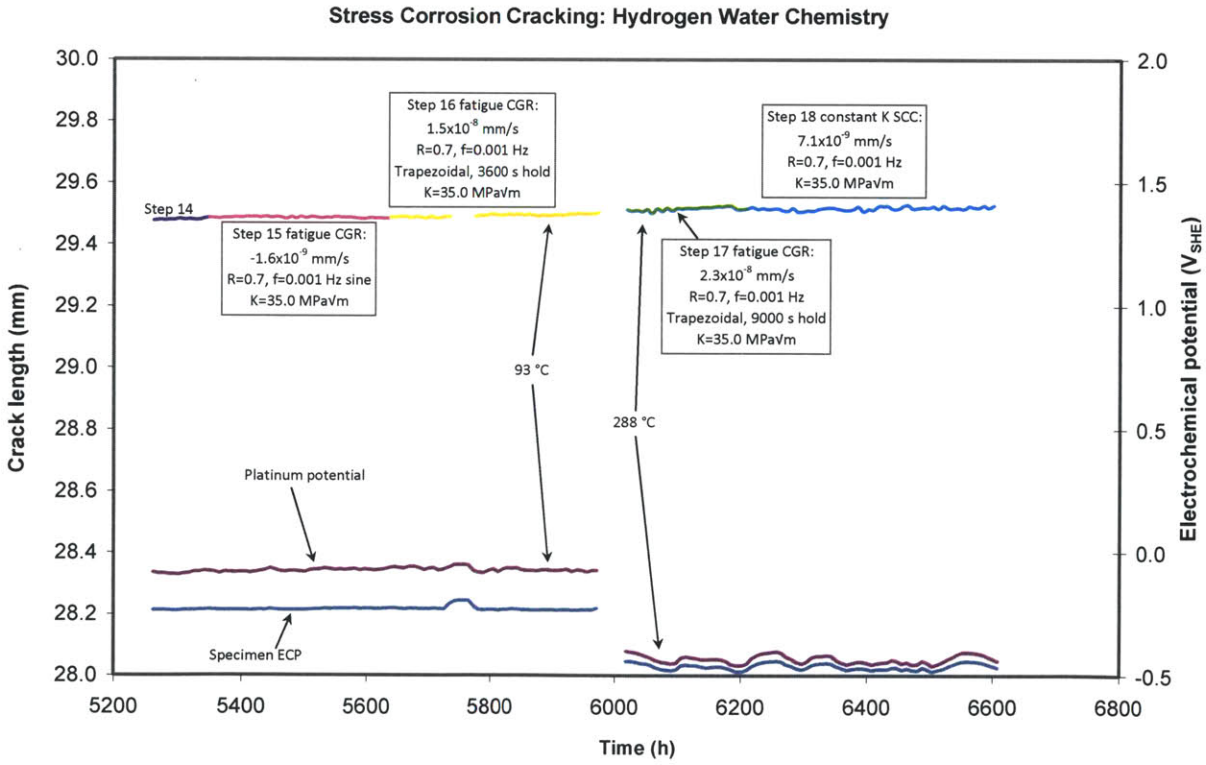

Figure 3-15: Effect of raising temperature on SCC in HWC

3.4 Discussion

The crack growth rate response is discussed here with specific attention to the effect of the potential perturbations near Ni/NiO equilibrium line. The fracture morphologies are also briefly presented, but a more complete fractographic analysis is presented in Chapter 4 and a discussion of the mechanisms contributing to crack propagation is presented in Chapter 6.

Cracking in NWC exhibited a SCC growth rate of approximately 1.2×10^{-7} mm/s. A crack growth rate of 3×10^{-7} mm/s was reported by Shen [5], who used a bolt-loaded U-bend specimen in similar aqueous conditions. The crack growth rates were measured *in-situ* in this work. Shen determined the growth rate by measuring the time to failure, which assumes that the crack tip is already conditioned to SCC conditions at the test beginning. Regardless, the crack growth rates measured in this work agree nicely with the limited availability in the literature. Other crack growth rate testing has been conducted on alloy X-750 in the HTH condition, but not in the environment of interest in this work.[4,6] These are the first results for BWR conditions that were measured *in-situ*. Figure 3-16 shows the SCC fracture surface. The top of Figure 3-16 corresponds to the last step in the crack tip conditioning process before transitioning to constant K. The resulting SCC induced crack propagation is predominantly intergranular and pseudo-intergranular (propagating directly adjacent to grain boundary $M_{23}C_6$ carbides) with small and localized regions of transgranular racking. It should be noted that, while the crack path appears to be intergranular, more detailed analysis, discussed later, will show that the actual crack path is likely near the grain boundary, but not on the grain boundary.

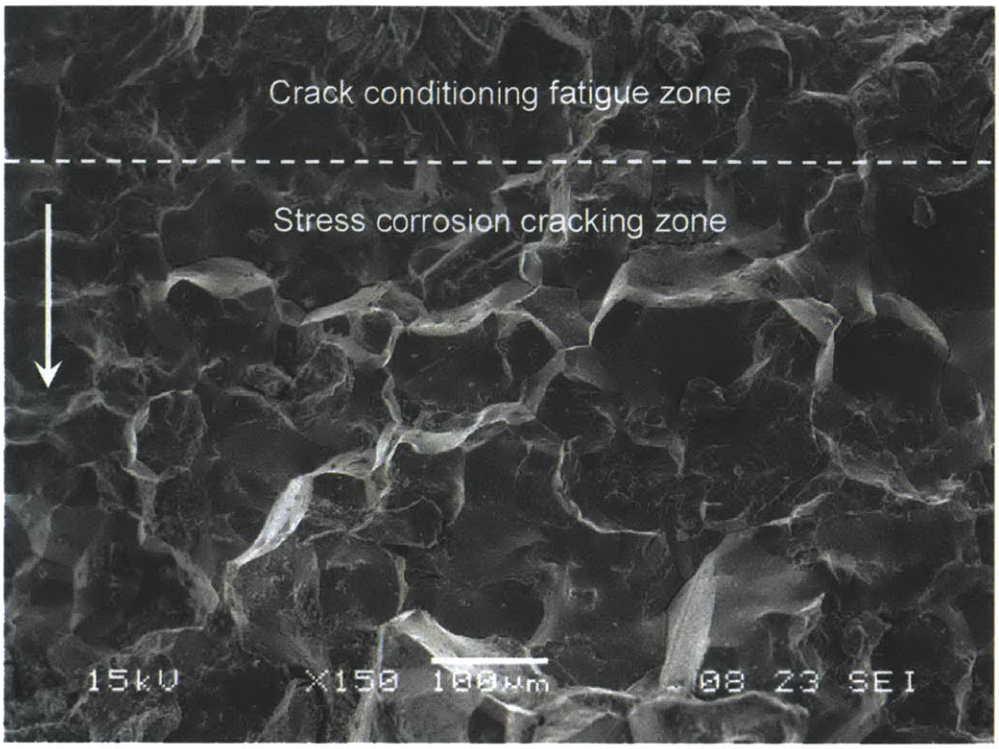

Figure 3-16: SCC and crack conditioning fracture morphology (NWC), arrow indicates crack propagation direction

The corrosion potential was lowered by switching from NWC to HWC. This was an important step because alloy X-750 has been previously reported to be susceptible to hydrogen embrittlement, albeit for non-HTH heat treatments, as discussed in Chapter 1. When the environment was switched from NWC to HWC, there was a clear change in crack growth rate, which indicates that specimen potential is extremely important to the SCC susceptibility. Figure 3-17 shows the fracture surface under HWC conditions. The lower region of Figure 3-17 corresponds to the post-SCC testing air-fatigue step. The SCC fracture in HWC is similar to that in NWC and is predominantly intergranular and pseudo-intergranular with localized regions of transgranular failure.

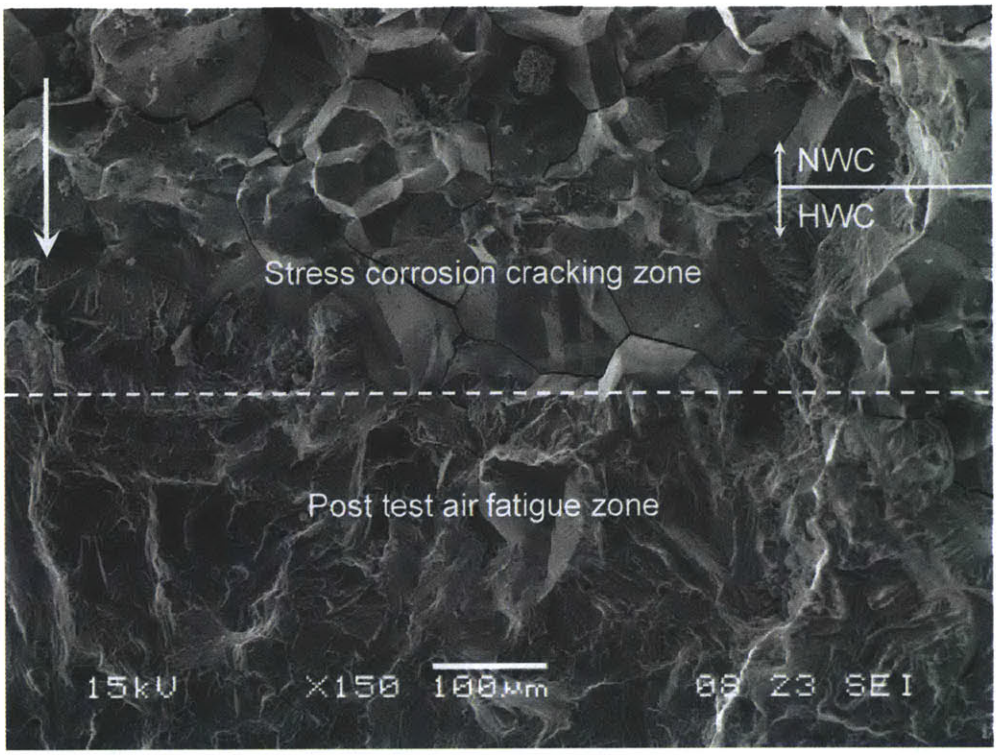

Figure 3-17: SCC (HWC) and post-test fatigue fracture morphology, arrow indicates crack propagation direction

3.4.1 Electrochemistry near Ni/NiO Equilibrium

This discussion is focused on the effect of traversing the Ni/NiO equilibrium potential, as shown in the Pourbaix diagram in Figure 3-8. The effects of crossing the metal-oxide phase boundaries for chromium and iron are not presented here because chromium and iron oxides are stable in the potentials of interest for this work.

The lower water stability line (H_2/H_2O) controls the corrosion potential in deaerated water chemistry. This line is parallel to the Ni/NiO line (and Cr/Cr_2O_3 and Fe/Fe_3O_4 lines). Thus, only perturbations in potential can change the corrosion potential proximity to the metal-oxide phase boundaries (changes in pH do not have an effect). The potential can be changed by applying external voltage control or by controlling the H_2 concentration. Traversing the Ni/NiO phase boundary has been shown to cause a distinct SCC response for alloy X-750. This same argument can be made about the effect of dissolved oxygen, albeit at a higher potential (O_2/H_2O equilibrium).

Oxygen is consumed as it migrates along a crack, which establishes an O_2 gradient. Subsequently, this establishes a potential gradient along the crack. This gradient concentrates

anions into the crack and decreases the non-H^+ cation concentration. The potential external to the crack controls this gradient can affect the CGR. Lowering the bulk potential, by switching from NWC to HWC, changed the potential gradient at the crack mouth and the CGR dropped by nearly one order of magnitude, as previously seen in Figure 3-7.

H_2 is not consumed within the crack, and additional hydrogen cations are produced as a byproduct of the corrosion process. Hydrogen within the crack can cause small shifts in corrosion potential at free surfaces and at the tip of a crack. Nickel-base alloys are exceptionally susceptible to this effect and can experience larger changes in crack growth rates with small changes in H_2, as a result of NiO dissolution as the potential is lowered below the Ni/NiO equilibrium. Iron-base alloys are not susceptible to this phenomenon because the chromium and iron oxides are stable over a wider potential range than NiO, which is illustrated in the Pourbaix diagram in Figure 3-12.

Temperature has a strong effect on the location of the Ni/NiO equilibrium boundary, as previously shown in Figure 3-12. Figure 3-18 shows the results from recent research that was focused on resolving the resolution of the Ni/NiO equilibrium location.[7]

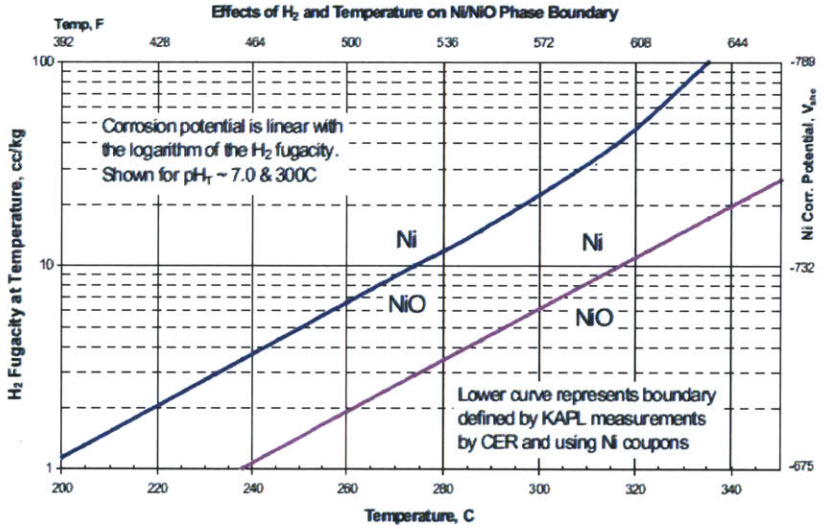

Figure 3-18: Effect of temperature on Ni/NiO equilibrium boundary, upper curve is theoretically calculated phase boundary, lower curve was measured at Knolls Atomic Power Laboratory [7]

Attanasio and Morton [8] demonstrated that the crack growth rate is largely controlled by the proximity to the Ni/NiO equilibrium boundary and that the peak rate was recorded at the transition. These results are shown in Figure 3-19 and indicate that the previously accepted

hydrogen concentration for the Ni/NiO equilibrium showed no correlation with cracking susceptibility. The region of highest crack growth rate corresponded closely with the updated Ni/NiO equilibrium. The crack growth rate is highest at the Ni/NiO equilibrium potential, which can be attributed to the stability of each phase in its proximity to the phase boundary. At low hydrogen concentrations Ni is extremely stable. As the hydrogen concentration increases the stability of NiO decreases until it reaches the Ni/NiO boundary. Continued increase in hydrogen concentration decreases the stability of the NiO and drives the crack growth rate down. This point is further presented by showing the crack growth rate as a function of the electrochemical potential away from the Ni/NiO transition boundary and can be seen in Figure 3-20.[8] As the electrochemical potential deviates from that of the transition the crack growth rate continues to decrease until it is sufficiently small, which also corresponds to the high stability of the Ni and/or NiO. Eventually the NiO will lose stability as it approaches the next phase boundary, but this is away from the hydrogen line and outside the scope of this analysis.

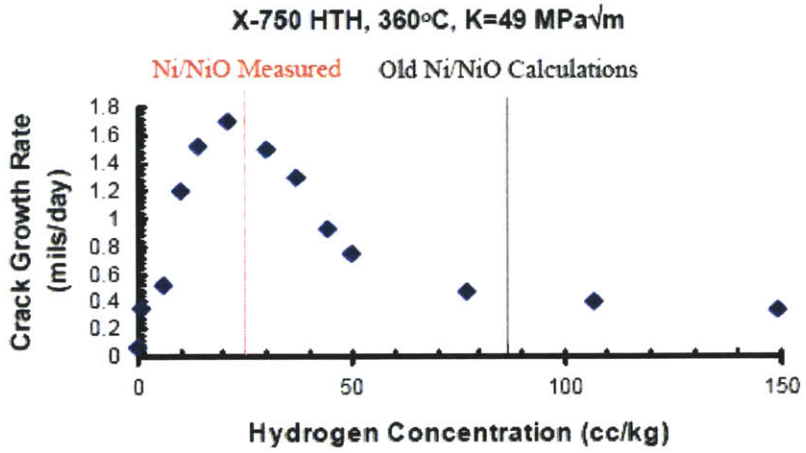

Figure 3-19: Crack growth rate of alloy X-750 in high-temperature water as function of hydrogen concentration [8]

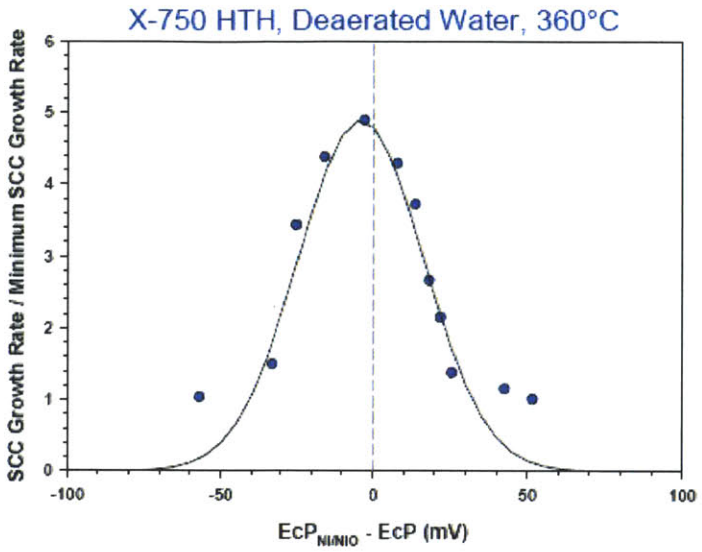

Figure 3-20: Crack growth rate of alloy X-750 in high temperature water as a function of potential [8]

3.4.2 Effect of Water Chemistry on Crack Growth Rate

The CGR decrease when the environment was switched from NWC to HWC is due to the effect of oxygen on ECP. Adding oxygen to the environment has two effects: 1. establishes the dissolved oxygen concentration in NWC, and 2. increases the bulk electrochemical potential (ECP). It was shown in Figure 3-8 that the bulk ECP, for NWC and HWC, is within the stable NiO range on the Pourbaix diagram. However, because oxygen is consumed as it migrates into and along the crack and results in deaerated conditions at the crack tip, which are close to the Ni/NiO equilibrium line. Thus, the crack tip potential is lower than the bulk potential, in HWC and much lower in NWC. Wada *et al.* showed the potential distribution along a crack as a function of dissolved oxygen content and flow rate for a simulated BWR environment.[9] Higher dissolved oxygen content (245-400 ppb) had large ECP gradient at the crack mouth. High flow rate also increased the potential gradient between the crack mouth and tip. Figure 3-21 shows the effect of varying the dissolved oxygen concentration on the oxygen penetration into the crack and the corresponding ECP along the crack. Dissolved oxygen conditions in NWC in this thesis are most representative of the 245 ppb dissolved oxygen curve in Figure 3-21. The distance oxygen is able to diffuse along the crack path before it is consumed is comparable between high and low concentrations (245 vs. 2 ppb), but the effect dissolved oxygen concentration has on ECP is high.

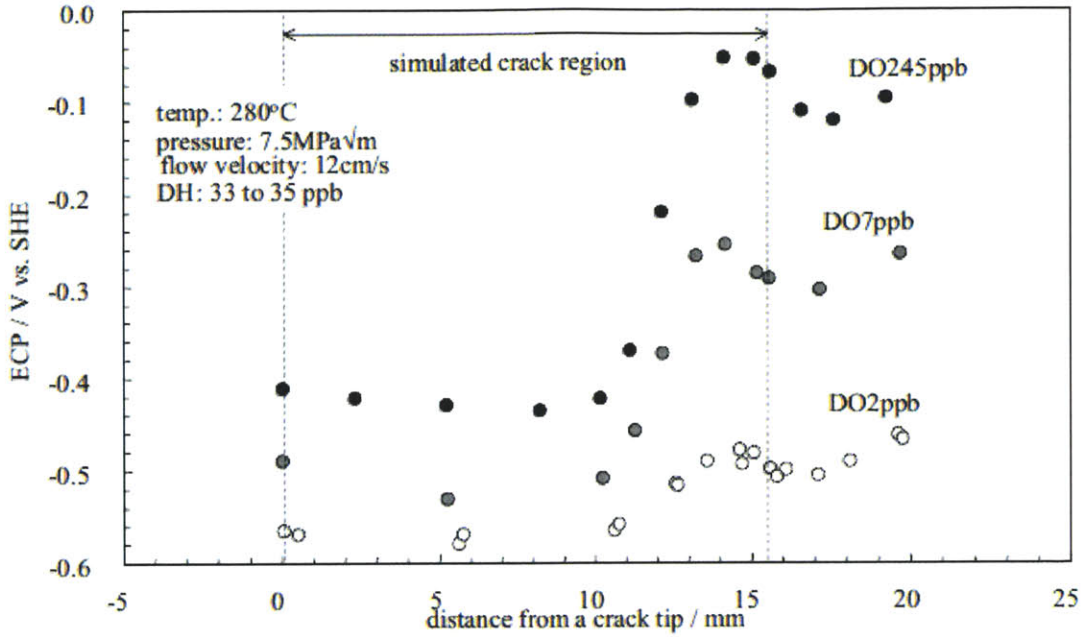

Figure 3-21: Effect of high flow velocity and varying dissolved oxygen content on crack ECP gradient [9]

Figure 3-22 shows the effect of dissolved oxygen vs. hydrogen on the ECP gradient across the crack. In NWC, the ECP gradient is very large, but in HWC the ECP gradient is small. There are two immediate effects of adding hydrogen to the environment: 1. oxygen scavenging, and 2. lowering of the ECP at the outer surface. In the test environment, oxygen scavenging is a short term effect that lasts only a few hours.* The main benefit to adding hydrogen to the environment is lower bulk ECP.

* In a nuclear reactor, oxygen will be generated by radiolysis. Addition of hydrogen into the cooling water enables continuous oxygen scavenging.

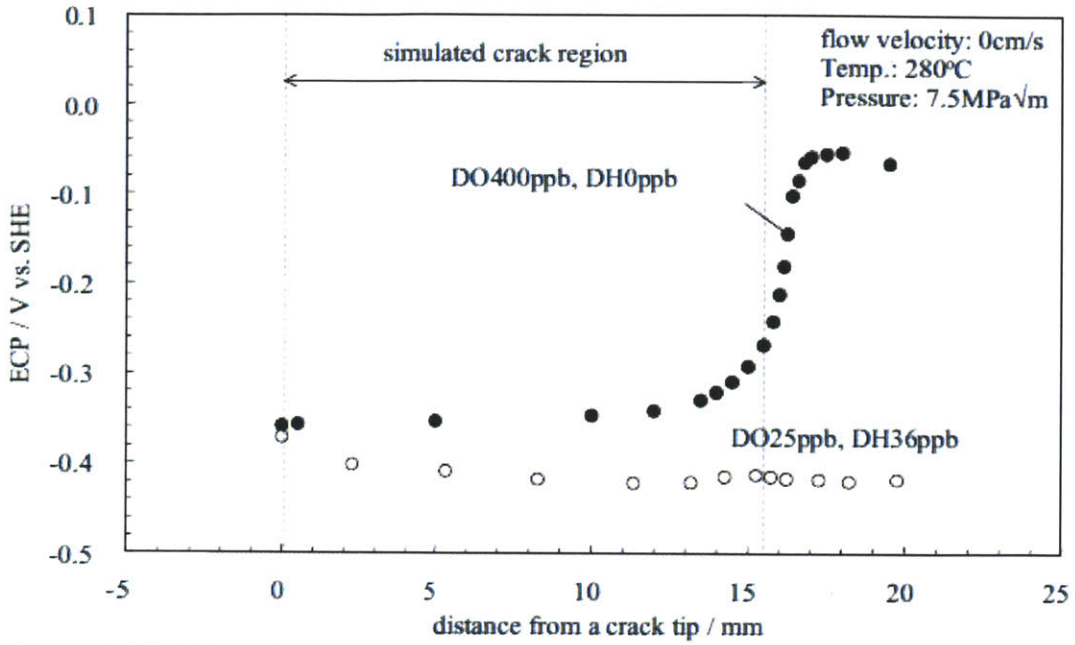

Figure 3-22: Effect of stagnant environment and varying dissolved oxygen content on crack ECP gradient [9]

The effect of the ECP gradient between the crack mouth and crack tip is known to play an important role in the cracking process. The bulk environment necessary for crack advance has two processes that operate in series that affect crack growth: ECP gradient and internal crack conductivity. A high ECP gradient at the crack mouth promotes cation migration out of the crack and into the bulk and anion migration into the crack. However, the ΔECP driven ion (e.g. oxygen) migration into the crack mouth is only high into the initial 10's of μm along the crack path, after which the ECP gradient is substantially reduced, or eliminated. Over this short distance, the ECP gradient facilitates migration of dissolved ions into the crack. Inside the crack, the diffusion process is driven by concentration gradient and is controlled by the environment conductivity along the crack. Although the conductivity of the bulk fluid is extremely low (≈ 0.06 μS/cm), the conductivity within the crack is high due to the presence of corrosion products. Diffusion of ions in and out of the crack is concentration driven and not potential driven (after the initial ΔECP affected range). This effect was described nicely by Staehle and is illustrated in Figure 3-23.[10] The benefit to a reduced corrosion potential has been recognized for some time and is a primary reason why many BWRs use NobelChem to achieve a lower ECP. [11-12]

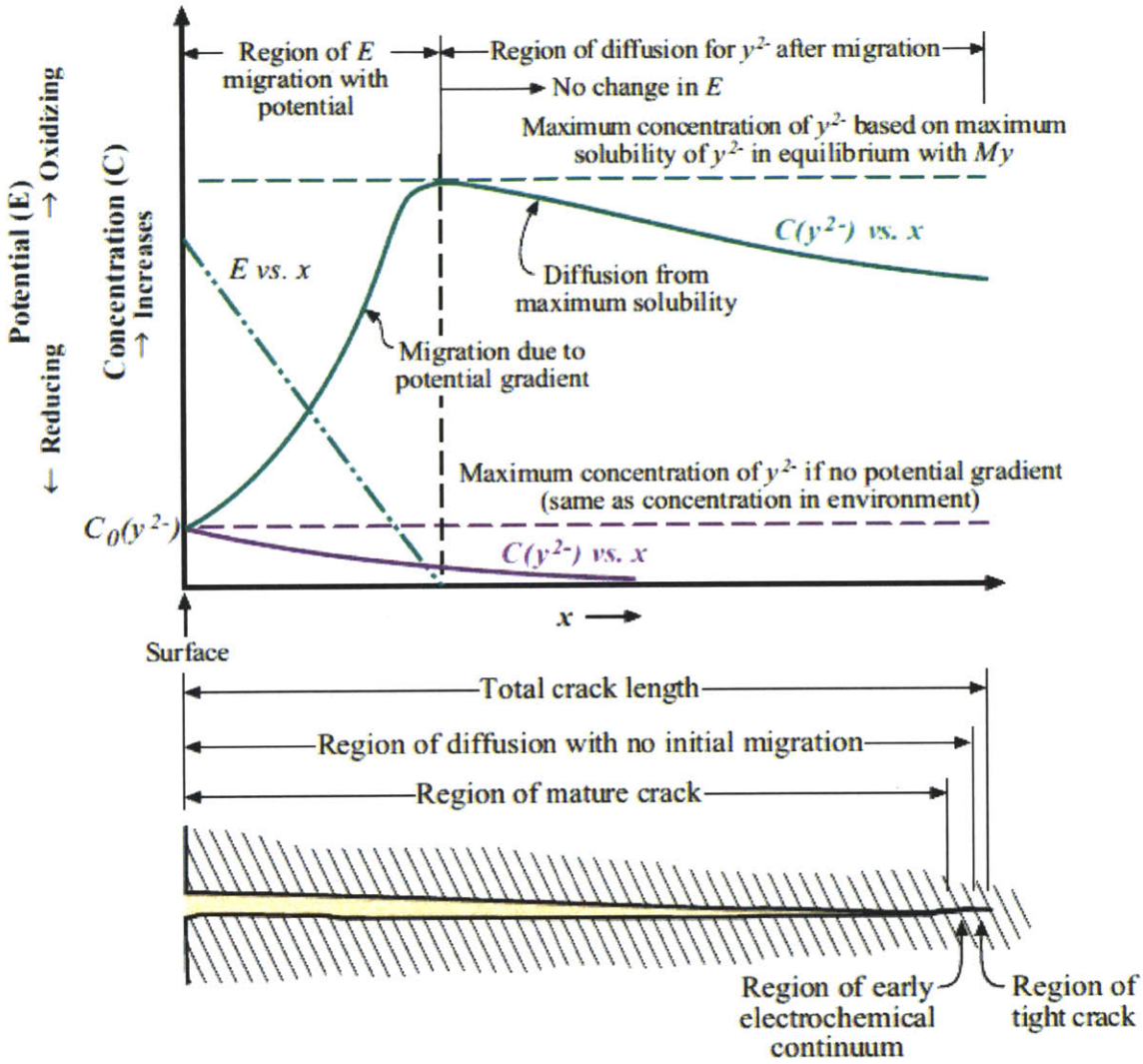

Figure 3-23: Schematic view of concentration (activity) vs. distance in an SCC crack for diffusion and migration conditions (assuming a negative gradient in potential and negative migrating species) [10]

Assuming that the ECP of the crack tip is approximately at the Ni/NiO equilibrium line, the potential difference between the crack tip and bulk is approximately 900 mV_{SHE} in NWC. This potential difference drops to approximately 200 mV_{SHE}, when the environment is changed to HWC. The results observed in the CGR testing indicate that the ΔECP is a strong contributor to SCC susceptibility in alloy X-750. This effect was also shown by Molander for comparing NWC to HWC on CGRs for alloy 182, which is a nickel-based weld metal.[13] Lowering the bulk potential, and the subsequent lower ECP gradient, results in smaller potential driven diffusion into the crack and is reflected by a lower CGR.

3.5 References

1. C.K. Elliott, "Effect of Thermal Treatment on the Fracture Properties of Alloy X-750 in Aqueous Environments", Ph.D. Thesis, Massachusetts Institute of Technology, 1985.

2. HSC Chemistry® 6.0 produced by Outokumpo Technology (www.outokumputechnology.com)

3. Attanasio and D.S. Morton, "Measurement of the Ni/NiO transition in Ni-Cr-Fe alloys and updated data and correlation to quantify the effect of aqueous hydrogen on primary water SCC", Proceedings from the Eleventh International Symposium on Environmental Degradation of Materials in Nuclear Power Systems – Water Reactors, ANS, 2003.

4. P.L. Andresen, P.W. Emigh and R.M Horn, "Stress corrosion crack growth rate response of AH & HTH alloy X-750 in high temperature water", Corrosion/03, Paper No. 03660, 2003.

5. Y. Shen and P.G. Shewmon, "Intergranular stress corrosion cracking of alloy 600 and X-750 in high-temperature deaerated water/steam", Metallurgical and Materials Transactions A, Vol. 22, pp. 1857-1864, 1991.

6. M. Yamamoto, J. Kuriya and S. Uchida, "Threshold for stress corrosion cracking initiation of alloy X750 under long-term uniaxial constant load test in high-temperature water,", Corrosion, Vol. 60, No. 3, pp. 229-237, 2004.

7. P.L. Andresen, P.W. Emigh, M.M. Morra and J. Hickling, "Effect of PWR primary water chemistry and deaerated water on SCC", Proceedings from the Twelfth International Symposium on Environmental Degradation of Materials – Nuclear Power Systems - Water Reactors, pp. 989-1008, 2005.

8. S.A. Attanasio and D.S. Morton, "Measurement of the Ni/NiO transition in Ni-Cr-Fe alloys and updated data and correlations to quantify the effect of aqueous hydrogen and primary water SCC", Proceedings from the Eleventh International Conference on Environmental Degradation of Materials in Nuclear Power Systems – Water Reactors, ANS, 2003.

9. Y. Wada, K. Ishida, M. Tachibana and M. Aizawa, "Effects of bulk water chemistry on ECP distribution inside a crevice", Proceedings from the Twelfth International Symposium on Environmental Degradation of Materials – Nuclear Power Systems - Water Reactors, 2005.

10. R.W. Stahle, "Critical analysis of "tight cracks"", Corrosion Reviews, Vol. 28, Nos. 1 and 2, pp. 1-103, 2010.

11. Y.J. Kim, L.W. Niedrach, M.E. Indig and P.L. Andresen, "Applications of noble metals in coatings and alloys for light water reactors", Journal of Metals, Vol. 44, No. 2, p. 14-18, 1992.

12. P.L. Andresen, "Application of noble metal technology for mitigation of stress corrosion cracking in BWRs", Proceedings from the Seventh International Symposium on Environmental Degradation of Materials – Nuclear Power Systems, NACE, p. 563-578, 1995.

13. A. Molander, "Electrochemical measurements in nuclear power environments", ICPWS XV, Berlin, September 8-11, 2008.

Chapter 4 - Fractographic Analysis

4.1 Introduction

This chapter presents the fractographic results for the SCC testing. The SCC morphology in alloy X-750 is predominantly intergranular and pseudo-intergranular. Pseudo-intergranular cracking appears to be intergranular at low magnification but actually propagates directly adjacent to the grain boundaries and was the predominant mode of cracking for grain boundaries with $M_{23}C_6$ carbides. Intergranular cracking was observed on grain boundaries without $M_{23}C_6$ carbides, which were either twin boundaries or highly-coherent grain boundaries. Localized regions of transgranular cracking were also observed. An overview of the cracking and fracture surface is shown in Figure 4-1. The cracking transitioned from transgranular fatigue cracking during the crack tip conditioning steps to a predominantly intergranular mode during constant stress intensity SCC. The end of the SCC test was marked with air fatigue cracking, which was used to separate the material for post-test fractographic analysis. A cross-sectional view of the intergranular crack path is shown in Figure 4-2. The polished cross-sectional view shows the large grain size, numerous twins (highly-coherent) boundaries, and sparse grain boundary Nb-carbides.

The SCC crack propagation character is as follows:

1. Crack propagation is pseudo-intergranular, intergranular, and transgranular in some cases.
2. Metal oxidation occurs along the crack path and is more severe along boundaries with $M_{23}C_6$ carbides.
3. Crack propagation mode is dependent on the grain boundary structure. Cracks propagated in a different mode on/near $M_{23}C_6$ containing boundaries vs. boundaries without carbides (coherent boundaries).
4. Crystallographic cracking can be main or secondary cracking. The main SCC cracks and the crack wall is the same as the fracture surface. Secondary SCC cracks are those that are cracks observed to propagate from the main fracture surface. When examining the crack path cross-section, secondary cracks are also those that branch off the main crack.
5. The fracture surface has regions of intergranular brittle-like cracking surface that have a smooth appearance.

6. Cracking is also observed ahead of active crack tips and appears as be grain boundary decohesion.
7. Fracture surface contains small regions of ductile fracture.
8. Transgranular cracks nucleate and grow off main and secondary intergranular fracture.
9. Nb-carbides locate on grain boundaries and are more stable than $M_{23}C_6$ carbides from a corrosion point of view. SCC cracks propagate either through or around Nb-carbides. If the local shear stress is high enough the Nb-carbides fracture and SCC cracks propagate through the Nb-carbides. More commonly, SCC cracks propagate around uncracked Nb-carbides.

Grain boundary and near grain boundary microstructure appears to have the strongest internal influence on the mode of crack propagation (external influence would be load and environment).

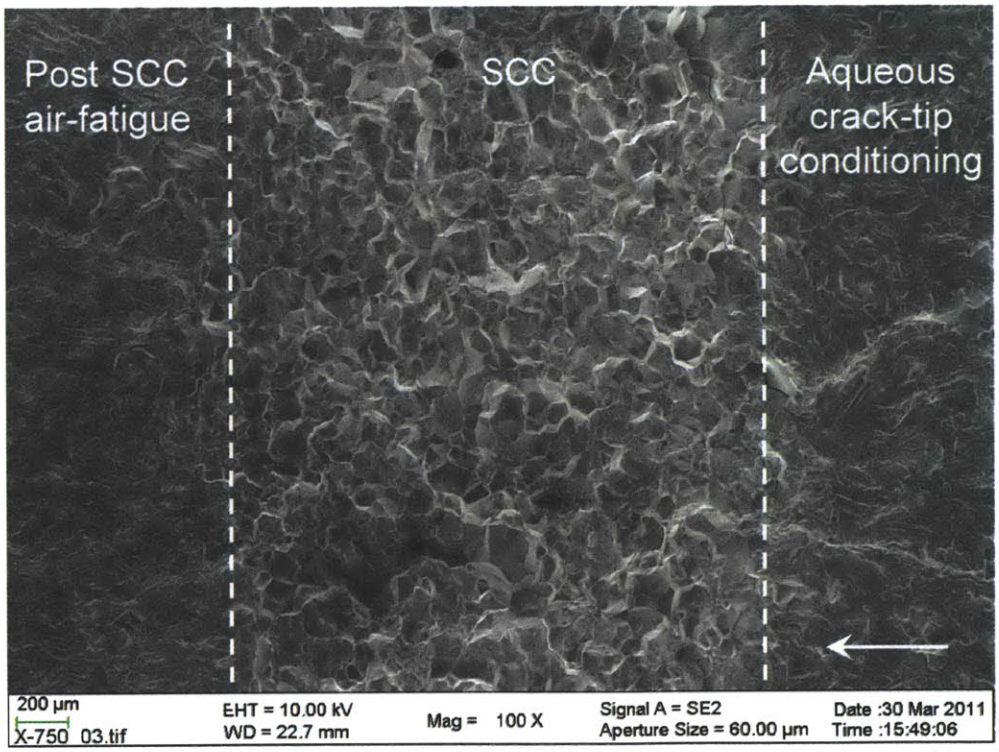

Figure 4-1: Overview of SCC and fatigue fracture surfaces, arrow indicates direction of crack propagation

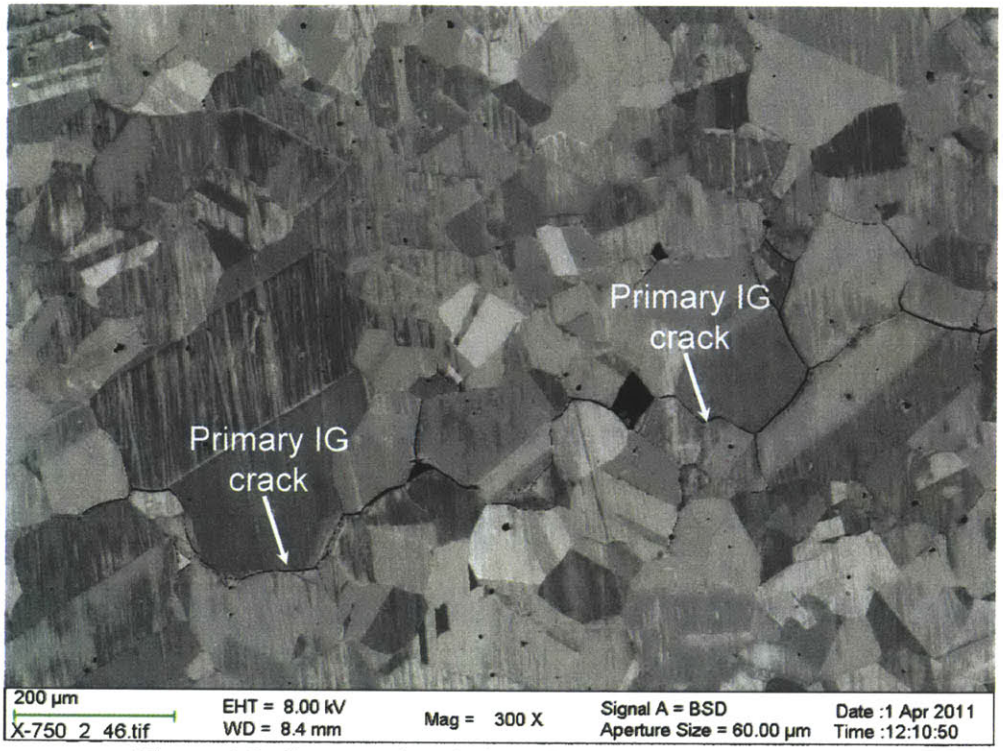

Figure 4-2: Cross-sectional view of intergranular crack path

4.2 Intergranular and Pseudo-Intergranular Cracking

Pseudo-intergranular (adjacent to $M_{23}C_6$ carbides) cracking which occurs in the γ' denuded zone and intergranular (along twins or highly-coherent boundaries) cracking are the most prominent crack paths observed. A representative main fracture surface is shown in Figure 4-3. The fracture surface has numerous Nb-carbides and sparse TiN-particles. These two phases pin grain boundaries and locate intergranularly, but they were not shown to contribute to the SCC susceptibility. However, the dissolution of Nb-carbides may contribute to Nb content at the crack tip. The Nb-carbide phase forms independently from other carbides and the "string" of Nb-carbides visible in Figure 4-3 is rare.

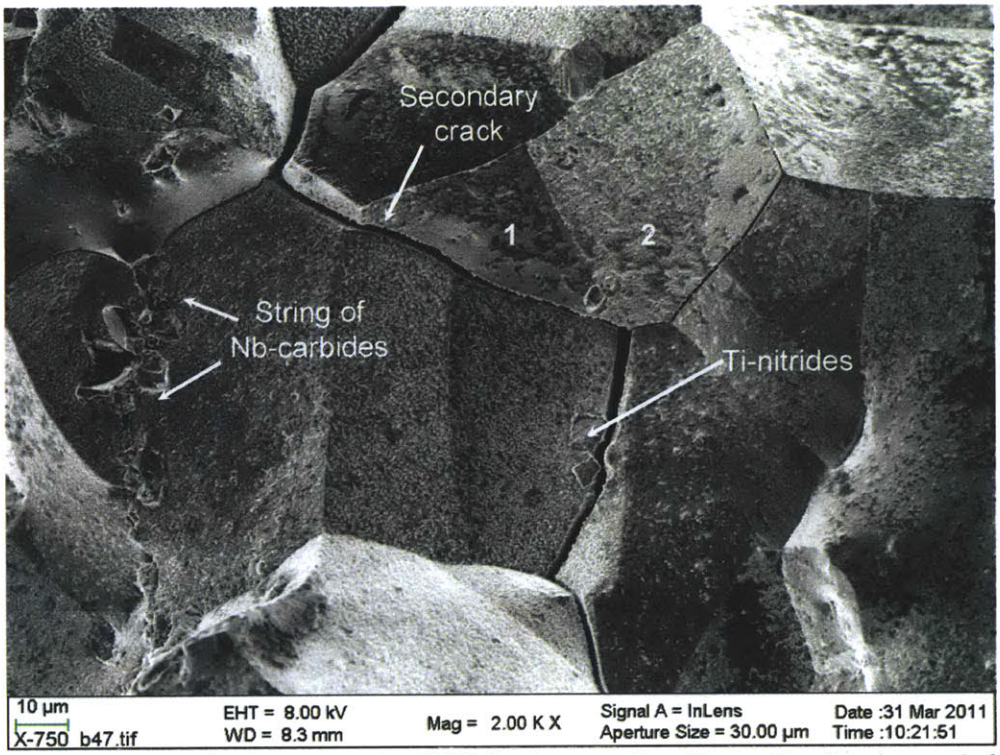

Figure 4-3: Representative intergranular SCC fracture surface (the walls of main crack from the fracture surface)

The two main types of intergranular fracture surfaces observed were either smooth or pitted, which corresponded to cracking along the twin or highly-coherent boundaries or adjacent to the $M_{23}C_6$ and grain boundaries, respectively. The smooth fracture surface is indicated by the "1" in Figure 4-3 and the pitted surface by "2". These regions are shown in higher magnification in Figure 4-4. The large dark regions on the smooth surface are nucleations of chromium-rich oxide. The regions with a dimpled appearance on the pitted surface are due to the tortuous path and associated with oxidation as the crack advanced around the periphery of the $M_{23}C_6$ carbides. Analyzing the dark regions inside the pits with energy-dispersive X-ray spectroscopy (EDS) indicated chromium carbide presence, which is shown in Figure 4-5.

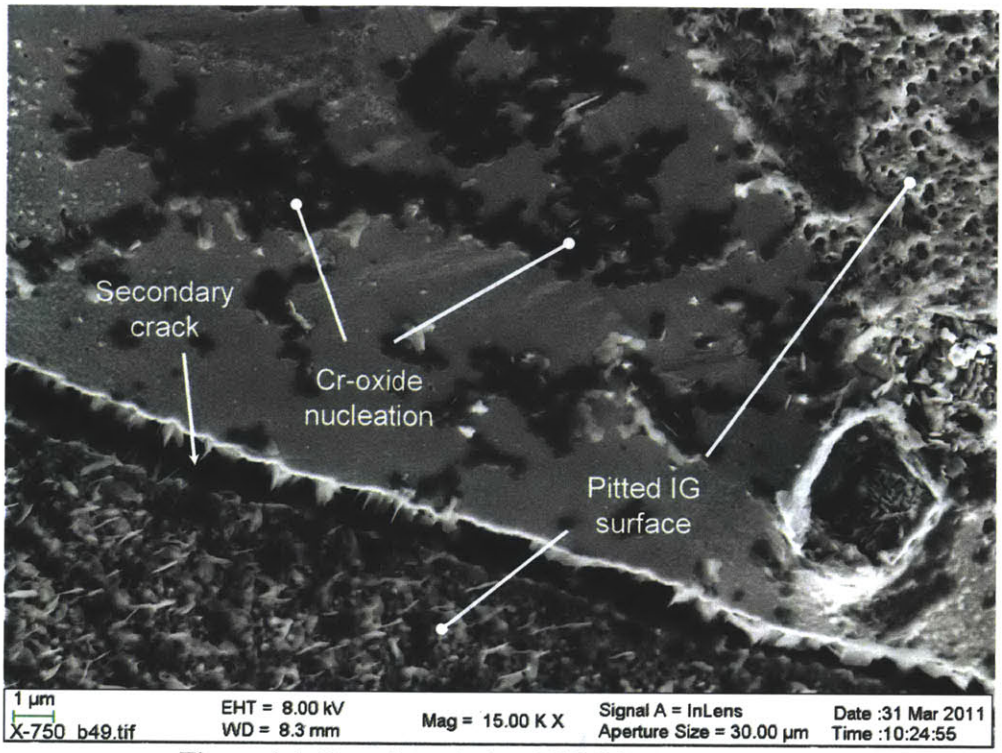

Figure 4-4: Smooth and pitted SCC fracture surfaces

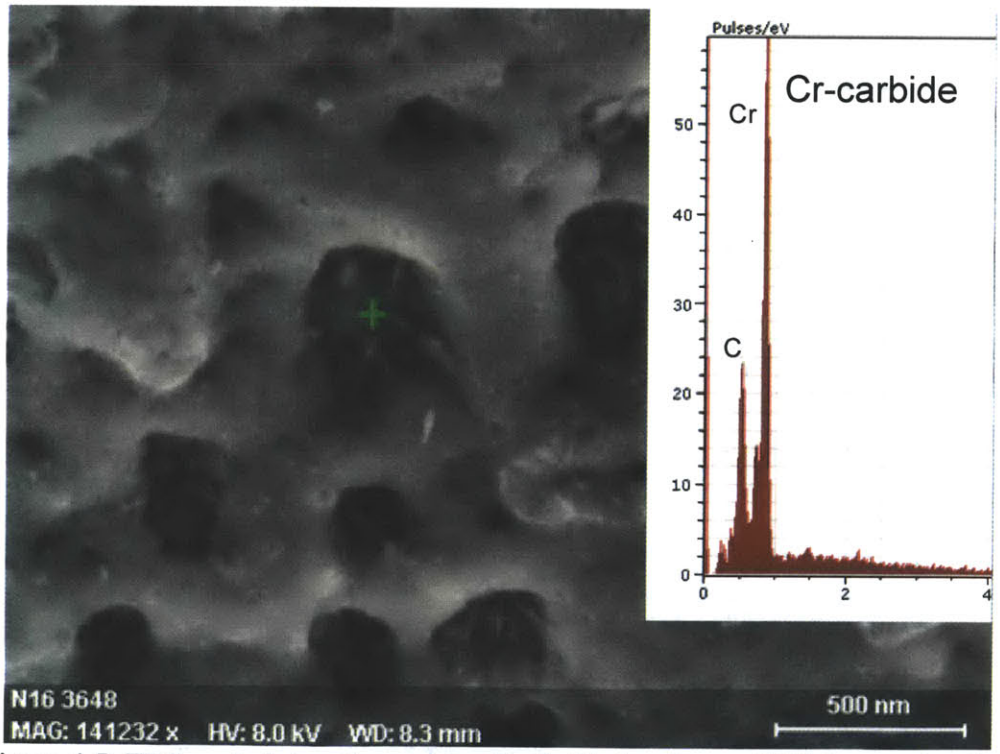

Figure 4-5: EDS analysis location and result of pitted region on SCC fracture surface

Examining a polished cross-sectioned of a SCC specimen clearly showed the difference in the crack morphology as a function of grain boundary type. SCC cracks propagate along both twin or highly-coherent grain boundaries and the "standard" boundary that contains a semi-continuous network of $M_{23}C_6$ type carbides. The cracking mode is different between these two types of boundaries, but a preferred cracking path was not observed. Figure 4-6 shows a crack propagating along a standard grain boundary. When the crack reaches a grain boundary triple point, it continues along two different paths. One path is a highly-coherent boundary, and the other path is a standard boundary. The crack has propagated approximately the same length on each boundary, which is further indication that one boundary type is not preferred. The lower images in Figure 4-6 are focused to the crack tips for each crack path. The crack tip corresponding to the highly-coherent boundary is smooth and appears to be propagating straight with only minor perturbations from the crack path trajectory. The crack tip of the crack on the standard boundary is following a torturous path around the grain boundary carbides.

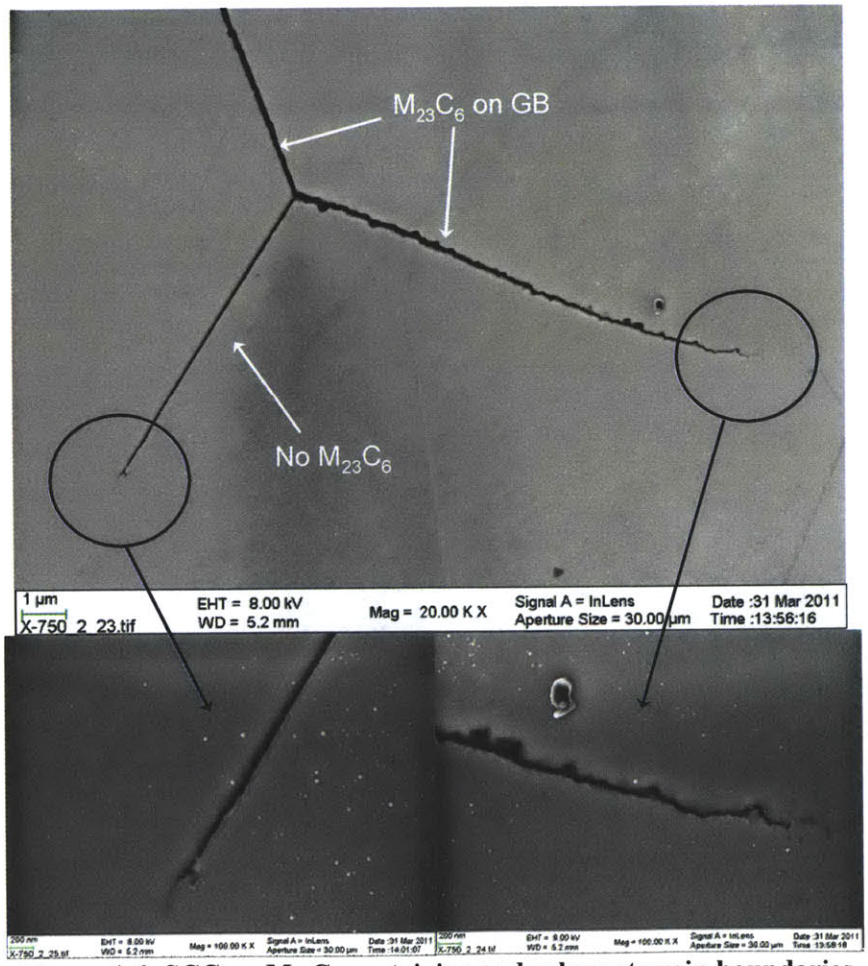

Figure 4-6: SCC on $M_{23}C_6$ containing and coherent grain boundaries

Figure 4-7 shows how the crack morphology changes when it transitions from one type of grain boundary to the next. The grain boundary on the left is a standard boundary that shows a wider crack path and a higher degree of oxidation. The grain boundary on the right shows that the crack is following slip-planes close to the grain boundary, but the grain boundary controls the crack propagation direction. Figure 4-8 is a higher magnification image of Figure 4-7 and shows the zig-zag like crack advance more clearly. The crystallographic planes of crack propagation are visible close to the highly-coherent grain boundary. The upper part of the crystallographic fracture shows that the fracture surface will exhibit a step-like structure.

Figure 4-9 shows a triple point along the crack path. The initial crack was advancing along a standard grain boundary and changes morphology to a "smooth" cracking as it transitions to the next grain boundary. Crystallographic vein-like contrast is not apparent within a region 400-500 nm directly adjacent to the standard grain boundary (region 1 in Figure 4-9). This narrow region may correspond to the γ' denuded zone (contains only fine γ'). It is important to note here that the intragranular γ' is coherent with the γ matrix. Thus, the visible crystallographic vein-like contrasts may be an electron scattering effect in the SEM image that shows the location of γ'. This "denuded-zone" feature (no visible crystallographic contrast) is commonly observed adjacent to the standard grain boundaries, but not the coherent boundaries. This indicates that there is no γ' denuded zone adjacent to the highly-coherent boundaries. Figure 4-9 clearly shows that the standard grain boundary experiences more severe selective oxidation than the highly-coherent boundary. This effect was also observed on the fracture surface.

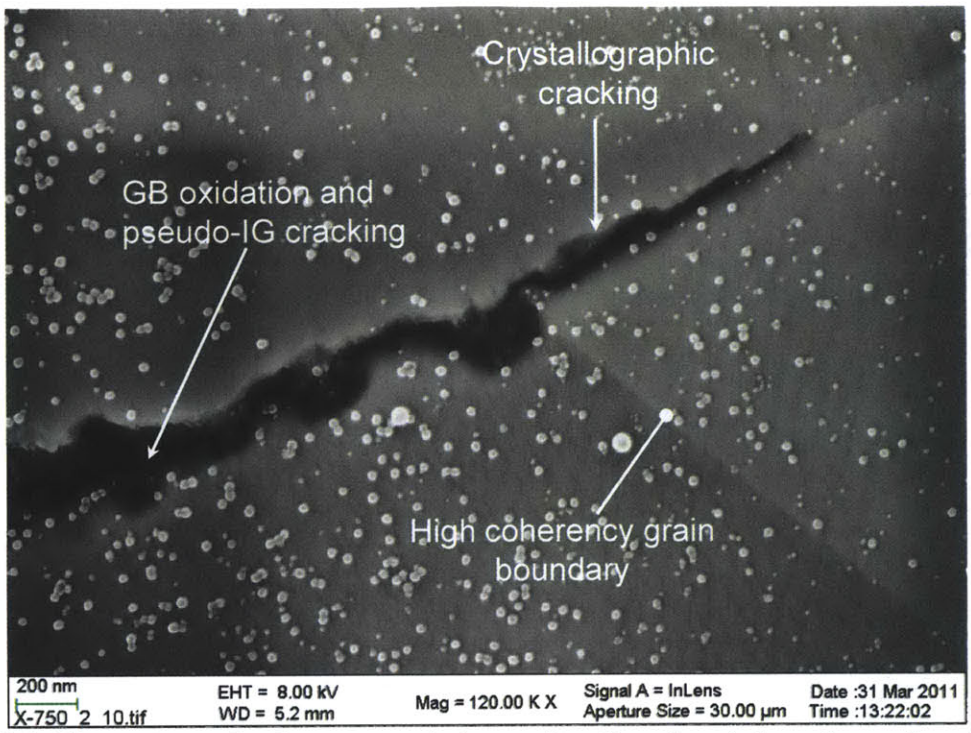

Figure 4-7: Change in crack advance morphology as function of grain boundary microstructure

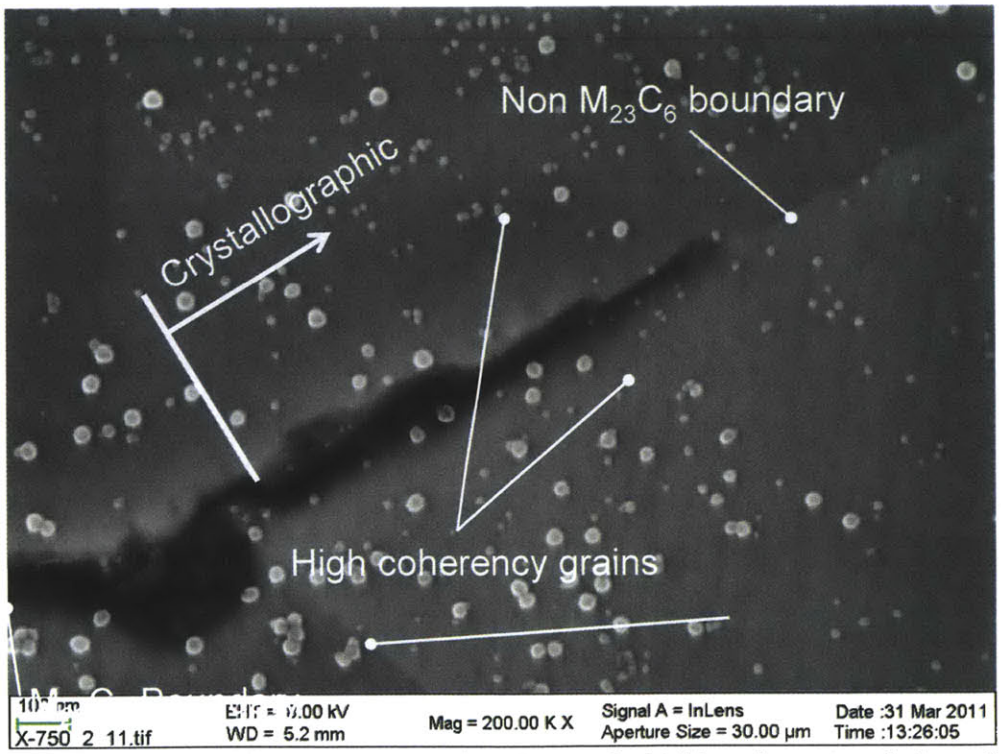

Figure 4-8: Crystallographic crack propagation close to the highly-coherent grain boundary

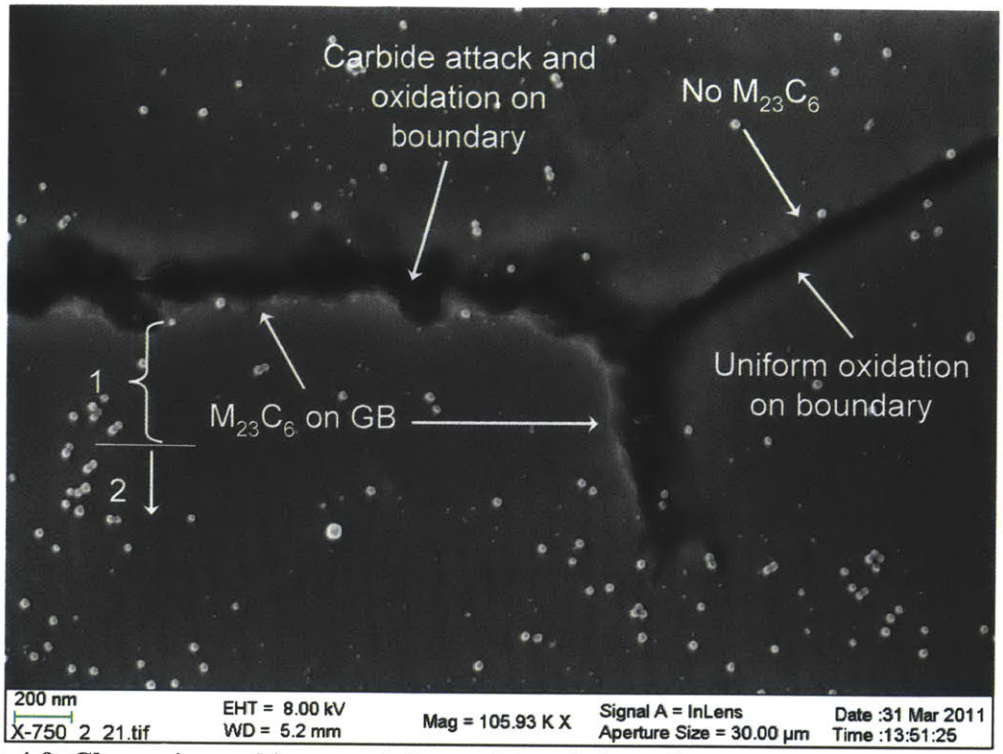

Figure 4-9: Change in cracking morphology with grain boundary structure. Note the vein-like contrast extending up to highly-coherent boundary but not to the standard grain boundary

Figure 4-10 shows multiple cracking mechanisms contributing to crack propagation. The grain boundary carbides are clearly visible along the uncracked grain boundary. Additionally, the grain boundary appears be experiencing decohesion several micrometers ahead of the crack tip. This is an indication that the grain boundary may serve as a preferential pathway for vacancy diffusion ahead of the crack and will be discussed in greater detail in Chapter 6. However, the decohesion may also be an indication of decohesion from shear loading. The exact cause of the decohesion is unknown.

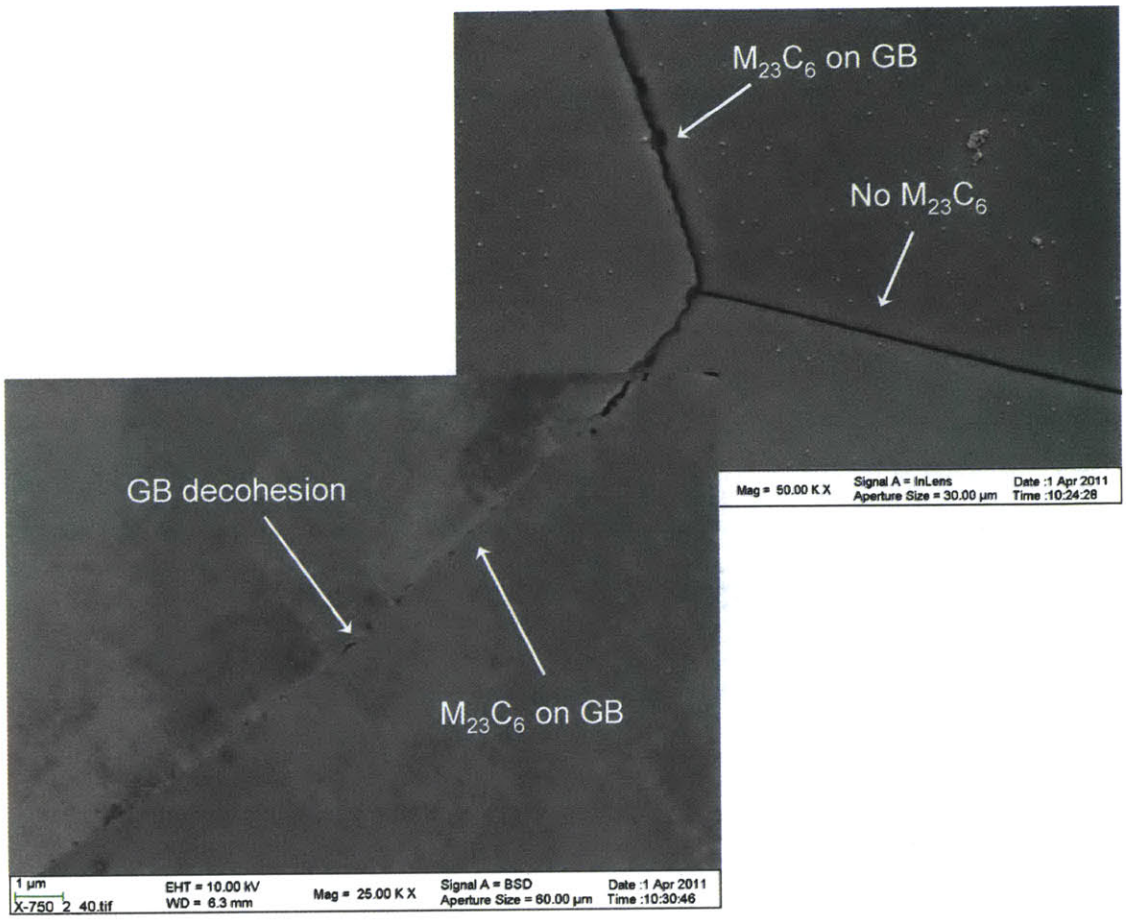

Figure 4-10: Grain boundary decohesion ahead of intergranular crack

The SCC fracture surface around the large TiN phase is shown in Figure 4-11, which was first identified in Figure 4-3. A secondary crack is propagating from the intergranular fracture surface along the interphase between the matrix and TiN-particle. The fracture surface is highly faceted and the two fracture surfaces are matching. Directly adjacent to the secondary crack (on the right side) is a region with pitting around $M_{23}C_6$ grain boundary carbides on the main fracture surface. Approximately 4-5 µm away from the secondary SCC crack is a twin or highly-coherent boundary. The cracking morphology changes across this boundary. The fracture surface on the far right side of Figure 4-11 exhibits slip steps and reduced oxidation. A higher magnification of Figure 4-11 is shown in Figure 4-12 and is focused on the interphase region between the matrix and TiN-particle. This region shows has crystallographic micro- and nano-cracking. Figure 4-13 shows the transgranular nano-cracking and is a higher magnification image of Figure 4-12.

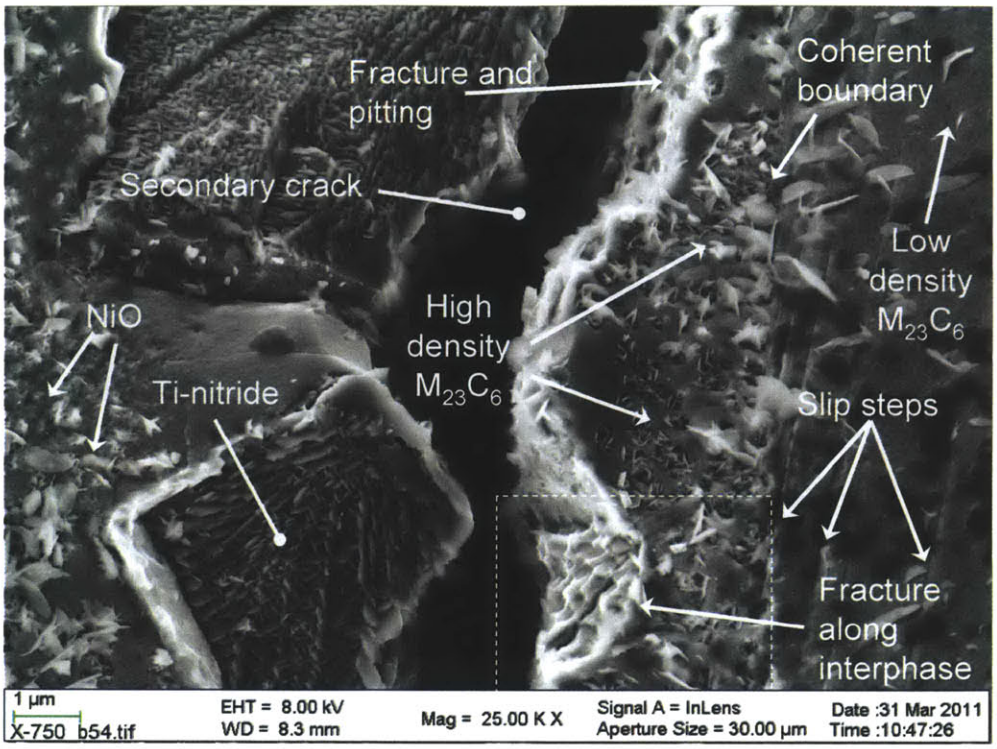

Figure 4-11: Intergranular TiN phase and associated fracture characteristics

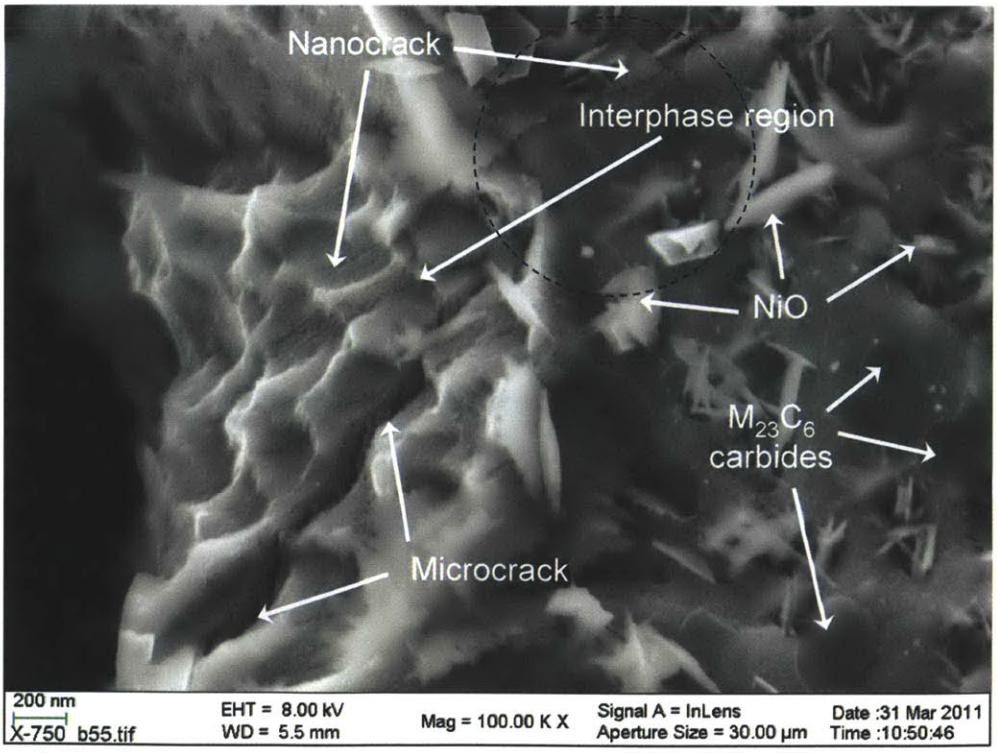

Figure 4-12: Matching fracture surface of TiN particle interphase showing faceted cracking

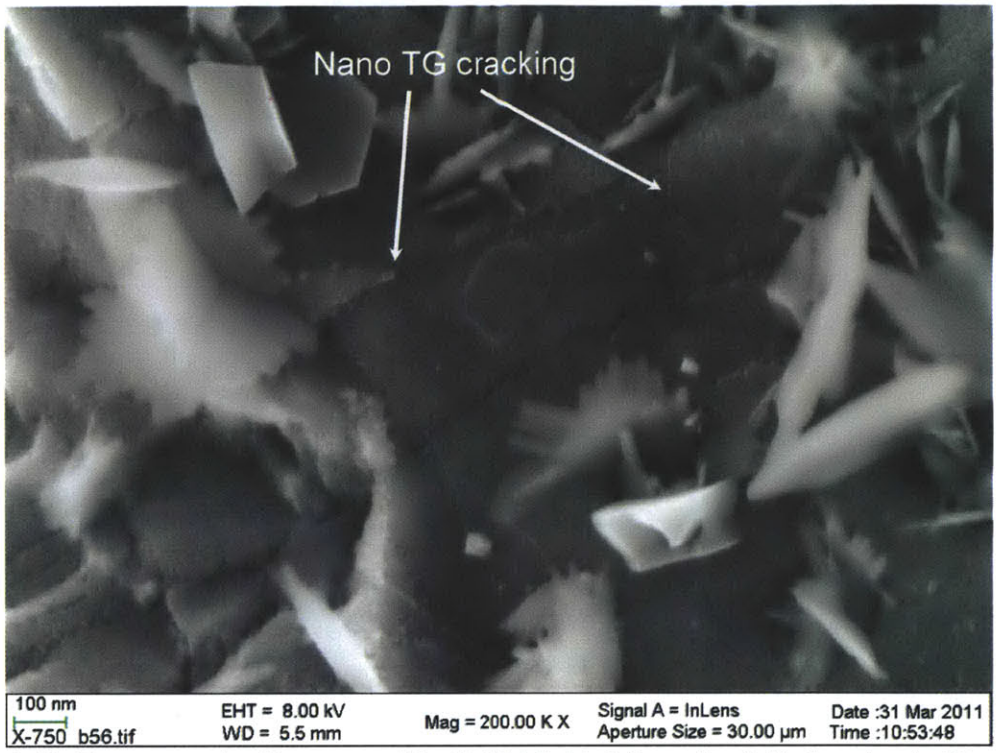

Figure 4-13: Transgranular "nano-cracking", highlighted from the dotted-region in Figure 4-14

The SCC cracks were observed to propagate around or through intergranular Nb-carbides. Figure 4-15 shows a cross-sectional view of the main SCC crack advancing around an intergranular Nb-carbide, and Figure 4-16 shows the main SCC crack advancing through an intergranular Nb-carbide particle. Figure 4-17 shows the EDS spectrum of the Nb-carbide and shows that the composition is rich in niobium and carbon, but it also has a small amount of titanium. The Nb-carbide phase is hard compared to the matrix and its fracture is caused by shear (Mode II) loading. The primary difference between the un-fractured Nb-carbide in Figure 4-15 and the fractured Nb-carbide in Figure 4-16 is the amount of shear loading locally on the material. The effect of grain boundary shear is also shown in Figure 4-18. Comparing these two regions, the fracture path in Figure 4-16 exhibits considerably more shear displacement, which is evident by the large separation (greater than 1 µm) between the crack walls. The lower image in Figure 4-16 shows that the Nb-carbide readily oxidizes. Nb-carbide fracture and oxidation contribute to the enriched Nb in the crack tip chemistry (discussed in greater detail in next chapter).

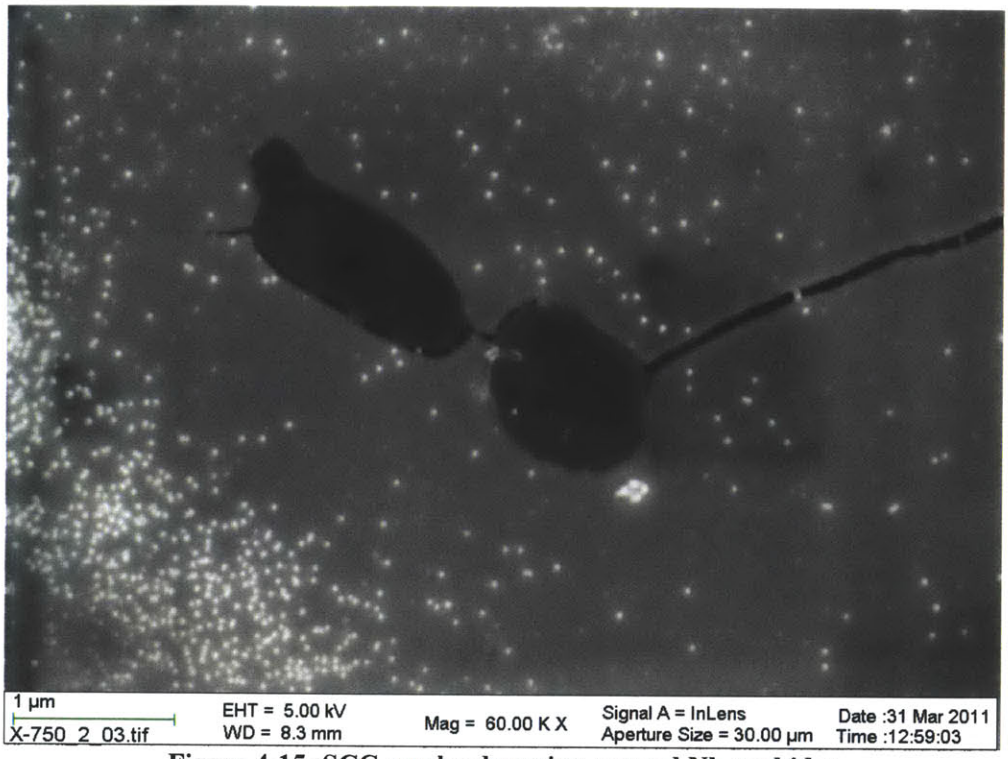

Figure 4-15: SCC crack advancing around Nb-carbides

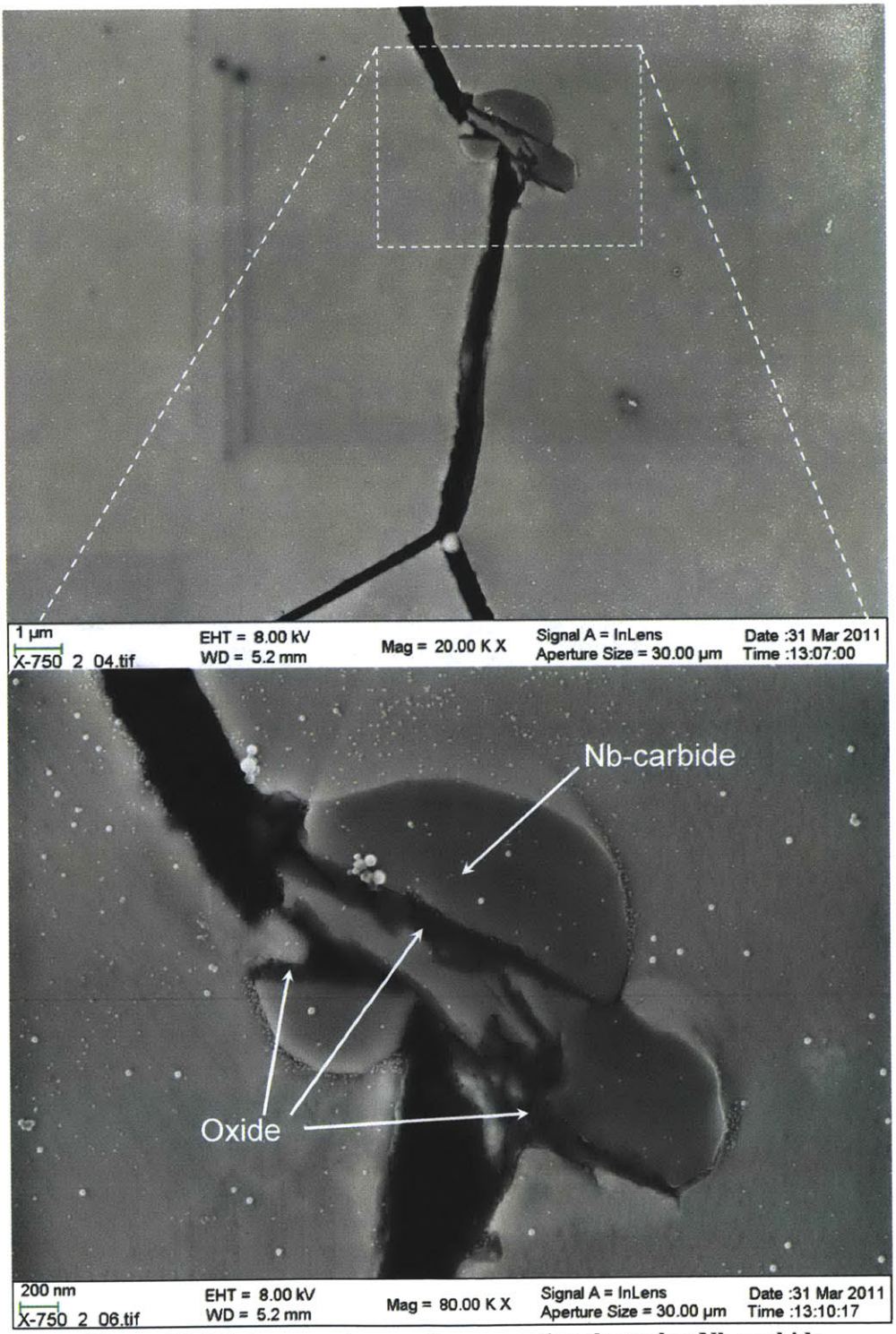

Figure 4-16: Intergranular crack propagation through a Nb-carbide

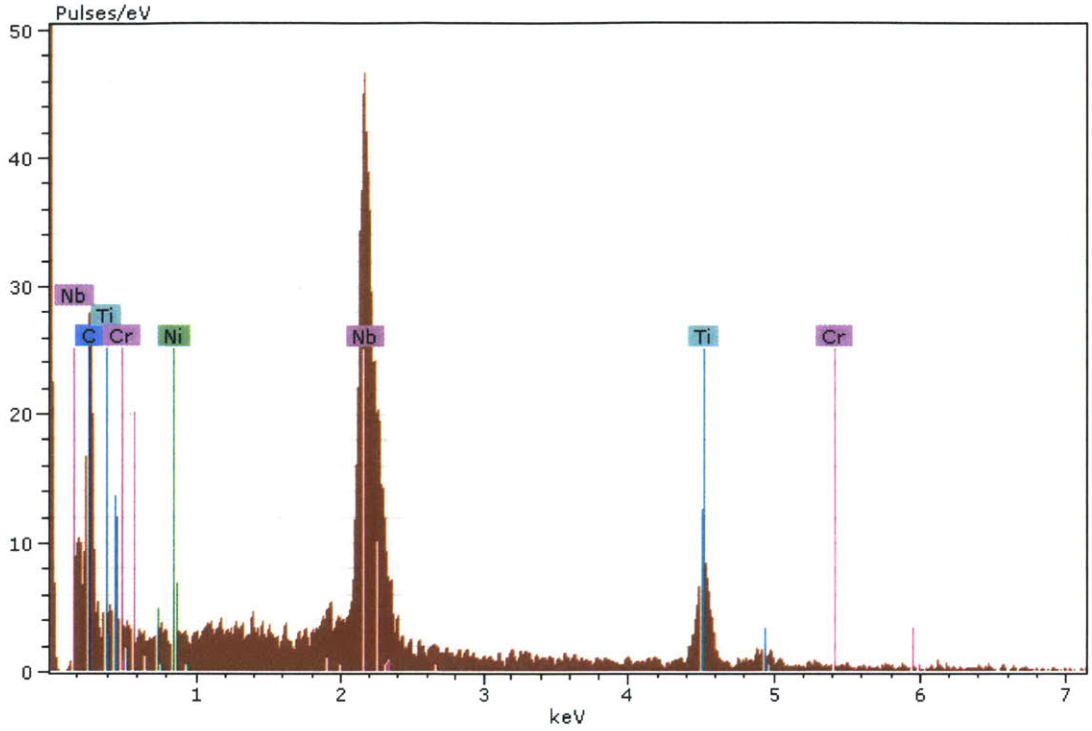

Figure 4-17: EDS spectrum of Nb-carbide phase

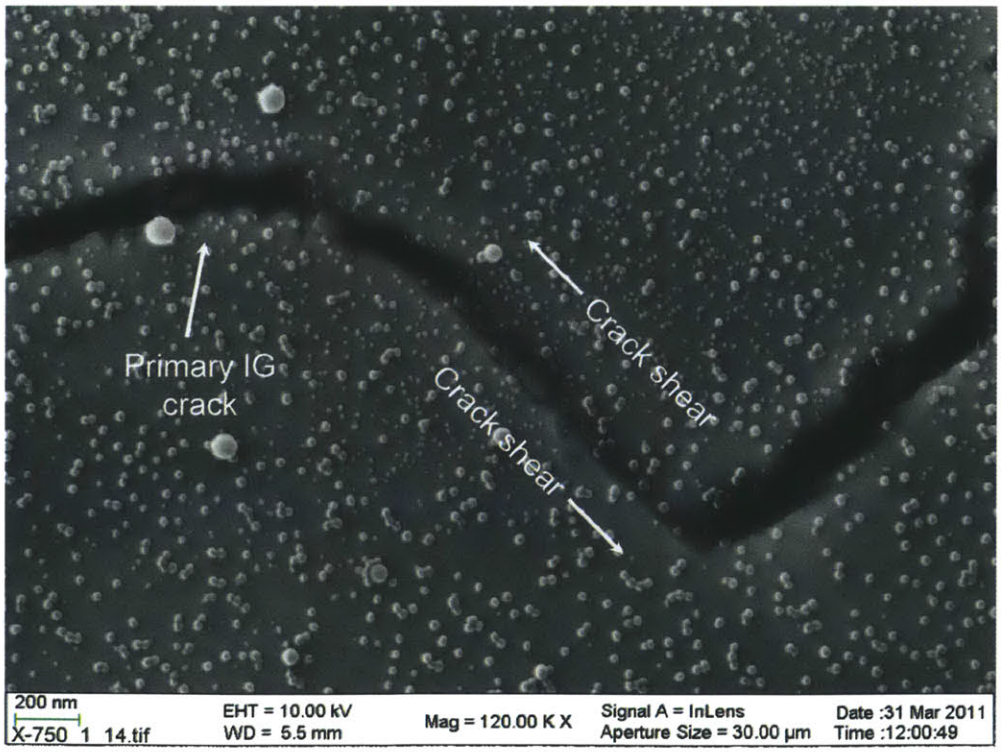

Figure 4-18: Shear loading of crack causing shear displacement of fracture surfaces

Figure 4-19 shows crack propagation along the grain boundary and through a Nb-carbide. The tip of the crack shows additional selective oxidation as it interacts with the $M_{23}C_6$ carbides. A large Nb-carbide is present in the upper-left region of Figure 4-19. The large size of this Nb-carbide is rare. Several micrometers ahead of the crack tip shows another example of grain boundary decohesion in Figure 4-19.

An elemental map was generated to further characterize the crack path and carbides. This is shown in Figure 4-20 and includes a map for carbon, titanium, niobium, chromium, and nickel. The map compilation clearly shows that the two large carbides in Figure 4-19 are rich in niobium, titanium, and carbon. Moreover, the elemental maps shows that the crack path is rich in carbon and chromium, which indicates that it occurs along a grain boundary with $Cr_{23}C_6$ precipitates and has enrichment of chromium oxide within the crack.

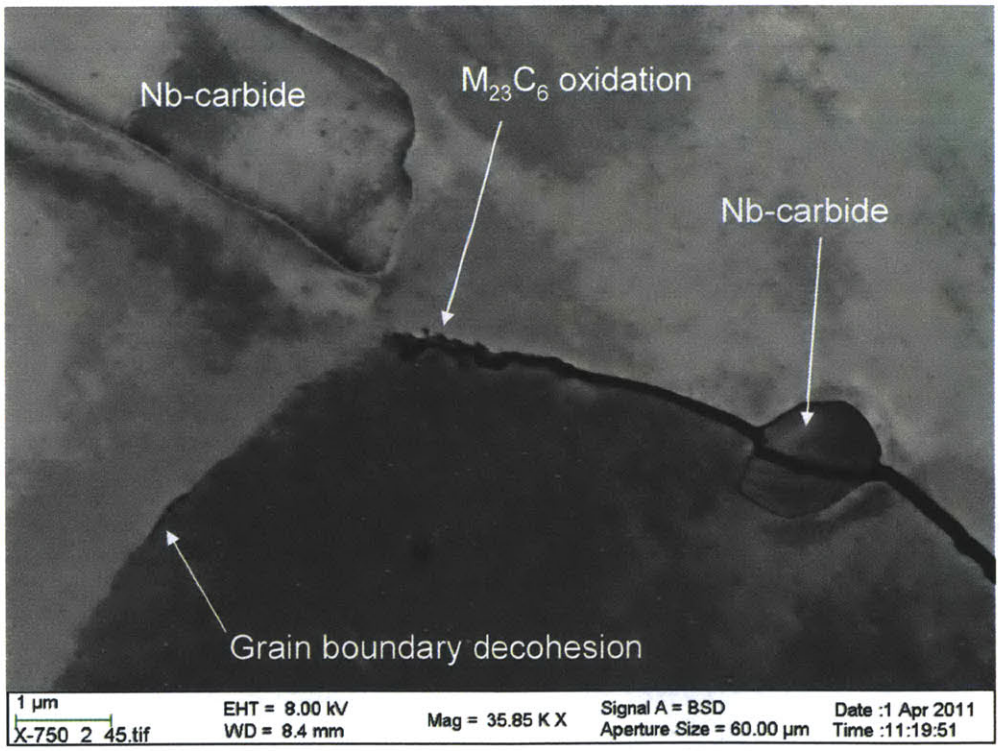

Figure 4-19: Cracking through Nb-carbide, selective oxidation of $M_{23}C_6$ containing grain boundary and grain boundary decohesion ahead of SCC crack

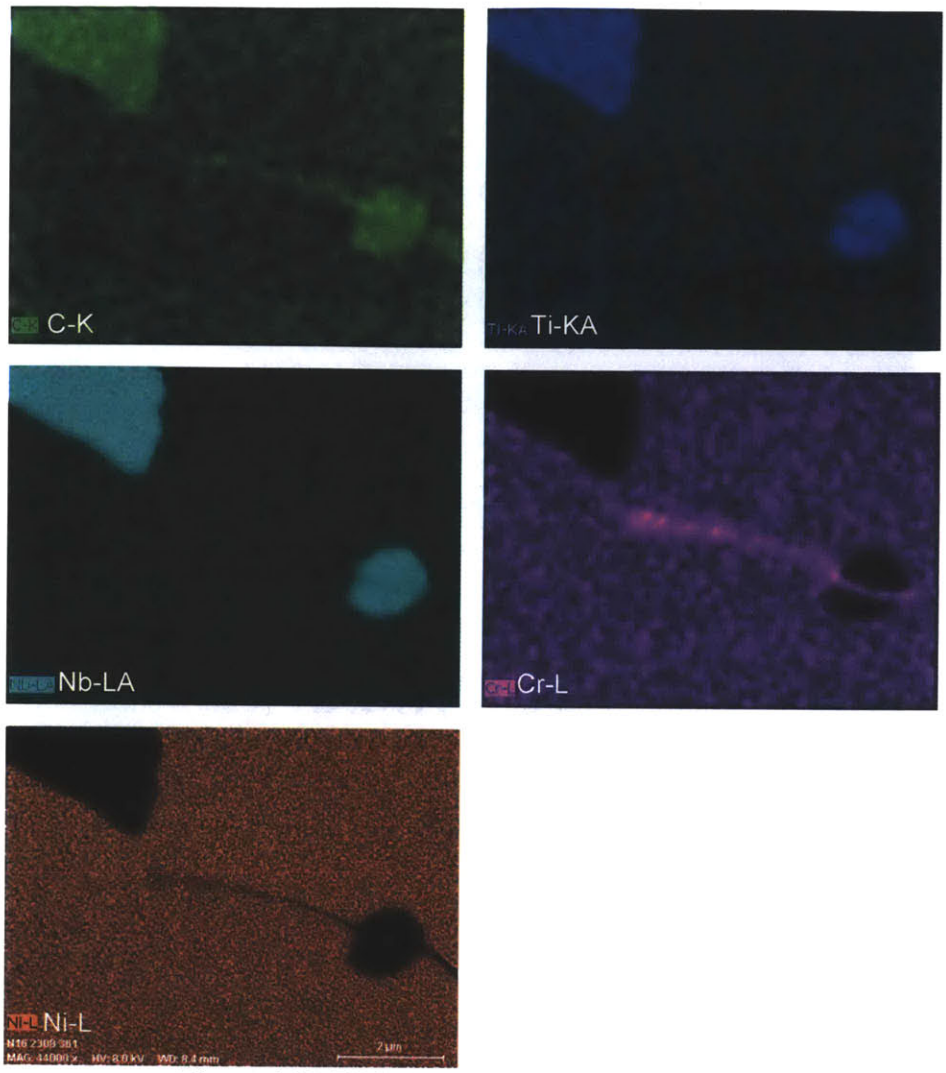

Figure 4-20: EDS elemental maps of Figure 4-19

4.3 Transgranular Cracking

Transgranular cracking was observed on the fracture surface and cross-sectional views; however, this mode of cracking was localized and typically occurred between two intergranular cracking regions. The transgranular fracture surfaces had a brittle-like appearance. Figure 4-21 shows the main fracture surface with a representative transgranular region. Transgranular cracking was observed as both highly-crystallographic planar cracking. Planar cracking propagates along a specific crystallographic plane (typically {110}) and the resulting surface shows slip steps ({111} planes) which results in a brittle-like and smooth crystallographic appearance. Figure 4-21 shows the planar crystallographic cracking in the lower and upper regions of the

transgranular zone and the planar fracture inside the twin in the middle region. These two modes are divided by a highly-coherent boundary. Figure 4-22 is a higher magnification view of the region highlighted within the dotted-line box in Figure 4-21 and shows the faceted crystallographic transgranular crack morphology inside the twin.

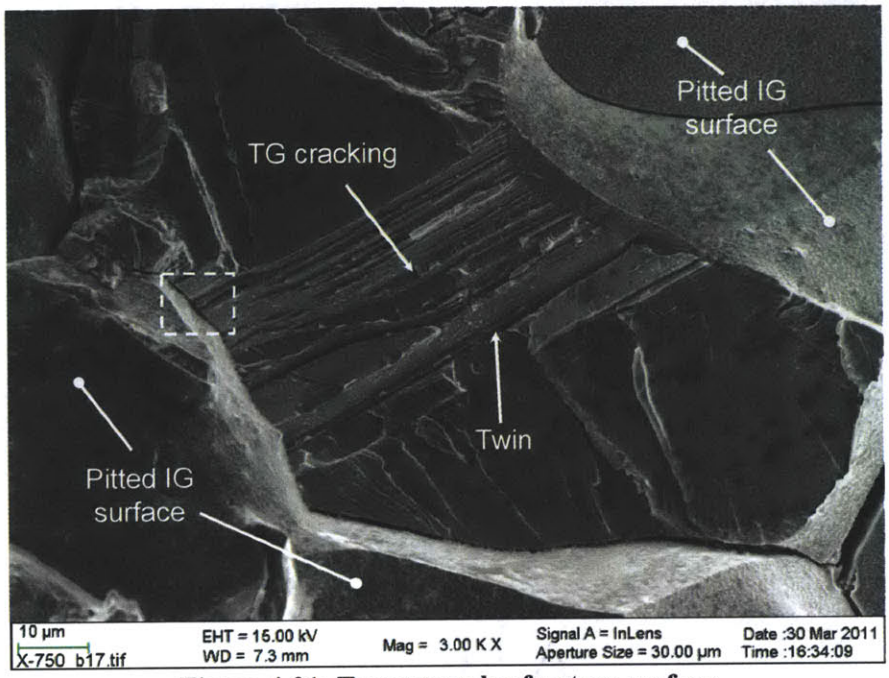

Figure 4-21: Transgranular fracture surface

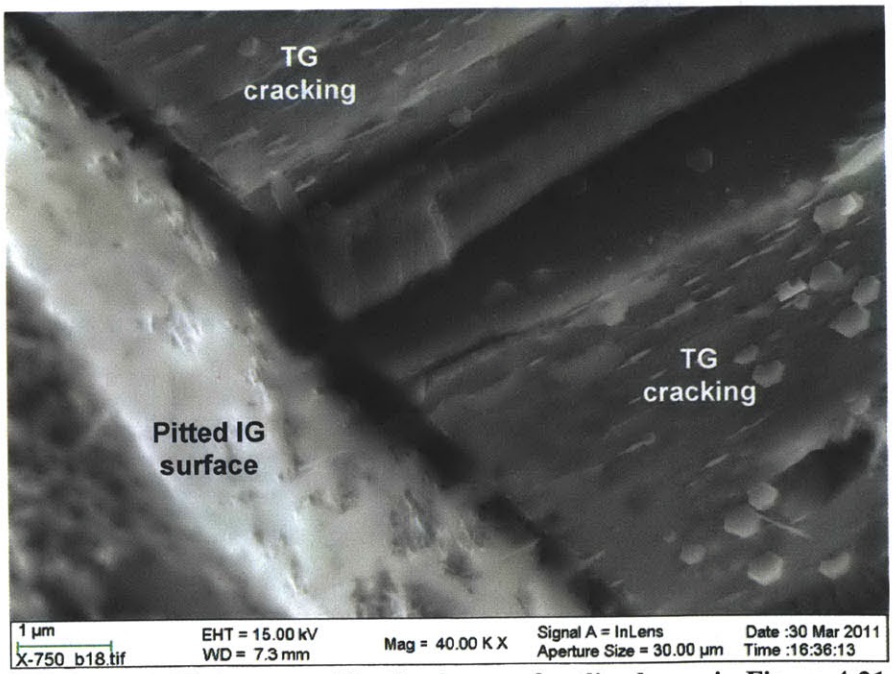

Figure 4-22: Higher magnification image of outlined area in Figure 4-21

A cross-sectional view of transgranular cracking is shown in Figure 4-23 and Figure 4-24 and indicates that the cracking is isolated between two intergranular regions. Figure 4-23 shows intergranular and transgranular cracking. The main intergranular crack path experienced considerable shear, which largely contributed to cracking. The grain boundaries are weaker than the grains which serve to constrain the system and result in shear-induced intergranular cracking. This constraint and shear also directly contributed to transgranular cracking, but the effect of shear is less pronounced than the intergranular effect. The Nb-carbide along the intergranular crack path is fractured, and the small cracks have propagated transgranularly into neighboring grains. Additionally, transgranular cracking in Figure 4-23 closely resembles the planar cracking observed in Figure 4-21, and it continuously changes the crystallographic plane over 10 μm or larger distance. Figure 4-24 shows more extensive planar transgranular cracking.

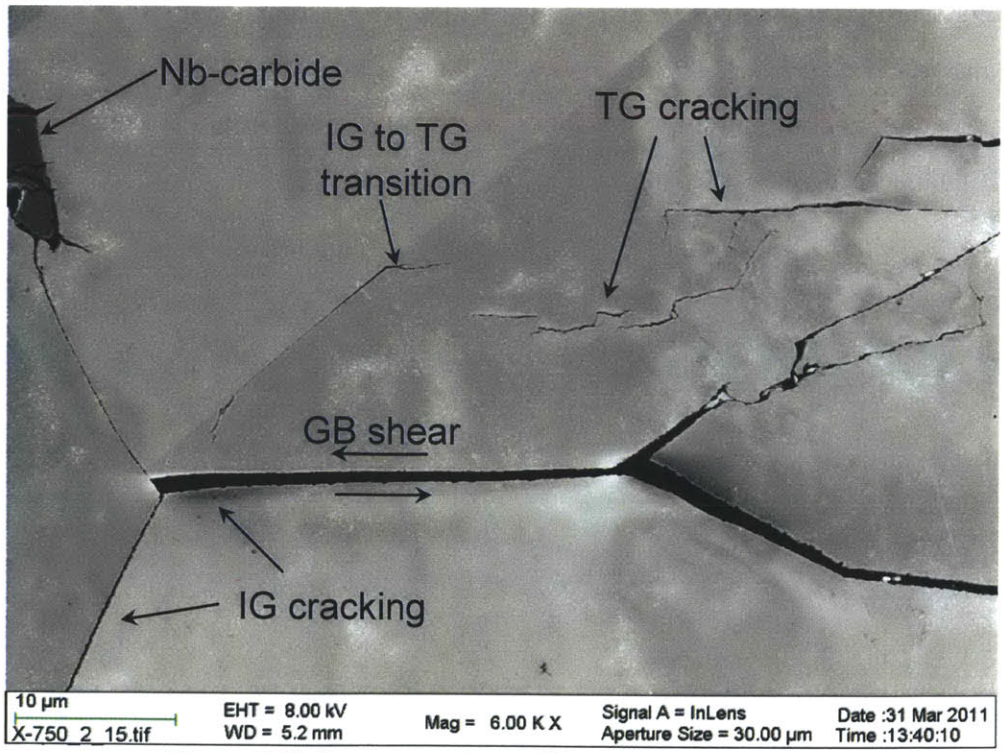

Figure 4-23: Transgranular and intergranular cracking

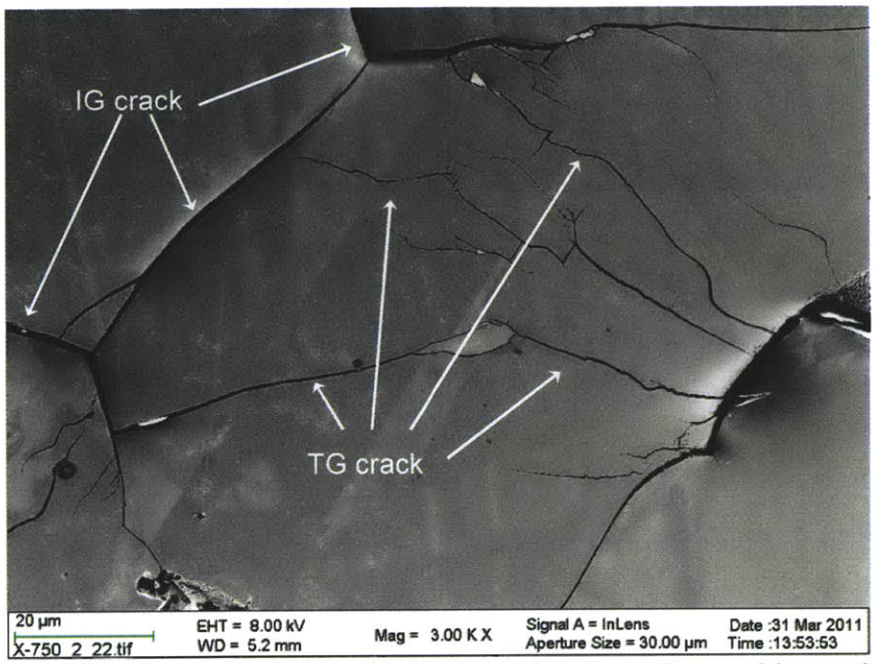

Figure 4-24: Transgranular cracking between intergranular cracking regions

Figure 4-25 shows a secondary transgranular crack propagating along a grain face on an intergranular fracture surface. The transgranular crack is following slip planes and also shows how shear loading is contributing to cracking. Several parallel transgranular cracks have been initiated from this secondary crack.

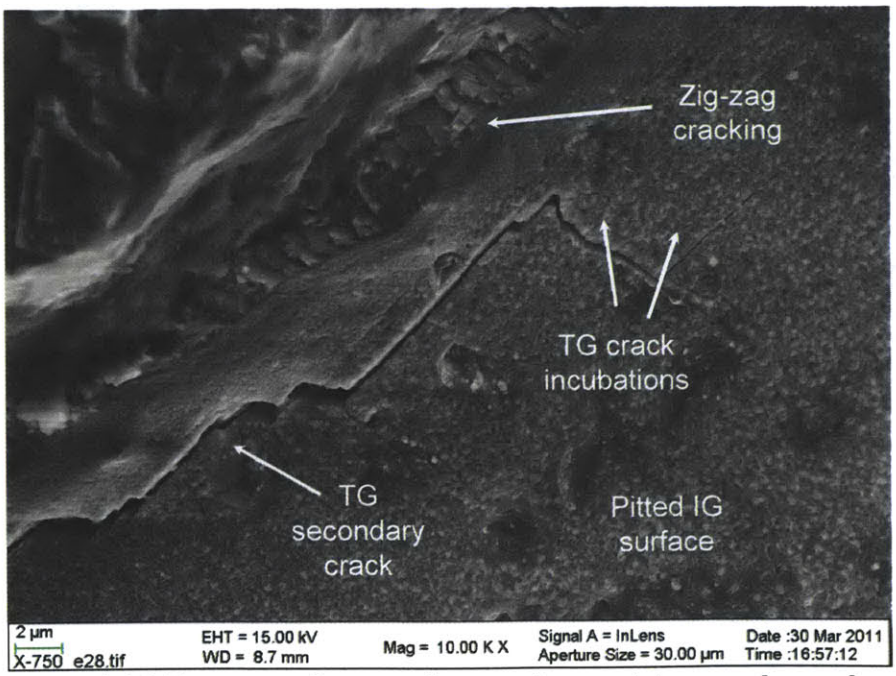

Figure 4-25: Transgranular secondary crack on an intergranular surface

4.4 Summary

This chapter presented the fractographic features and some analysis of the SCC behavior. The cracking mode was predominantly intergranular and pseudo-intergranular. Transgranular cracking was observed in localized regions. Grain boundaries containing a semi-continuous network of $M_{23}C_6$ carbides had a pitted-like appearance, which was due to the path the crack took as it propagated adjacent to the grain boundary carbides. Cracks that propagated along twin or highly-coherent boundaries resulted in a fracture surface with a smooth appearance. The macro fracture surface topography showed many large intergranular secondary cracks and small secondary transgranular cracks. No preferential path was observed between intergranular and pseudo-intergranular cracking. The grain boundary structure had the strongest influence on the mode of crack propagation. Cracks propagated in a tortuous path around the grain boundary $M_{23}C_6$ carbides and in a smooth path along twin or highly-coherent grains. Grain boundaries that contained $M_{23}C_6$ carbides experienced more extensive selective oxidation than the highly-coherent boundaries.

Intergranular Nb-carbides and TiN particles were not observed to contribute significantly to the crack propagation morphology. Cracks propagated around or through the Nb-carbides, which appeared to be controlled by the amount of shear stress contributing to the overall stress state. The Nb-carbides were fractured in regions of high shear loading and the cracks propagated around the carbides in regions with low shear stress. The TiN particles were also passed along the particle interphase, and the surface adjacent to the interphase cracking was highly faceted and experienced secondary transgranular micro- and nano-cracking.

Chapter 5 - Crack Tip Characterization

5.1 Introduction and Overview

The exact mechanisms of environmentally assisted cracking have proven difficult to establish because mechanical and electrochemical processes occurring at the crack tip cannot be directly observed in bulk specimens. The proposed mechanisms for SCC are based on observations from laboratory tests and field failures, based on metallographic observations and crack growth rate response, as well as estimates of the actual crack tip conditions. This chapter covers stress corrosion crack tip characterization. In this work, two main techniques are used to further understand the driving mechanisms of crack growth at the crack tip: atom probe tomography (APT) and scanning electron microscopy (SEM). Together these two techniques bridge the gap between nano- and micro-scales and are able to offer unique insight to the active SCC processes in this work. The "standard" method utilized by many researchers to characterize crack tips has been SEM, SIMS, and to a lesser degree, ATEM.[1-3] APT is the first method to provide sub-nanometer resolution with high reliability elemental analysis. Additionally, tomographic techniques are now being employed to characterize crack tips.[4] APT and tomographic analyses, along with the standard methods, are achieving resolutions and complemental techniques to allow unique insight for crack characterization.

- Section 5.2: Atom probe introduction
- Section 5.3: Crack tip and specimen lift-out procedure
- Section 5.4: Crack tip 1: analysis of corrosion tunnels, analysis of element/compound presence within bulk ahead of tunnels, near-crack γ' changes
- Section 5.5: Crack tip 2: 2D composition profiles of crack up to tip and oxygen penetrations laterally from crack wall
- Section 5.6: Crack wall 1: crack wall oxide characterization and γ' mapping as a function of proximity to crack
- Section 5.7: Discussion and summary

5.2 Atom Probe Introduction

Atom probe microscopy was used in this thesis work to characterize the tips of stress corrosion cracks and the base microstructure. This method was chosen because it offers three-dimensional elemental identification and microstructural reconstruction capabilities with sub-nanometer resolution.

5.2.1 Brief History of Atom Probe

Atom probe microscopy is a material science characterization method that was invented in the late 1960s.[5] This technique is closely related to Field Ion Microscopy, which was developed in the early 1950s and was the first technique to achieve atomic resolution.[6] Modern atom probe tomography (APT) is able to achieve atomic resolution in three dimensions. In recent years, atom probe microscopy technique has made superb advancements that have considerably improved the performance of three-dimensional reconstruction capabilities, data collection rates, and expansion of the type of material able to be analyzed.[7] Acceptable materials range from pure metals and simple model alloys to complex multicomponent engineering alloys, semiconductors, and some ceramics. Additionally, coupling site-specific sample removal and preparation using a dual-beam focused ion beam (FIB) microscope has further expanded the materials characterization capabilities.

5.2.2 Atom Probe Theory

The atom probe microcopy technique is technically a destructive method because it removes ions from a sample surface. This method works by a controlled evaporation process (field evaporation) and the evaporated ions are impacted onto a detector. The high voltage field applied to the atom probe tip can range from 5-15 kV, which is directly related to the sharpness of the specimen tip. The induced stresses from the voltage field push many materials close to theoretical strength limit. Materials with few defects can successfully evaporated within an atom probe microscope. When samples contain internal defects, especially large defects such as grain boundaries and cracks the failure likelihood increases significantly. This is the primary reason why little literature has been produced that shows atom probe results of grain boundaries and crack tips. However, advances in sample preparation techniques have greatly facilitated successful reconstructions of grain boundaries, and to a lesser extent, crack tips, and the literature on these defects is becoming more available.[8-11]

A schematic of the atom probe process is shown in Figure 5-1. A sharp atom probe needle consisting of the material to be analyzed is placed in a high vacuum ($\approx 10^{-11}$ Pa) and reduced to cryogenic temperatures (20-100 K). The sample is grounded and pulsed with a laser to initiate field evaporation from the tip. The field on the apex of the needle, F, is given by (1):

$$F = \frac{V}{k\, r_t}, \tag{1}$$

where:

V = applied voltage

r_t = needle tip radius

k = numerical constant, typically ranging from 2-5.

Thus, the tip of the atom probe needle needs to be extremely sharp to keep the pulsed voltage low. Typical atom probe needle tips have a diameter between 80 - 100 nm. The application of the pulsed voltage to the sample allows for individual ions on the sample surface to have their electric field (atomic bonding) temporarily disrupted. This results in ionized atoms being released from the atom probe tip at a known time. The delay between the time of atom ejection (same time as the voltage or laser pulse) from the tip and ion detection allows for time-of-flight and mass-to-charge ratio calculations. Thus, the location and element identification can be determined.

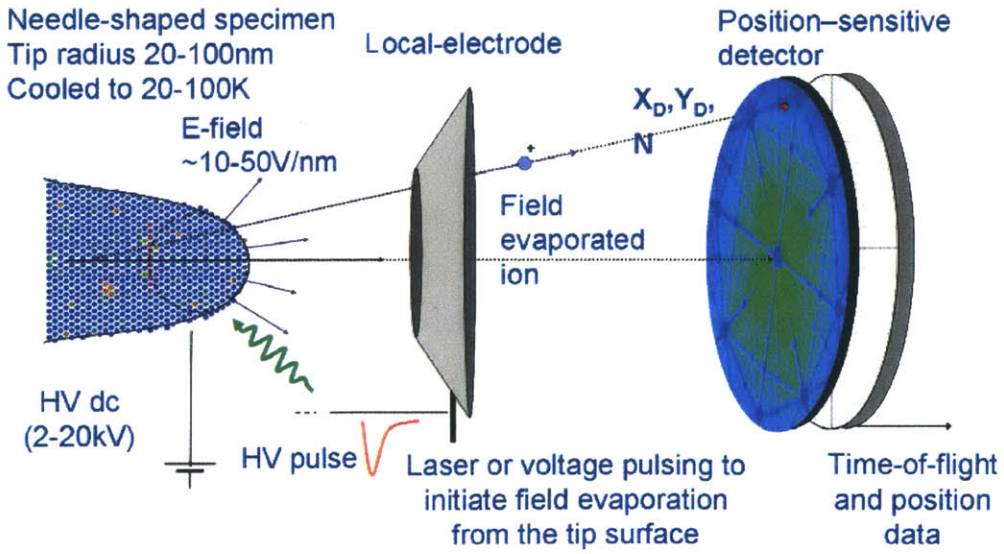

Figure 5-1: Atom probe tomography schematic [12]

The atom probe used in this work was a localized electron atom probe (LEAP) manufactured by Ametec, Inc. The reconstruction was performed with Integrated Vosulation and Analysis Software (IVAS), also produced by Ametec, Inc. The specimen preparation was performed on a Helios NanoLab dual-beam FIB. A step-by-step process of sample preparation with the FIB is provided in Appendix A.

Sample preparation for APT is extremely important. The two methods used for this microscopy technique are electron polishing and site-specific lift-out with a focused ion beam (FIB) microscope. The FIB lift-out technique was use in this work. Specimen lift-out is briefly presented here and a more detailed description for the sample lift-out and preparation is presented in Appendix A.

Helpful definitions for terminology used to describe atom probe results:

Proxigram: A proxigram is a technique for the analysis of interfaces and presents a plot of concentration versus distance. This is analogous to a liner concentration profile. The distance is measured as the proximity of each point to a reference surface, which is user defined. The surface can be any shape, orientation, and complexity as long as it is closed and continuous. The surfaces are user defined and are generated by calculating the isosurface of a scalar 3D field. Positive and negative proximities correspond to the point of space being on the outside and inside of the user established isosurface, respectively. [13]

Isosurface: An isosurface is a shortened term for an isoconcentration surface corresponding to a particular elemental concentration threshold. The isosurface is generated from the concentration space using the marching cubes algorithm.[13-14]

Oxide: The term "oxide" in the context of atom probe refers to oxygen and the corresponding cation (in this case metal cation) being treated as one particle. Oxygen and a cation are treated as an oxide particle if they are detected in close enough proximity where an oxide is likely. The atom probe is not able to distinguish correct stoichiometry of complex oxides (where more than one cation is required). For example, Cr_2O_3 is the thermodynamically stable oxide in much of

this work, but the atom probe will detect CrO, CrO_2, and CrO_3, which means that chromium and oxygen are next to each other and most likely an oxide. The stable form of nickel-oxide is NiO and can be detected because it is comprised of two atoms. If a cluster of oxygen is present in the lattice without sufficient cations the APT software treats the oxygen as non-oxide. Additionally, if two or more oxygen atoms are detected in the same location it may be treated as O_2. This does not indicate dissolved O_2 gas is in the matrix, only that more than one oxygen atom is present.

Oxygen: The term "oxygen" is used to describe oxygen atoms that have not reacted with a metal ion to form an oxide (e.g. NiO). These oxygen atoms can be trapped within the lattice due to oxygen diffusion along dislocations or other lattice defects. The oxygen atoms can also be present within the crack features as a corrosion product.

This chapter is organized into sections based on APT reconstructions. Each section highlights a different aspect of the cracking characteristics. The samples will be referred to as the crack tip 1, crack wall 1, bulk, etc. in the discussion. The results and discussion for each sample is as follows:

5.3 Specimen Lift-out and Sharpening

The crack tips were removed from the 1TCT specimen after completion of crack growth rate testing, as outlined in Figure 5-4 in Chapter 5. The final conditions for SCC in the crack tips analyzed in this work were HWC at 288 °C. Each sample was polished to a mirror finish with the final polishing step using 0.05 μm SiO_2 dispersion polish.

The visible surfaces contained a cross-section of the crack path. Figure 5-2 shows crack tip locations for FIB lift-out. The solid arrows indicate the two crack tips of interest that were used for APT analysis in this chapter. The two dashed arrows indicate other crack tips; however, due to their close proximity to the lift-out volume, these two crack tips were disrupted by the FIB milling process. A region containing the tip and approximately 20 μm in front of the tip was designated as the lift-out area for the APT samples. The lift-out volume containing one crack tip and specimens located ahead of the crack tip is shown in Figure 5-3 and Figure 5-4. Figure 5-3

is the final lift-out volume containing the crack. Figure 5-4 shows an APT blank being mounted on a silicon micropost, which is used to hold the final sharpened sample in the atom probe microscope. After the APT blank is securely mounted on a micropost, the next step is to sharpen an APT tip with a series of annular milling steps, which are described in detail in Appendix A.

Once the atom probe tips have been correctly prepared, they are transferred to the LEAP for analysis. Each atom probe tip was run until it was fractured. Specimen fracture was common because nearly every sample contained internal defects, such as a crack tip, that served as a stress concentrator and facilitated physical failure.

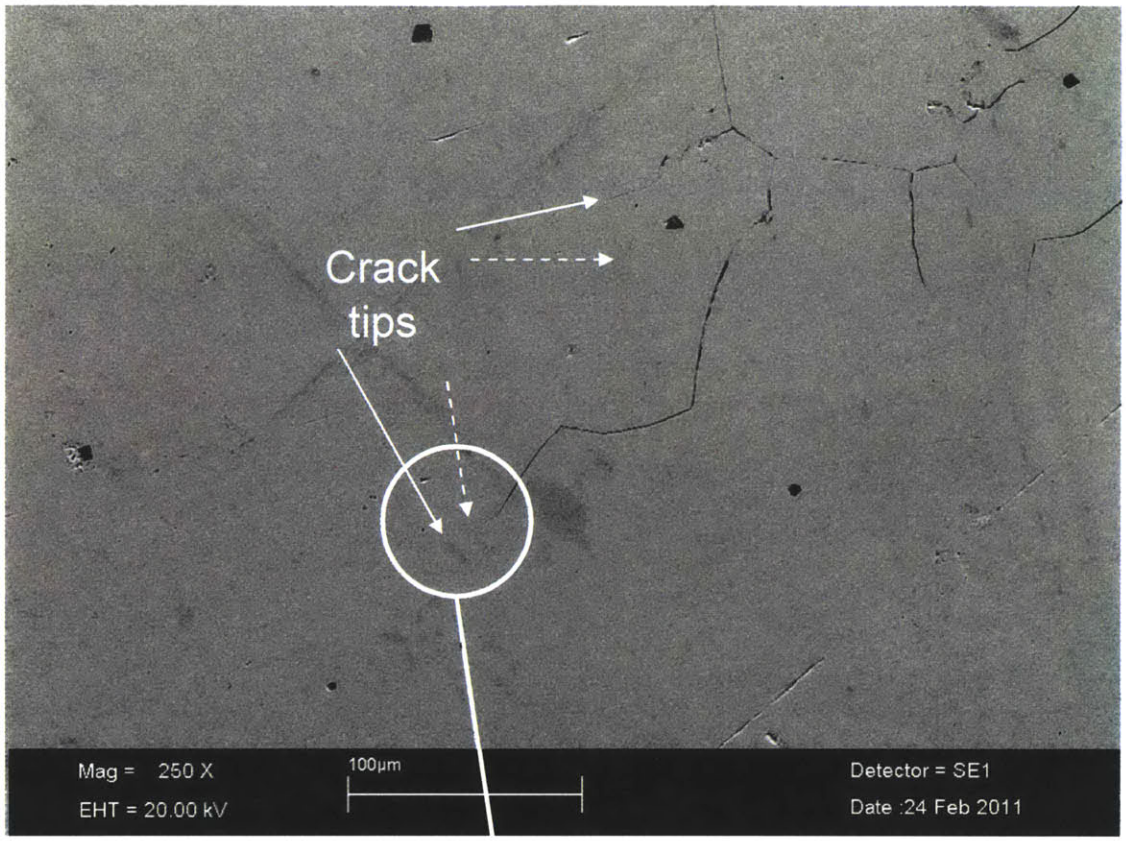

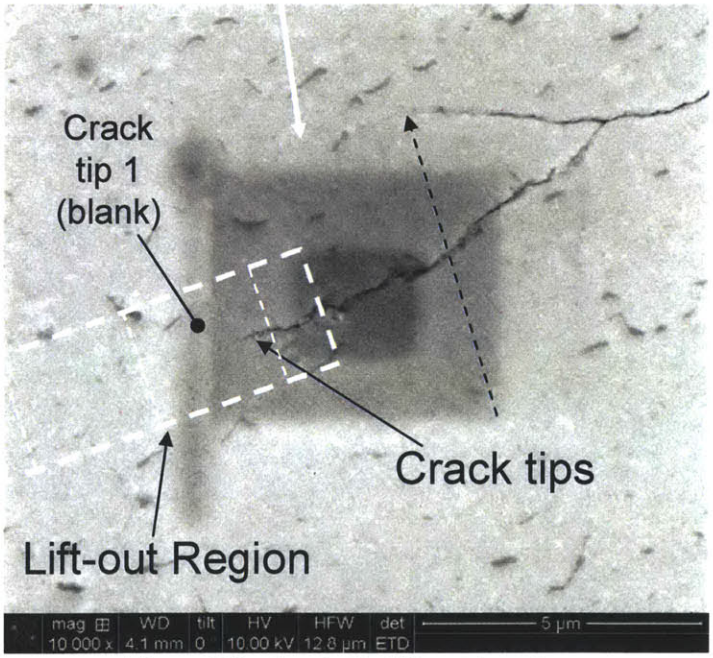

Figure 5-2: Crack tip lift-out location

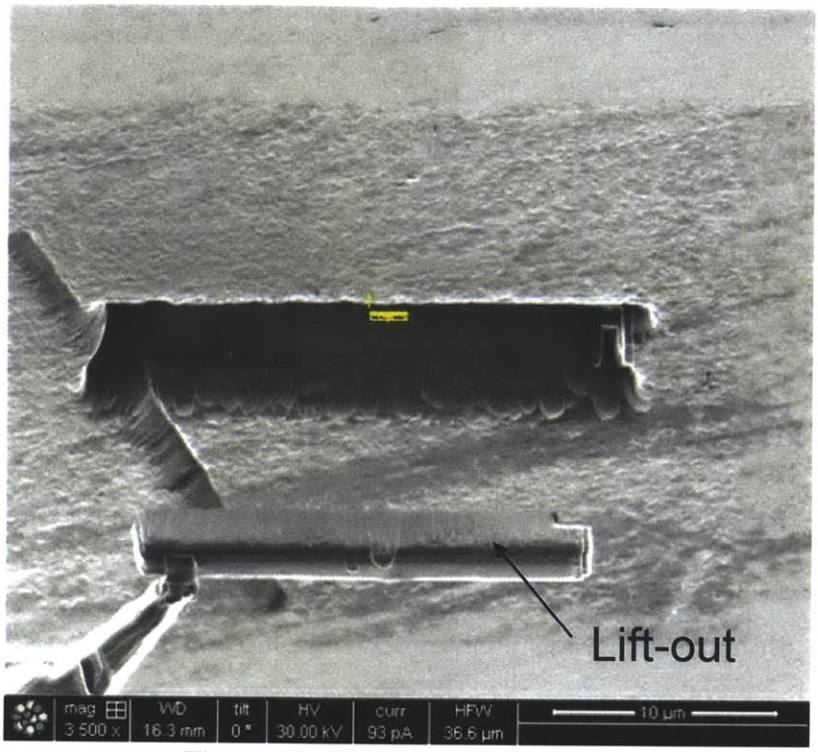

Figure 5-3: Lift-out wedge (example)

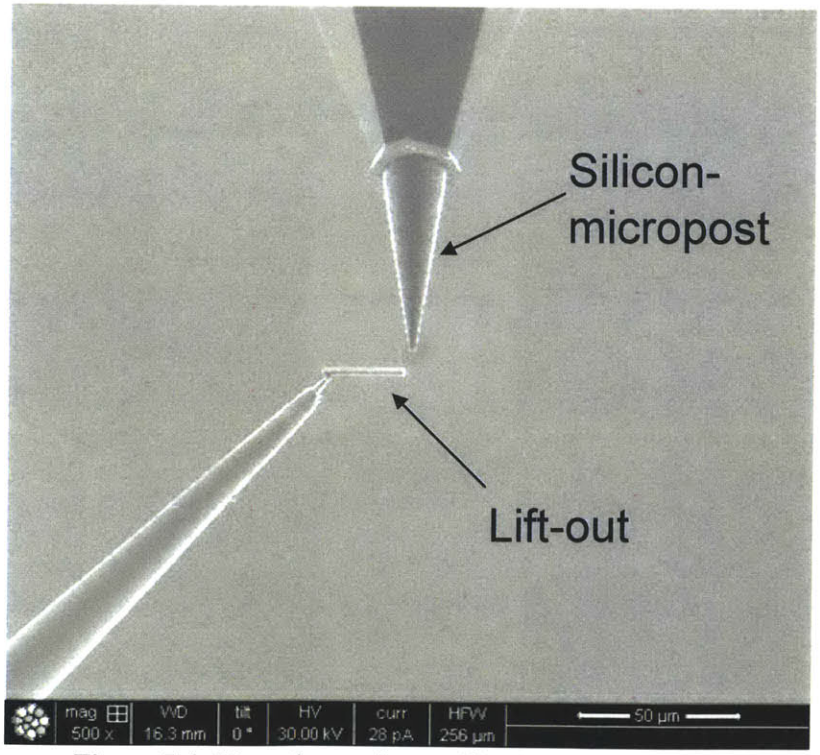

Figure 5-4: Mounting wedge on Si-micropost (example)

5.4 Crack Tip Characterization: Crack Tip 1

This section presents the results for the LEAP analysis of an SCC crack tip, which was successfully captured and reconstructed. This crack tip is referred to as Crack Tip 1 in the subsequent discussion. The analysis for this crack tip reveals several key features that contribute to SCC, which are finger-shaped tunnels propagating into the metal ahead of the main crack front and further oxygen transport into the bulk ahead of each tunnel.

Figure 5-5 shows the triangular blank mounted on the silicon micro-post that contains Crack Tip 1. The crack terminates within the specimen blank and the dashed line on the surface depicts the approximate crack path. An arrow also indicates the location where the crack terminated in the surface of the polished surface. The surface crack is not visible because a layer of platinum was deposited to protect the sample from gallium implantation during the sharpening process in the FIB. When the lift-out section was initially oriented at the crack tip it was assumed that the crack propagated generally straight. However, the initial milling on this blank revealed that the crack propagated at a slight angle through this blank, which is indicated by the dashed line. The final sharpened APT tip is also shown in Figure 5-5. The final diameter of this APT tip was approximately 80 nm.

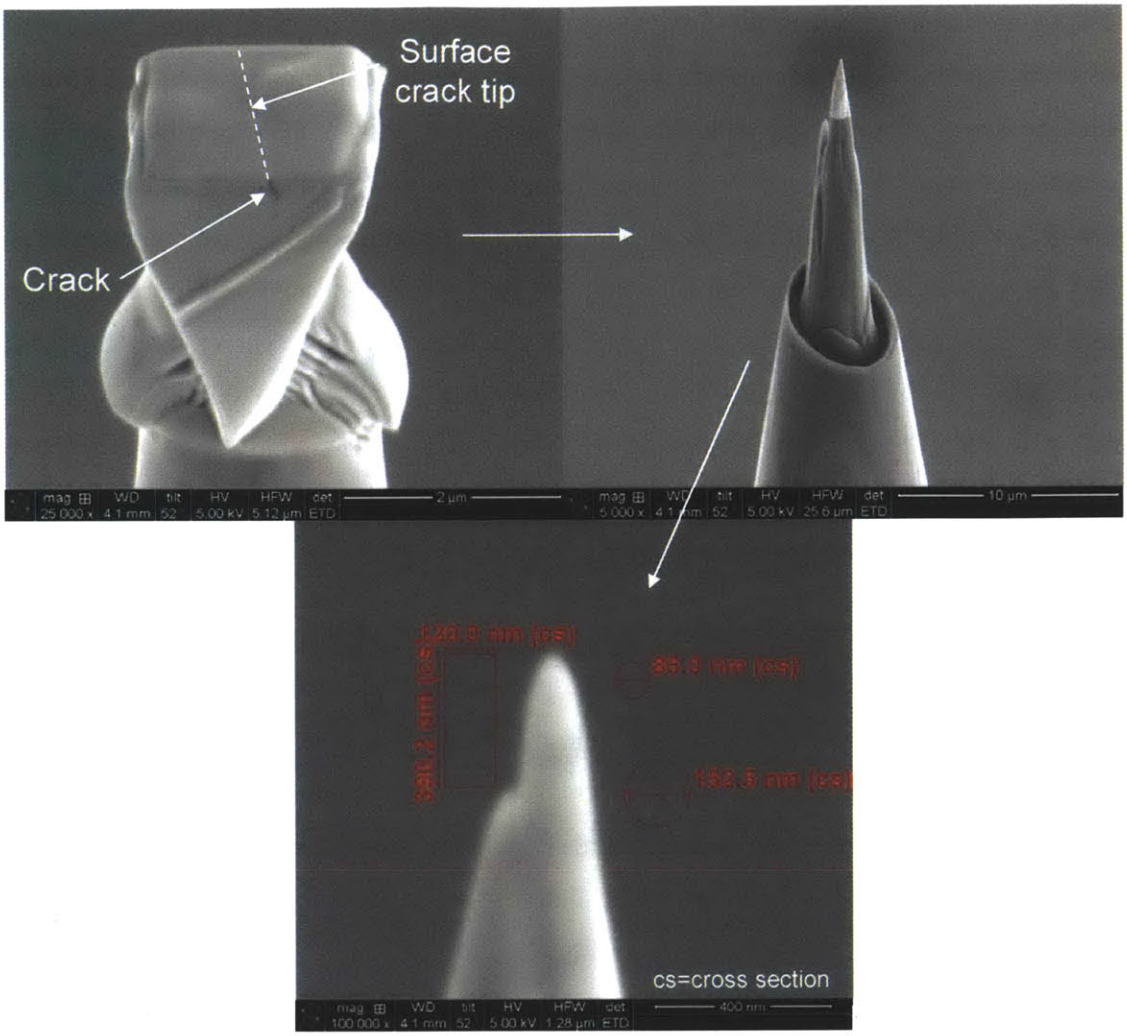

Figure 5-5: APT blank, sharpening, and final tip (example)

5.4.1 Crack Tip 1 Reconstruction

The reconstruction of the APT was completed, and the results are presented here. This tip was run in two batches in the LEAP. The first section was run until approximately 2 million atoms were collected. The LEAP was stopped due to abnormal pulsation behavior, which is indicative of a fractured sample. The sample was removed from the LEAP, examined in the SEM, and determined to be intact and in good shape. The tip was returned to the LEAP and analysis was continued. This second run stopped upon specimen fracture, which corresponded to approximately 2.8 million additional atoms. The reconstruction presented in this section corresponds to the second run in the LEAP (2.8 M atoms).

The reconstruction of the crack tip is shown in Figure 5-6 and Figure 5-7. Figure 5-6 shows the reconstruction with nickel, chromium, oxygen, nickel-oxide, chromium-oxide, and iron-oxide particles present. The nickel and chromium atoms are shown in a considerably reduced concentration because together they account for approximately 85% of the atoms and would hide any features visible through the surface. The dotted line outlines the approximate crack shape and the arrow indicates propagation direction. Figure 5-7 is the same as Figure 5-6 but also includes an isosurface to elucidate the crack walls and other features. The crack wall surface is represented with an 8 at% surface comprised of NiO, CrO_x, FeO_x, and oxygen. The arrows in Figures 4-6 and 4-7 indicate the direction of crack propagation, which is towards the back vertical scale bar. It is important to note here that the γ' precipitates are not highlighted in Figures 4-6 and 4-7, but are in close proximity to the crack. The γ' distribution will be discussed shortly.

The most notable feature of the crack tip is the presence of "tunnels" ahead of the main crack front. These tunnels are not empty but are rich in oxygen and oxide, predominately nickel and chromium oxide. The very tip of the main crack is rich in chromium- and nickel-oxides and spinel oxide forms in the crack wake that also includes iron-oxide. The spinel oxide is a combination of nickel-oxide, chromium-oxide, and iron-oxide, which is location dependent.

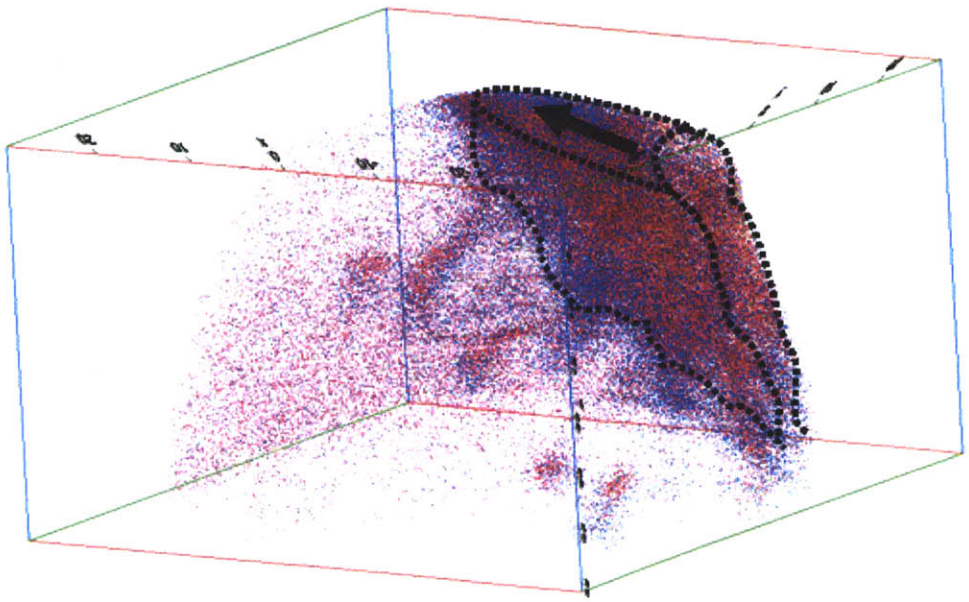

Figure 5-6: Reconstruction of crack tip with oxide constituents present. (Ni and NiO shown in blue, Cr and CrO shown in red, arrow indicates direction of crack propagation, demarcations are 10 nm wide)

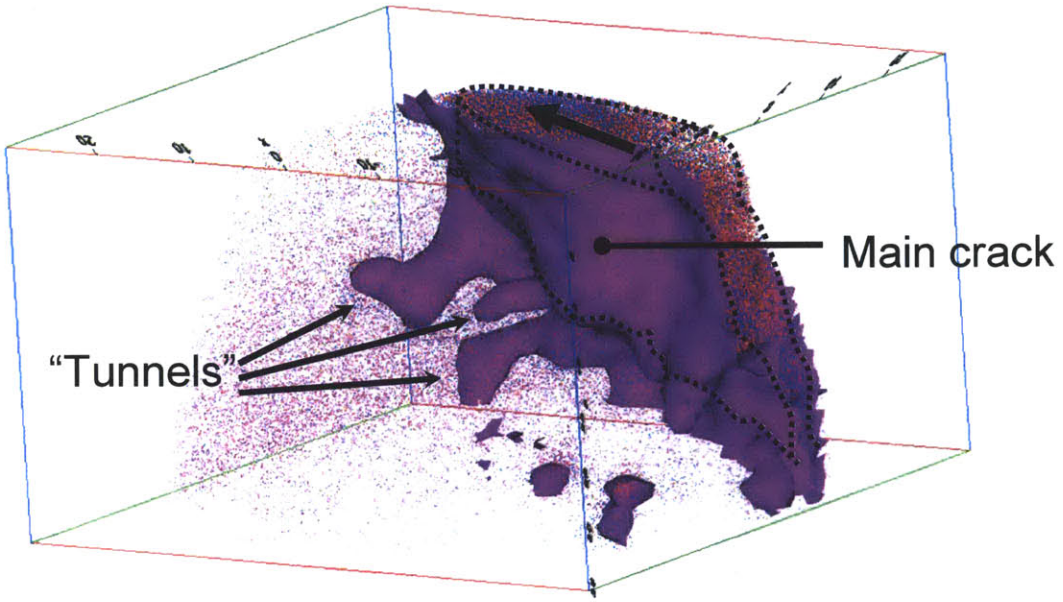

Figure 5-7: Reconstruction of crack tip with 8% oxide isosurface superimposed on oxide constituents (Ni and NiO shown in blue, Cr and CrO shown in red, arrow indicates direction of crack propagation, demarcations are 10 nm wide)

5.4.2 Crack Tip Composition Analysis

The crack tip chemistry was determined by measuring all of the elements inside the crack outlined in Figure 5-8, and the composition is recorded in Table 5-1. Next, the elemental distribution across a 10 nm thick cross-sectional slice was analyzed. Figure 5-9 shows the elemental distribution, and Figure 5-10 shows the location and orientation of the cross-sectional slice. The crack tip is largely composed of chromium, iron, nickel, titanium, copper, niobium, aluminum, and vanadium oxides, in addition to oxygen. Refer to the chapter introduction as to how the APT classifies an oxide. No preferential segregation of manganese, silicon, carbon, or boron was observed. The presence lf a large amount of niobium is attributed to selective oxidation and transport of niobium atoms from intergranular niobium-carbides on the crack path. Also, the presence of γ' precipitates is indicated with the circular outlines on the aluminum and titanium maps. Sulfur and phosphorus were not detected.

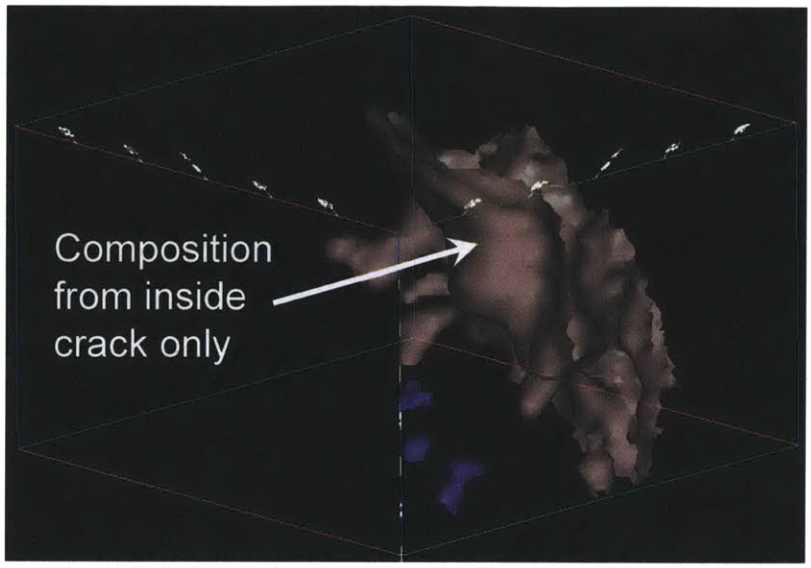

Figure 5-8: Outer crack surface for tip composition analysis

Table 5-1: Crack Tip 1 composition

Element	Composition (at %)	% sigma uncertainty	Element	Composition (at %)	% sigma uncertainty
Ni	37.081	0.090	CrO_x	24.703	0.077
Cr	6.501	0.033	NiO	11.591	0.045
Fe	3.616	0.024	O	6.191	0.044
Ti	0.378	0.008	FeO_x	2.579	0.028
Al	0.365	0.008	NbO_x	0.668	0.013
Mn	0.218	0.006	MnO	0.280	0.007
Si	0.138	0.005	TiO	0.467	0.009
Cu	0.967	0.012	AlO	0.275	0.007
Nb	0.025	0.002	VO	2.084	0.018
V	0.019	0.002	OH	0.782	0.011
C	0.107	0.004	OH2	0.541	0.009
B	0.003	0.001			
P	0.000	0.000			
S	0.000	0.000			

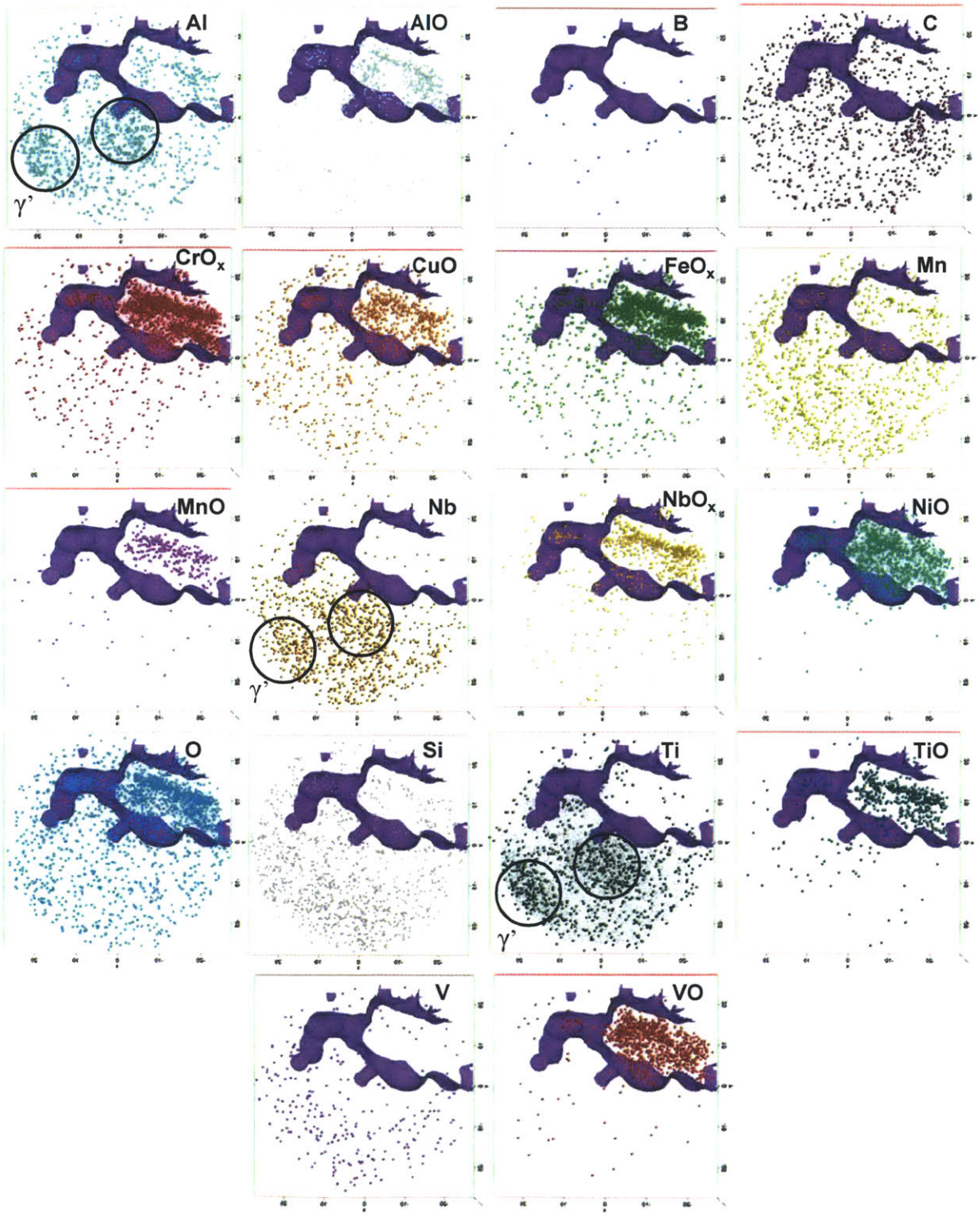

Figure 5-9: Individual elemental analysis of crack tip composition, crack shape is represented with an 8 at% oxide isosurface, demarcations are 10 nm apart

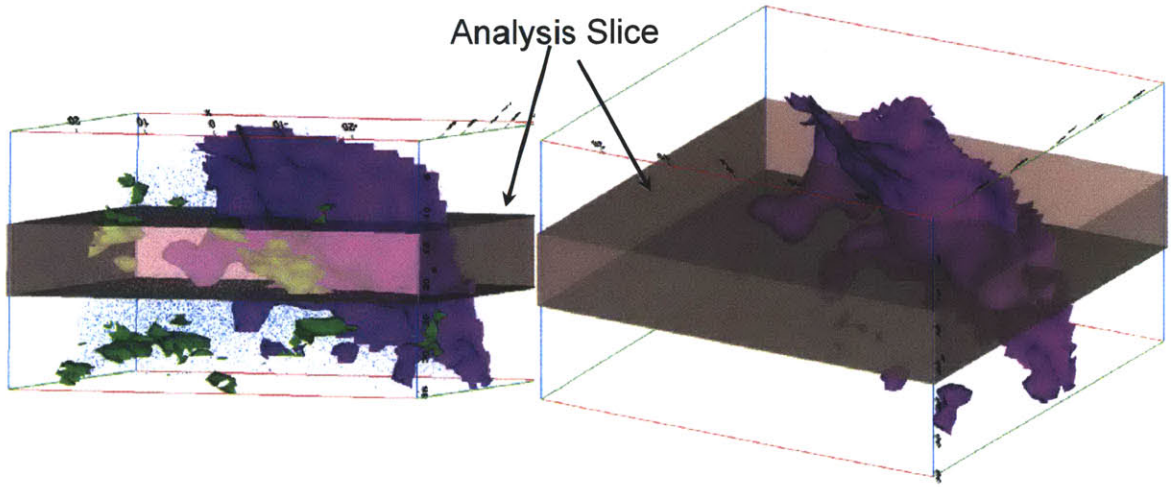

Figure 5-10: Location and orientation used for 10 nm cross-section composition analysis

5.4.2 Oxygen/Oxide Tunneling Analysis: 2D Concentration Profiles

A two-dimension composition profile was generated for the two most prominent tunnels in Figure 5-7 to further determine the composition ahead of the crack tip. The tunnels in Figure 5-11 are defined by a 3.4 at% chromium oxide isosurface superimposed on nickel oxide concentrations contours and are simply shown to establish an initial orientation of the penetration geometry and a starting point for further discussion. By varying the analysis parameters one is able to highlight the elemental enrichment as a function of position within the analysis volume. For example, increasing the elemental enrichment threshold for chromium oxide, for the representative isosurface, would result in a smaller tunnel more representative of the core. Likewise, lowering the isosurface concentration threshold would show wider chromium-oxide features because that particular surface represents a lower elemental composition than the composition within the tunnel core.

Two dimension composition profiles were used to determine the length of penetration and composition as a function of element and distance. The two analyzed penetrations were isolated within a 10 nm thick analysis volume. Figures 4-8 through 4-11 show the results of the composition and distribution analyses. The penetrations show enrichment of oxygen, chromium oxide, nickel oxide, aluminum oxide, and niobium oxide. The results are presented in a series of concentration profiles of individual atoms superimposed upon a map outlining the oxygen

concentration contours. The sizes of all of the visible atoms have been artificially increased as a visual aid.

The oxygen profiles clearly show oxygen diffusing head of the crack into the tunnels and ahead of the tunnels into the matrix. In addition to oxygen enriching in the penetrations, enabling oxidation, oxygen was also located several nanometers ahead of the oxide penetrations within the uncracked bulk. Nickel oxidation within the penetrations follows a clear path, resulting in a tight core of nickel oxide. Chromium oxidation (Figure 5-13) is also present within the penetrations but is in lower concentration. The resulting oxide is a chromium-nickel spinel.

Figure 5-14 shows the distribution of niobium and niobium oxide. Niobium shows a fairly homogeneous distribution ahead in the vicinity of the penetrations. Niobium oxide follows the same distribution as nickel and chromium oxides; namely, along a deliberate path.

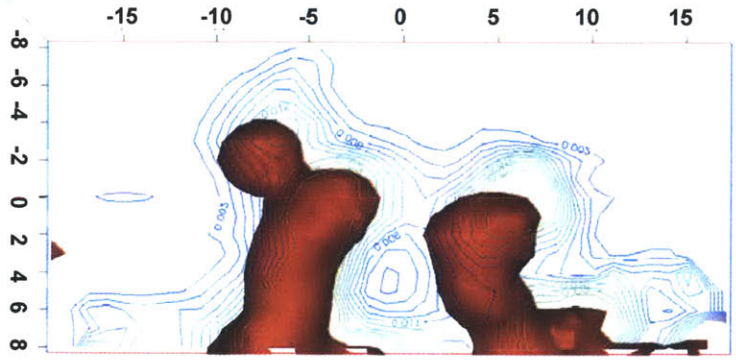

Figure 5-11: 3.4 at% chromium oxide tunnels superimposed on nickel oxide contours (tunnels growing from tip of crack into bulk metal: only tunnels shown)
(SCC tip ends below tunnels and 2D profiles by 3-4 nm)

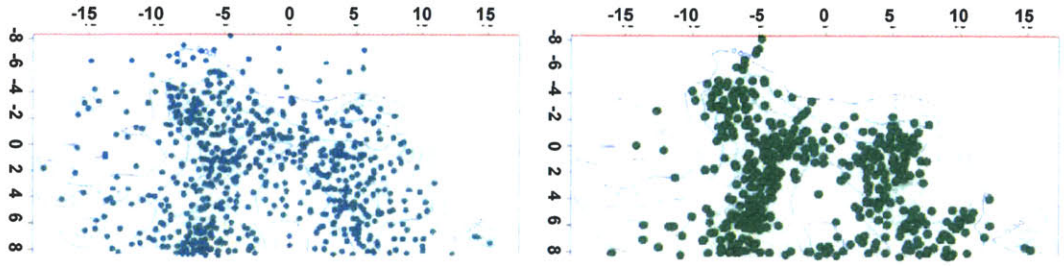

Figure 5-12: Oxygen (left) and nickel oxide (right) distribution ahead of crack
(atoms superimposed on oxygen contour map)
(SCC tip ends below 2D profiles by 3-4 nm)

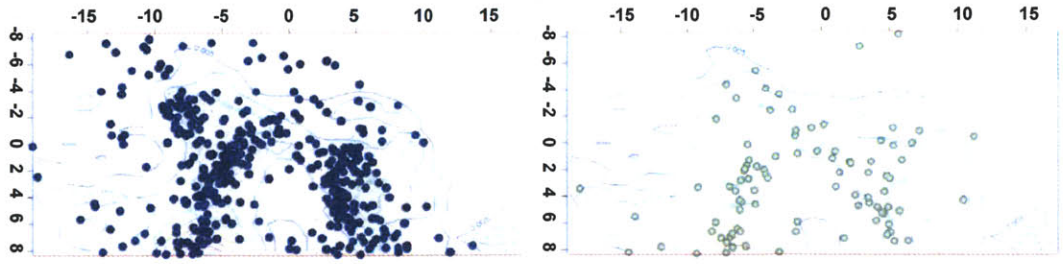

Figure 5-13: Chromium oxide (left) and aluminum oxide (right) distribution ahead of crack (atoms superimposed on oxygen contour map) (SCC tip ends below 2D profiles by 3-4 nm)

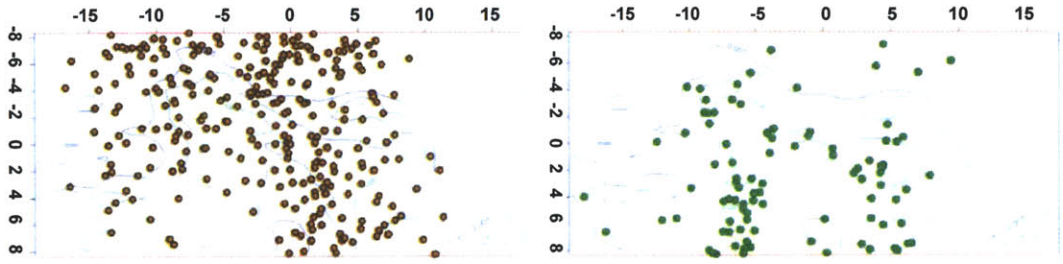

Figure 5-14: Niobium (left) and niobium oxide (right) (atoms superimposed on oxygen contour map) (SCC tip ends below 2D profiles by 3-4 nm)

The propagation pathway is highlighted in Figure 5-15, which superimposes nickel oxide isosurfaces at various concentrations on nickel oxide contours. The longest oxide pathway within this APT reconstruction penetrates ahead of the crack approximately 15 nm (4-5 lattice parameters). Increasing nickel oxide concentrations shows that the core of the penetration is 2.5-3.0 at% nickel oxide and approximately 5 nm in diameter. The concentration of oxide decreases within penetration depth, which directly follows the oxygen available for oxidation. A 15 nm penetration corresponds with 0.6 at% nickel oxide concentration. The oxidation pathway appears to progress in a circular shape. This suggests that oxygen may be diffusing ahead of the crack along, but not exclusively, dislocations. The smaller penetrations away from the crack wall penetrate straight into the bulk. The pathway for the smaller oxygen penetrations is likely crystallographic, which will be discussed shortly.

It is important to note here that the oxygen and oxides detected in each of the "tunnels" ahead of the main crack are only enriched to a few atomic percent. This means that the majority of each "tunnel" is base material, namely nickel and chromium metal atoms and is more of an

oxide/metal sponge structure. The lower concentration (in comparison to the remainder of the tunnel composition) of oxygen and oxides indicates that oxygen is diffusing ahead of the main crack front on specified and ordered pathways. Higher concentrations of oxide would indicate selective oxidation, thus enabling a pathway for additional oxygen/oxide. No specific oxidation pathway was identified. Oxygen diffusion along a crystal defect, such as along a dislocation or by vacancy/oxygen partitioning is the likely mechanism for the "tunnel" formation, due to the "enrichment" being only a few atomic percent. The first reported instance of oxygen ahead of a crack tip was by Scott and Combrade who used nanoSIMS to suggest that oxygen was diffusing along the grain boundary ahead of the crack.[1] The analysis by Scott and Combrade did not have achieve sufficiently high resolution to determine if tunneling was occurring, as observed in this work.

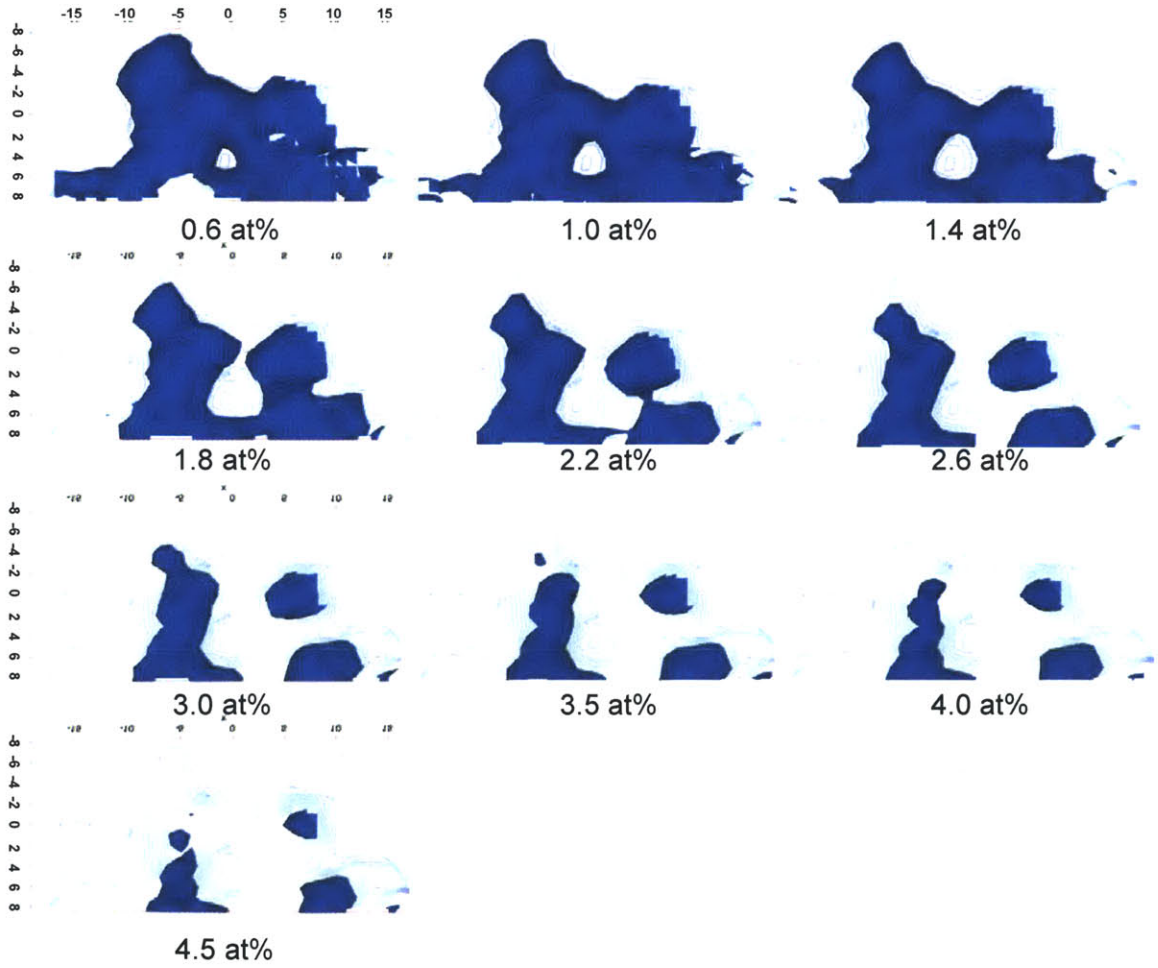

Figure 5-15 Nickel oxide reconstructions with isosurfaces representing various concentrations (SCC tip ends below tunnels and 2D profiles by 3-4 nm (11-12 nm on y-axis)) (NiO contours in background)

5.4.3 Tunnel Pathway Analysis

Three main tunnels and the composition directly in the tunnel propagation pathway were further characterized. One dimensional concentration profiles were constructed to determine the effect microstructural composition ahead of each tunnel. The measurements were obtained by constructing a 10 nm diameter isolation cylinder to measure the composition within and in front of each corrosion tunnel as a function of distance. The composition was measured in 0.5 nm steps and averaged over the 10 nm diameter. The amount of sampled material ahead of each corrosion tunnel tip is approximately 10-15 nm in length.

Figures 4-13 through 4-15 show the results of the analysis for tunnel 1. Figure 5-16 shows the location and direction of the tunnel and analysis cylinder. Figure 5-17 shows the oxygen and oxide profiles at and ahead of the tunnel tip. Figure 5-18 shows the profiles of the main alloying elements. Figures 4-16 through 4-18 show the results of the analysis for tunnel 2. Figure 5-19 shows the location and direction of the tunnel and analysis cylinder. Figure 5-20 shows the oxygen and oxide profiles and Figure 5-21 shows the main alloying elements. Figures 4-19 through 4-21 show the results for the analysis for tunnel 3. Figure 5-22 shows the location and direction of the tunnel and analysis cylinder. Figure 5-23 shows the oxygen and oxide profiles and Figure 5-24 shows the main alloying elements. The dashed lines in Figures 4-13, 4-16, and 4-19 outline the general crack shape and the thick arrows indicate the direction of crack propagation.

Elemental composition was determined ahead of each tunnel. The primary alloying elements (Ni, Cr, Fe), primary oxides (CrO_x and NiO), and oxygen are shown to illustrate the microstructural changes within the material ahead of and within each tunnel. The vertical dotted line in each composition profile identifies the approximate tip of each tunnel. The tunnel tip was determined by evaluating the element and compound composition. The tip of each tunnel exhibits a sudden decrease of oxygen and oxides. The oxygen and oxide concentrations ahead of each tip maintained an elevated concentration approximately 5-6 times higher than bulk measurements away from the tunnel "boundary" as defined above.* The oxygen concentration is approximately 0.75 at% along each tunnel, which is approximately 5-6 times the background

* The "tunnel" boundary is not a strict edge because it is defined by the isosurface, which is user defined based on the assigned elemental concentration.

oxygen measurements away from each corrosion tunnel. This clearly shows that oxygen is enriched ahead of each tunnel and suggests that the tunnel is following this oxidation pathway. Chromium oxide (CrO_x) is enriched to approximately 0.5 at% in the pathway directly ahead of each corrosion tunnel. The amount of oxidized chromium ahead of each tunnel is approximately 5-6 times the bulk measurements taken 20-30 nm away from the tunnels. It was not possible to measure the bulk composition to determine the length of oxygen diffusion (distance for the oxygen concentration to reach background levels) ahead of each tunnel because the APT sample was not sufficiently wide for this measurement. The edge of the reconstructed APT tip was only a few nanometers further than the oxygen diffusion length shown in each concentration profile.* Higher chromium oxide levels clearly indicate that chromium is the preferred element for oxidation, which is thermodynamically predicted.[15] Nickel oxide is present in quantities less than approximately 0.1 at%, but is still enriched about 5-6 times above background concentrations. This shows that chromium-nickel spinel is forming and that chromium oxide is the dominant oxide.

The trends of the main elements in the material (Ni, Cr, and Fe) do not follow as clear trends as oxygen and the oxides. The three main elements all exhibit either enrichment, depletion, or no change depending on the tunnel. These measurements are dependent upon several factors, including the presence of secondary phases in sample area (e.g. γ') and directional dependence of composition. The effect of secondary phases results in a variable composition measurement depending if the measurement is taken within, directly adjacent, or far field to a precipitate. The variations of Ni, Cr, and Fe measurements directly correspond to the reverse trend in Ti and Al (Figure 5-24), which are the primary elements in the γ'. Thus, it is difficult to conclude that small changes in Ni, Cr, and Fe are contributing to a crack pathway. A comparison of the main alloying elements near tunnel #2 with the bulk levels, from Table 2-3, is shown in Figure 5-25. These bulk measurements were taken several hundred micrometers from the crack tips. No clear enrichment/depletion of main alloying elements is observed. However, the presence of enriched oxide and oxygen ahead of each tunnel are clear and suggest that oxidation ahead of an active SCC crack is a plausible as an active mechanism contributing significantly to crack propagation.

* The "analysis cylinder" shown in each tunnel analysis actually intersected the APT sample edge

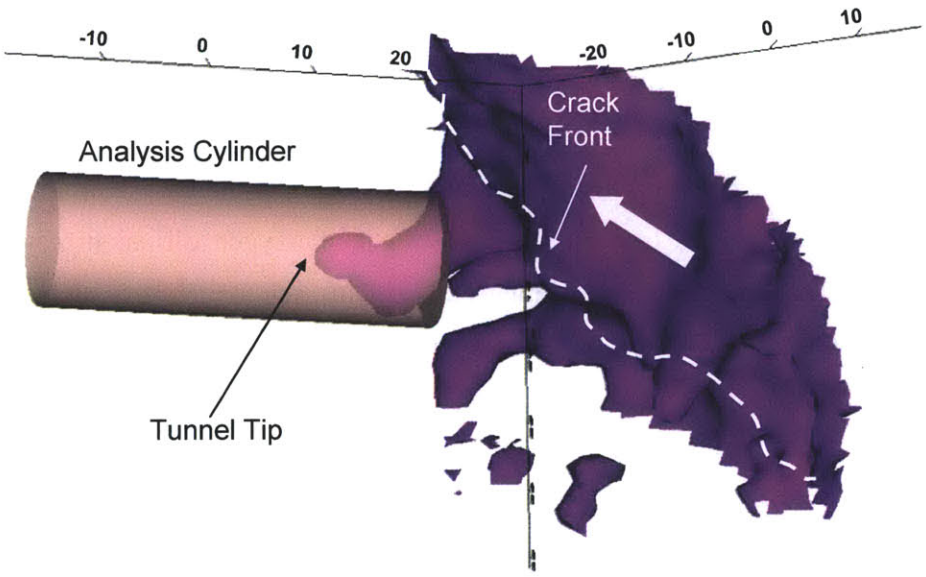

Figure 5-16: Location and orientation of 10 nm diameter cylinder to measure the elemental composition as function of distance at and ahead of tunnel #1

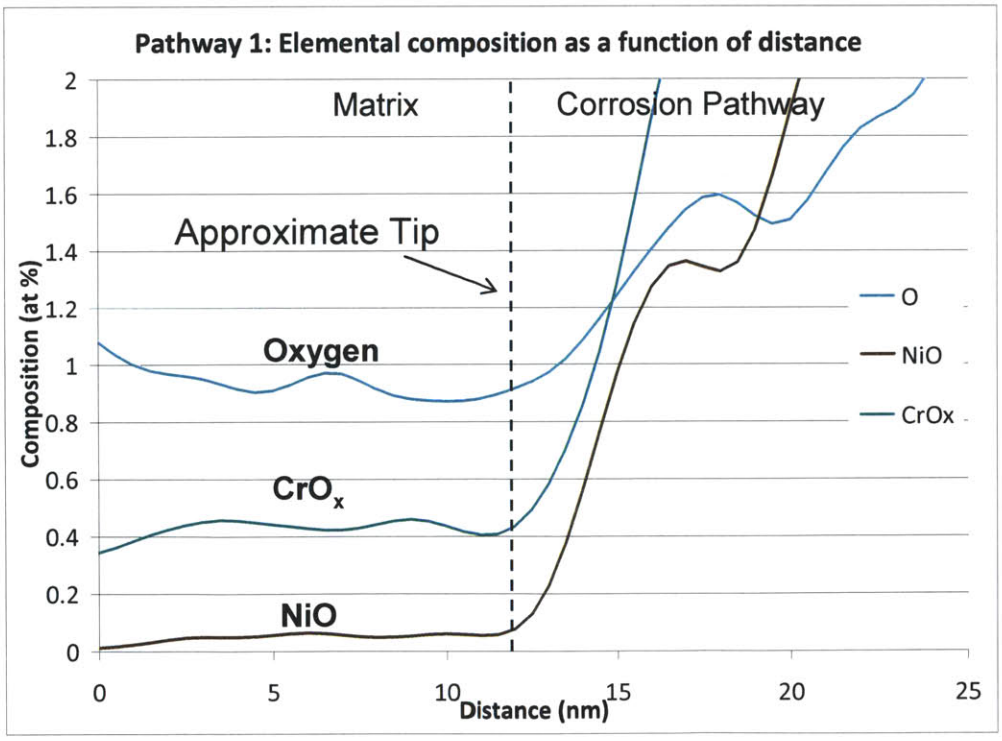

Figure 5-17: Elemental composition as function of distance (tunnel #1) Focused on oxygen and oxide profiles

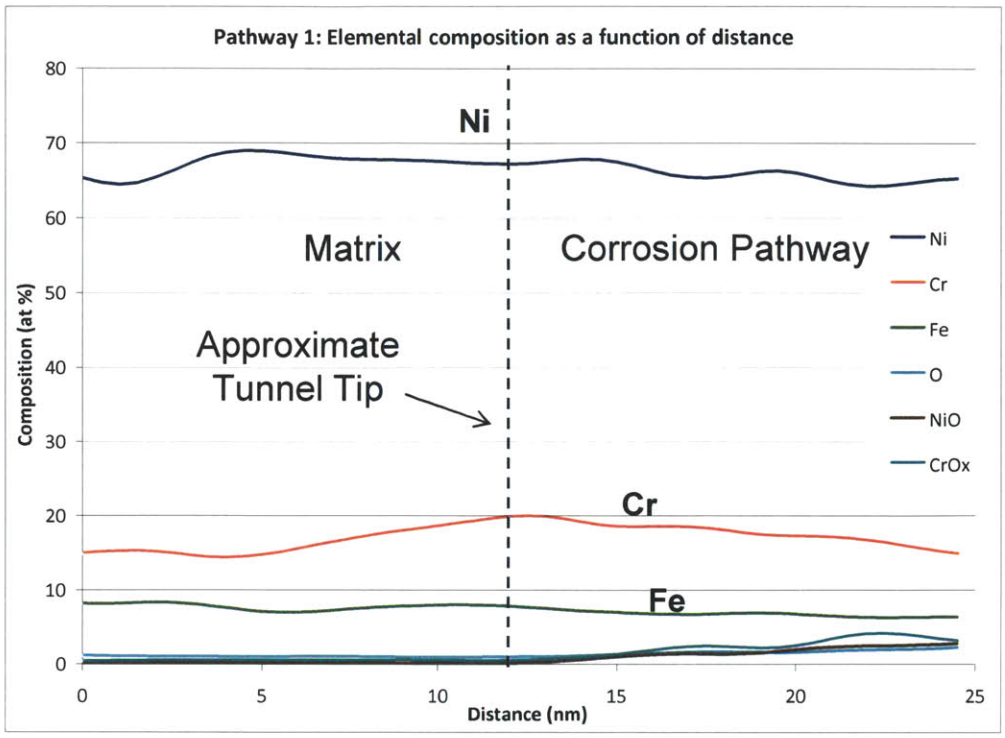

Figure 5-18: Elemental composition as function of distance (tunnel #1) Focused on main alloying elements

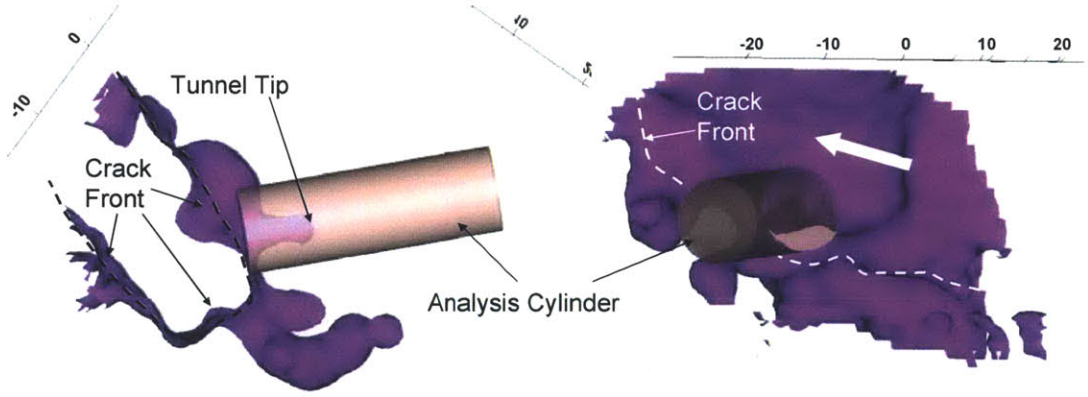

Figure 5-19: Location and orientation of 10 nm diameter cylinder to measure the elemental composition as function of distance at and ahead of tunnel #2

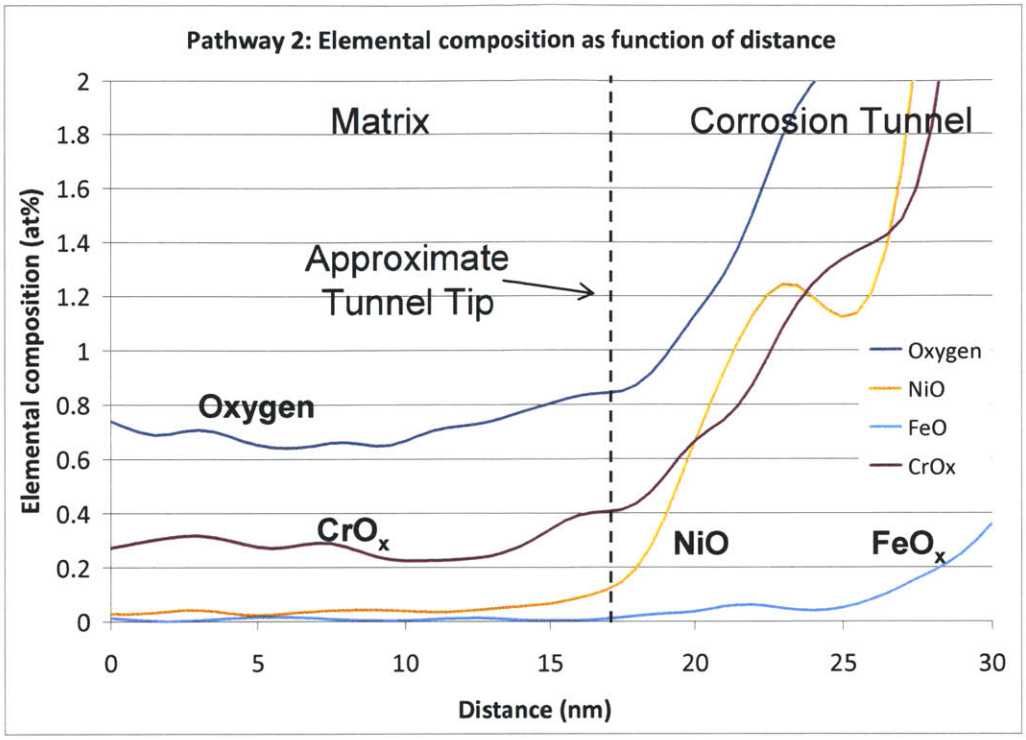

Figure 5-20: Elemental composition as function of distance (tunnel #2) Focused on oxygen and oxide profiles

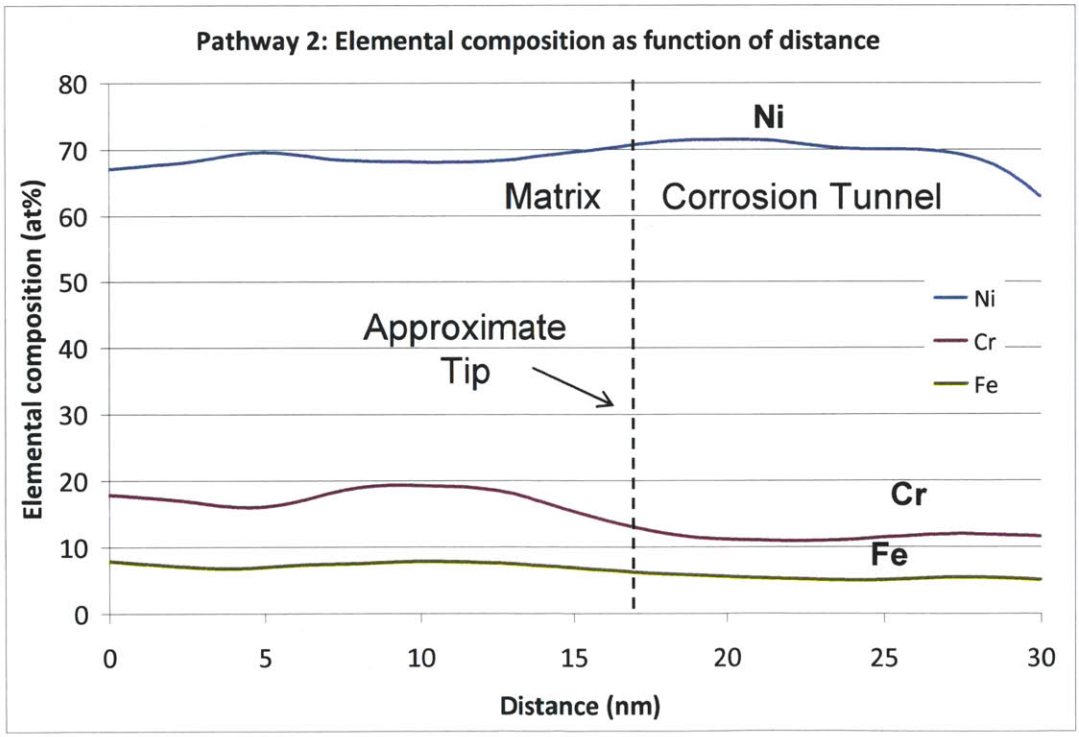

Figure 5-21: Elemental composition as function of distance (tunnel #2) Focused on main alloying elements

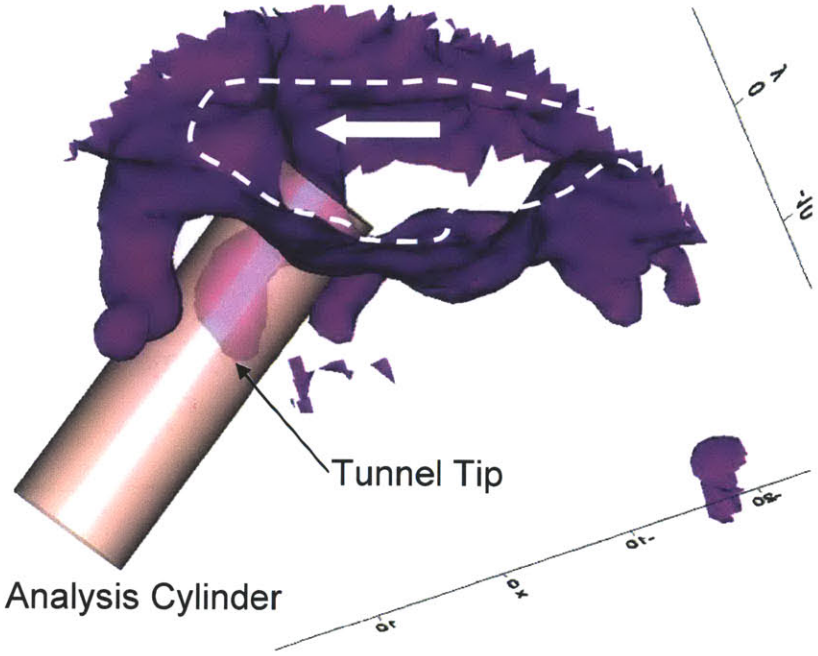

Figure 5-22: Location and orientation of 10 nm diameter cylinder to measure the elemental composition as function of distance at and ahead of tunnel #3

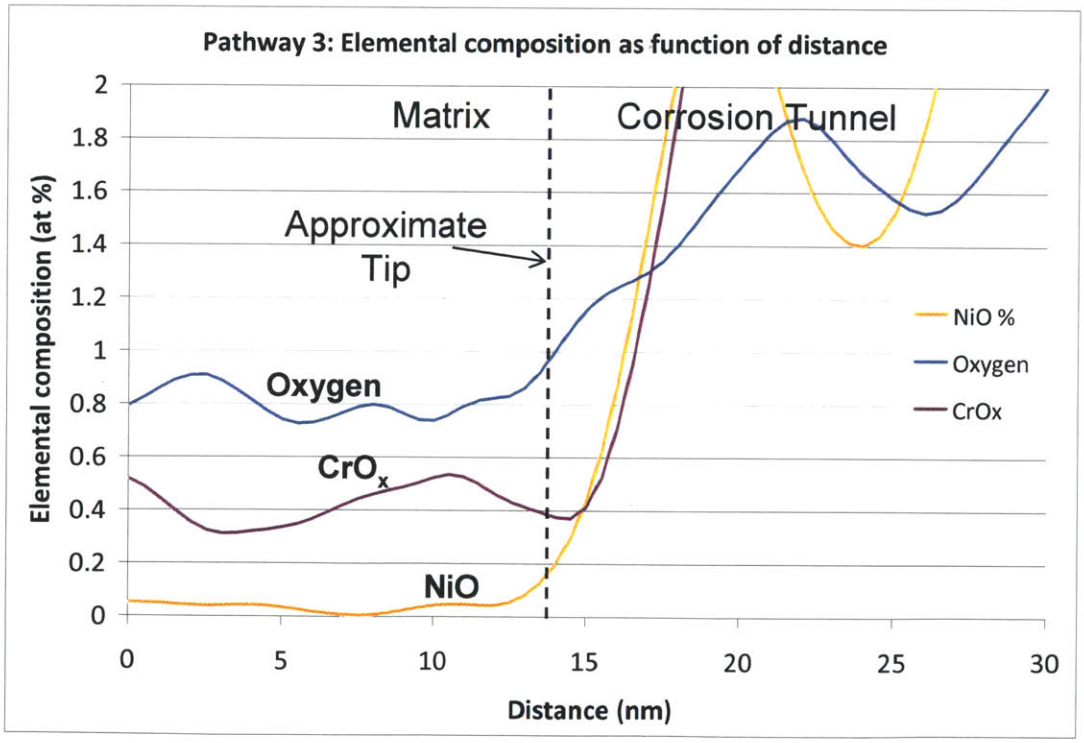

Figure 5-23: Elemental composition as function of distance (tunnel #3) Focused on oxygen and oxide particles

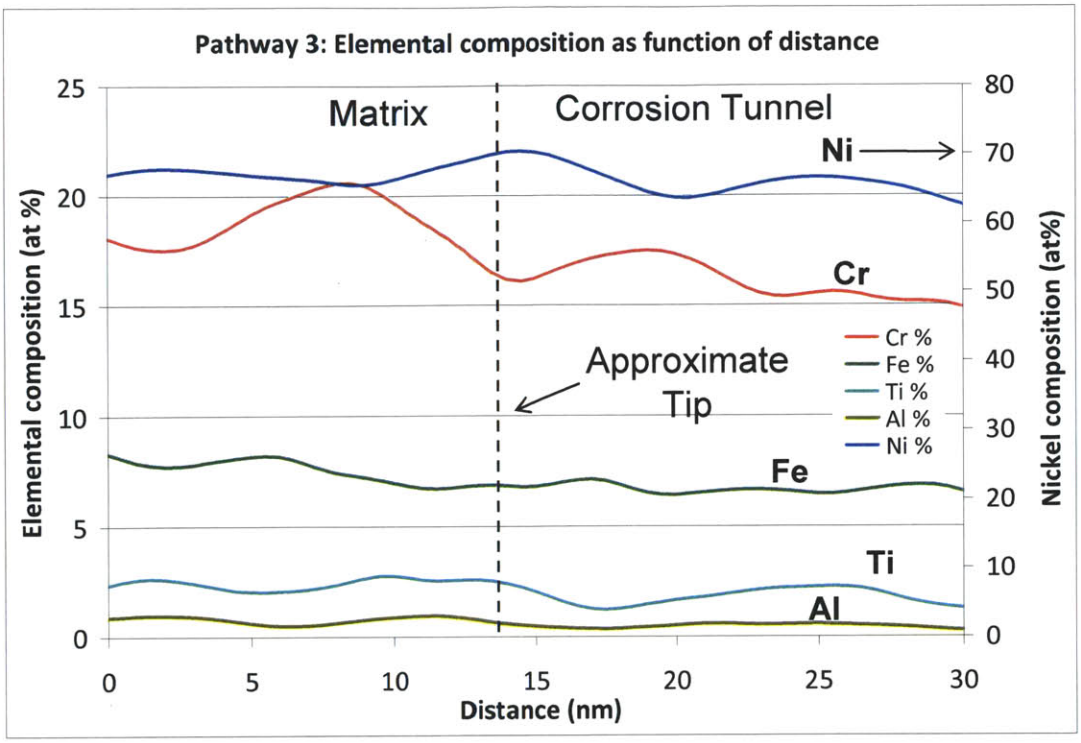

Figure 5-24: Elemental composition as function of distance (tunnel #3) Focused on main alloying elements

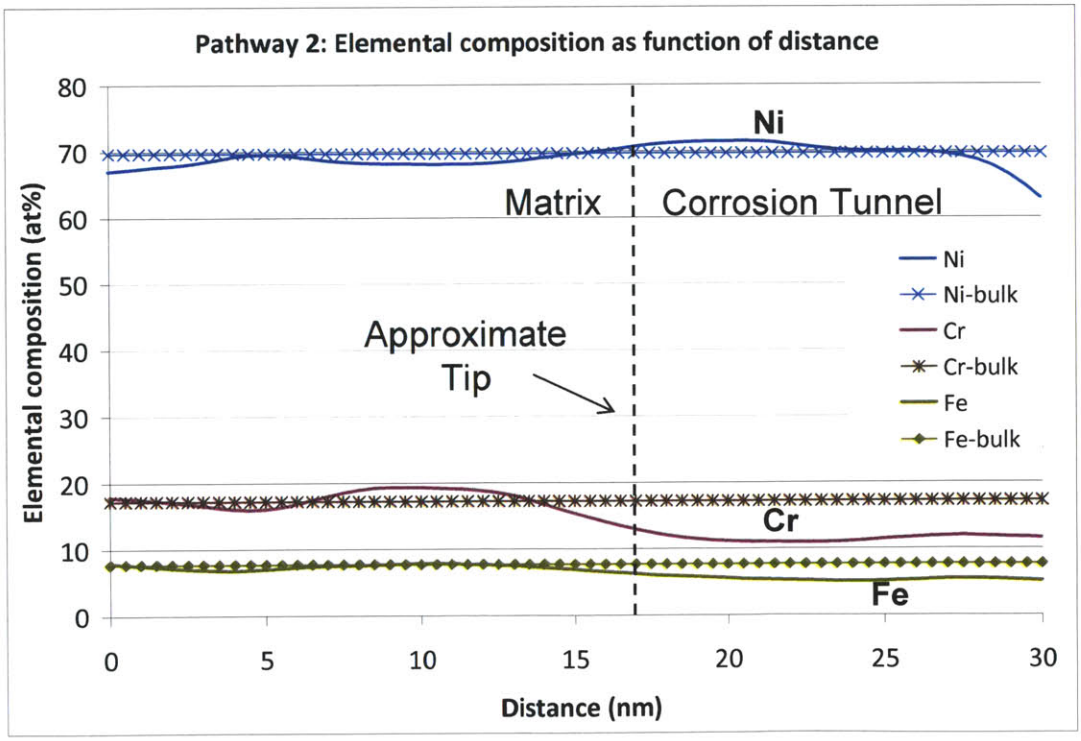

Figure 5-25: Comparison of matrix near crack pathway to bulk composition

5.4.3 Crack Pathway with Respect to Grain Boundary Location

Previous work has documented the presence of a γ' denuded zone directly adjacent to the $M_{23}C_6$ carbides along the grain boundary.[16] This is a very narrow zone of approximately 20-50 nm in width. However, it is important to note here that the zone directly adjacent to the grain boundary carbides is only denude of large γ': small γ' is still present, as previously seen in Figure 2-6. Figure 5-26 shows the SCC crack tip with the γ' is within 5 nm of the crack walls (γ' was present, but not shown, in the above discussion of this crack). The dashed line in Figure 5-26 roughly shows the side profile of the crack shape and the thick arrow indicates the direction of crack propagation.

It was shown in Chapter 2 that bulk γ' have an average diameter approximately 10-12 nm with a spherical geometry. The γ' precipitates near the crack in Crack Tip 1 are not in the same size and shape as the bulk γ'. The shape is no longer spherical but a longitudinal orientation. Much of γ' present in Figure 5-26 can be considered fine γ' due to its small size (< 10 nm diameter). The γ' is also sparser than present within the bulk measurements. The large γ' in the middle of Figure 5-26 may be multiple γ' precipitates in close proximity or an actual distorted γ'. It will be shown shortly that the elongated γ' shape in Figure 5-26 is present at other crack tips, which may be a result of an SCC process. A more detailed discussion about the change in aluminum content in γ' will be presented shortly.

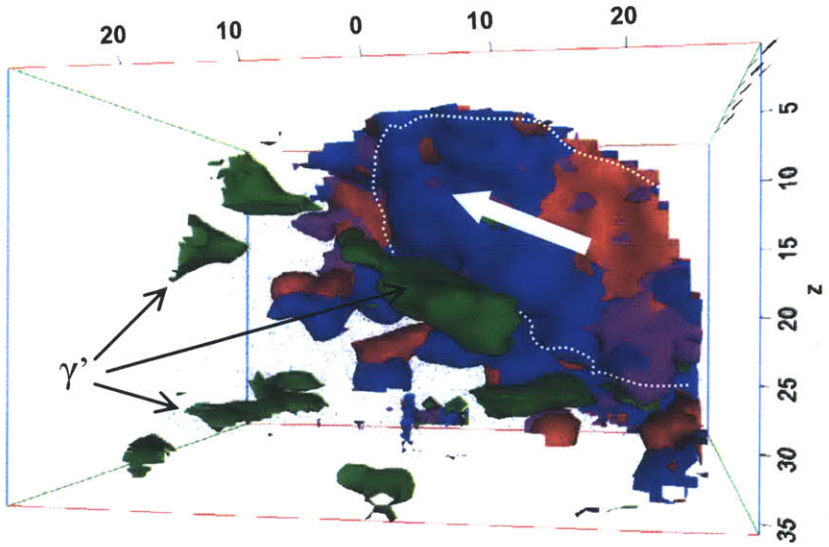

Figure 5-26: γ' distribution within close proximity to the crack path (γ' surface represented by 8 at% Ti isosurface)

Several proxigrams were computed in order to characterize the composition of the near grain boundary γ', as compared to bulk γ'. The proxigrams characterize the elemental composition within the γ' center, and averages the elemental composition at incremental steps outward from the γ'/matrix interface. Figure 5-27 shows the proxigram corresponding to the average of all γ' in Figure 5-26. Figure 5-28 shows the proxigram of the γ' indicated by the middle arrow in Figure 5-26. The crack wall is approximately 5 nm away from the γ' analyzed in Figure 5-26. The crack wall is directly behind the γ' (oriented directly into the page), and the crack is propagating from right to left. The nominal crack wall is outlined with a dotted line, and the tunnels are propagating away from the crack wall. The vertical dashed line in each of these proxigrams corresponds to the nominal interface between γ'/bulk. These results clearly show that the aluminum concentration is 3-4 at% near the crack. The bulk γ' has 6.6 at% aluminum. It is important to note here that the scatter in the individual γ' proxigrams is higher than when averaged over all γ' due to statistical sampling. The uncertainty associated with the elemental measurements for all of the atom probe plots is presented in Appendix B. Analyzing a smaller volume records fewer atoms and small perturbations in concentration affect the composition measurement more than for a larger sampling size. However, it is sufficient to mention here that the uncertainty is small. Regardless of the higher scatter, a clear trend suggests that the γ' in close proximity to the crack is aluminum deficient, as compared to bulk γ'. These results agree nicely with γ'/crack analyses to be discussed shortly.

Figure 5-29 shows a proxigram of bulk γ' and illustrates the nominal composition of this phase and the surrounding matrix. This APT sample was obtained far greater than 100 μm from the crack tip. Figure 5-29 clearly shows that the bulk γ' contains approximately 6.5 at% aluminum, which is approximately two times the aluminum content as the near-crack γ'. The titanium concentration in bulk γ' is approximately 11-12 at%, which is comparable to the ≈ 11 at% titanium in the near-crack γ'.

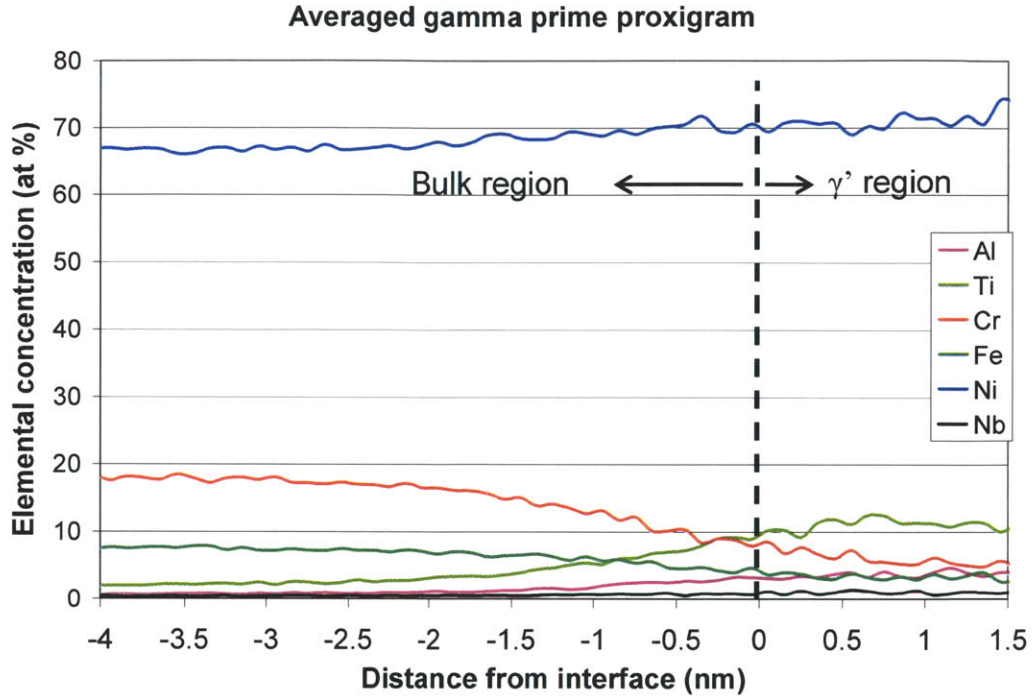

Figure 5-27: Proxigram of averaged γ' composition in Crack Tip 1

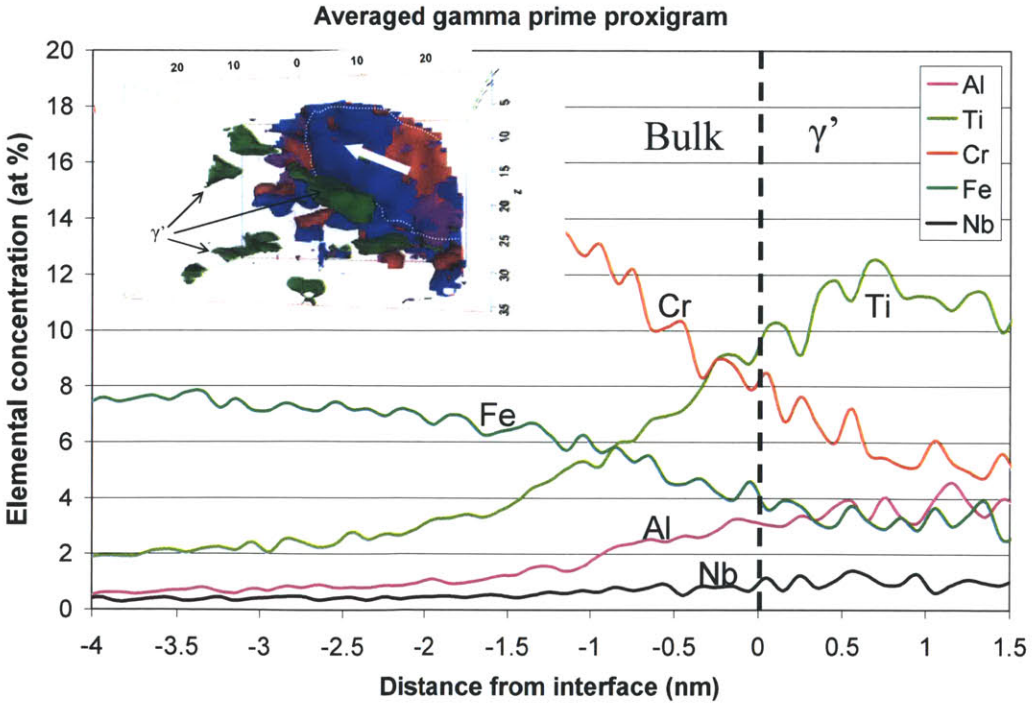

Figure 5-28: Proxigram for γ' located close to crack wall (γ' indicated by arrow)

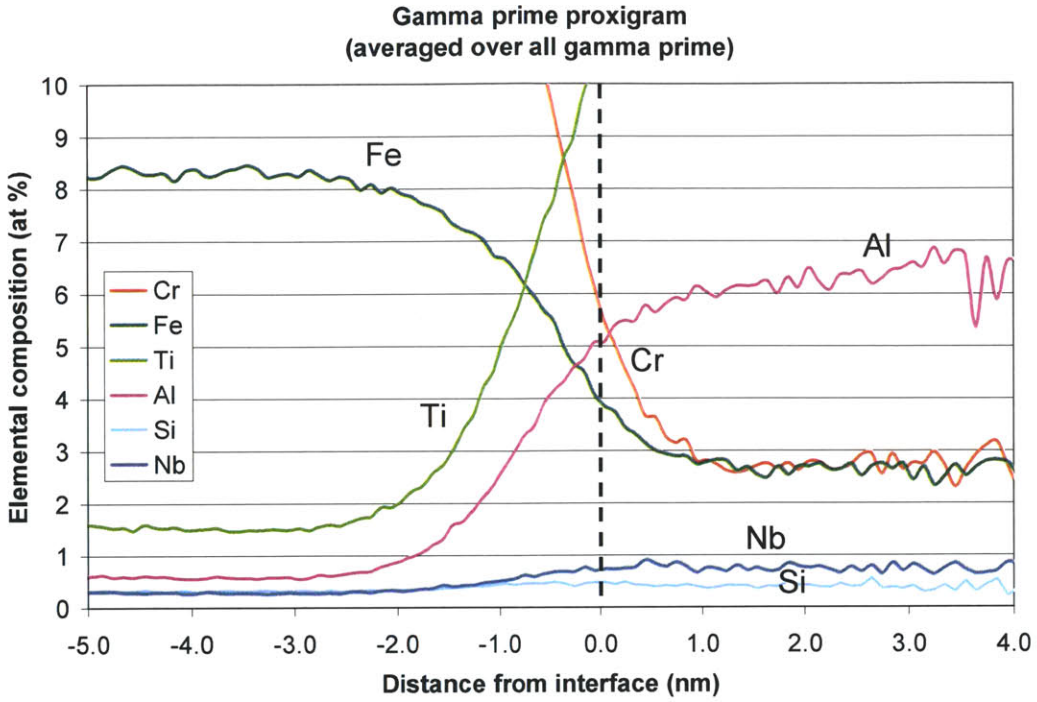

Figure 5-29: Proxigram of bulk γ' and surrounding base material

Another important indicator as to the location of the crack path, with respect to the grain boundary, is the width of the sensitized zone in alloy X-750. Elliott [17] has characterized the near grain boundary chromium in HTH treated alloy X-750. The chromium concentration measured ≈20 nm away from the crack in the APT reconstruction was approximately 17 at%, which is close to the bulk composition. Figure 5-30 shows that the width of the sensitized zone in alloy X-750 is only approximately 100-150 nm, and this width is dependent upon the proximity to a $Cr_{23}C_6$ carbide. The sensitized width is wider directly adjacent to a grain boundary $Cr_{23}C_6$. The minimum chromium concentration is approximately 12 wt% at the grain boundaries. These results agree nicely with the APT reconstruction based on the matrix (non crack) concentrations and the size and distribution of γ'. The crack is propagating in the γ'-denuded zone, which has reduced number of γ' precipitates.

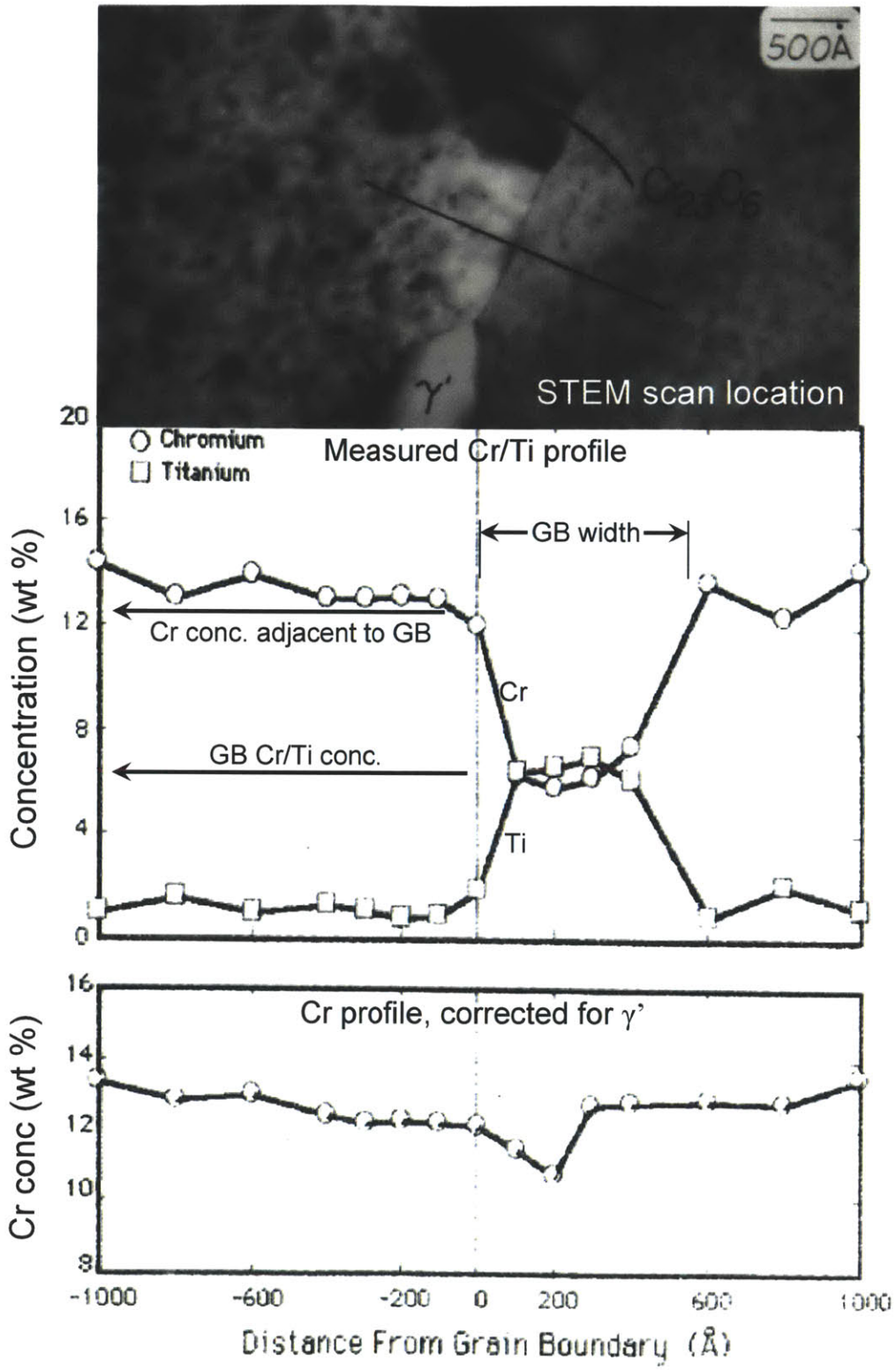

Figure 5-30: Average near grain boundary chromium profile in HTH, measured Cr-profile (top) and corrected for γ' Cr-profile (bottom) [17]

5.5 Crack Tip 2

Crack Tip 2 was extracted from the main crack tip shown in Figure 5-31. The wedge blank mounted on a silicon micro-tip is shown in Figure 5-32. It can be seen that the crack extends through the blank. The final APT tip was milled down to the cracked area, such that the top of the sharpened tip included the oxide along the crack wall and a small amount of uncracked material tip above the oxide layer. The SEM image of the final APT tip, with the tip of the crack visible, is shown in Figure 5-33. The open crack is visible on the upper left region of the tip. The crack is propagating in a near vertical orientation into the tip. The lower region of the visible crack in the APT tip corresponds approximately to the bottom of the reconstructed volume.

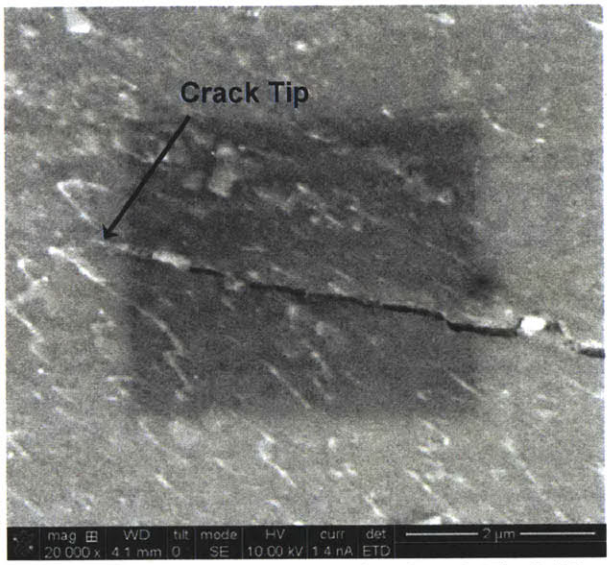

Figure 5-31: Crack tip location for Crack Tip 2 lift-out

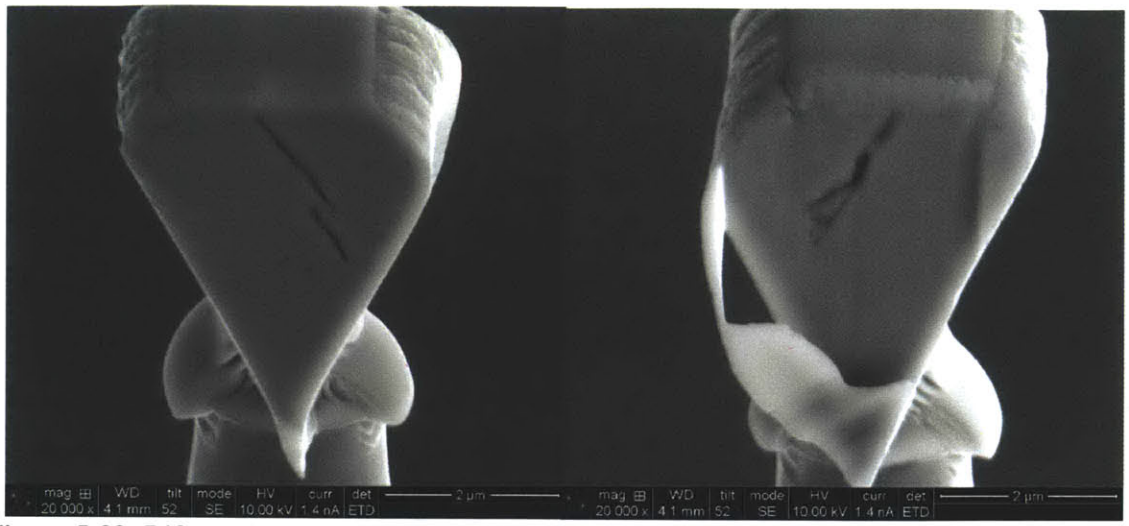

Figure 5-32: Lift-out blank for cracked tip. Upstream crack on left, downstream crack on right (upstream is closer to crack tip)

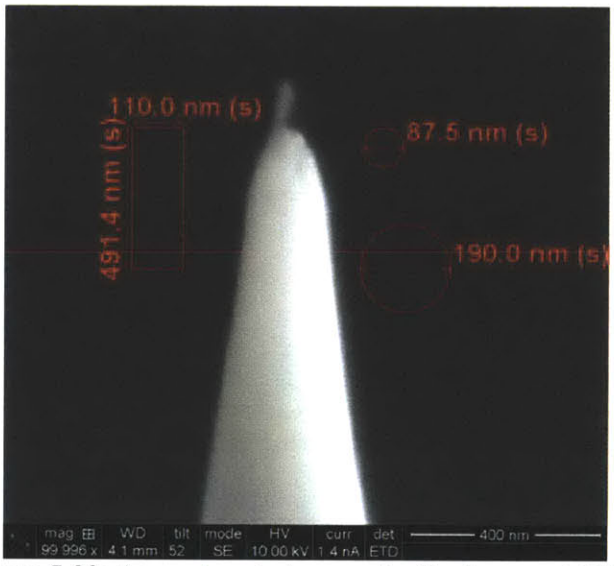

Figure 5-33: As-analyzed atom probe tip, image at 100kx

The APT reconstruction is shown in Figure 5-34. The image on the left of Figure 5-34 shows the γ' precipitates and crack walls, represented by an oxygen plus oxide isosurface. The image on the right in Figure 5-34 only shows the γ' precipitates to more clearly characterize the size, shape, and distribution. The crack is oriented such that it is growing directly out of the page and the walls are outlined with the dashed lines. The γ' phase is sparsely distributed around Crack Tip 2, and several precipitates are located at the tip and along the crack flanks. In Figure 5-34, γ' is represented by an 8 at% titanium isosurface, which also closely corresponds to approximately 3.5 at% aluminum isosurface. Similar with Crack Tip 1, the γ' is also present directly along the

periphery of the crack wall. The shape of γ' is similar to that for Crack Tip 1, which is oblong and distorted from the spherical bulk γ'. Moreover, the composition of γ' near the crack path is different than that of bulk γ', primarily with respect to aluminum concentration. In this particular example, the aluminum composition is approximately 3.5 at%, compared to 6.6 at% for bulk γ'.

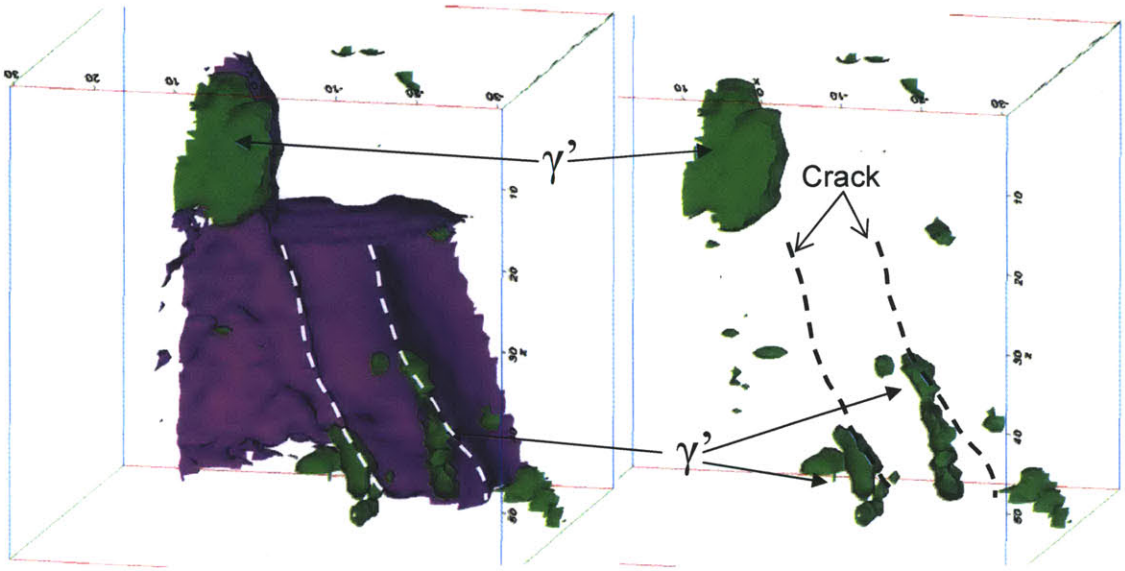

Figure 5-34: γ' location with respect to crack (crack growing out of page), dimensions in nn (crack surface (purple) is represented by 10 at% isosurface comprised of NiO, CrO_x, FeO_x, and oxygen, γ' phase (green) is represented by a 8 at% titanium isosurface)

To document the compositional profile across the crack, a one-dimensional composition profile was generated, and is shown in Figure 5-35. The orientation of the reconstructed volume in Figure 5-35 has the crack growing directly into the page and the walls are outlined by the dashed lines. The view is from the inside of the crack looking towards the tip. The physical crack tip is obscured by the 10 nm diameter composition analysis cylinder. The analysis cylinder is oriented normal to the crack wall and compositional measurements were taken every ½ nanometer. Figure 5-36 shows the compositional plot of the profile across the crack. The crack is enriched oxygen, nickel oxide, chromium oxide, and iron oxide. The crack interface has an oxide interaction layer of approximately 2-3 nm thick. Outside this interaction layer the nickel and chromium concentrations reach bulk composition levels. The crack internals have location dependent layers of oxide enrichment. Chromium oxide is the predominant bulk constituent within the

crack. Nickel oxide is present within the crack, but not as prevalent as chromium oxide. Nickel oxidation follows the crack walls more closely. Iron oxide is also present within the middle of the crack, albeit to a lesser degree than chromium and nickel. The nominal concentration of iron in alloy X-750 is 8 wt%, making it a minority constituent. Thus, although Fe_3O_4 is thermodynamically stable within the crack tip environment, the availability of iron to react with oxygen is reduced.

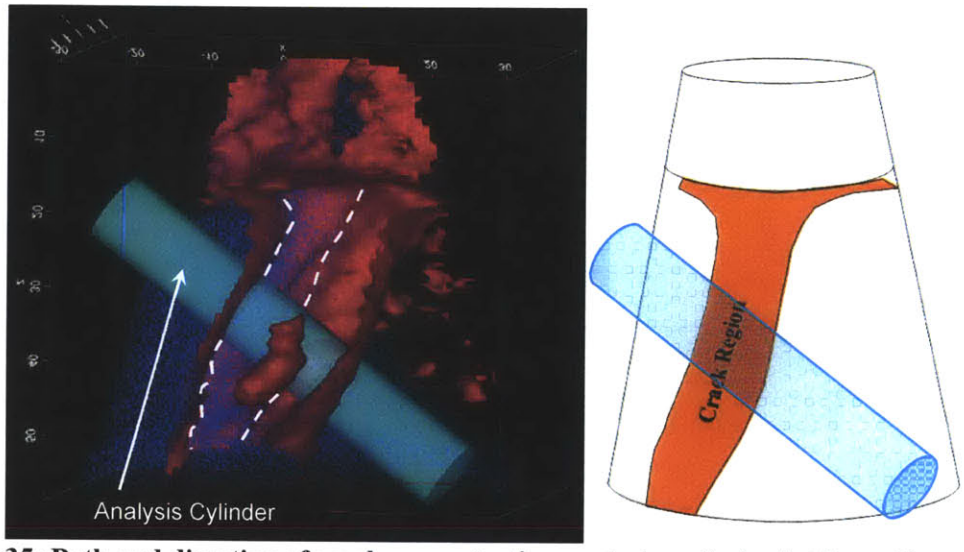

Figure 5-35: Path and direction of crack concentration analysis, cylinder is 10 nm diameter, scale demarcations have 10 nm spacing

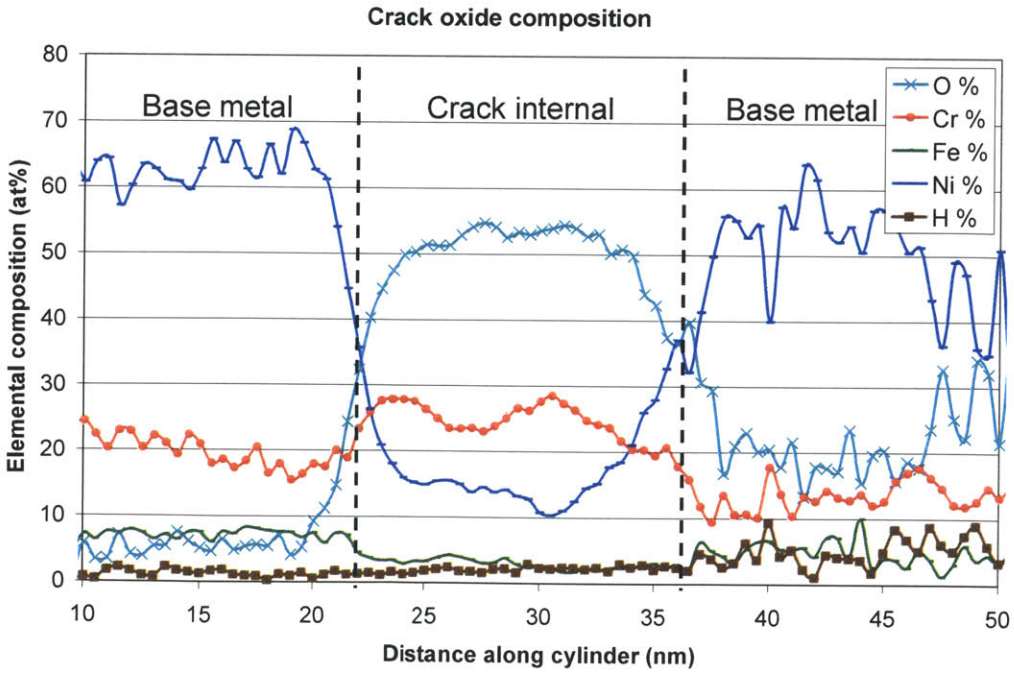

Figure 5-36: Crack oxide elemental concentration profile

The elemental distribution across a 10 nm thick cross-sectional slice was analyzed. Figure 5-37 shows the location and orientation of the cross-sectional slice and Figure 5-38 shows the elemental distribution. The quantitative composition of Crack Tip 2 is recorded in Table 5-2 and is divided between metal atoms and oxide. The crack tip is largely comprised of chromium, nickel, iron, copper, niobium, and vanadium oxides, in addition to elemental oxygen. Additionally, the aluminum and titanium rich regions at the crack tip are associated with the presence of a γ' precipitate. Boron, phosphorous, and sulfur were not detected.

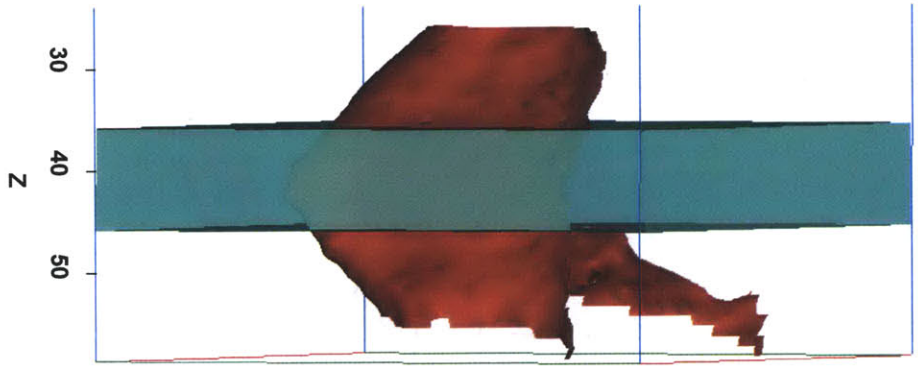

Figure 5-37: Location of 10 nm cross sectional slice for elemental analysis

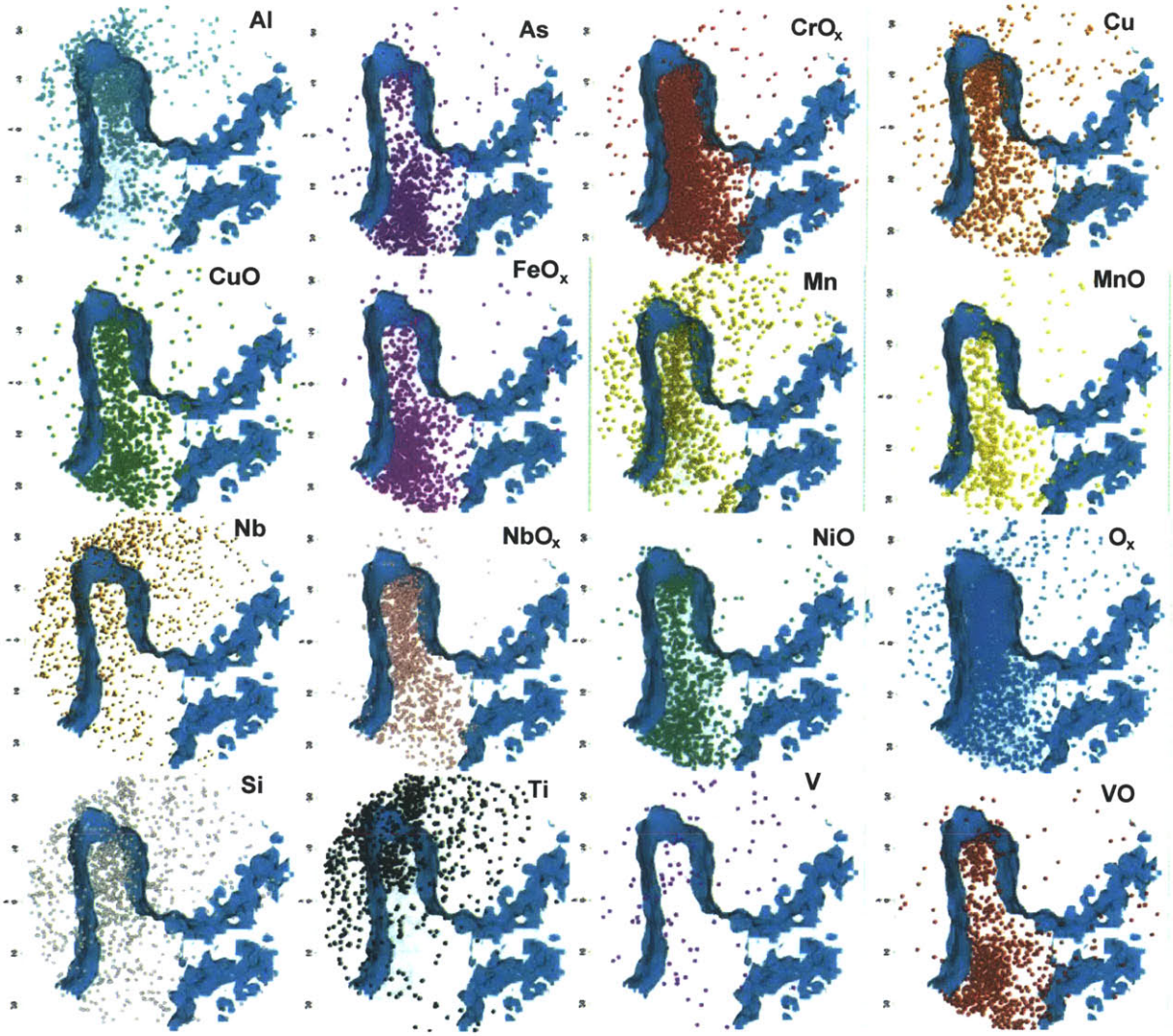

Figure 5-38: Crack Tip 2 elemental analysis, demarcations have 10 nm spacing

Table 5-2: Crack Tip 2 composition

Element	Composition (at %)	% sigma uncertainty	Element	Composition (at %)	% sigma uncertainty
Ni	17.394	0.042	CrO	53.057	0.052
Cr	4.048	0.019	O	8.728	0.040
Fe	2.054	0.014	NiO	5.022	0.022
Ti	0.333	0.005	FeO	1.615	0.012
Cu	0.680	0.008	NbO_x	1.647	0.012
Al	0.525	0.007	MnO	0.225	0.004
As	0.359	0.006	CuO	0.459	0.006
Mn	0.283	0.005	VO	0.453	0.006
Si	0.092	0.003	AlO	0.347	0.006
Nb	0.076	0.003	OH	2.160	0.014
V	0.005	0.001	OH2	0.337	0.005
B	0.000	0.000			
S	0.000	0.000			
P	0.000	0.000			

Figure 5-39 is a view from the inside of the crack looking towards the tip. The crack walls are indicated by the dotted lines. Figure 5-40 is the same reconstruction, rotated 90°, and shows the crack growing from right to left. The crack wall and general shape is indicated by the dotted line. The tip of the crack appears to be about 5-10 nm outside the reconstructed volume. Although this crack reconstruction did not capture any material ahead of the crack tip, this crack represents a good sample to analyze the oxide characteristics of the crack up to the tip, including oxygen penetrations propagating away from the crack walls.

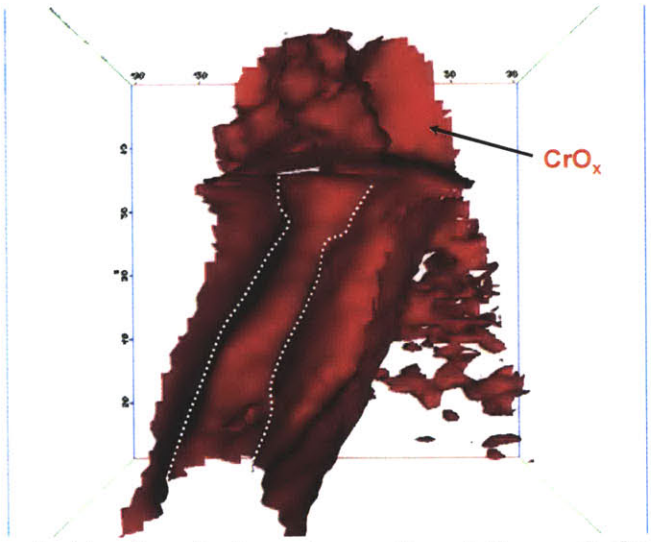

Figure 5-39: View from inside of crack, downstream of crack tip, crack shape is represented by a 2 at% CrO_x isosurface, scale demarcations have 10 nm spacing

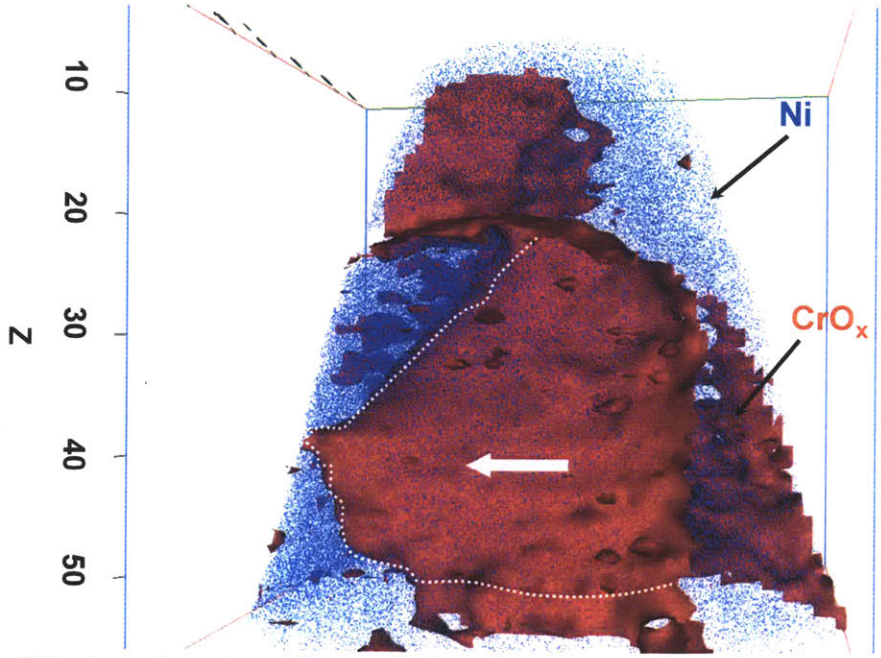

Figure 5-40: Side view of crack and tip, crack shape is represented by a 2 at% CrO_x isosurface, 20% of nickel atoms are visible, scale demarcations have a 10 nm spacing

The colors in Figures 5-41 through 5-43 are as follows: the oxygen is represented by the yellow surface, chromium oxide is the red surface, nickel oxide is the blue surface, and iron oxide is the green surface.

The oxygen present at the crack tip is shown in Figure 5-41, which is a close-up view of the crack tip (crack growing from right to left). The general shape of the crack is provided by the dotted line, and the thick arrow indicates the direction of propagation. The crack tip has features that suggest incubation of oxygen tunnels ahead of the crack tip, similar to Crack Tip 1. The oxygen penetrations will be covered in detail shortly. Figure 5-42 shows a cross-section of the crack tip with the crack growing from back to front (out of the page). The crack was sliced approximately 20 nm from the tip. The crack internals show that iron oxide is not present at the tip, but a nickel-chromium spinel is the primary oxide leading to the tip. Nickel-chromium-iron spinel oxide is formed further from the crack tip within the wake.

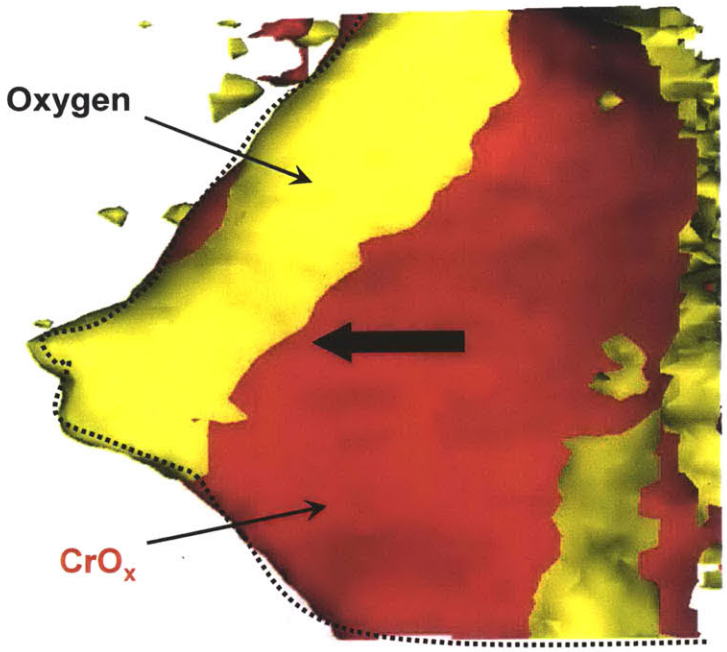

Figure 5-41: Crack tip close-up with oxygen 3 at% oxygen isosurface, 2 at% CrO_x isosurface, arrow indicates direction of crack propagation

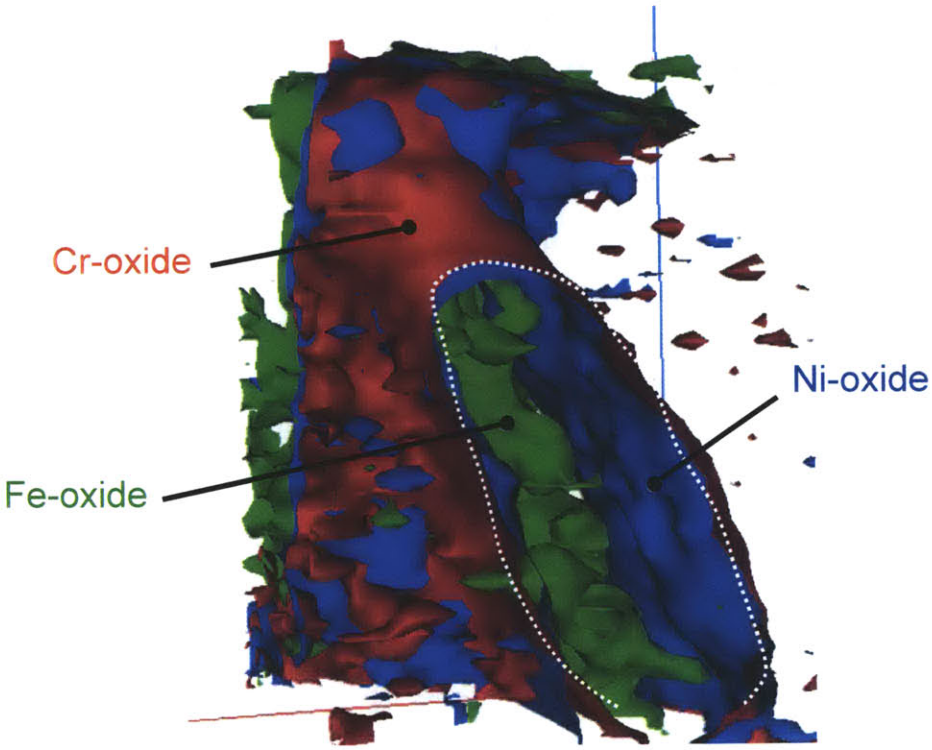

Figure 5-42: Cross-section of crack, ≈20 nm from tip, isosurfaces: 2 at% CrO_x, 1 at % NiO, 0.75 at% FeO_x, crack growing out of page

The crack tip was sliced with a 5 nm thick analysis volume to further analyze the composition as a function of location. The location of this slice is shown in Figure 5-43. A two dimensional concentration map of the oxygen within the crack (the crack is propagating from bottom to top) is shown in Figure 5-44. The oxygen contours clearly show that oxygen is present up to and in front of the crack tip. Furthermore, oxygen penetrates in finger shapes in front and to the side of the crack walls.

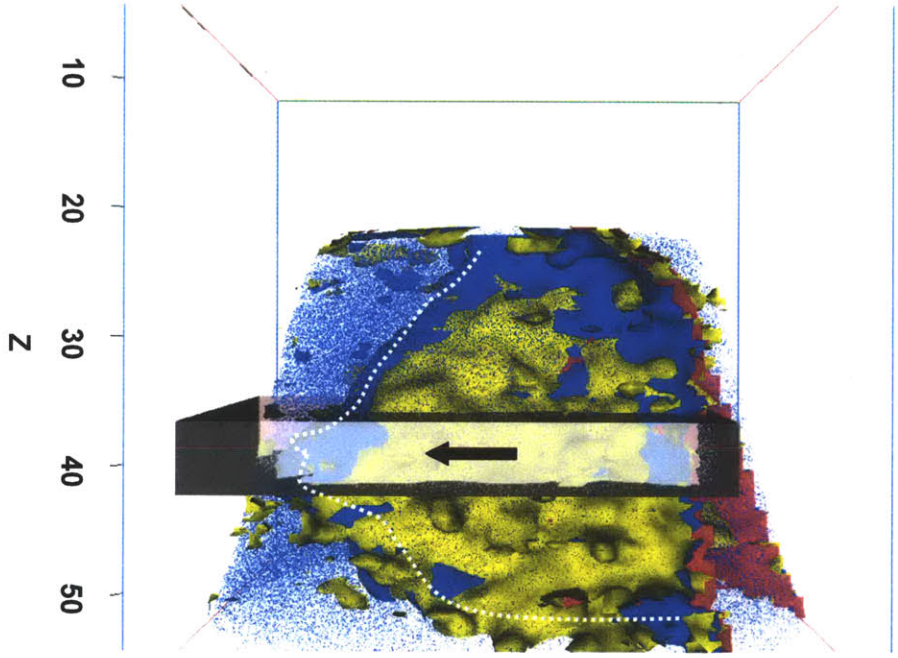

Figure 5-43: 5 nm thick analysis volume of cross-section

The crack shape and direction in the following 2D concentration profiles is outlined by the dark line superimposed on each profile. The superimposed line is not drawn to scale and is only intended to highlight the general crack shape.

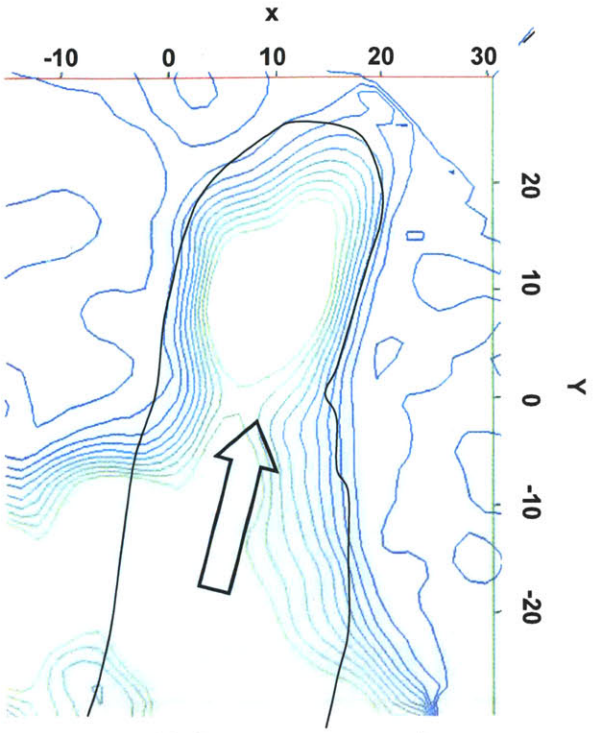

Figure 5-44: Oxygen concentration contours

A chromium oxide concentration map is shown in Figure 5-45, and the nickel oxide map is shown in Figure 5-46. Comparing these two maps it is clear that chromium oxide is the dominant oxide within the crack, but nickel oxide is the dominant oxide at the front of the crack, albeit in low concentration. It is important to note here that nickel oxide is the dominant oxide at the crack tip, but not necessarily ahead of the crack tip. The analysis for Crack Tip 1 clearly showed that chromium-oxide is forming ahead of the "tunnel" penetrations. The analysis for Crack Tip 2 is focused on the main crack, not tunneling ahead of the crack.

The nickel oxide concentration more closely follows the oxygen concentrations, which further suggests that nickel may be the initial oxidizing element. Within the crack, chromium oxide reaches levels greater than 19 at%. Iron oxide is also present in the crack but is the lowest of the major alloying constituents. Iron oxide, even at low concentration, is detected no closer than approximately 25-30 nm from the crack tip. Recall that in alloy X-750, iron is alloyed at 8 wt%, compared to 18 wt% for chromium, and about 70 wt% nickel. Thus, although Fe_3O_4 is the stable iron oxide in the alloy/environment system, the low alloying content keeps the iron oxide as a minor oxide contributor. Figure 5-47 shows the iron oxide concentration map.

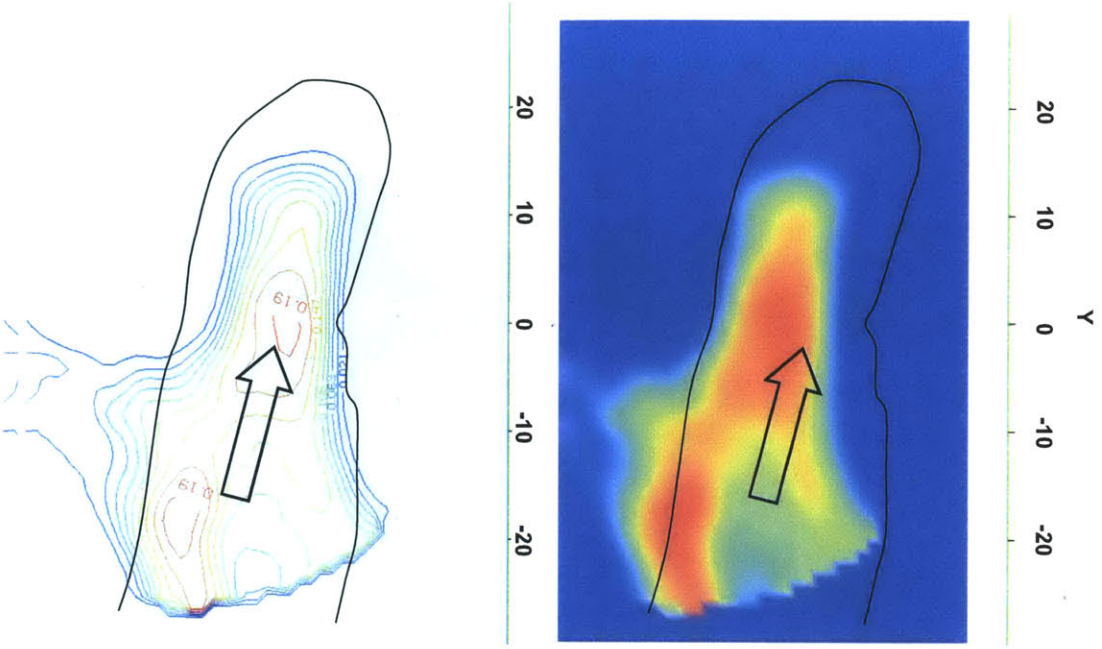

Figure 5-45: Chromium oxide distribution at crack front

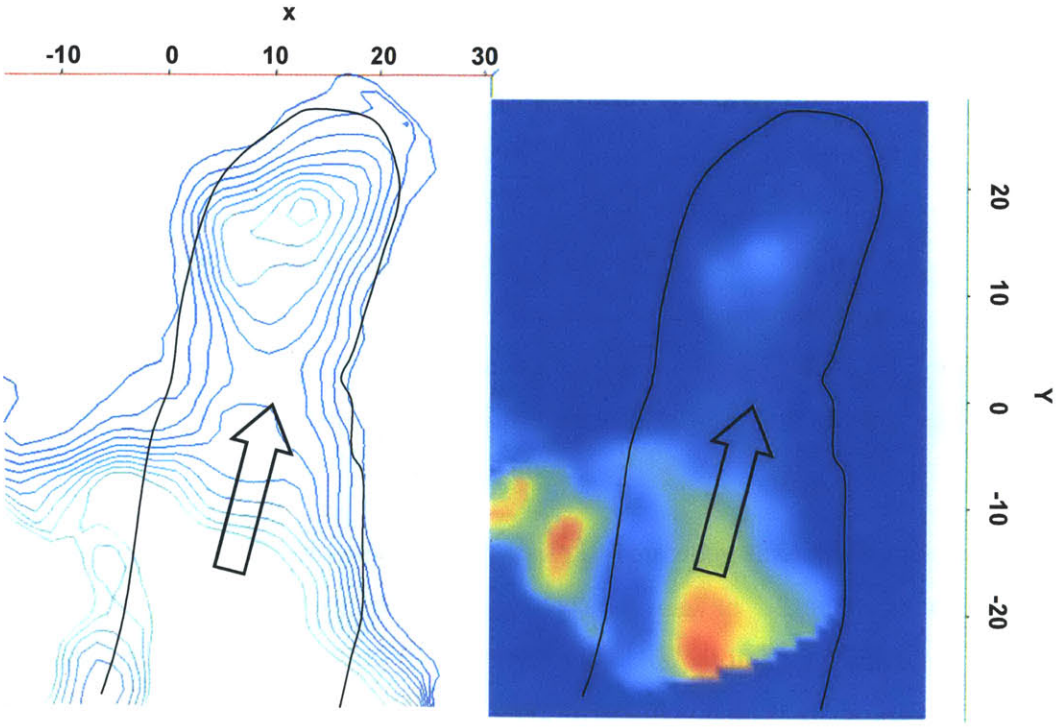

Figure 5-46 Nickel oxide distribution at crack front

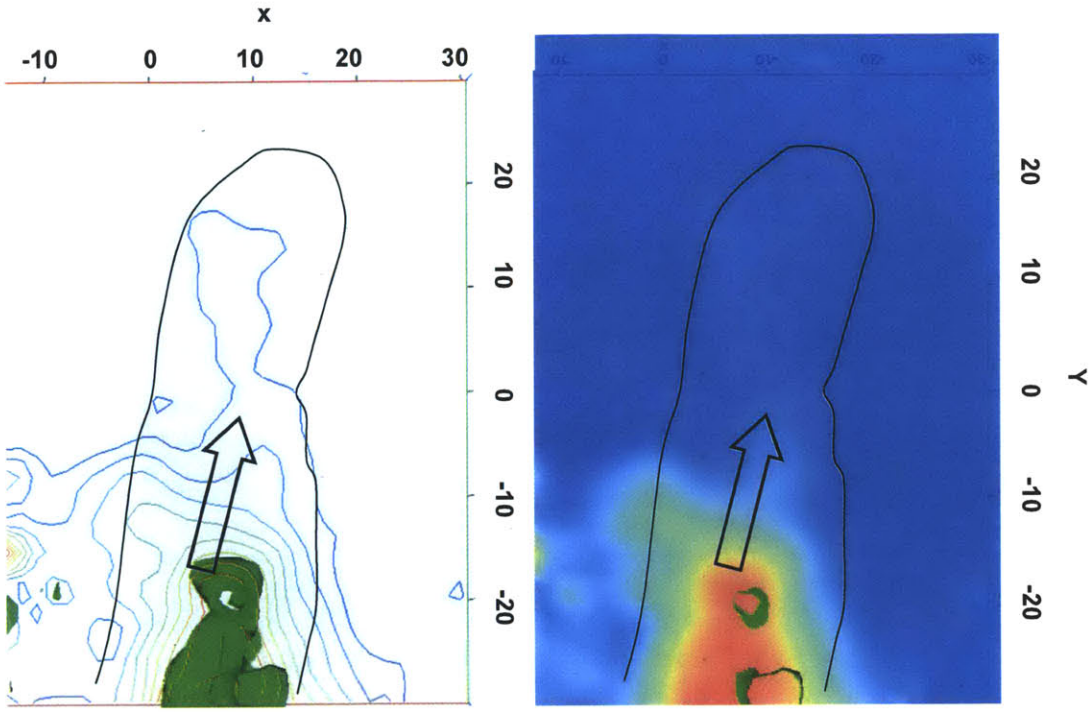

Figure 5-47: Iron oxide distribution at crack front

The APT reconstruction of Crack Tip 2 also clearly shows oxygen penetrations away from the crack wall. These features are highlighted in Figure 5-48, and are surrounded by dashed ovals. The orientation of the crack is such that it is growing from back to front (directly out of the page) and the crack walls are outlined by the white dotted lines. The periodicity of the oxygen penetrations propagating away from the crack wall suggest that oxygen transport into the base metal is following crystallographic features. Although the flatness projection of the oxygen penetrations laterally from the crack wall is an artifact of reconstruction, the penetration effect is real.

A 2D concentration profile was generated to more clearly show the shape and periodicity of the oxygen penetrations. The 2D oxygen concentration profiles show that oxygen is penetrating laterally from the crack wall and that oxygen penetration from the crack walls into the bulk is a real effect for this crack tip. The box highlighting the oxygen penetrations in the lower region of Figure 5-48 is also the analysis volume for the penetrations. Figure 5-49 shows a 2D oxygen concentration profile for four of the oxygen penetrations in Figure 5-48. The penetrations have an even spacing of approximately 4 nm and penetrate away from the crack wall up to 10 nm.

This concentration profile clearly shows the penetration periodicity and that oxygen is migrating into the bulk laterally from the crack flanks.

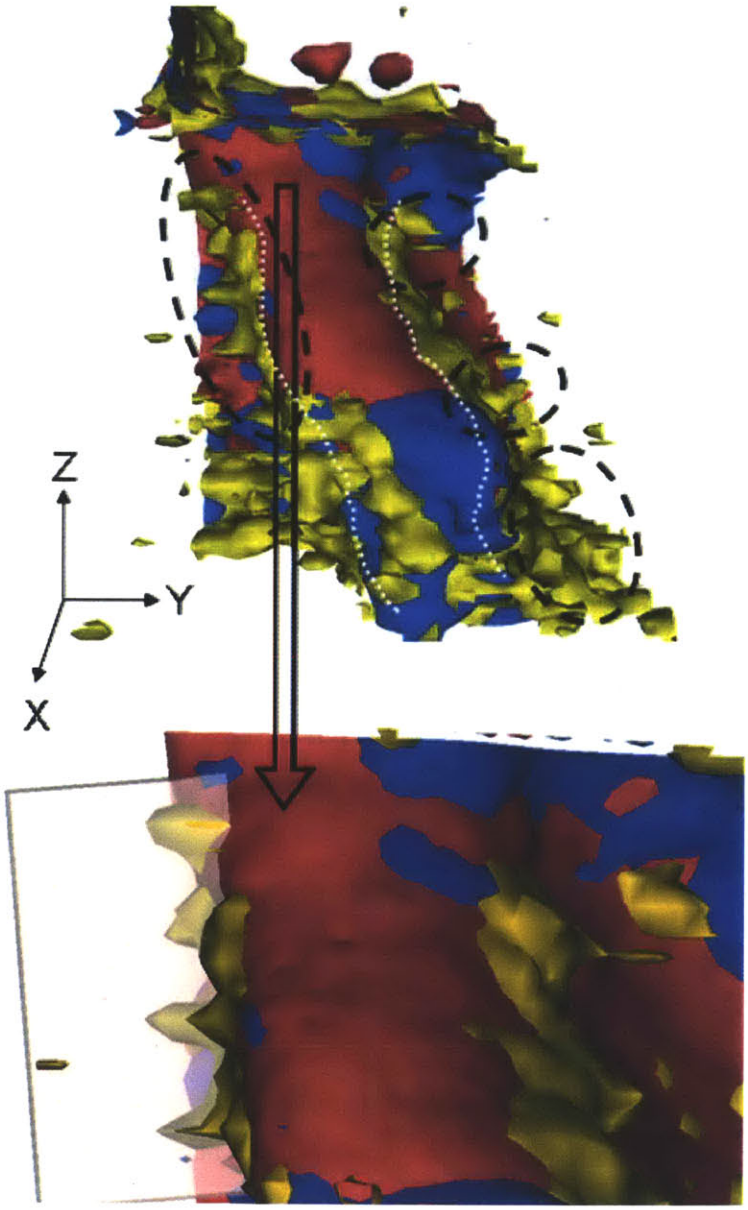

Figure 5-48: Oxygen penetrations lateral from crack walls
Analysis volume for 2D concentration profile highlighted in lower image
(crack growing directly out of page)

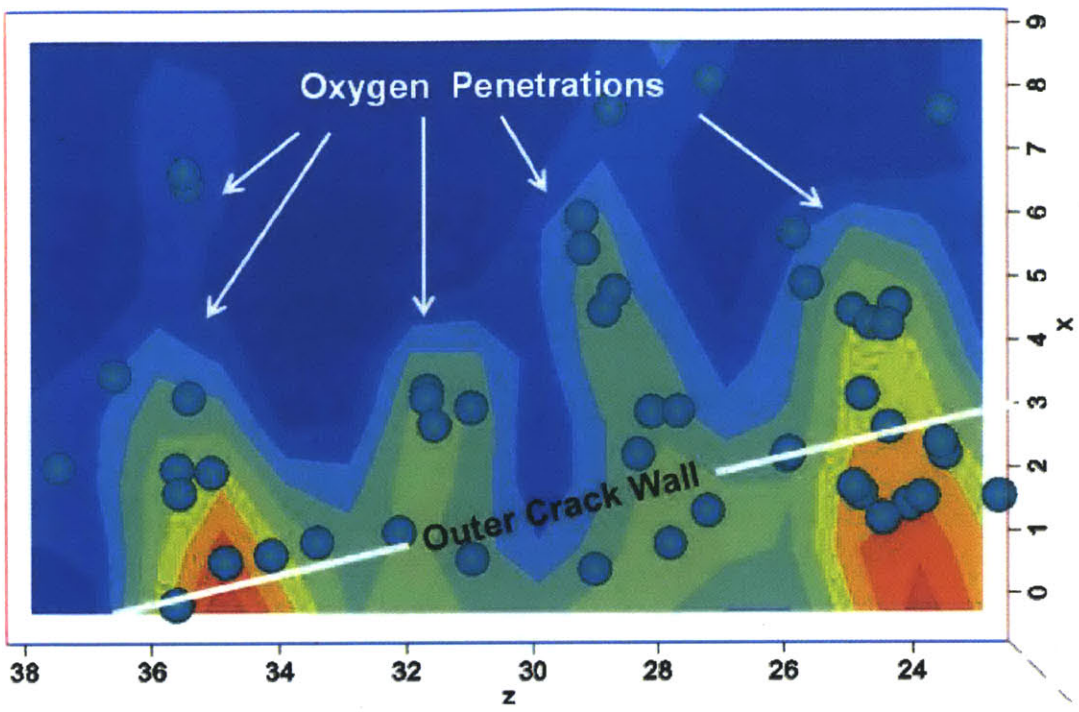

Figure 5-49: 2D concentration profile of lateral oxygen penetrations (oxygen atoms artificially increased to 0.3 nm radius) (dimensions in nm)

5.6 Crack Wall 1: Near Crack Tip with γ' Characterization

The APT reconstruction presented in this section is focused on two topics: γ' characterization as a function of distance to the crack and the crack wall oxide. The APT reconstruction in this section is referred to as Crack Wall 1.

An ideal atom probe tip to document the local microstructure, with respect to a crack, would be one where the tip was oriented normal to the crack path. However, the yield rate of an atom probe tip with such characteristics would be very low due to the higher fracture susceptibility. Thus, the sample prepared for this APT reconstruction was shaped with the crack growing across the tip at a low angle, with respect to the centerline of the final tip. The crack tip was not captured within this APT reconstruction and the orientation of the crack with respect to the reconstruction is shown in Figure 5-50.

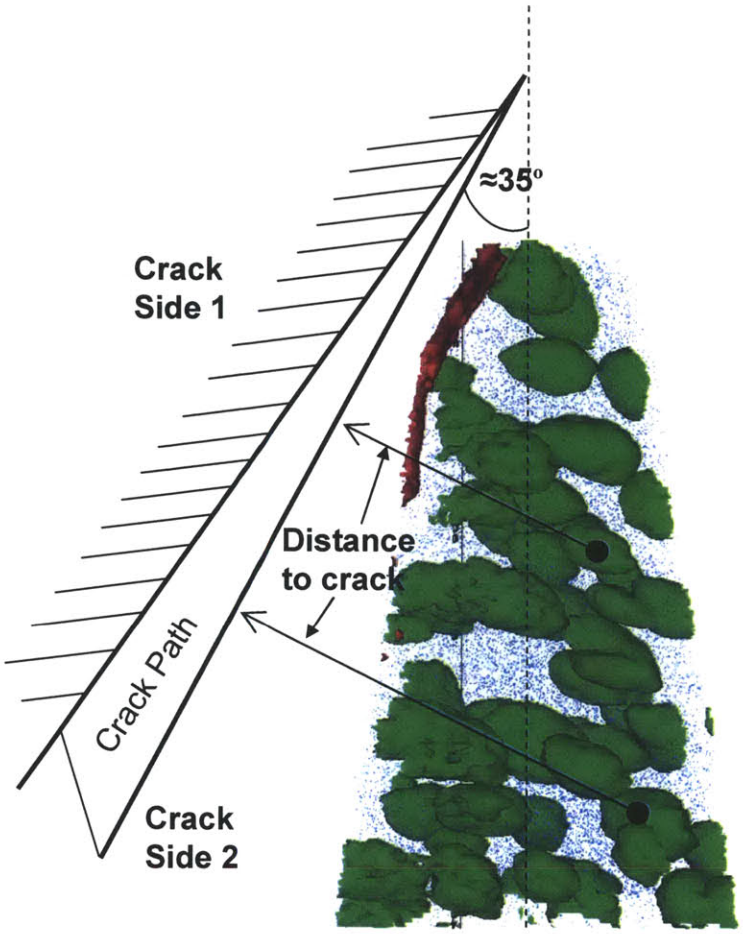

Figure 5-50: Orientation of sample reconstruction with respect to crack

The atom probe reconstruction intersected the crack wall, as evident by the chromium-nickel-iron spinel oxide on the upper region of the reconstruction. The very tip of the atom probe specimen is within 15-20 nm of the stress corrosion crack tip. Crack Wall 1 sample was aimed at capturing the lead tip of the crack. However, the last sharpening step lowered the top of the sharpened tip to just below the crack tip. This sample was able to capture the edge of the crack wall and provides a long γ' analysis range to document the change of γ' composition as a function of distance from approximately 100 nm away from the crack wall. Moreover, crack wall oxide characterization is presented.

The distance between the sample tip and the crack wall was estimated by calculating the oxide composition and comparing the composition to the position on Crack Tips 1 and 2. The peak chromium enrichment in Crack Wall 1 is approximately 10 at%, which is comparable to the internal edge of the crack in Crack Tips 1 and 2. The oxide captured in the reconstruction of

sample Crack Wall 1 is consistent with the full width of an active crack wall in close proximity to the crack tip. This sample is instrumental in documenting the microstructural changes that may: (1) contribute to cracking through electrochemical interaction with γ' or (2) provide a local chemistry favorable for the lowest resistance path of crack propagation.

Using both the final shape of the atom probe tip, as milled in the FIB, and the 3D reconstruction, it was possible to estimate the distance of each γ' precipitate from the crack. It was assumed that the crack was growing straight for 80-100 nm in the region near the APT reconstruction, as outlined by the sketch in Figure 5-50. The composition of five γ' particles were analyzed with a proxigram and the results are tabulated in Table 5-3. Figure 5-51 shows the change in composition of γ' with respect to distance from the crack. Figure 5-52 shows the change in bulk composition with respect to distance from the crack. This clearly shows that the aluminum content decreases in close proximity to the crack. The nominal aluminum content in γ' is 6.6 at%, which was determined from an APT tip analysis far field from an active stress corrosion crack. Aluminum is the only element with substantial changes. The other five studied elements showed little or no change over the 100 nm range. Based on these results, the affected γ' distance is on the order of 100 nm. The γ' within very close proximity to the active crack has an aluminum content of approximately half that of the bulk γ' value (3.7 vs. 6.6 at%). Figure 5-53 shows a visual representation of the change in aluminum composition as a function of distance. Each progressive image depicts an increasing aluminum isosurface. The γ' closest to the crack are depleted of aluminum while those far from the crack are largely unaffected.

Table 5-3: Gamma Prime vs. Bulk as function of distance from crack: averaged values

Isosurface	Region	Element (Atomic %)					
		Ni	Cr	Fe	Ti	Al	Nb
0	Matrix	64.78	18.57	7.48	1.34	0.33	0.36
(6 nm)	γ'	67.05	5.32	2.9	12.64	3.73	1.08
3	Matrix	66.15	18.96	7.78	1.5	0.24	0.35
(22 nm)	γ'	67.07	4.67	3.08	12.8	4.02	1.11
15	Matrix	64.75	17.89	7.39	2.43	0.53	0.44
(38 nm)	γ'	66.28	4.21	2.70	11.69	3.76	1.06
25	Matrix	65.49	19.14	7.91	1.48	0.33	0.39
(42 nm)	γ'	67.66	4.43	2.58	12.08	4.79	0.99
62	Matrix	64.73	19.73	7.94	1.88	0.58	0.08
(95 nm)	γ'	64.71	4.00	3.01	14.52	6.65	1.18

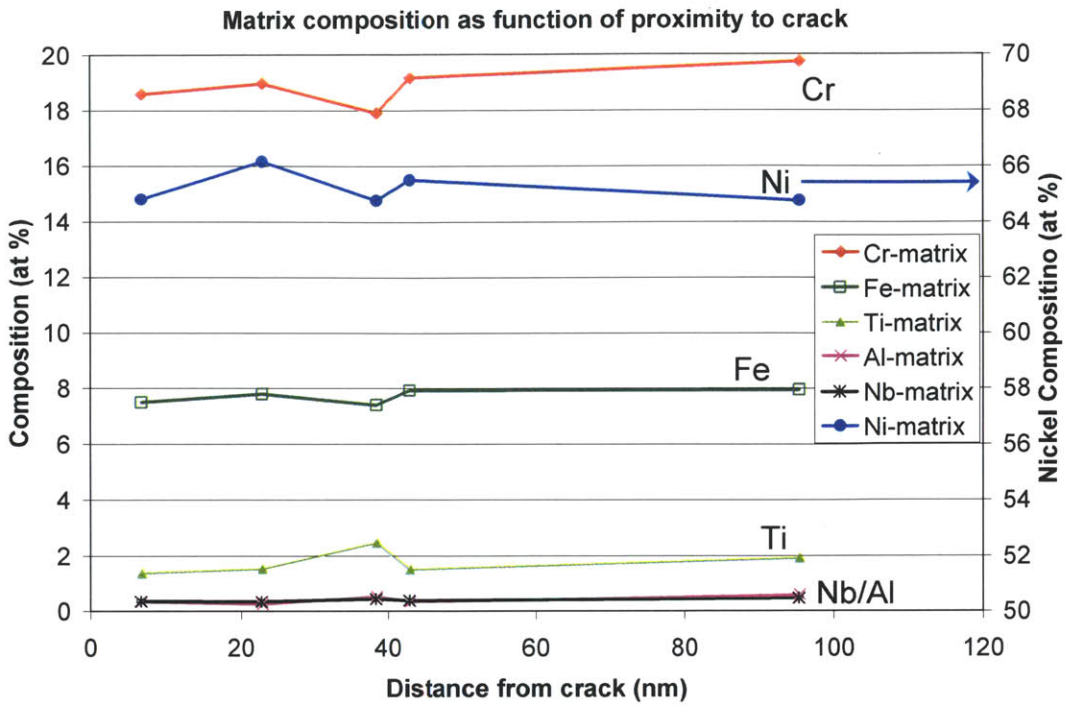

Figure 5-51: Matrix composition as function of distance from crack, distance measured as outlined in Figure 5-50. Matrix composition is directly adjacent to γ'

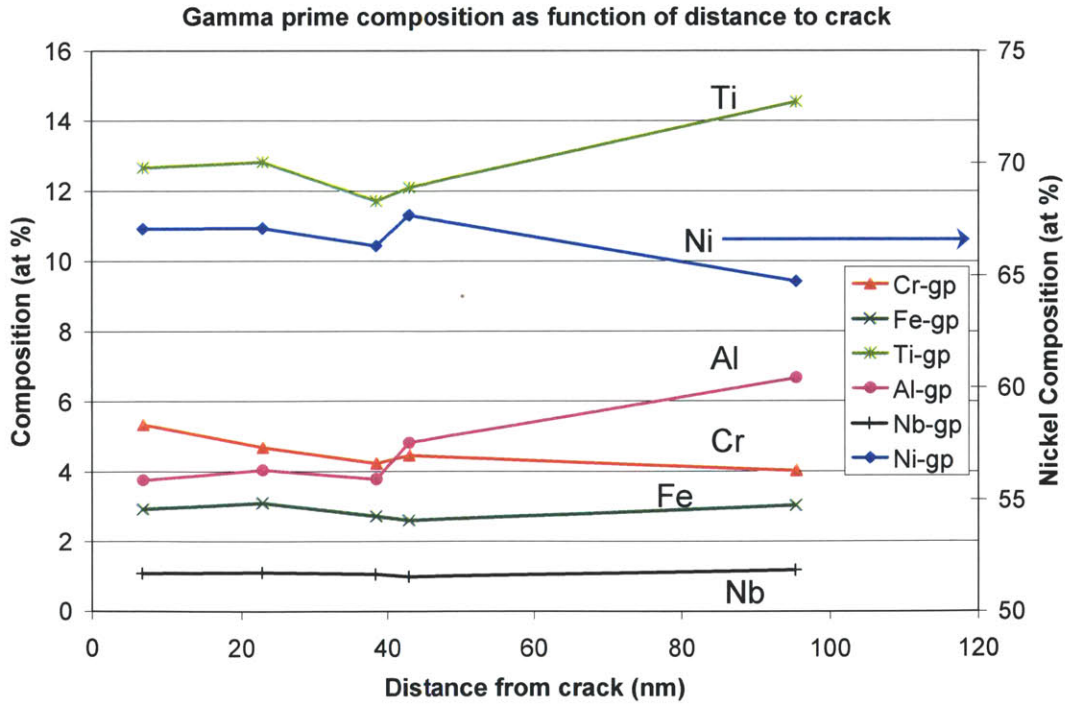

Figure 5-52: γ' composition as function of distance from crack wall, distance is measured as outlined in Figure 5-50

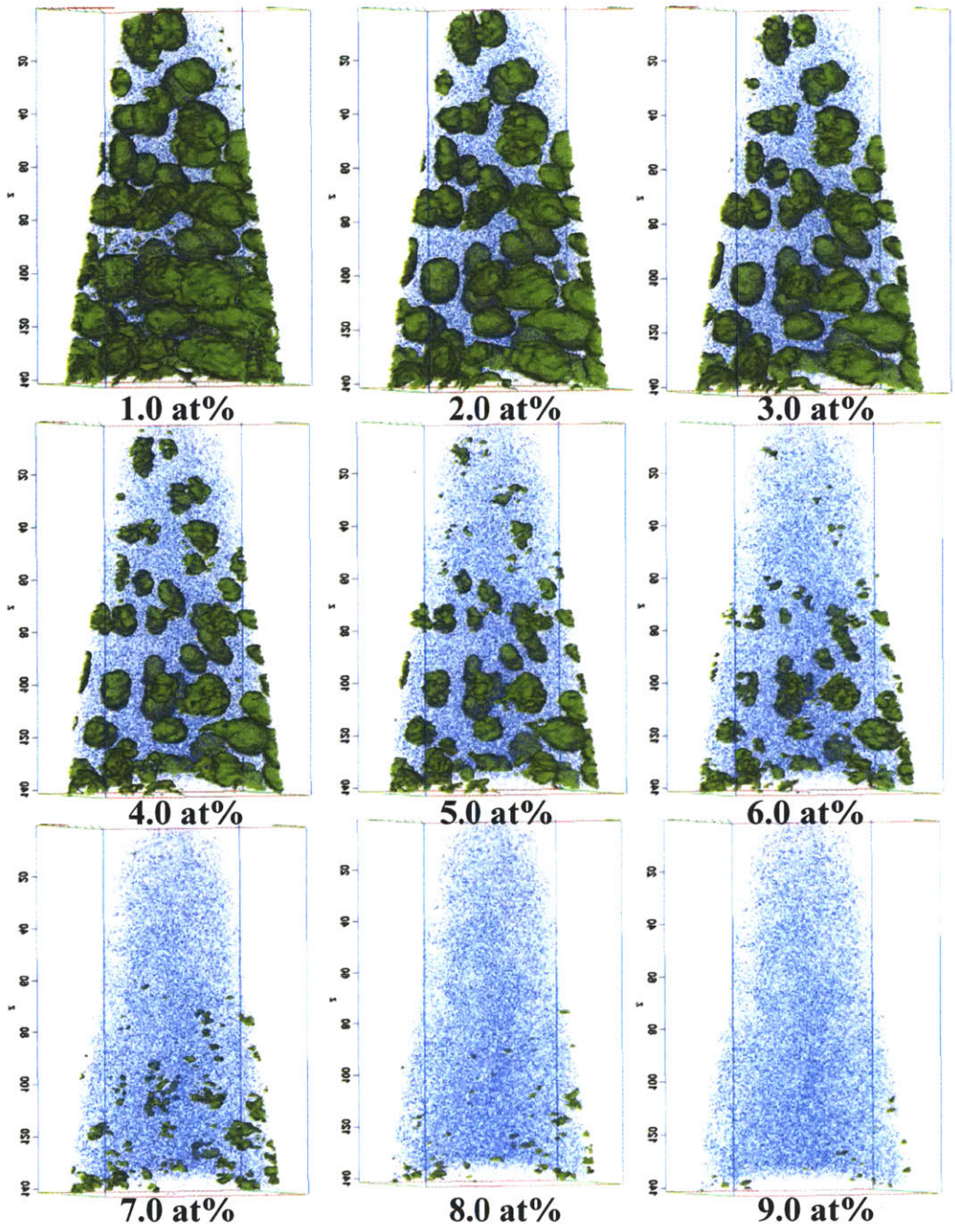

Figure 5-53: Aluminum concentration distribution in γ' near crack, 20 % of nickel atoms visible, scale demarcations 10 nm apart

5.6.1 Crack Wall 1: Crack Oxide Characterization

The crack oxide present on the Crack Wall 1 APT reconstruction is further characterized in this section. The oxide location is highlighted in Figure 5-54: γ' precipitates are not shown. The crack orientation in Figure 5-54 is the same as illustrated in Figure 5-50. This characterization was accomplished by removing the oxide (using the IVAS reconstruction software) from the APT sample to isolate the elemental analysis. A series of isosurfaces and two dimensional composition profiles were performed and are presented here.

Figure 5-55 shows three isosurfaces with nickel and chromium oxide. The chromium oxide threshold was held constant at 3.5 at%, and the nickel oxide threshold was varied between 2 - 4 at%. Nickel oxide forms as a spinel with chromium oxide. Nickel is oxidized in areas where chromium has not yet oxidized. This may be due to a competition for oxygen between nickel and chromium or dependent upon the location of oxygen penetrations, which can lead to crack widening, as presented in the previous section for Crack Tip 2.

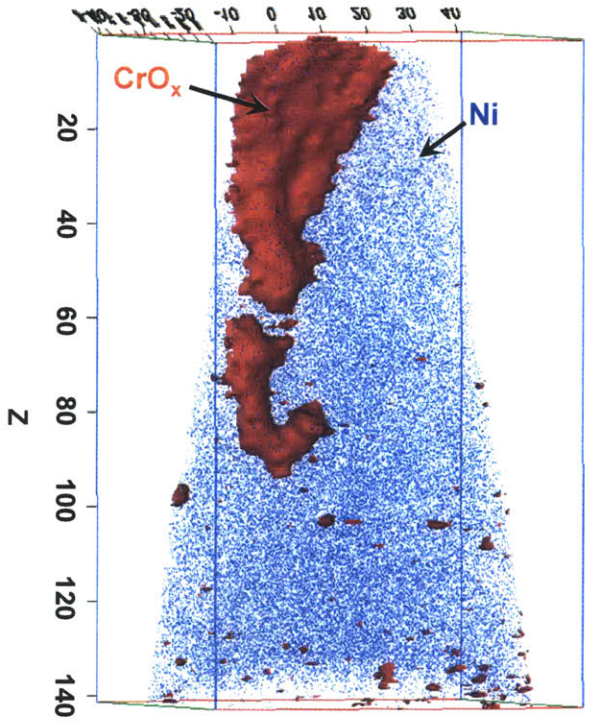

Figure 5-54: Crack oxide location, oxide represented by 4 at% CrO_x, 20% of nickel atom visible

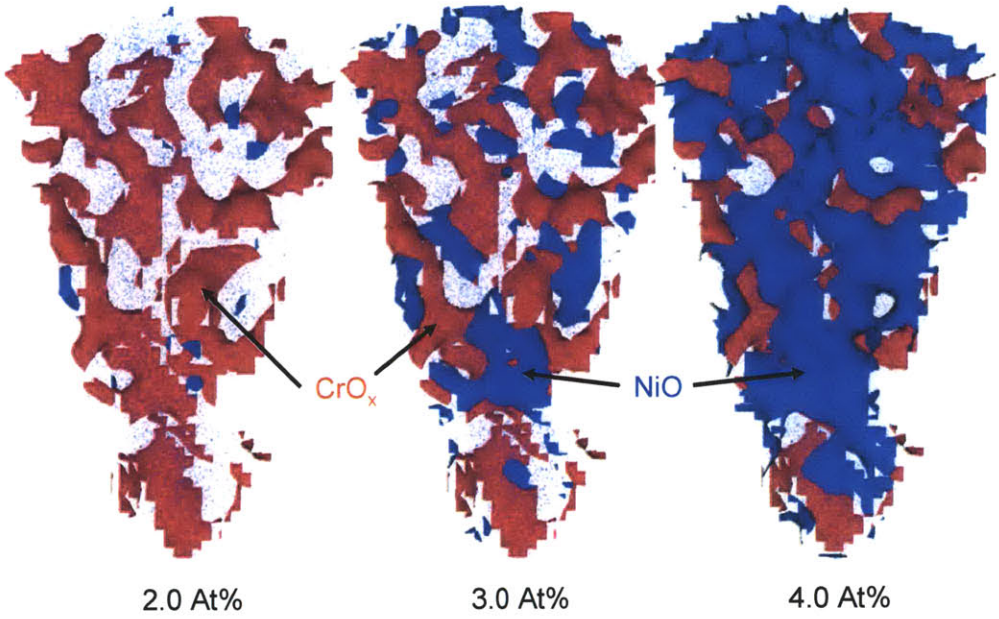

Figure 5-55: Crack wall oxidation
(varying NiO enrichment, chromium oxide held constant at 3.5 at%)

A series of two dimensional composition profiles were generated for nickel and chromium oxides. Figure 5-56 shows the plot of nickel oxide. The upper plot is color coded, with red being the highest levels of oxide. The peak nickel oxide is approximately at 9.5 at%. Figure 5-57 shows the composition profiles for chromium oxide. Chromium is oxidized to comparable levels as nickel oxide, but is more concentrated. Figure 5-58 is a cross-section composition profile that compares the penetration depth of nickel oxide to chromium oxide. Chromium oxide is highly concentrated in the region corresponding to the internal crack wall. Nickel oxide is also enriched inside the crack wall but also maintains higher concentrations in the outer crack wall and into the bulk. The levels of enriched nickel oxide within the bulk, as compared to chromium, may be due to nickel being the host element, while chromium is an alloying element. The partial pressure of oxygen is lower where nickel is oxidizing, but alloy X-750 contains about 3.5x more nickel than chromium. Chromium oxide (Cr_2O_3) has a more negative free energy than nickel oxide and will typically oxidize first and then nickel, but the oxide forms in reverse order in this sample. Nickel oxide has the fastest kinetics, but chromium oxide has the most stable thermodynamics. Chromium oxide may be present at the innermost oxidation layer, but the analysis may be overwhelmed by nickel oxide, which makes it difficult to detect small chromium oxide contributions.

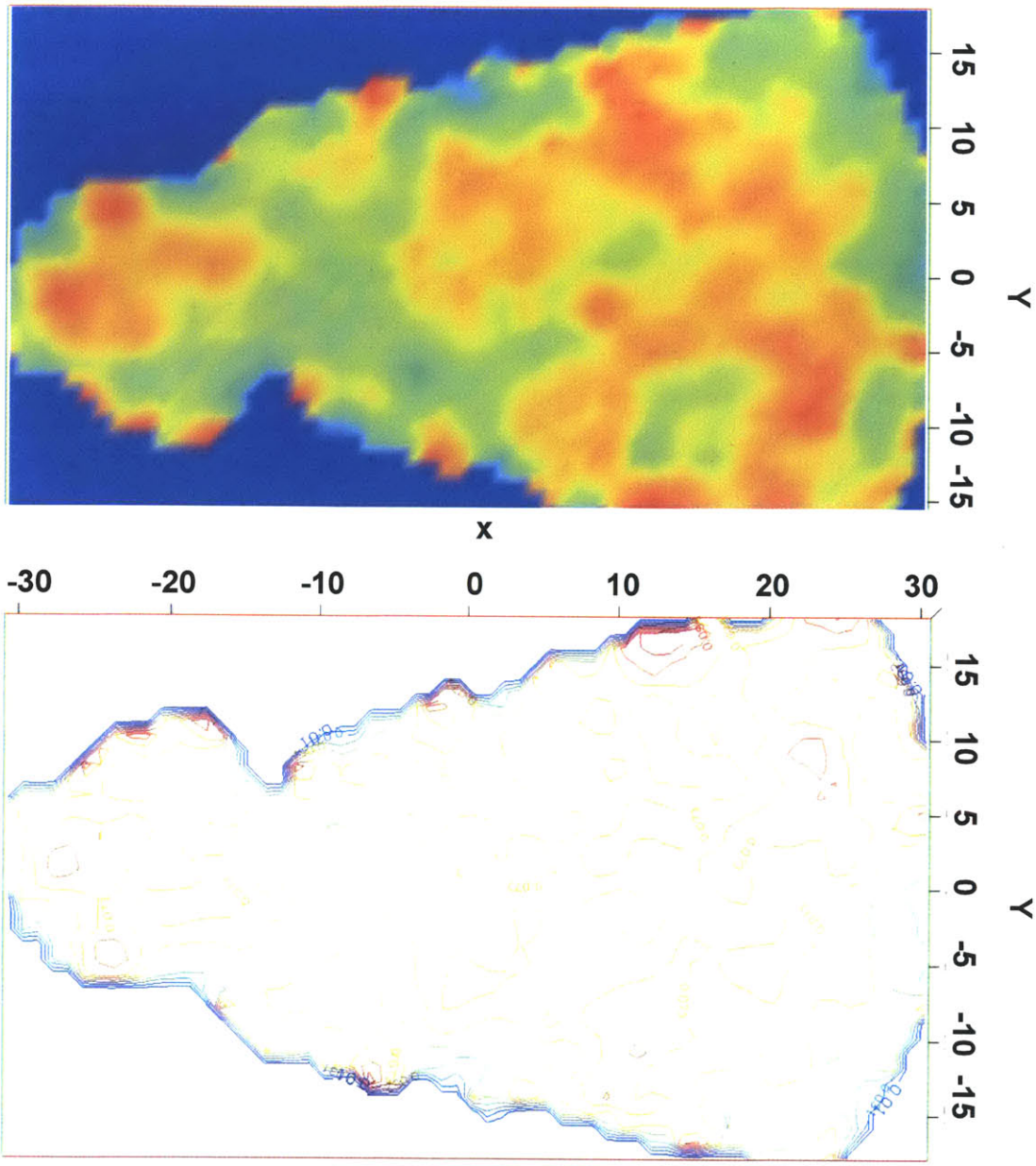

Figure 5-56: Nickel oxide concentration maps

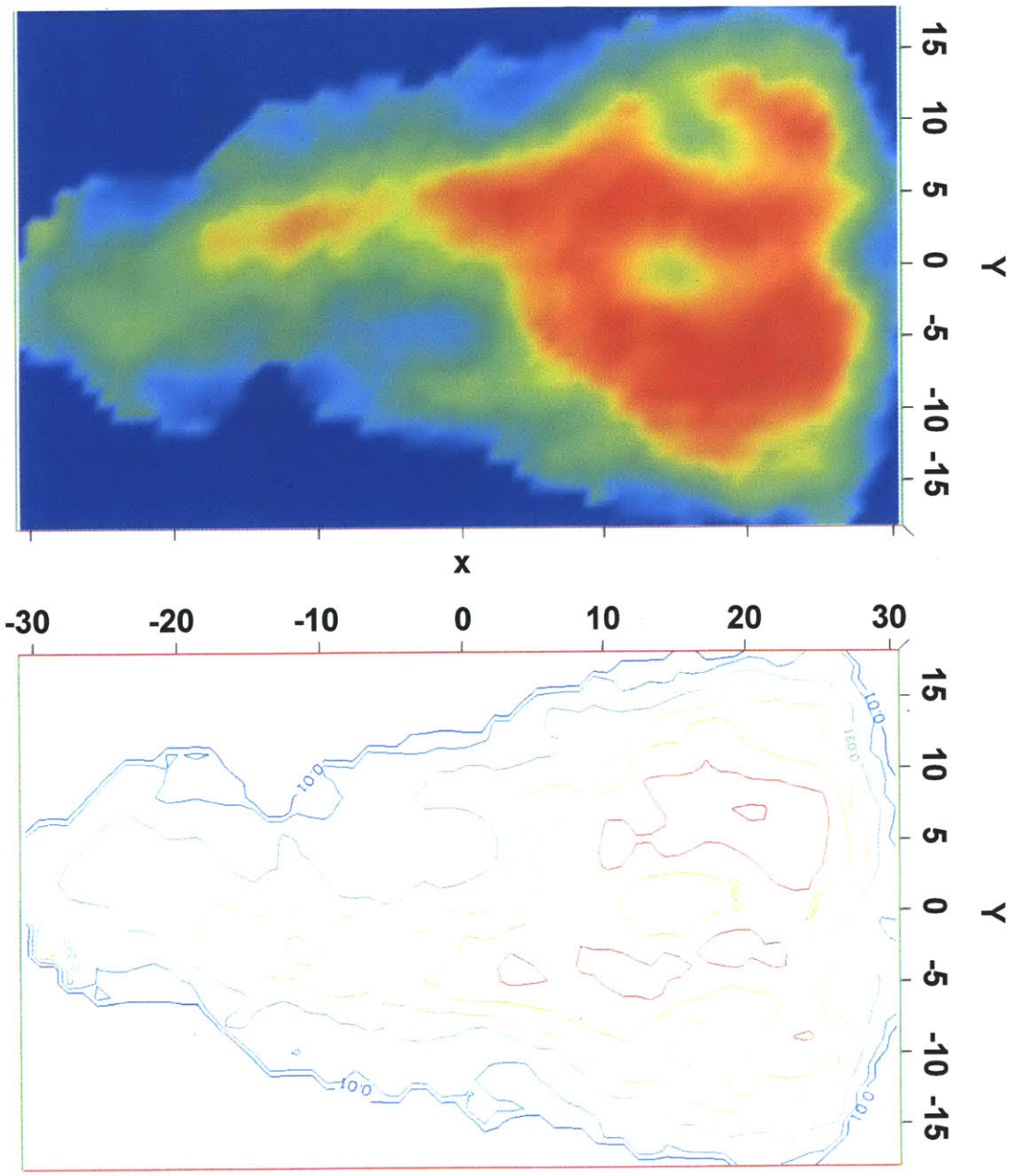

Figure 5-57: Chromium oxide concentration maps

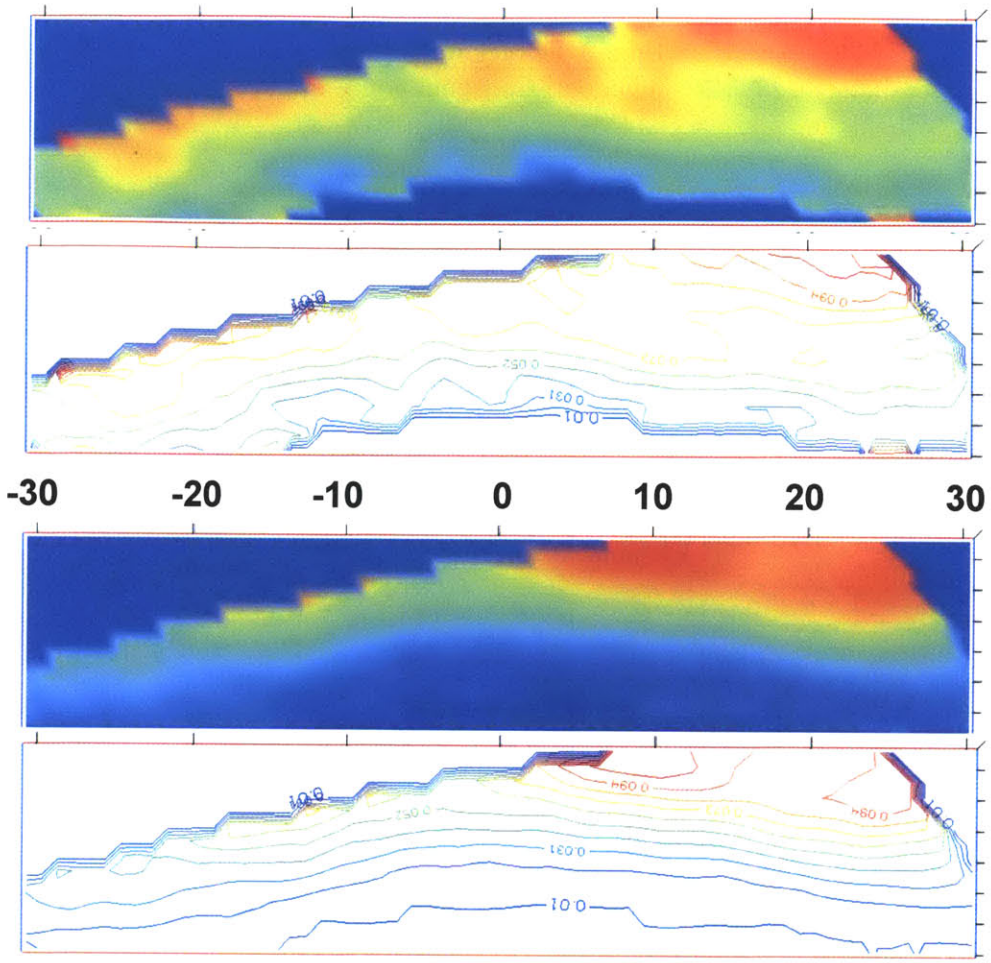

Figure 5-58: Nickel oxide (top two plots) and chromium oxide (bottom two plots)

The oxide types detected in the crack wall are recorded in Table 5-4 and the complete composition of all elements and compounds detected (other than oxides) in the oxide layer is recorded in Table 5-5. Sulfur and phosphorus were not detected. The crack oxide is composed of multiple oxides with CrO_x being the most prominent. The other oxides present, in order of highest to lowest concentration are: NiO, vanadium-oxide, iron-oxide, and manganese-oxide. In addition, the oxide contains only 41 at% Ni, 7 at% Cr, and 3.4 at% Fe, which indicate that the oxide layer is a network of oxide and metal structure.

Table 5-4 Crack wall oxides

Oxide Type	Concentration (at%)
CrO_x	22.19
NiO	8.20
O	6.089
VO	2.29
FeO_x	1.79
NbO_x	0.79
MnO	0.49
AlO	0.196

Table 5-5: Crack wall oxide composition

Element	Concentration (at%)
Ni	41.265
Cr	7.158
Fe	3.406
Cu	1.124
Ti	0.258
Al	0.331
As	0.401
Mn	0.177
Co	0.168
Si	0.125
Mo	0.097
Nb	0.043
Zr	0.035
NbC	0.029
C	0.026
B	0.009
S	0.000
P	0.000

5.7 Discussion and Summary

Several APT reconstructions of SCC crack features in alloy X-750 were performed. The results for the crack tip characterization have highlighted processes that contribute to SCC, but the results also raise further questions that need to be resolved. Regardless, the APT has proven to be very valuable for SCC crack characterization. The results from this characterization work are summarized below:

- Crack Tip 1 exhibited corrosion "tunnels" growing from the tip of SCC cracks. These tunnels are a network of both metal and oxide. The "tunnel" tip is identified by a sudden decrease in oxide content. However, oxygen and chromium oxide are present directly ahead of each "tunnel" at levels 5-6x higher than bulk readings. This indicates that oxygen is diffusing ahead of the crack along specific pathways, such as crystallographic planes or along dislocations. Nickel oxide is also present ahead of each "tunnel" but to a much less extent than chromium oxide.

  The γ' size, distribution, and composition were also documented in this APT reconstruction. The size and distribution is similar in the γ'-denuded zone, as presented in literature, which is referred to as "fine" γ'. The composition of γ' directly adjacent to the SCC crack is deficient in aluminum content, as compared to bulk γ'.

  The bulk material ahead each corrosion tunnel only has a small amount of oxidized metal atoms, most of which are chromium oxide (0.8-1.0 at%). The total affected bulk material is only approximately 2 at% or less: most of the bulk ahead of each tunnel is unaffected. No enrichment or depletion effect of Ni, Cr, or Fe was observed in the bulk directly ahead of the SCC crack or corrosion tunnels.

- Crack Tip 2 clearly exhibited numerous oxygen penetrations laterally from the crack walls into the bulk. Oxygen was shown to clearly penetrate from the crack flanks. The periodicity of oxygen penetrations indicates that they occur along crystallographic features.

  The oxide within the crack is a chromium-nickel-iron spinel. Iron oxide is not present at the crack tip and is detected about 25-30 nm behind the tip. Chromium-nickel spinel is detected up to the crack tip, with chromium being the most prominent.

  The γ' size, distribution, and composition were similar to that of Crack Tip 1.

- Crack Wall 1 reconstruction showed the γ'-effected zone to be approximately 100 nm wide. The γ' precipitates directly adjacent to the crack were deficient in aluminum, which is a result of a heat treatment effect and not a corrosion-induced microstructural change. These results are consistent with the γ' in Crack Tip 1 and 2 reconstructions.

The composition of the crack wall oxide was presented and is a mixture of chromium-nickel-iron and other minor oxides.

- No $M_{23}C_6$ carbides, or any other grain boundary carbides, were located in an APT specimen in this thesis. Based on the evidence presented here and relating the results to literature results it is postulated that the crack propagating adjacent to the grain boundary. Furthermore, the $M_{23}C_6$ carbides on the grain boundary are too large to capture completely in an APT reconstruction. Small-sized grain boundary carbide is approximately the same size as the largest APT reconstruction presented in this work.

- The reduced distribution of γ' and reduced aluminum content in γ' at the crack tip suggests a galvanic effect may be active between the crack propagation pathway and γ', which may result in partial γ' dissolution. This is evident by the presence of aluminum, aluminum-oxide, and hydroxide radicals at the crack tip. AlO(OH) is the stable form of aluminum hydroxide for the crack tip conditions. The compound is too complex to detect with APT, but AlO and OH were detected. The exact electrochemical mechanism at the crack tip that involves γ' is unclear. Further work is necessary to more completely characterize this phenomenon.

5.8 References

1. P. Laghoutaris, J. Chene, C. Guerre, O. Raquet, M. Sennour, R. Molins, F Viallant and P. Scott, "Contribution to understanding of stress corrosion cracking of alloy 600 in PWR primary water," Energy Materials: Materials Science and Engineering for Energy Systems, Vol. 3, No. 2, pp. 119-125, 2008.

2. S.M. Bruemmer and L.E. Thomas, "High-resolution analytical electron microscopy characterization of corrosion and cracking at buried interfaces," Surface and Interface Analysis, Vol. 31, Issue 6, pp. 571-581, 2001.

3. S. Lozano-Perez and C.A. English, "A multi-scale approach to stress corrosion cracking," NACE, Paper 8495, 2008.

4. S. Lozano-Perez, P. Rodrigo and L.C. Gontard, "Three-dimensional characterization of stress corrosion cracks," Journal of Nuclear Materials, Vol. 408, Issue 3, pp. 289-295, 2011.

5. E.W. Muller, J.A Panitz and S.B. McLane, "The atom-probe field ion microscope," *Review of Scientific Instruments,* Vol. 39, Issue, 1, pp. 83-86, 1968.

6. T. Tsong, *Atom Probe Field Ion Microscopy: Field Ion Emission and Surfaces and Interfaces at Atomic Resolution*, Cambridge University Press, Cambridge, 1990.

7. M.K. Miller and R.G. Forbes, *Atom probe tomography*, Materials Characterization, Vol. 60, pp. 461-469, 2009.

8. J.M. Cairney, D.W. Saxey, D McGrouther, S.P. Ringer, "Site-specific specimen preparation for atom probe tomography of grain boundaries", Physica B, Vol. 394, Issue 2, pp. 267-269, 2007.

9. K. Thompson, D. Lawrence, D.J. Larson, J.D. Olson, T.F. Kelly and B. Gorman, "In situ site-specific specimen preparation for atom probe tomography", Ultramicroscopy, Vol. 107, pp. 131-139, 2007.

10. A. Atrens, J.Q. Wang, K. Tiller and H.O. Andren, "Atom probe field ion microscope measurements of carbon segregation at an α:α grain boundary and service failures by intergranular stress corrosion cracking", Corrosion Science, Vol. 48, pp. 79-92, 2006.

11. A. Cerazo, *et al.,* "Atom probe tomography today," Materials Today, Vol. 10, No. 12, pp. 36-42, 2007.

12. World wide web: http://www-fim.materials.ox.ac.uk/techniques.html, accessed April 11, 2011.

13. O. Hellman, J. Vandenbroucke, J. Blatz du Rivage and D. N. Seidman, "Application software for data analysis for three-dimensional atom probe microscopy", Materials Science and Engineering A, Vol. 327, pp. 29-33, 2002.

14. W.E. Lorensen and H.E. Cline, ACM SIGGRAPH Computer Graphics, Vol. 21, pp. 163-169, 1987.

15. H.J.T. Ellingham, Journal of Society of Chemical Industry (London) Vol. 63, pg. 125, 1944.

16. M.T. Miglin and H.A. Domain, "Microstructure and stress corrosion resistance of alloys X750, 718, and A286 in light water reactor environments", Journal of Materials Engineering, Vol. 9, No. 2, pp. 113-132, 1987.

17. C.K. Elliott, "Effect of thermal treatment on the fracture properties of alloy X-750 in aqueous environments", Ph.D. Thesis, Massachusetts Institute of Technology, 1985.

Chapter 6 – Integration and Discussion

6.1 Introduction and Overview

The SEM fractographic analyses strongly suggested that the SCC crack path was pseudo-intergranular and intergranular. This conclusion would be consistent with that reported by other investigators, although Elliott [1] has suggested that the crack path, while immediately adjacent to the grain boundary, is not actually on the grain boundary at all times. Recall that the grain boundary morphology consists of the following:

1. Intergranular carbides that, while nucleating on the grain boundary, have a preference for grains with more favorable orientation into which the nucleated carbide grows. The lattice parameter of $Cr_{23}C_6$ is almost an exact multiple of the matrix lattice parameter, which results in "coherency" of growth into the grain with optimum orientation with respect to the carbide planes.

2. Carbide precipitation is preferential to grain boundaries with poor coherency. High coherency grain boundaries do not show carbide precipitation in general.

3. The near grain boundary γ' size is much smaller than the intergranular γ' size.

The results of this work provide additional insight into the nature of crack propagation based on high resolution SEM and the results of the atom probe analysis. The SCC crack propagation character observed in this work is as follows:

1. Crack propagation is pseudo-intergranular, intergranular, and transgranular in some cases.
2. Metal dissolution occurs along the crack path and is more severe along boundaries with $M_{23}C_6$ carbides.
3. Crack propagation mode is dependent on the presence of $M_{23}C_6$ carbides on grain boundaries. Grain boundaries without $M_{23}C_6$ carbides or twins are highly coherent. Cracks propagate in a different mode on/near $M_{23}C_6$ containing boundaries vs. boundaries without carbides (coherent boundaries).
4. Crystallographic cracking via slip can be main or secondary cracking.
5. Full-grain length brittle cracking occurs and is evident by a smooth fracture surface.

6. Cracking can be incubated ahead of active crack tip and appears as grain decohesion.
7. Fracture surface contains localized regions of ductile fracture.
8. Transgranular but crystallographic cracks nucleate and grow off main and secondary cracks.

These fracture and crack features are presented and discussed in the next two sections and are divided into a section focused on grain boundary structure and then followed by fracture surface characterization.

Comparison of existing SCC models with the observed behavior of alloy X-750 SCC is also presented in this chapter. Four models are considered that simultaneously describe features of the SCC and fracture process. These are the slip-dissolution model developed by Ford and Andresen [2], corrosion-deformation interaction model developed by Mignin [3], internal oxidation and fracture model developed by Scott and LeCalvar [4], and the vacancy-creep model presented by Aaltonen [5]. Each of these models provides some unique attributes for describing specific features observed in alloy X-750 SCC under the environmental conditions in this work. The applicability of each model to alloy X-750 SCC is discussed within each section. However, no one model can completely describe the environmental fracture process observed in this work. The four models discussed in this work provide the most complete characterization of the observed phenomena. All four models will be tied together and suggestions will be made as to how the models interact and contribute to a description of the overall SCC of alloy X-750.

6.1.1 Grain Boundary Structure

Grain boundary and near grain boundary structure appears to have the strongest internal influence on the mode of crack propagation (external influences would be load and environment). Several examples of grain boundary structure are shown in Figure 6-1 through Figure 6-3. Figure 6-1 shows how the grain boundary can be covered with $M_{23}C_6$ carbides while the neighboring grain can have different grain boundary morphology with no carbides. One grain has a boundary with a semi-continuous network of $M_{23}C_6$ carbides (predominantly $Cr_{23}C_6$). The carbides can grow into one specific grain or can alternate between grains. Figure 6-2 and Figure 6-3 are cross-section views of a crack path along grain boundaries. Figure 6-2 clearly shows the resulting crack path along a $M_{23}C_6$ containing boundary and how the mode changes between grains when the boundary structure changes. The crack that advances along a grain

boundary with carbides exhibits a more tortuous path and considerably more metal oxidation appears to occur. The increased oxidation on the grain boundaries with the $M_{23}C_6$ carbides is partially due to oxidizing the chromium in $Cr_{23}C_6$ carbides. Grain boundary structure is dependent upon coherency of adjacent grains and the morphology can change abruptly between grains, which is why one grain boundary may have carbides but the next may not if the coherency is high. Figure 6-2 also shows a crack path that clearly changed propagation mode at a grain boundary intersection. The main crack was growing on a boundary with carbides, but cracking also started along a carbide-free boundary. Additional cracking is visible ahead of each wide crack tip that advances further along the boundary. The further cracking is a few hundred nanometers long and shows the tortuous path on the grain boundary with carbides and a relatively smooth path on the highly-coherent boundary. Figure 6-3 is similar to Figure 6-2 in that it shows a distinct cracking transition between grain boundary types. Figure 6-3 also shows the severity of metal oxidation, via carbide attack, after the crack has passed and the fracture surface is exposed to the environment. Metal oxidation occurs on both types of boundaries but is more prevalent on boundaries with carbides.

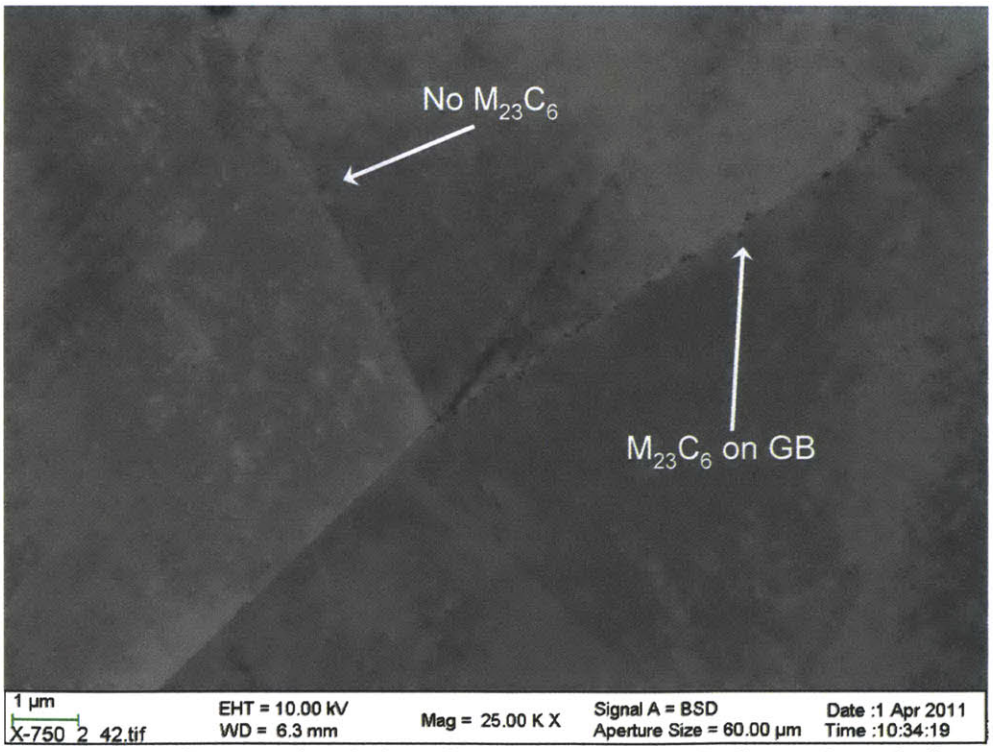

Figure 6-1: Cross-sectional view of both coherent and $M_{23}C_6$ type boundaries

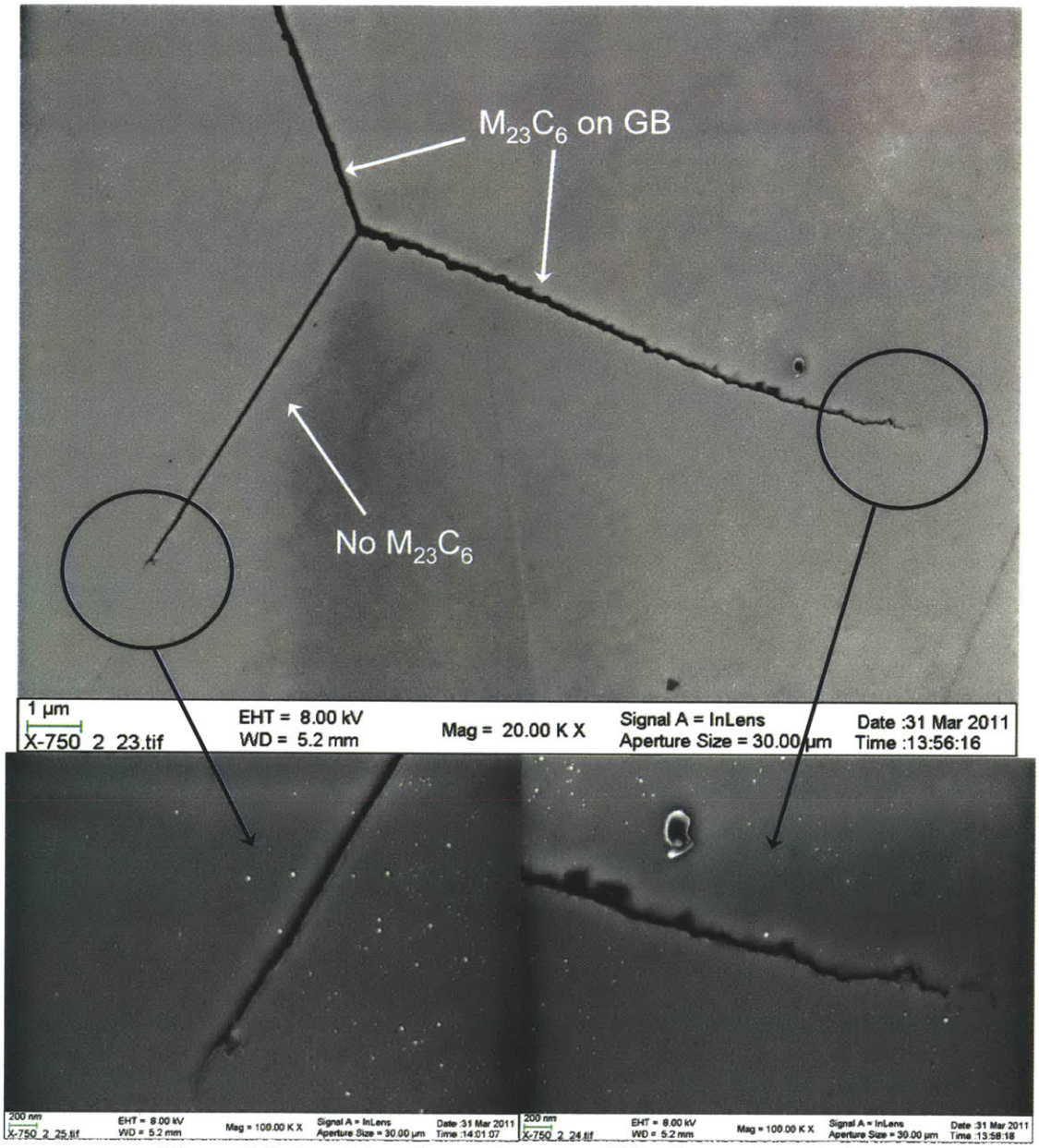

Figure 6-2: Cracking along coherent and $M_{23}C_6$ type boundaries

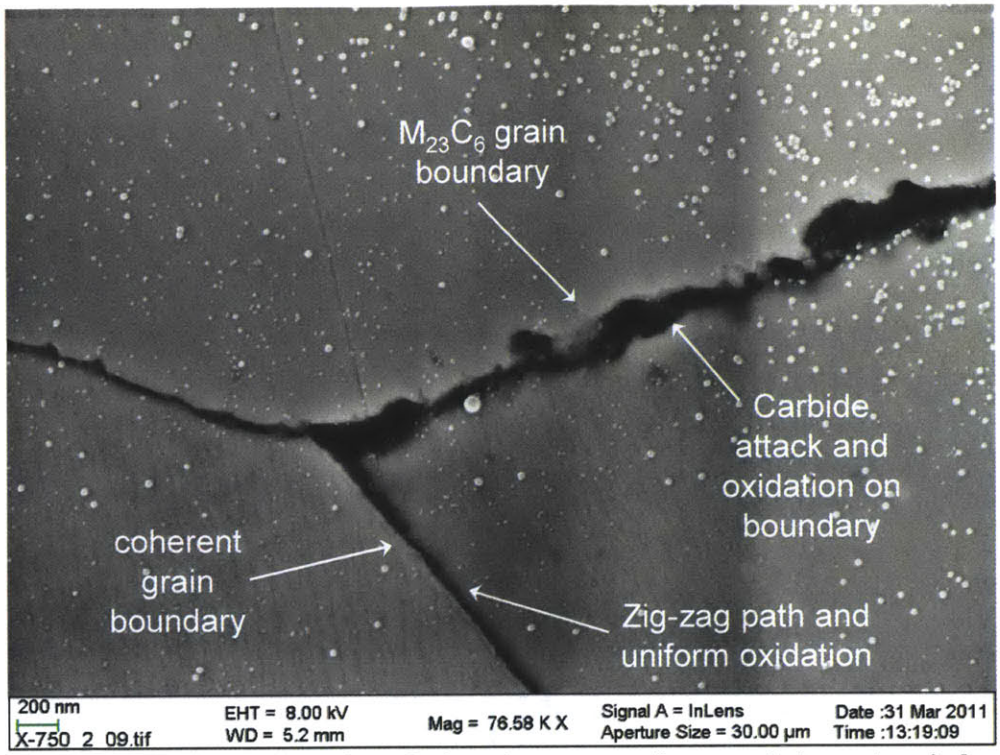

Figure 6-3: Cross-sectional view of crack changing propagation morphology at grain boundary junction (transitioning from $M_{23}C_6$ to coherent boundary)

6.1.2 Fracture Surface Morphology

The fracture surface is predominantly intergranular or pseudo-intergranular. Transgranular cracking is limited and in highly localized regions, typically between two intergranular surfaces. The pseudo-intergranular cracking can easily be mistaken for intergranular cracking because it propagates in close proximity to the grain boundary but offset by 20-50 nm outside the $M_{23}C_6$ carbides. Pseudo-intergranular cracking advances in the grain along the periphery of the $M_{23}C_6$ grain boundary carbides and not on the grain boundary. The fracture surface corresponding to cracking near the $M_{23}C_6$ appears to be a highly pitted surface, which corresponds to the rough and tortuous path the crack takes to propagate. The pitted surface does not necessarily indicate ductile fracture. Evidence showing that brittle-like fracture also occurs during cracking will be presented shortly. The fracture surface for cracking on the periphery of grain boundary carbides is rich in chromium oxide. The chromium can be oxidized from bulk chromium and chromium carbides ($Cr_{23}C_6$).

Smooth cracking also occurs in a pseudo-intergranular manner. These crack surfaces appear much smoother than the surfaces with $M_{23}C_6$ but still have clearly visible carbides (or carbide

craters) on the surface. These visible carbides are predominantly Nb-carbides, which are not known to assist or retard crack propagation. The smooth fracture surfaces are a clear indication of brittle-like fracture.

The crack morphology is dependent upon grain structure and $M_{23}C_6$ carbide and γ' precipitate density and location. Figure 6-4 shows regions with selective oxidation, which is due to a change in crystal structure. The lighter color strips on the cracking surface are indicative of twin or highly-coherent boundaries. The carbide and precipitate density varies between standard grain boundaries and twin or high-coherency boundaries and results in a selective oxidation for certain crystal orientations. Moreover, the ordered structure of the varying regions of $M_{23}C_6$ density is a clear indication of the crystallographic facilitated carbide precipitation and growth.

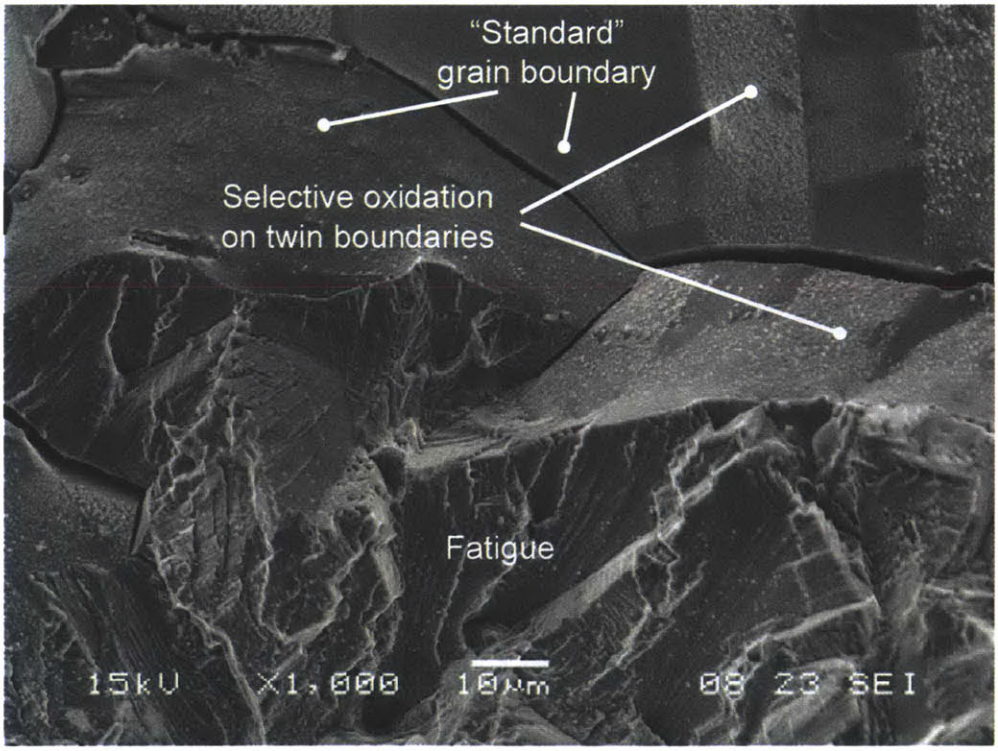

Figure 6-4: Effect of crystal orientation on degree of $M_{23}C_6$ density

Figure 6-5 is another view of the SCC fracture surface with a secondary crack propagating normal to the fracture surface. This figure shows the pitted morphology as the crack propagates around $M_{23}C_6$ carbides and pitting through oxidation occurs. The right side of Figure 6-5 has a coherent grain boundary with a smooth fracture surface and visible slip planes. The slip planes on the smooth fracture surface indicate that crystallographic slip, without pitting, is contributing

to the cracking. The dark spots on the smooth fracture surface correspond to nucleations of chromium oxide. Directly to the left of the smooth fracture surface is a non-coherent grain boundary, which is the predominant type of cracked grain boundary observed in this work. The Ti-nitride indicated in Figure 6-5 has a matching fracture surface on the opposite side of the crack. The Ti-nitride is a sparsely distributed phase in many nickel superalloys and is not known to affect crack dynamics.[6] Figure 6-6 is a higher magnification view of the region enclosed by the dotted lines in Figure 6-5. The "flakes" in Figure 6-5 and Figure 6-6 are incubations of NiO. Figure 6-6 shows the faceted interphase (between γ matrix and $M_{23}C_6$ phases) fracture on the crack wall and that the crack follows a tortuous path the crack as it propagates along the periphery of the $M_{23}C_6$ carbides. Microcracks and nanocracks are also present on the fracture surface, which clearly show that brittle-like fracture is occurring and being driven by crystallographic features. These small cracks are advancing away from the main SCC crack and into the bulk material and are a good example of the secondary cracks propagating in a transgranular mode. The nanocracks clearly show that they are advancing along specific crystal slip planes based on the ordered behavior.

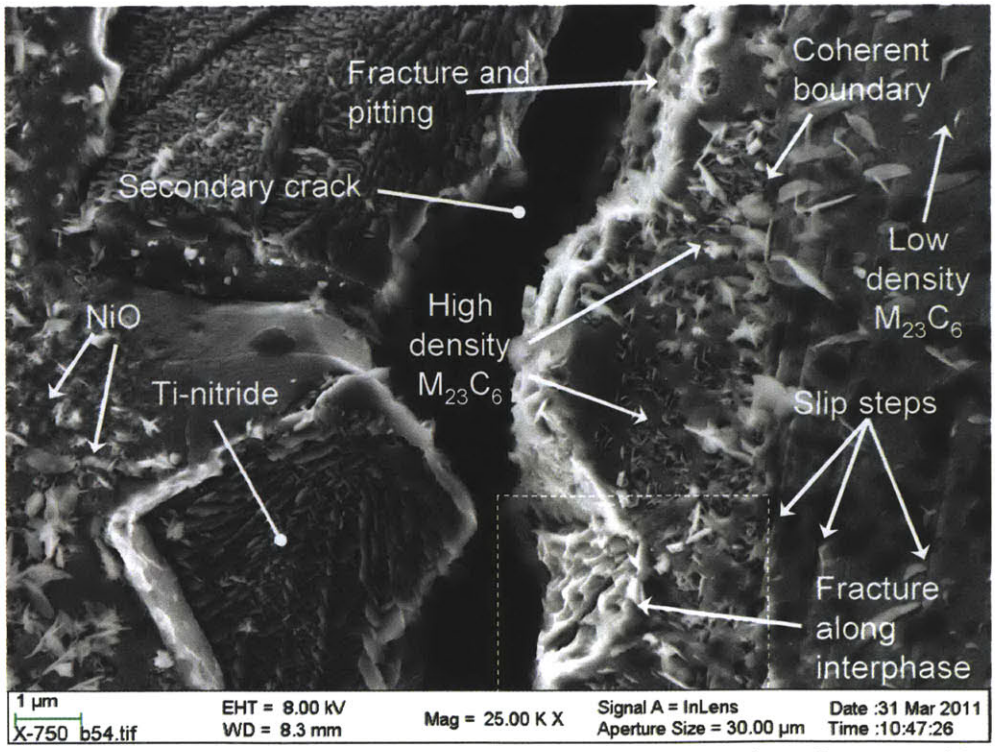

Figure 6-5: Secondary-crack cross-section on the main fracture surface: fracture with pitting results in a rough fracture surface and crystallographic slip fracture results in a smooth fracture surface

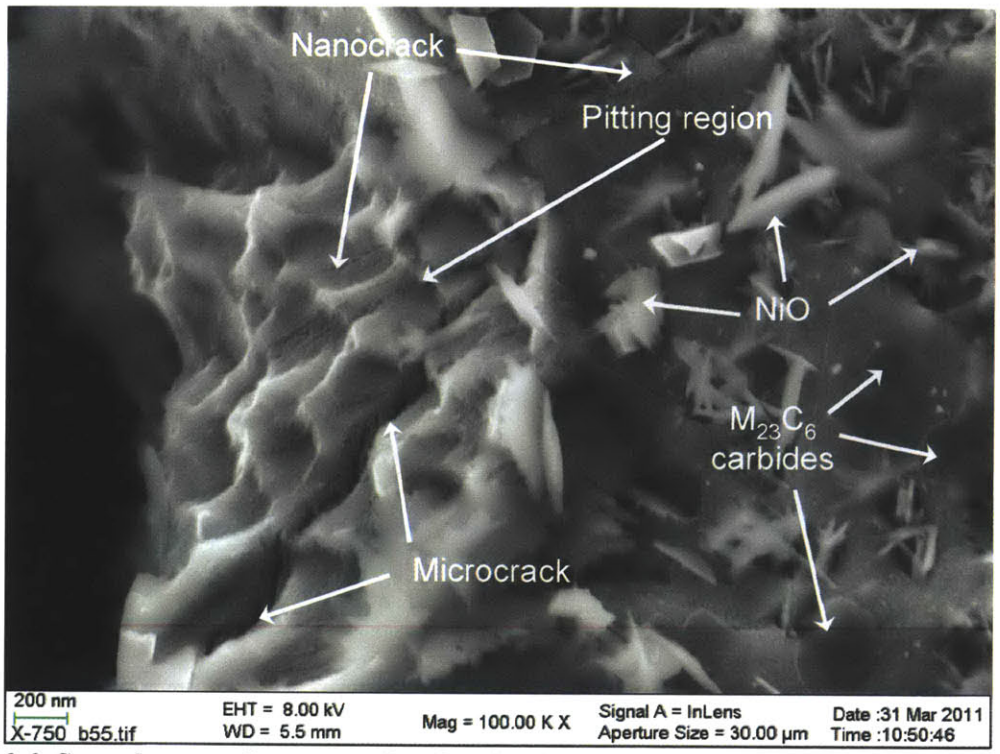

Figure 6-6: Secondary-crack cross-section showing faceted interphase fracture and micro cracks (dotted lines in Figure 6-5 enclose the same region as this figure)

Many of the grain boundaries have the carbides preferentially growing into one grain. The grain that has the majority of the carbides will exhibit an outward dimpled or pitted surface, while the matching surface will have an inward dimpled or pitted structure (the term "dimpled" here does not refer to ductile fracture). Figure 6-7 and Figure 6-8 show both the fractures surfaces that exhibit fracture with pitting around the $M_{23}C_6$ carbides and smooth fracture. Figure 6-9 shows a grain boundary that exhibits preferential carbide growth into one grain. Region 1 in Figure 6-7 and Figure 6-8 corresponds to the region with little carbide growth and region 2 is the matching region in the opposite grain. The upper region in Figure 6-7 corresponds to a single grain which shows that the direction of carbide growth is dependent upon the matching grain and that this effect varies within individual grains. Figure 6-8 is a close-up view of the region in Figure 6-7 enclosed by the dotted line. Figure 6-9 shows a cross-section of a crack with preferential carbide growth towards the upper grain. The labels in Figure 6-9 correspond to the fracture morphologies in Figure 6-7 and Figure 6-8.

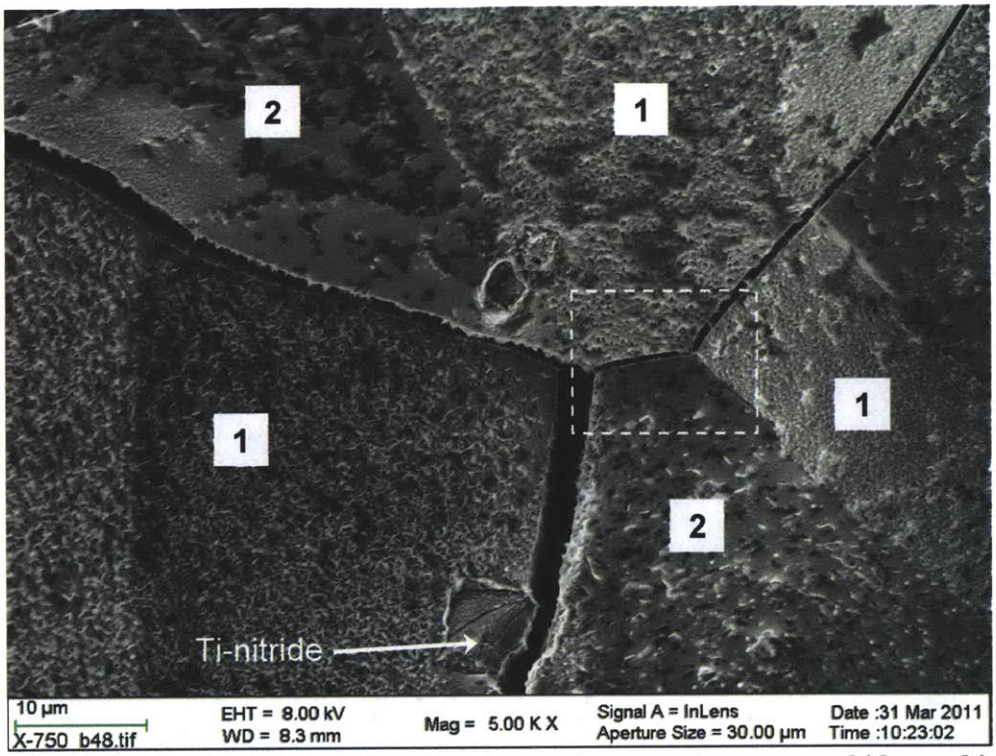

Figure 6-7: Fracture surface with two morphologies related to near-carbide cracking

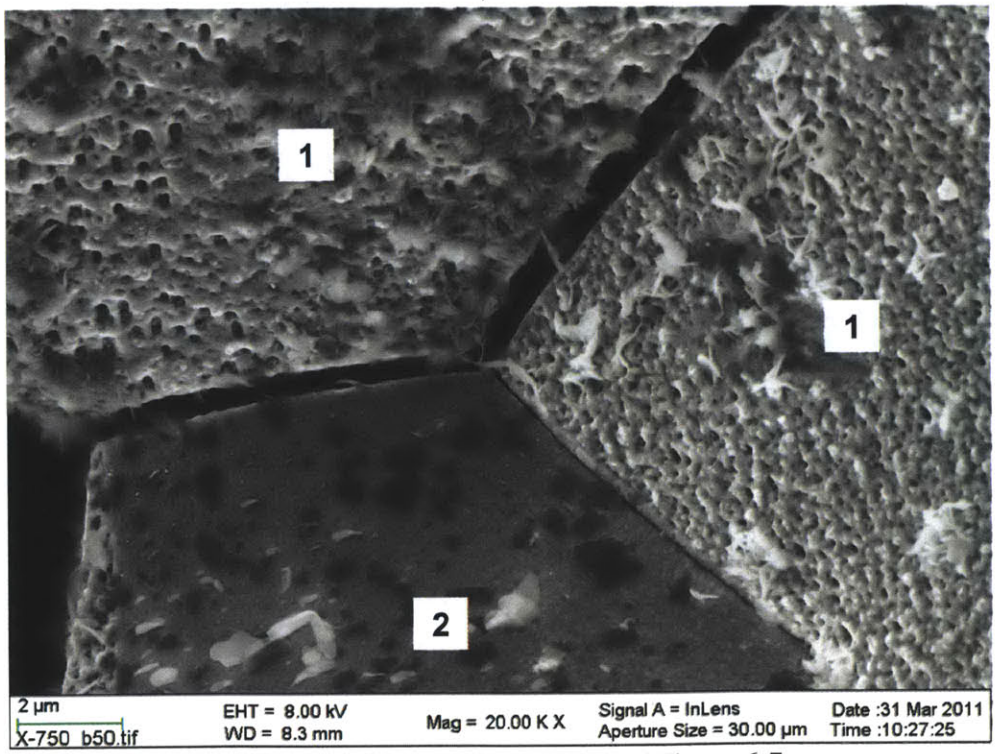

Figure 6-8: Higher magnification of Figure 6-7

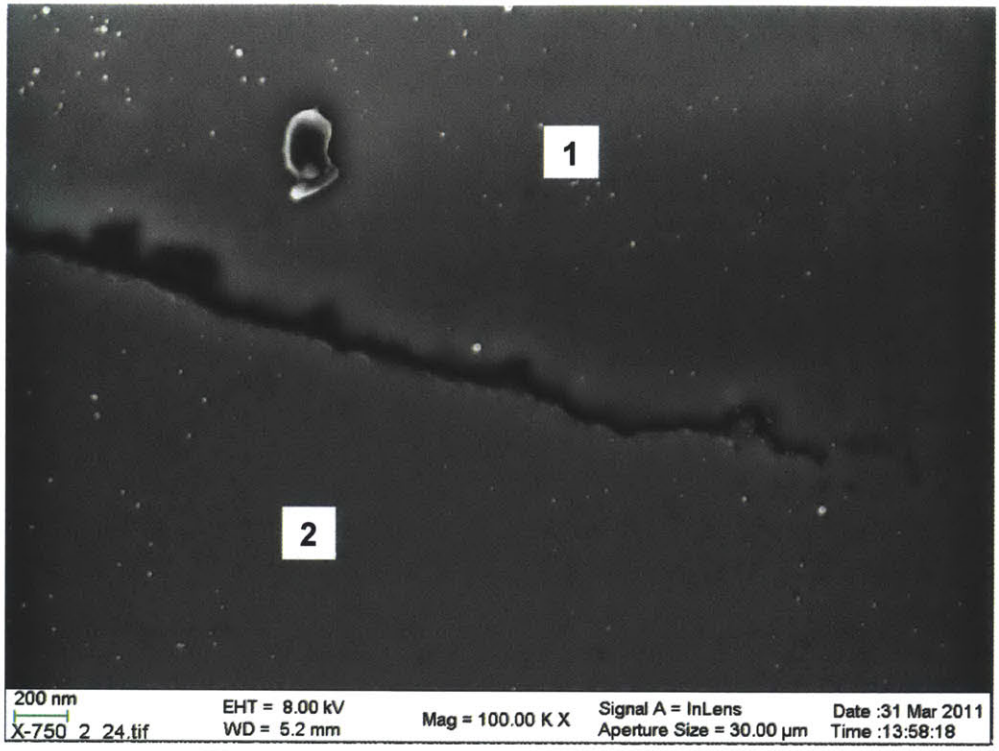

Figure 6-9: Cracking along $M_{23}C_6$ type boundary

Although the fracture surface clearly shows that intergranular cracking is the predominant mode of fracture, small regions of transgranular fracture account for a small fraction of the cracking process. In addition to the secondary transgranular cracking, larger scale transgranular cracking also occurs as a primary cracking mechanism. Transgranular cracking is typically surrounded by intergranular cracking regions. This phenomenon is shown in Figure 6-10 and Figure 6-11. Figure 6-10 shows a micrograph of the fracture surface with both trans- and intergranular cracking, and Figure 6-11 is a cross-section of transgranular cracking occurring between regions of intergranular cracking.

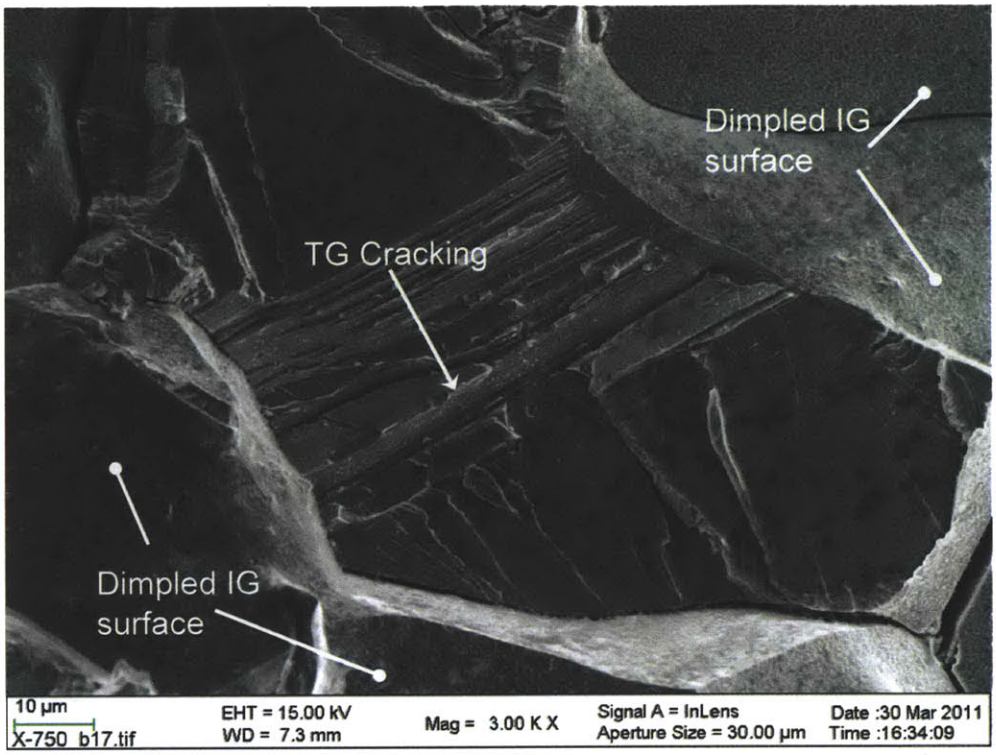

Figure 6-10: Localized transgranular cracking between intergranular regions

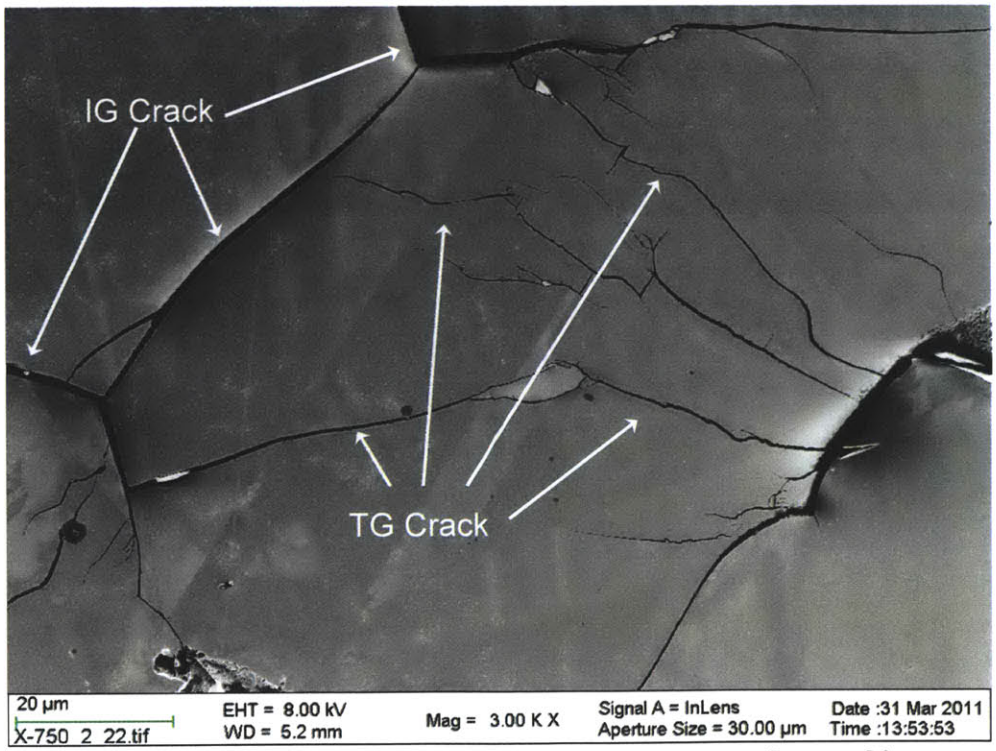

Figure 6-11: Cross-sectional view of localized transgranular cracking

6.2 Slip Dissolution/Oxidation Model

The slip dissolution/oxidation model for SCC is based on the film rupture and repassivation process. This theory (film rupture) was first postulated by Logan in 1952.[7] Other names for this phenomenon are active path dissolution, stress/strain enhanced dissolution, and surface film rupture dissolution. The slip dissolution mechanism has been widely studied, and there are varying viewpoints concerning the driving mechanisms surrounding the central slip dissolution theory.[8-12]

The basic premise behind this model is that a slip step forms at the crack tip and ruptures the protective surface film via shear stress. This process is shown in Figure 6-12 with planar slip (shown by planar dislocation movement) resulting in slip-steps inducing film rupture on the surface. When the oxide is disturbed such that sufficient electrolyte access to the bare metal occurs, anodic dissolution occurs on the bare metal surface. It is also possible for the associated cathodic process to result in the production of hydrogen which can enter the metal at the crack tip. The metal dissolution/oxidation during repassivation determines the crack extension. Thus, this model is a stress/strain initiated and electrochemically driven process.

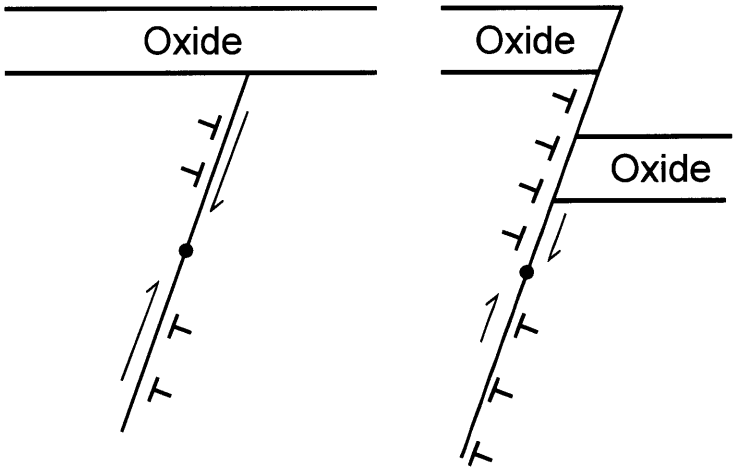

Figure 6-12: Crack tip film rupture schematic

The slip dissolution mechanism is based on the Faradaic relationship between the surface oxidation charge density and the amount of metal transformed from the metallic to the oxidized

state.[2] Using Faraday's Law, the crack propagation rate can be predicted by Equation (1) and the process is shown schematically in Figure 6-13:

$$\overline{V_t} = \frac{M}{z\rho F}\frac{Q_f}{\varepsilon_f}\dot{\varepsilon}_{ct}, \tag{1}$$

where:

Q_f = oxidation charge density passed between film rupture events

$\dot{\varepsilon}_{ct}$ = crack tip strain rate

M, ρ = atomic weight and density, respectively, of the crack tip metal

F = Faraday's constant (96,500 C/mol)

z = number of electrons involved in the overall oxidation of a metal atom

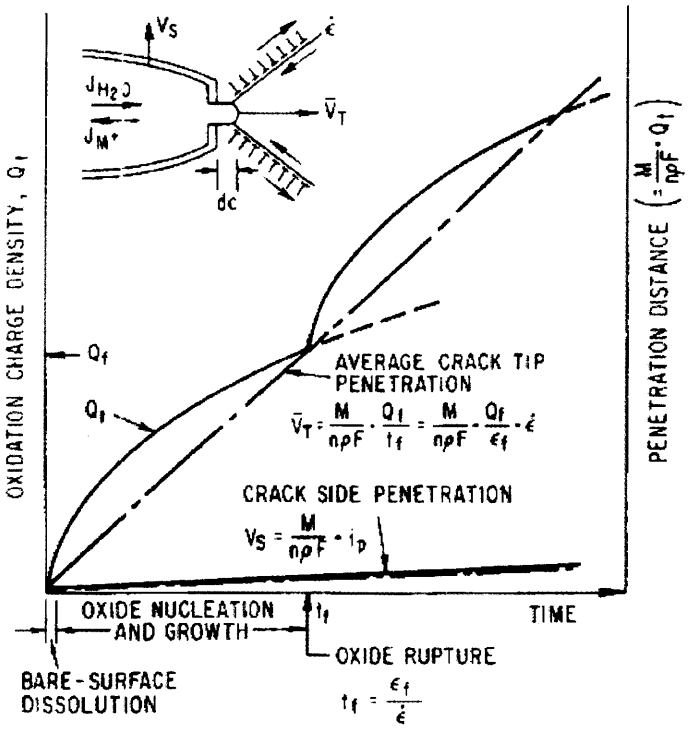

Figure 6-13: Slip dissolution/oxidation mechanism [13]

The oxidation rate is dependent upon the kinetics that controls crack tip repassivation. Equation (1) can be reformulated to the following expression:

$$\overline{V_t} = A\left(\dot{\varepsilon}_{ct}\right)^n, \tag{2}$$

where:

A, n = constants that depend on material and environment and are related to the oxidation reaction rates in the specific crack tip/environment system [14]

The dissolution rate is directly related to the dissolution current density, i_o, for a short time, t_o, immediately following the film rupture event. The dissolution current decays during repassivation. This relationship is shown in Equation (3):

$$i_t = i_o\left(\frac{t}{t_o}\right)^{-n}, \tag{3}$$

where:

i_t, i_o = current density at t, exchange current density, respectively

t, t_o = elapsed time, repassivation time, respectively

The strain, film rupture, dissolution, repassivation series of events is very quick and it is concluded once the repassivation process inhibits additional metal dissolution. Most engineering alloys (e.g. stainless steels and nickel alloys in most applications) repassivate quickly. The slip dissolution process is hypothesized to be constantly occurring at the crack front, and the periodicity of oxide rupture will be higher than the repassivation time. Thus, overall crack propagation rate can be obtained by integrating equation (3), resulting in equation (4):

$$\overline{V_t} = \frac{M}{z\rho F}\frac{i_o t_o^n}{(1-n)}\dot{\varepsilon}_{ct}, \tag{4}$$

The model based on film rupture and repassivation can be used to qualitatively describe SCC in certain alloy systems. However, these models are not a correct theoretical description and therefore cannot be recognized as a true model. The main inconsistency in the film-rupture model is that it fails to take the role of external stresses into account, which supplies the crack tip strain rate. Together, these are the driving forces for surface oxide rupture. The model further

fail to account for contributions of mechanical-chemical effects in dissolution acceleration.[15-16] The terms i_o and $\dot{\varepsilon}_{ct}$ indirectly take the mechanical-chemical effects into account since, while they are real valuables, the actual measurement is impossible, so they become adjustable parameters. For example, i_o, cannot be measured for the exact environment at the crack tip because the exact environment is unknown.

The total amount of metal dissolution is directly dependent on the rate of oxide repassivation. The interaction of the metal and environment determine the rate of repassivation. If repassivation occurs very quickly, little base metal reacts with the electrolyte (small incremental crack extension), but the crack tip remains sharp. If a metal takes a long time to repassivate, much metal may be lost. A blunt crack may form if the anodic dissolution occurs on the crack flanks in addition to the tip. If the dissolution current at the tip is not much greater than the crack flanks then crack blunting will occur. An intermediate repassivation rate may be the most detrimental because it undergoes a medium crack extension, but the crack remains sharp, which keeps the stress intensity high and favors further crack growth.

Further description of the ongoing processes during slip-oxidation repassivation is described here in a seven-step process, initially presented by Jones [17] for transgranular cracking:

1. Film rupture: When the metal is strained, dislocations travel on preferential slip planes. When a dislocation reaches the metal/oxide interface, it will fracture the oxide due to applied shear stress. The oxide cleaves and exposes fresh metal to the electrolyte.

2. Repassivation: This occurs on a varying timescale and is dependent upon the electrolyte and base metal. Repassivation occurs by oxidizing fresh metal by the oxidants in the electrolyte. Until the metal has reestablished the protective oxide, base metal will be lost via dissolution, thus extending the crack.

3. Anodic dissolution: This occurs at the fresh metal between the film rupture sites. If anodic dissolution is allowed to continue it will ultimately blunt the crack. If repassivation occurs quickly (e.g. anodic dissolution occurs over a short period of time) the crack tip will remain sharp, but crack growth will only be a small increment.

4. Vacancy formation: Vacancies form at the ruptured sites from anodic dissolution. The location of these vacancies is dependent upon the local microstructure. This can result in

5. Divacancy formation: Saturation of vacancies at the dissolution locations will cause vacancies to diffuse into critical lattice sites. Agglomeration of vacancies can lead to divacancy formation.

6. Initiation of surface cracks: This occurs on close packed planes with enhanced slip due to vacancy or divacancy agglomeration.

7. Brittle-like crack propagation: This occurs after crack initiation and under plane-strain conditions. Cleavage fracture propagates due to accumulation of divacancies on prismatic plans, which results in transgranular cracking.

The cycle is repeated on film free brittle fracture surfaces, omitting the initiation step no. 6, as a crack continues to grow.

6.2.1 Application of Slip Dissolution/Oxidation to SCC of Alloy X-750

The fracture characteristics for the environmental conditions in this work exhibit many clear signs of slip dissolution/oxidation. The formation of oxides (primarily a nickel-chromium spinel) occurs as bare metal is continuously exposed to the aqueous environment. Examining the main and secondary cracks from the fracture surface as well as the cross-sectional crack path and orientation, it is evident that some oxidation is occurring. Some aspects of the slip-dissolution/oxidation model are observed within each of SCC models discussed in this chapter, such as the effect of vacancy formation and diffusion. However, it is clear that other mechanisms are active as a part of the alloy X-750 cracking process that are not adequately addressed by the slip dissolution/oxidation process, such as how oxygen is penetrating ahead of the active SCC crack tip. However, it is uncertain whether the slip dissolution model is the primary driver for crack propagation or only a subsequent effect of oxidation once fracture has occurred.

Figure 6-14 shows that the dissolution is most severe for cracking that propagates along boundaries with $M_{23}C_6$ carbides present compared to the crystallographic slip driven fracture on twin or highly-coherent grain boundaries. This can be attributed to the tortuous path the crack is taking adjacent to the grain boundary carbides. For a given forward distance of crack advance,

more fresh metal will be exposed and oxidized when cracking occurs adjacent to the grain boundary carbides than for crack propagation along a more coherent boundary. Additional crystallographic features are visible in Figure 6-14 that show how the planes are disrupted approximately 200 - 250 nm adjacent to the grain boundary with $M_{23}C_6$ carbides, but the plane features continue unperturbed to the coherent grain boundary. The γ' denuded zone adjacent to the $M_{23}C_6$ grain boundaries contribute to this effect (there is no γ' denuded zone adjacent to the coherent boundaries). Figure 6-15 shows the crack interacting with a Nb-carbide and continuing nearly undisturbed, which is further evidence that an active dissolution mechanism is occurring at the crack front and that the Nb-carbides contribute little to the SCC susceptibility of the alloy.

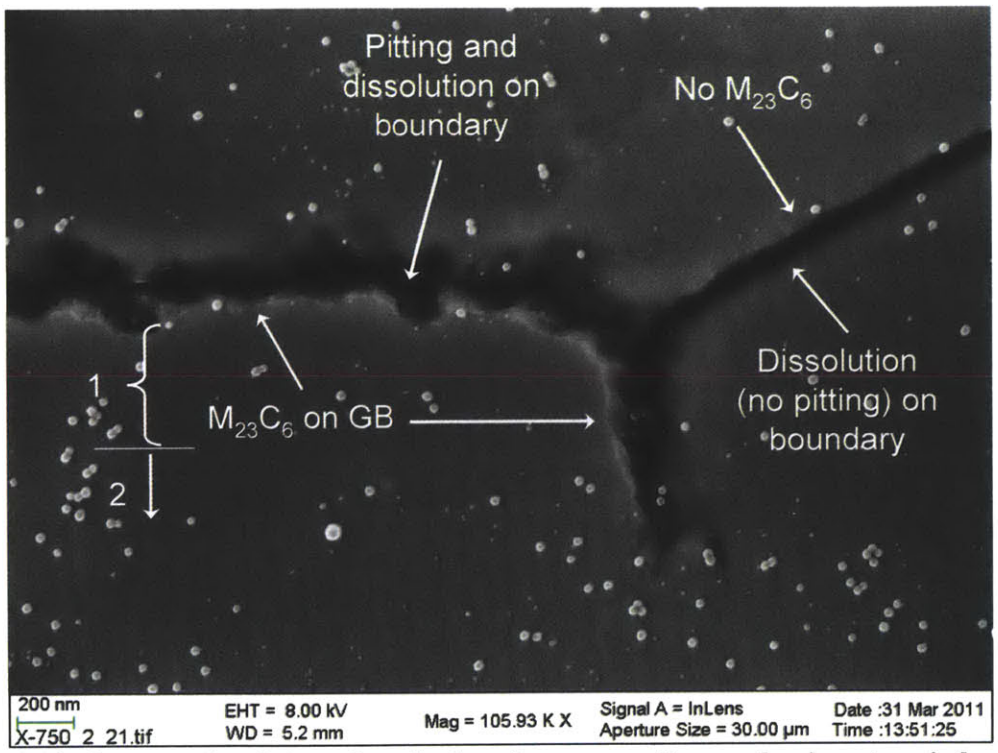

Figure 6-14: Cross-sectional view of crack changing propagation mechanism at grain boundary junction (transitioning from $M_{23}C_6$ to coherent boundary)

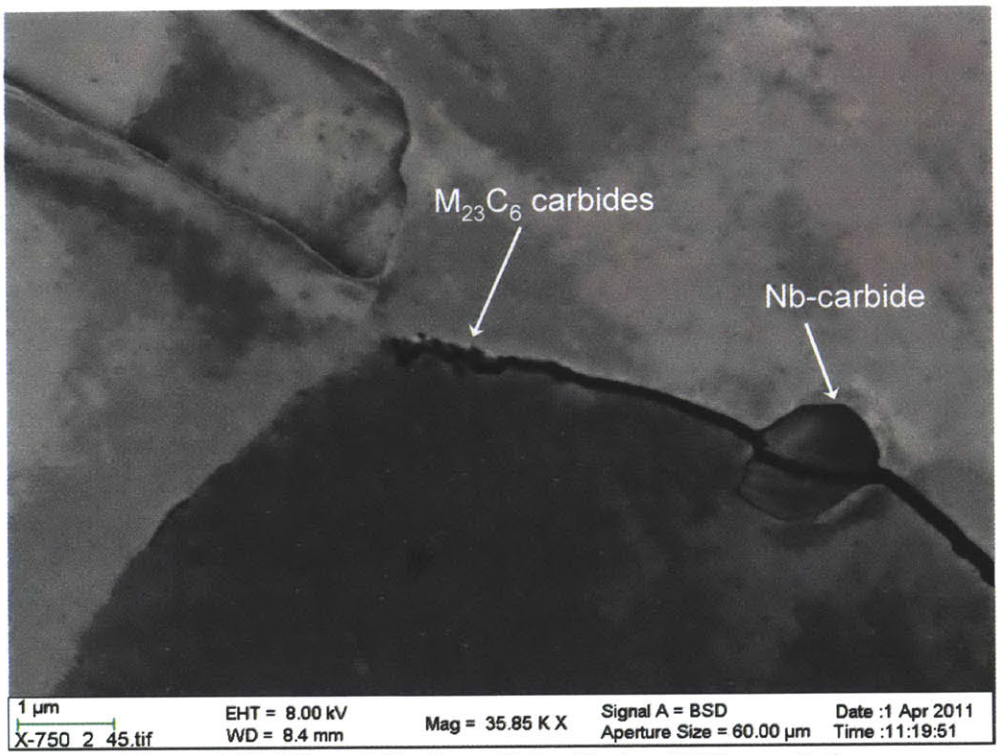

Figure 6-15: Nb-carbides have little effect on SCC morphology

The slip-dissolution/oxidation mechanism may also contribute to vacancy accumulation at and ahead of the crack tip as vacancies are produced as a product of dissolution.[17] These vacancies will diffuse ahead of the crack as they are driven by a negative vacancy concentration gradient and towards the region of higher stress (this is more completely covered in Section 6.5). These vacancies can agglomerate ahead of the crack at the grain boundary carbide/matrix interface, which eventually leads to fracture at the interface would result in the observed crack morphology. The oxidation step produces a nickel-chromium spinel oxide. Chromium is available from the matrix at the crack tip and immediate crack walls and also from reaction with the $Cr_{23}C_6$ carbides. Additionally, $Cr_{23}C_6$ or any other Cr-carbide will react with water to form Cr_2O_3 and either H_2 or CH_4. No dissolution will occur. Nickel is widely available from the matrix as it is the most plentiful element in the alloy.

Void initiation in alloy X-750 is also manifested by the separation of the interface between the carbides and the FCC matrix. The earliest model to describe this phenomenon was presented by Ashby [18] and was based on dislocation loops resulting in tensile stresses at the particle-matrix interface. It was hypothesized that for void initiation, the strain generated dislocation loops created a local stress concentrator for mechanical-induced separation. This is a potential model

for the observed cracking along the grain boundary carbides, but not necessarily along the twin or highly-coherent boundaries. However, the local stress would be from dislocation pile-ups and not necessarily loops.

The slip-dissolution/oxidation model also could account for the regions of brittle-like fracture with localized regions of plastic deformation. The processes outlined above account for fracture on planes where slip and film rupture occur. It is assumed that the brittle-like fracture occurred first, then when the remaining ligaments of metal exceeded the fracture toughness the crack propagated and resulted in plastic deformation, as evidenced by the plastic fracture features on the crack surface.

The film-rupture model has been proposed as a driving mechanism for SCC in alloy X-750.[19] Post-crack characterization of AH treated material showed that oxidation was taking place at the crack tip as a result of exposure to an LWR environment. The crack contained oxides different from those outside and these differences suggested non-uniformity in solubility and repassivation kinetics (selective oxidation during repassivation). These features suggest an oxide fracture/oxidation mechanism for crack propagation, but not one associated with slip at the crack tip.

6.3 Corrosion-Deformation Interaction Model

The corrosion-deformation interaction (CDI) model is one that describes pseudo-intergranular cracking. This model was developed by Magnin *et al.* [3] based on observations from testing alloy 600 in aqueous conditions. The premise behind this model is that the crack advances on slip planes while it closely follows the direction of the grain boundaries, as shown in Figure 6-16. During slip, fresh metal is exposed and subsequently oxidizes (during anodic dissolution). The crack path will exhibit predominantly intergranular cracking surface with zig-zag fracture paths in localized regions on the surface. It is important to note here that CDI is only reported for localized pseudo-intergranular cracking on an intergranular fracture surface. This model explains the localized slip-step cracking phenomena. The exact location of the crack with respect to the grain boundaries will be addressed in detail.

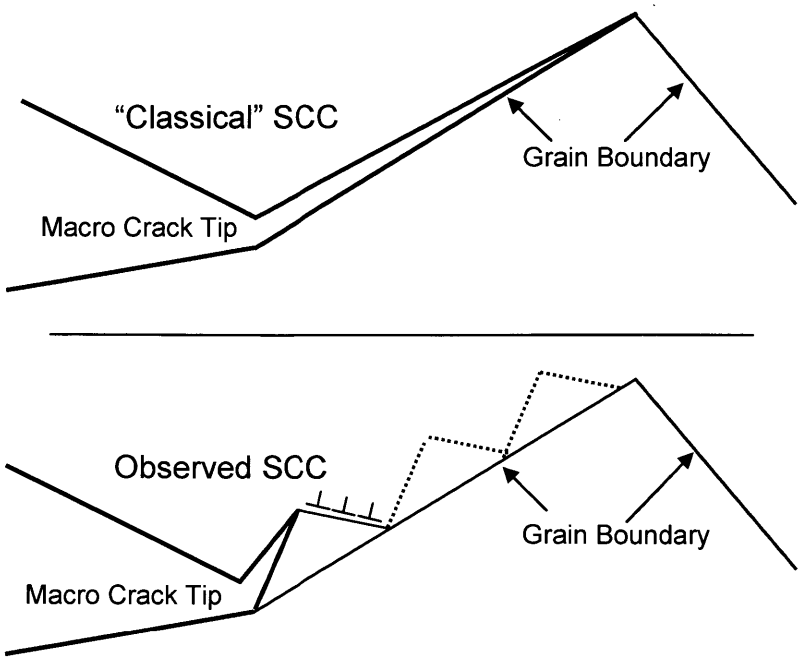

Figure 6-16: Macro SCC propagation method in alloy 600 [3]

This model of crack propagation is focused on the micro-fracture scale (several μm length scale), not the nano-scale which is focused on atomic interactions at the crack tip. This model is directly pertinent to alloy X-750 under the test conditions in this work. However, this model is unable to provide a full description of the active SCC mechanisms observed in this work.

The proposed event timeline is as follows [3]:

1. Localized anodic dissolution and hydrogen absorption on {111} slip planes takes place at the crack tip within the vicinity of the grain boundary. (Dissolution can also take place on the grain boundary).
2. Slip-step formation is then promoted by the localized dissolution. This will favor the motion of the corresponding glide dislocations and their emission by stress concentration and easier shearing due to hydrogen absorption on the {111} slip planes (and perhaps to vacancy formation related to dissolution). Thus, as for transgranular SCC, the role of corrosion (dissolution and hydrogen absorption) is essential but indirect. It induces a local enhancement of plasticity. It must be also noted that the role of absorption (of H for instance) is similar to the role of dissolution to enhance the local plasticity on {111} slip

3. The dislocations emitted from the slip steps and the corresponding crack will form dislocation pile-ups against the transgranular precipitates (or dislocation bundles) in the vicinity of the grain boundary. The stress relaxation from these precipitates is prevented by the initial hardening due to the applied load. Thus, as for TGSCC, two regions must be considered: a small region with enhanced plasticity and a larger one which has been hardened.
4. The microcrack formation at an obstacle is then possible in two ways as shown by:
    a. Either the fracture occurs on {111} microfacets by decohesion due to stress concentration and hydrogen absorption.
    b. Or the fracture, related to the dislocation pile-up formation, takes place on the grain boundary itself according to its orientation with regard to the main stress axis.

    The first case corresponds to a pseudo-intergranular cracking and the second one to a true intergranular cracking. But the cause of cracking is identical for both cases.

5. The pseudo- and true-intergranular fractures can be discontinuous (by a zig-zag on {111} microfacets for pseudo-intergranular cracking) as demonstrated by the following calculation. Equation (5) describes the dislocation interactions:

$$F_i^{FR} = \sigma_a b_i - \sigma_0 b_i + \frac{\hat{\mu}}{2\pi}\sum_{j\neq i} b_i b_j \frac{1}{x_i - x_j}$$

$$F_i^{MC} = \frac{K_a b_i}{\sqrt{2\pi x_i}} - \sigma_0 b_i + \frac{\hat{\mu}}{2\pi}\sum_{j\neq i} b_i b_j \frac{1}{x_i - x_j}\sqrt{\frac{x_j}{x_i}}, \qquad (5)$$

where:

F = force per unit length on a dislocation located at a distance x_i

FR =Frank-Read dislocation source

MC = microcrack dislocation source

μ = μ (shear modulus) for screw dislocations, and

μ = $\mu/(1-\nu)$ for edge dislocations

σ_a = applied stress

σ_0 = critical stress that dislocations must overcome to move

K_a = applied stress intensity factor

b = Burgers vector

For the atomically sharp crack, $K_a = \sigma_a\sqrt{2\pi a}$, where "a" is one quarter of the main crack length. Equation (5) can be simplified by making the units of distance and stress to be respectively **b** and $\mu/2\pi$, as shown by Equation (6) to put the force into units of stress:

$$\sigma_i^{FR} = \sigma_a - \sigma_0 + \sum_{j \neq i} \frac{1}{x_i - x_j}$$

$$\sigma_i^{MC} = \sigma_a\sqrt{\frac{a}{r_i}} - \sigma_0 + \sum_{j \neq i} \frac{1}{x_i - x_j}\sqrt{\frac{x_j}{x_i}}, \qquad (6)$$

This system can be solved using a Hilbert transformation as shown elsewhere [20]. Dislocations are assumed to be nucleated at a distance r_0 ahead of the sources ($r_0 << R$) as soon as the local stress is positive, as done by Hirsch *et al.* [21] The respective load densities versus the position *x* from the source are provided in Equation (7):

$$n^{FR}(x) = 2\frac{\sigma_a - \sigma_0}{\hat{\mu}b}\sqrt{\frac{x - r_0}{R - x}}$$

$$n^{MC}(x) = 2\frac{\sigma_a\sqrt{\frac{a}{x}} - \sigma_0}{\hat{\mu}b}\sqrt{\frac{x - r_0}{R - x}}, \qquad (7)$$

where:

n(x) = load density as function of position, *x*

The total number of dislocation pile-ups is described in Equation (8):

$$N^{FR}(x) = (\sigma_a - \sigma_0)\frac{R}{2}$$

$$N^{MC}(x)=\left(\sigma_a \frac{4}{\pi}\sqrt{\frac{a}{R}}-\sigma_0\right)\frac{R}{2}, \tag{8}$$

where:

$N(x)$ = total number of dislocation pileups as a function of distance, x

The shear stress on the dislocation at the tip of the pile up is due to the applied stress and the pile-up and can be derived from (8) and shown in Equation (9).[22]

$$\sigma^{FR}(x)=\frac{\pi}{4}N(\sigma_a-\sigma_0)$$

$$\sigma^{MC}(x)=\frac{\pi}{4}N\sigma_a\sqrt{\frac{a}{R}}\ , \tag{9}$$

where:

σ = shear stress on the dislocation at the tip of the dislocation pile

The classical relation defining the stress intensity factor of an atomically sharp microcrack can be applied to pile-ups, with z > R, to compare the form of their stress gradient, as shown in Equation (10):

$$K_{pile-up}=\lim_{z\to R}\sqrt{2\pi(z-R)}\sigma(z)$$

$$K_{pile-up}^{FR}=(\sigma_a-\sigma_0)\sqrt{2\pi R}$$

$$K_{pile-up}^{MC}\approx\sigma_a\sqrt{2\pi a}=K_{crack} \tag{10}$$

where:

K = effective stress intensity at the crack tip due to the applied stress and dislocation network

If σ_a is close to σ_0, strong pile-ups cannot exist in a homogeneous strain field (for a given value of R) and the stress on or around the pinned dislocation will not reach the critical value for cracking-induced fracture. If σ_a is much greater than σ_0, according to equations (9) and (10), it is seen that FR and MC pile-ups are equivalent when R=a, and thus MC pile-ups behave as FR pile-ups. However, when a/R becomes large, the effect of MC pile-ups is much greater than FR

pile-ups in the bulk material, making more probable the nucleation of microcracks. If adsorption decreases K_{IC} and the energy of cohesion on the {111} or {100} microfacets, then a microcracking is strongly favored for MC pile-ups in comparison to FR pile-ups. Subsequently, microcracking is widely observed on the alloy X-750 fracture surface and supports the above discussion for both the intergranular and transgranular cracking.

6.3.1 Application of Corrosion-Deformation Interaction to Alloy X-750

The adaptation of the CDI model for SCC is easily applied to site-specific fracture locations in alloy X-750. It is important to note here that the CDI mechanism active in alloy X-750 is only relevant for a crack propagating between two grains of high-coherency and some transgranular cracking, but not along the grain boundaries with $M_{23}C_6$ carbides. Figure 6-17 shows how the SCC crack clearly changed its propagation plane as it transitioned between a grain boundary with $M_{23}C_6$ carbides and started along a high-coherency boundary.

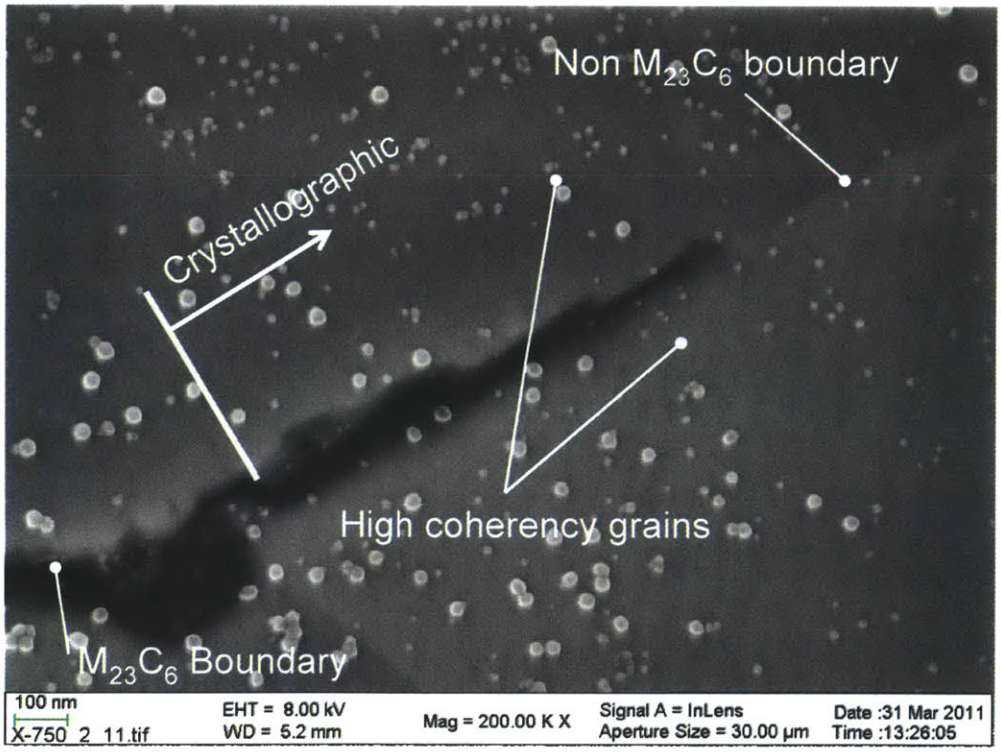

Figure 6-17: SEM micrograph showing crystallographic slip and crack propagation along coherent grain boundary (notice no grain boundary carbides and the crystallographic planes up-to and across the coherent grain boundary)

The CDI model was developed for alloy 600, which can have similar grain boundary characteristics as alloy X-750, namely the semi-continuous $M_{23}C_6$ grain boundary carbide

network (alloy 600 also has M_7C_3 carbides on grain boundary, but predominantly $M_{23}C_6$). However, one important difference is that alloy X-750 is alloyed with aluminum and titanium, which precipitates to form the intermetallic γ' phase. A γ' denuded zone exists directly adjacent to the grain boundaries and is approximately 50-100 nm wide, which is dependent upon the type of carbide immediately adjacent to the denuded zone large carbides will have a larger denuded zone). The penetration depth of the zig-zag crack path is on the same length scale as the width of the γ' denuded zone. When a slip-step advances it may be prevented from further slip when it encounters the high energy barrier of γ'. This is a possible explanation for the smaller slip-step zig-zags observed in alloy X-750 as compared to alloy 600.

Figure 6-18 shows TEM micrographs of Alloy X-750 in the HOA condition (over aged at 760 °C for 100 h, compared to the HTH aged at 704 °C for 20 h) which clearly shows the $M_{23}C_6$ grain boundary carbides, γ', and a narrow γ' denuded zone.[23] Alloy X-750 in the HOA condition is shown here instead of HTH because the features are more easily identified. The relevant feature in Figure 6-18 to this discussion is the narrow γ' denuded zone. Although the TEM micrographs correspond to the HOA and not the HTH condition, the distribution of γ' is the same, but the size of γ' is different. HOA treatment results in γ' coarsening compared to the small γ' size (10-12 nm diameter) in HTH. The γ' denuded zone in alloy X-750 (HTH or HOA) is up to 200 nm in the periphery of NbC (lower image in Figure 6-18) and as little as 10s of nanometers near typical $M_{23}C_6$ carbides. The average γ' denuded zone width is around 50-75 nm. Moreover, Mills [24] reported that the γ'denuded zone is not actually denuded, but denuded of coarse gamma prime. Fine γ' is present up to the grain boundaries.

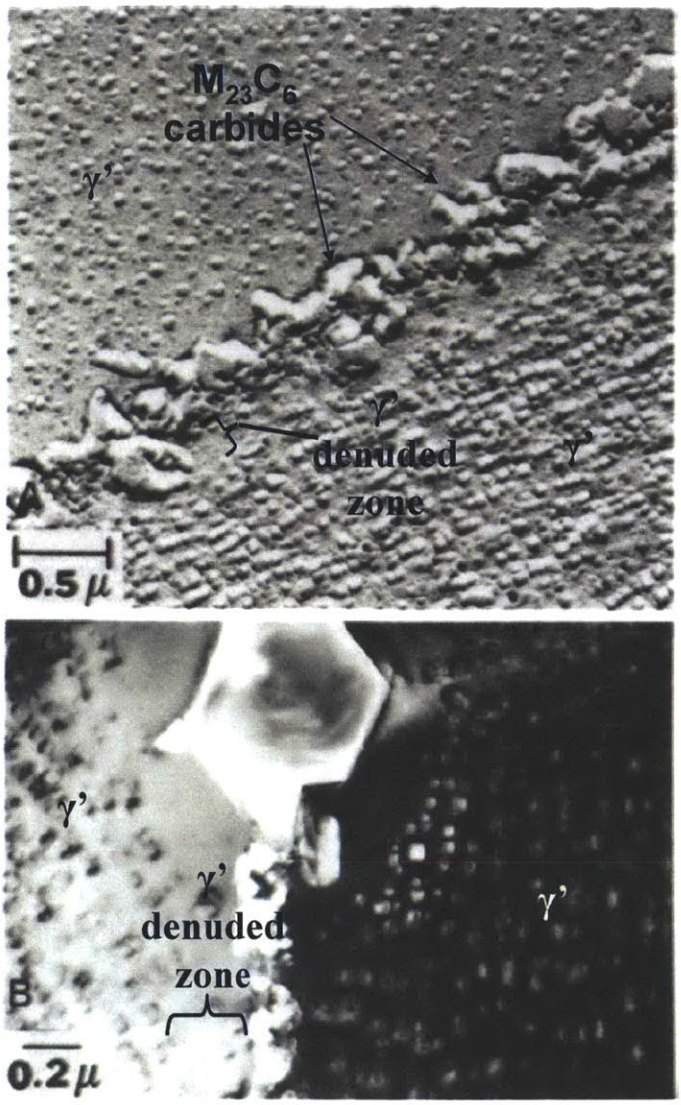

Figure 6-18: TEM micrographs of alloy X-750 in the HOA condition [24]

Figure 6-19 shows SEM micrographs of the crack tip in alloy X-750 with the zig-zag pathway of the furthest 5-10 μm of the crack path. Figure 6-20 shows this same zig-zag morphology on the fracture surface (arrows indicate slip steps). This phenomenon was observed on several crack fronts in several locations. This zig-zag cracking has been previously reported for alloy 600, which was referred to as pseudo-intergranular cracking along the grain boundary.[25] The crack transitions between trans- and intergranular cracking, while propagating near a grain boundary. Figure 6-21 shows an adaptation of the CDI model for the γ' alloy X-750. Constraint of the crack path in alloy X-750 is largely controlled by the intragranular γ' phase. The crack will propagate in close proximity to the grain boundary and zig-zag between the grain boundary and

intragranular γ' phase, which results in a pseudo-intergranular propagation mode. The transgranular cracking can also be described with the CDI model. Transgranular cracking, both as main and secondary, shows localized regions of the "zig-zag" pathway, which is cracking along the {111} planes. The regions of transgranular planar (smooth surface) cracking corresponds to cracking on the {110} planes.

Fracture can occur on grain boundaries because of pile-up formation depending on the relative orientations of the grain boundary and the {111} planes with regard to the main stress axis. Small grain materials, such as alloy X-750 in the AH heat treatment, are expected to undergo true intergranular fracture. Large materials, such as the HTH treatment of alloy X750 tested in this work, the pseudo-intergranular fracture is more frequent because of the dislocation sinks at grain boundaries are farther apart.

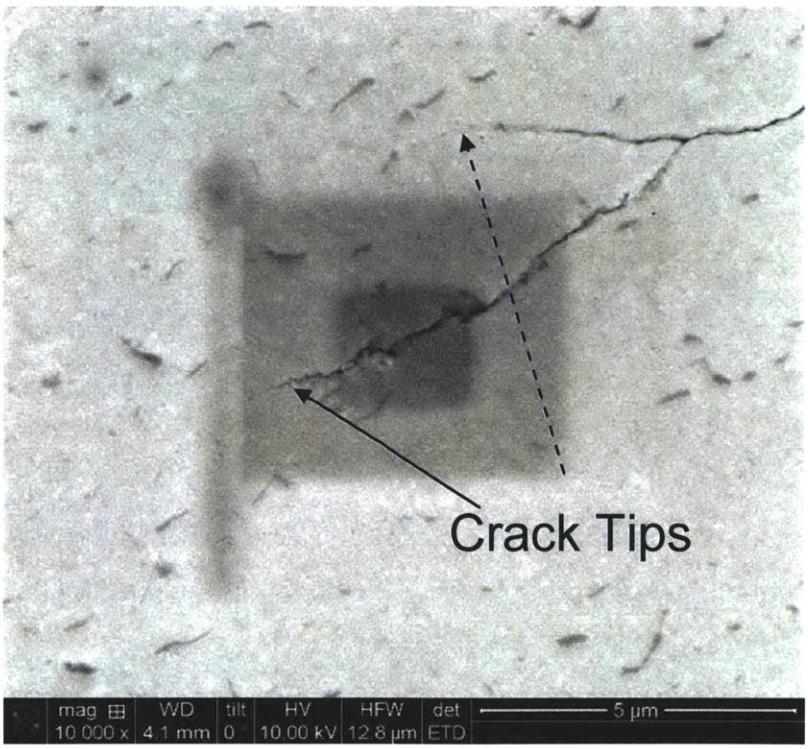

Figure 6-19: Crack tips exhibiting zig-zag propagation pathway (rectangular dark regions are contamination from the electron beam in the SEM)

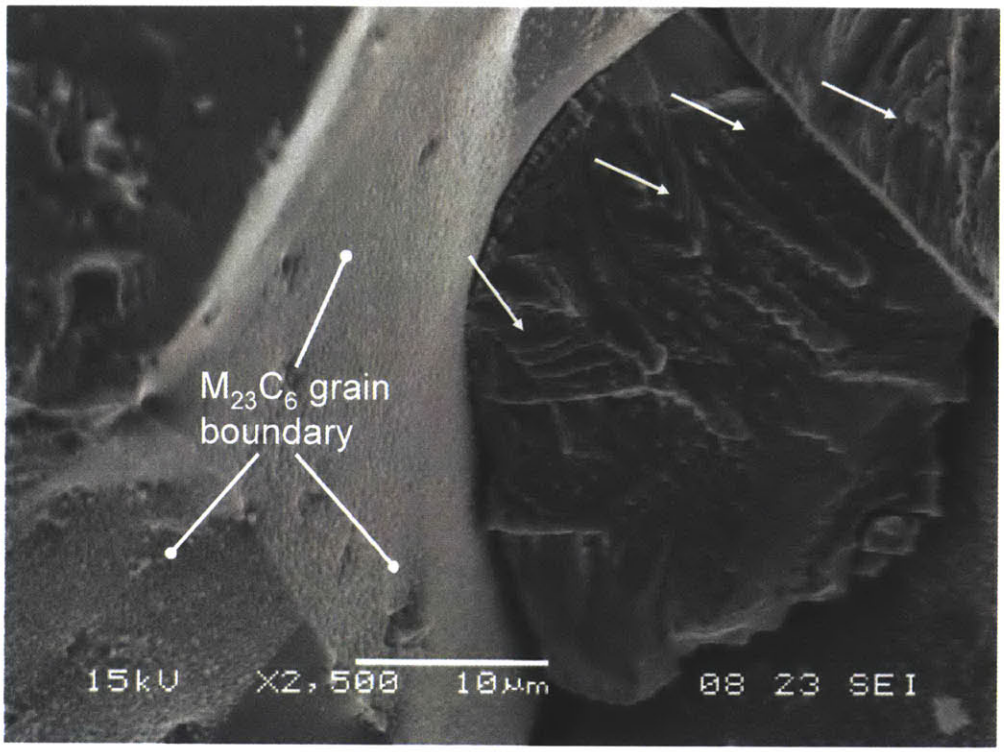

Figure 6-20: Fracture surface showing zig-zag pathway (arrows indicate slip steps)

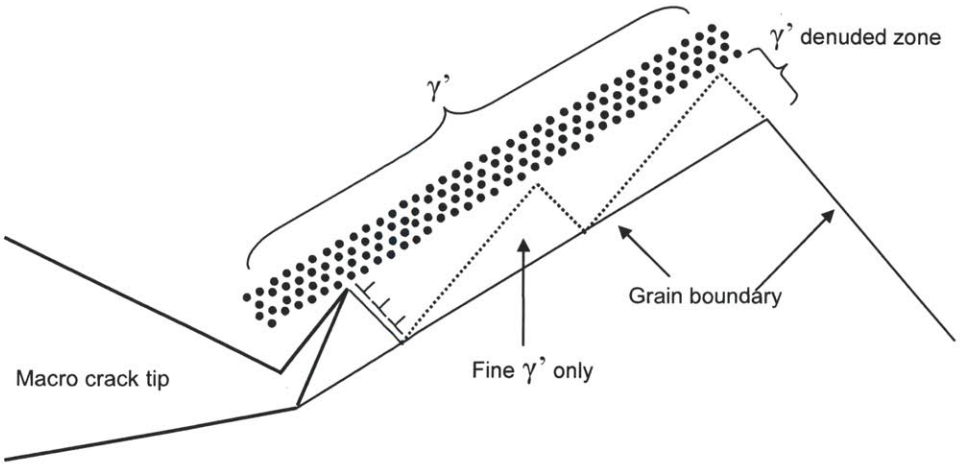

Figure 6-21: Possible SCC propagation mechanism in alloy X-750 on highly-coherent or twin boundaries (γ' not drawn to scale)

The discussion relevant to the hydrogen effects on the CDI model was intentionally omitted from this section. Hydrogen plays a role in each SCC model and these effects are addressed at the end of this chapter.

6.4 Internal Oxidation Model

The internal oxidation model is based on oxygen diffusion ahead of an active crack, resulting in matrix embrittlement and was first presented by Scott.[4,26] The internal oxidation theory is a solid state (diffusion) driven corrosion process in which the less noble alloying elements oxidize while leaving the base material largely unaffected.[27] For example, in nickel alloys, chromium and iron are the elements susceptible to oxidation. This theory is largely applied to nickel-base alloys in atmospheres with low oxygen partial pressures, such as the alloy/environment system covered in this work. Low oxygen partial pressures satisfy the thermodynamics to enable the solvent metal (e.g. nickel) remain unoxidized while oxidizing the minor alloying elements (e.g. chromium and iron). In this work it will be shown that chromium oxidizes as a protective film and locally ahead of the crack tip. Iron largely reacts to form oxide within the crack wake and does not contribute to crack tip oxide.

Much of the criticism of the internal oxidation theory is based upon the known diffusion coefficients of oxygen in nickel-based alloys. Moreover, any oxidation driven crack growth phenomenon is very dependent on heat treatment, which establishes the structure of grains and grain boundaries and largely controls the oxygen diffusion pathways and traps. Grain boundaries provide a region of mismatch that aid in enhanced oxygen diffusion [28], and the presence of grain boundary carbides can serve as traps. Balance between the grain boundary features that either enhance or retard oxygen diffusion determines the transport efficiency; grain boundaries are typically regions for enhanced oxygen diffusion. The kinetics of internal oxidation are too slow to be the only mechanism contributing to SCC. However, internal oxidation combined with another mechanism, such as vacancy migration provide a strong argument for the necessary diffusion path to account for internal oxidation as the driver of crack propagation.

Testing alloy X-750 in hydrogen water chemistry in BWRs is closely analogous to alloy 600 in PWRs. The electrochemical potential of the sample in HWC is in close proximity to the Ni/NiO

equilibrium, as are the conditions in primary water PWRs. Much work has been focused on SCC in the region of the Ni/NiO transition, and it was documented that maximum SCC susceptibility is at the Ni/NiO equilibrium, but decreases at both higher and lower potentials.[26,29] The SCC susceptibility is high at the Ni/NiO equilibrium and decreases at higher and lower potentials. This is an indication that oxidation is an active mechanism for SCC. Iron and chromium are less noble than nickel and are able to oxidize at potentials lower than the Ni/NiO equilibrium and are susceptible to internal oxidation. Hydrogen is also produced in the corrosion process. Hydrogen may not participate in the oxidation process, but may migrate into the metal and have a role in increasing the SCC susceptibility, but this effect may be limited to dislocation mechanics and is addressed at the end of this chapter. Moreover, due to the multiple effects simultaneously occurring during SCC, it is difficult to determine the effect hydrogen has on crack growth rates in high-temperature water. However, recent experimental results suggest that hydrogen does have a deleterious effect on the fracture toughness of a material in typical reactor operating temperatures.[30] Hydrogen embrittlement on mechanical properties [31] and SCC [1] in austenitic materials is typically a low-temperature phenomenon.

The role of hydrogen in this discussion is limited to the formation of bubbles ahead of the crack. Hydrogen has additional impacts on this, and the other theories, and is addressed in greater detail at the end of the chapter.

6.4.1 Internal Oxidation Kinetics

Grain boundary embrittlement in nickel and many nickel-base alloys can occur due to stresses induced by internal oxide, gas bubble formation, presence of embrittling elements, or by a layer of oxygen atoms along the grain boundary.[32] It is known that reacting carbon, oxygen, and hydrogen (each of these elements is present in alloy X-750) together will yield methane and water. In addition, direct reaction between carbon and hydrogen is possible but is less efficient and requires a higher temperature (>400 °C) in the presence of a nickel catalyst (e.g. nickel alloy). Reactions between CO or CO_2 and hydrogen are favored around 300 °C, which is the temperature range of interest in this work.[37]

Gas Bubble Kinetics

Gas bubbles have been detected just beyond the tips of stress corrosion cracks in alloys 600 and X-750.[33-35] Shewmon postulated that these bubbles were methane, which followed the reaction between hydrogen and dissolved carbon.* In this model, the growth of the gas bubbles ahead of the SCC crack tip is controlled by nickel diffusion and leads to the time-to-failure creep based equation (11):

$$t_f = \frac{0.12kT(2b)^3 h(\theta)}{D_b \delta \Omega (P+\sigma)}, \tag{11}$$

where:

k = Boltzmann's constant

T = absolute temperature

b = bubble spacing

$h(\theta)$ = function of bubble surface energy γ and angle θ between bubble surface and grain boundary

D_b = grain boundary self diffusion coefficient

δ = grain boundary thickness

Ω = atomic volume

P = internal gas pressure

σ = applied tensile stress

A bubble model was also presented by Wood and Kear [36] which was focused on helium bubble growth in irradiated stainless steels. This model was focused on the critical hydrostatic stress, σ_c, for unstable bubble growth:

$$\sigma_c = \frac{2}{3}\left(\frac{32\pi\gamma^3}{9n_o kT}\right)^{1/2} = \frac{4\gamma}{3R_c}, \tag{12}$$

* Note: this is for steam environments because this reaction is not favored at 300 °C. The thermodynamics for hydrogen and carbon to react and form methane is favorable at temperatures greater than 400 °C.

where:

γ = surface energy

n_o = gas content

R_c = critical radius

For a given stress, σ, the time for unstable bubble growth and failure of the bubble affected zone is given for the time required for the gas content to reach n_o. This expression is given by Equation (13):

$$t_f = \left(\frac{128}{81} \frac{\pi \gamma^3 C_b}{kTG} \right) \frac{1}{\sigma^2}, \tag{13}$$

where:

C_b = bubble area on gain boundary orthogonal to applied stress

G = gas generation rate per grain boundary unit area

Wood and Kear further presented an approximate relationship for bubble nucleation density, which is shown in Equation (14):

$$C_b \approx \left(\frac{8 \; z \; a \; G}{\pi^2 D_b \; \delta} \right)^{1/2}, \tag{14}$$

where:

z = number of sites explored per gas atom diffusion step

a = interatomic spacing ($\Omega^{1/3}$)

D_b = grain boundary diffusion coefficient

Combining Equations (13) and (14) yields:

$$t_f \approx \left[\frac{128}{81} \frac{\pi \gamma^3}{kT} \left(\frac{8 \; z \; a \; G}{\pi^2 D_b \; \delta} \right)^{1/2} \right] \frac{1}{\sigma^2} \tag{15}$$

Equation (15) can be modified to account that the gas generation rate, G, may depend on the diffusion of oxygen into the bulk or along the grain boundary by distance, x. These are second-order chemical reactions, and the in-depth analytical solution is described by Kofstad [27] and Roberts [37]. These interactions have been simplified and approximated by Equation (16) [4]:

$$G = \frac{1}{2}\frac{dn}{dt} = \frac{1}{2}\frac{D_o N_s}{X\ \Omega}, \tag{16}$$

where:

N_s = surface solubility (of oxygen)

D_o = oxygen grain boundary diffusion coefficient

Equations (15) and (16) can be combined to yield Equation (17) for the time to failure. The time to failure depends inversely on the oxygen diffusion along the grain boundary. Stress plays a strong role, and the time to failure is decreased by the square of the inverse of the applied tensile stress:

$$t_f \approx \left[\frac{512}{81}\frac{\gamma^3 a^2}{kT\ D_o}\left(\frac{z\ X}{\delta\ N_s}\right)^{1/2}\right]\frac{1}{\sigma^2} \tag{17}$$

Scott and LeCalvar presented predictions based on the above equations.[4] These calculations predict bubble spacing and internally applied stress due to bubble formation. Bubbles were predicted to range from 5 to 20 nm in diameter and could result in an applied stress up to 800 MPa. It was also noted that the time to reach unstable bubble formation is about one order of magnitude too low to accurately predict crack growth rates, and it was postulated that the discrepancy is rooted in the diffusion coefficient for oxygen.

The crack tip velocity (crack growth rate) can be calculated using the above equations. The result of the CGR derivation is presented in Equation (18) as a function of stress intensity at the crack tip, K_1,

$$x_p = \frac{1}{6\pi}\left(\frac{K_1}{\sigma_p}\right)^2, \tag{18}$$

where:

x_p = process zone radius, which is a fraction of the plain strain plastic zone

σ_p = stress contour that defines the plain strain plastic zone radius*

and the subsequent CGR is shown in Equation (19) and predicts that it is directly proportional to the stress intensity at the crack tip and the stress defining the contour of the plastic zone [4]:

$$\frac{dx}{dt} = \frac{x_p}{t_f} = \sigma_p K_1 \left(\frac{81\ kT\ D_o}{512\ \gamma^3\ a^2} \right) \left(\frac{\delta\ N_s}{6\ \pi\ z} \right)^{1/2} \tag{19}$$

It should be noted here that Equation (19) fails to account for any threshold stress levels (threshold K_1), which is an important concept. Moreover, much of the uncertainty of Equation (19) in correctly predicting the crack growth rate stems from the oxygen diffusion coefficient. Oxygen diffusion is a highly localized phenomenon and strongly depends on oxygen diffusion paths, traps such as grain boundary features [36], local precipitate density, and other crystallographic defects.

The above internal oxidation discussion was largely focused on oxygen diffusion with the possibility of generating internal stress due to bubble formation. Another important phenomenon associated with oxygen diffusion is internal oxidation. Internal oxidation was first proposed as a plausible mechanism of IGSCC in pressurized water reactors by Scott and Le Calvar in 1993.[4] These experiments were focused on IGSCC of alloy 600. The premise of this mechanism is that internal oxidation occurs when atomic oxygen dissolves into an alloy and oxidizes a more reactive alloying element than the base metal. Internal oxidation is well known as an active mechanism of high temperature (500-800 °C) gas cracking of nickel base alloys and more experimental proof is being accumulated which indicates that internal oxidation is an active SCC mechanism. Scott and LeCalvar postulated that internal oxidation is active at LWR temperatures, but little evidence has been presented because oxidation is much slower at 300 °C than at higher temperatures. Internal oxidation at crack tips in aqueous environments results in a competition for oxygen with other corrosion reactions at and near the crack tip. Moreover, the deaerated conditions at the crack tip result in no dissolved oxygen available for corrosion reactions, but H_2O is present. Secondary ion mass spectroscopy (SIMS) and analytical

* Note: This is not the equation for the plastic zone radius. The plastic zone radius uses the yield strength, σ_y.

transmission electron microscopy (ATEM) results have both suggested that oxygen penetration ahead of crack tips as feasible hypothesis of SCC.[38-40] Oxygen has been detected ahead of crack tips and along secondary grain boundaries. These regions are not in contact with aqueous solution and the oxygen can only have migrated ahead of the crack by solid state diffusion. NanoSIMS has provided higher resolution analysis of trace element segregation to grain boundaries (i.e. boron) and further validate the internal oxidation theory.[41-42]

Oxygen diffusion ahead of the crack without oxidation is described by Equation (20) [26]:

$$x = \left(\frac{2\ D_0 N_0 t}{V\ N_B} \right)^{1/2}, \qquad (20)$$

where:

x = distance of oxygen diffusion

V = valency ratio of oxygen to metal in oxide

N_B = mole fraction of oxidizing metal

Attempts have been made to use Equation (20) to predict the crack growth rate, *dx/dt*, but these predictions usually are two to three orders of magnitude smaller than experimentally measured rates for alloy 600. One of the assumptions for the predictions in Equation (20) is that all of the metal must be oxidized (e.g. Cr to Cr_2O_3) in order for the crack to advance. This is one shortcoming of this model because it solely relies on brittle fracture due to oxide formation. In reality, there could be a combination of brittle-like fracture of the oxidized regions and ductile rupture between these regions. The role of accurate oxygen diffusion coefficients arises again in the accuracy of this model. Either the oxygen diffusion coefficients must be higher than those used in the crack growth rate predictions or some other mechanism is contributing to the rate that is not included in the above expressions. It has been suggested that part of these discrepancies can be resolved if the oxygen diffuses along a possible metal/oxide interface which would result in higher diffusion rates.[43-44] The other option is oxygen diffusion along a grain boundary, which would result in higher diffusion rates. However, the important aspect of this theory is that oxygen is able to diffuse ahead of the crack along the boundary without being caught in traps or oxidizing with grain boundary carbides, which is common for $Cr_{23}C_6$ and other carbide species.

In secondary-side SCC of alloy 600, Scott reported that grain boundaries that intersected the intergranular crack were found to be oxidized at distances ranging from a few nanometers near the crack tip to several microns near the crack mouth. Although this was reported on secondary grain boundaries, this clearly showed that oxygen diffusion along the grain boundaries was occurring.[32-33,45] Grain boundary oxidation was also reported by Gendron [39] and Thomas [40] in PWR secondary side alloy 600 tubing. Oxidation was detected using SIMS and it was documented that oxygen was present along secondary grain boundaries, but no impurities. This clearly showed that oxygen was able to migrate along the grain boundary, but the impurities within the aqueous solution were confined to the main stress corrosion crack.

Oxidation was also reported to proceed along a few "finger" penetrations ahead of SCC crack tips. Bruemmer and Thomas [46] have used an analytical TEM (ATEM) to measure the chemistry and structure of a several crack tips in 300 series austenitic stainless steels from actual and simulated LWR environments. Figure 6-22 shows finger-like porous structures that were observed at the end of several crack tips which extended into the metal and beyond the corrosion-product oxide. The elongated pores in the 300 series stainless steel extend ahead of the physical crack tip and are independent from the porous oxide observed at the crack tip. The mechanism of penetration ahead of the SCC crack tip is unknown, but these features support an internal oxidation mechanism. The oxidation penetrations reported by Bruemmer and Thomas are not directly analogous to the corrosion tunnels observed in this work, but they are a similar phenomenon that strongly suggests that oxidation does occur ahead of some SCC cracks.

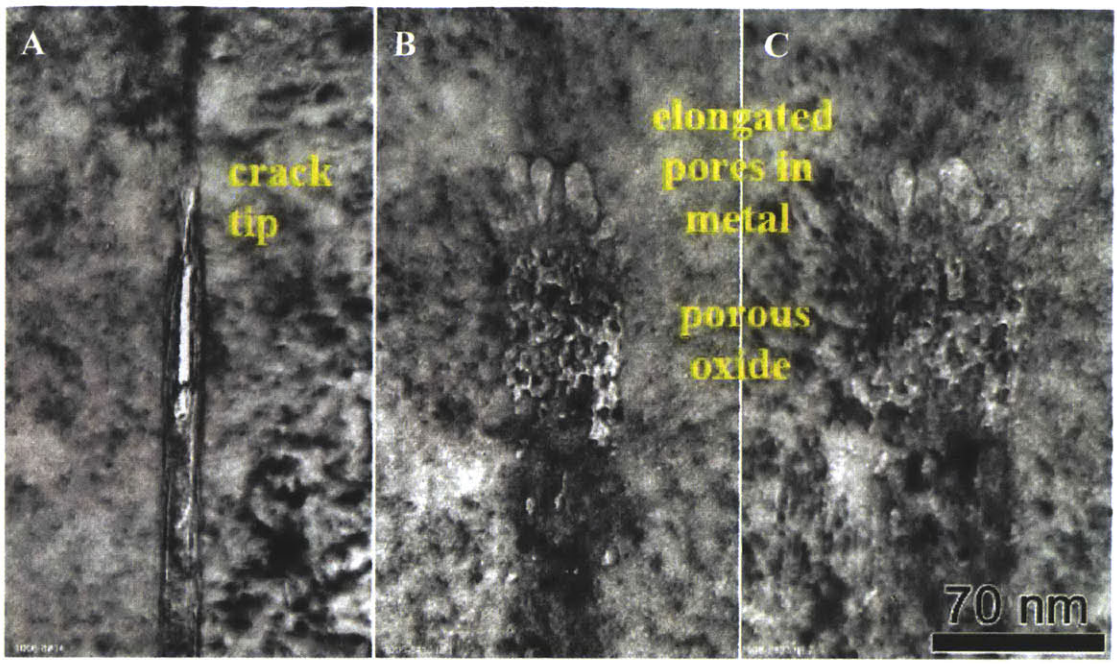

Figure 6-22: Crack tip shown at 3° tilt inclinations using underfocus TEM brightfield: (a) crack edge-on at 0°, (b) 30° inclination, (c) 45° inclination [46]

6.4.2 Application of Internal Oxidation Phenomenon to Alloy X-750

The internal oxidation phenomena, as presented by Scott and LeCalvar [4] and Shen and Shewmon[34] provide valuable insight to processes contributing to crack propagation in alloy X-750, but do not fully describe the overall processes. The applicable concepts of internal oxidation in relation to the observed experimental testing of alloy X-750 are discussed here.

The operating point of HWC in BWRs is in close proximity to the Ni/NiO equilibrium, which would favor internal oxidation as a plausible mechanism for SCC of alloy X-750. Moreover, the higher potential cracking in NWC would also favor internal oxidation as a plausible SCC mechanism because of the excess oxygen available in solution. It has been widely postulated that a SCC crack tip is deaerated and is close to the Ni/NiO equilibrium in nickel-based alloys. Thus, the crack tip is deaerated in both NWC and HWC and internal oxidation still occurs, albeit at a lower rate in HWC compared to NWC. One explanation of this phenomenon is the availability of oxygen at the crack tip. In NWC, the dissolved oxygen is approximately 200 ppb, and in HWC, dissolved oxygen is essentially non-existent (in the bulk solution). Oxygen is present at the crack tip in both environments but is more plentiful in NWC. The dissolved oxygen in the bulk solution is consumed very quickly along the crack and is unlikely to be present at the actual crack tip. However, water presence at the crack tip can result in several

reactions and subsequent events. 1). Oxygen (in water) can react with the alloy and produce an oxide compound. 2). Oxygen can diffuse through a pre-existing oxide along the crack wall and can react with the fresh cations at the oxide/metal interface, or can continue to diffuse into the base alloy. 3). Oxygen can diffuse in front of the crack along a dislocation, grain boundary, or other crystallographic defect or feature. 4). Oxygen can migrate towards the crack mouth and out into the bulk solution. The most likely of these reactions are items 1), 2), and 3) because these are all reactions that are taking place at the crack tip or within a few nanometers of the crack tip. The evidence based upon the experimental testing in this work agrees with items 1), 2), and 3). Oxygen is clearly present at and in front of the crack tip in HWC in alloy X-750. Moreover, along the crack flanks nickel is oxidized deeper than chromium, which clearly proves that oxygen is penetrating into the base metal and reacting with both nickel and chromium (nickel oxide may appear to be oxidizing first because it is ≈70 wt% compared to 17 wt% of chromium; regardless, both nickel and chromium oxide are forming away from the crack flanks). These oxygen penetrations were identified in several APT reconstructions, and they clearly document oxygen penetrating into the base metal and suggest a crystallographic pathway due to the regular periodicity of penetrations.

Item number 2) is the most straightforward in most corrosion systems and is identified as an active process with the presence of oxide along the crack flanks in close proximity to the crack tip. Both ATEM and APT have clearly documented oxide at the crack tip.

Item number 3) is the most elusive to prove, but conclusive evidence with ATEM analyses have previously suggested that oxidation at and in front of the crack tip is occurring.[46] SIMS has clearly shown oxygen presence along grain boundaries ahead of a crack tip and has shown considerable evidence of secondary grain boundaries oxidizing.[41] The APT data in this work is the first to clearly show the corrosion tunnels and oxygen diffusion ahead of the narrow corrosion tunnels into the base material. The free oxygen and oxide measurements reliably show that oxygen penetration is occurring ahead of an active SCC crack tip.

Several key experimental results show that oxygen does diffuse ahead of the crack tip and into the bulk from the crack flanks. These results were presented in the previous chapter and were discussed here in more detail. The evidence strongly suggests that internal oxidation as a contributing factor to the crack propagation under the experimental environment in this work. Figure 6-23 shows a 2D concentration profile of chromium oxide "fingers" ahead of the main

SCC crack tip. These fingers penetrate into the bulk material approximately 15 nm (the tip of the active SCC crack is a few nanometers below the protrusions in Figure 6-23). The concentration contours around the chromium oxide "fingers" correspond to the measured oxygen present ahead of the crack. The oxygen appears to follow certain pathways, but not strictly so. Oxygen concentration is highest along the "finger" trajectory, but oxygen also diffuses laterally from these oxygen enriched regions.

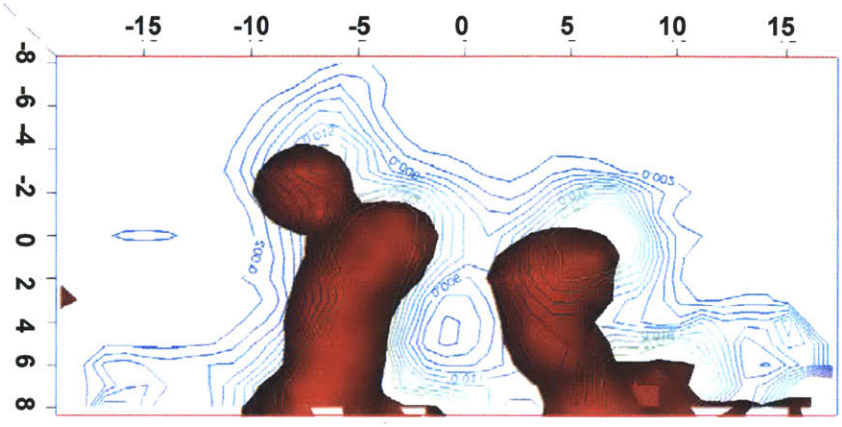

Figure 6-23: Oxygen concentration profiles surrounding CrO_x oxide penetrations

Figure 6-24 shows the analysis volume of one of the oxide "fingers" and focuses on analyzing the composition as a function of distance within and ahead of the "finger". Figure 6-25 shows the elemental composition as a function of distance for the "finger" highlighted in Figure 6-24. The "finger" shape protruding ahead of the main SCC is rich in oxygen and oxide and depleted of the main three alloying elements, namely nickel, chromium, and iron. Increase in metal oxides corresponds to the decrease in solute and solvent atoms. Nickel oxide and oxygen decrease sharply at the tip of the oxide "finger". In the material ahead of the oxide "finger" nickel oxide is sparse, but chromium oxide and oxygen are enriched, which is an indication that chromium oxide is the dominant oxide at the crack tip. Chromium oxide advances ahead of the "fingers" at approximately 0.8-1.0 at % and oxygen is also present at about the same enrichment. Within this localized path, chromium oxide and oxygen are approximately 5-6 times higher than compositional measurements away from the analysis volume.

The presence of enriched chromium oxide and oxygen ahead of each "finger" can be attributed to two possibilities: (1) oxygen is diffusing along an ordered pathway (dislocation, vacancy

pathway, crystallographic defect, etc.) ahead of the crack tip and into the bulk to ultimately form chromium oxide and (2) the oxide "finger" is actually a converging shape that grows more narrow with penetration depth. Both options are possible and would ultimately contribute to the same effect. Thus, even considering the measurement uncertainty, oxygen and chromium oxide are in the bulk material ahead of the "fingers".

Additional examples of oxygen and oxide enrichment ahead of each oxide "finger" have been presented in the experimental results chapter, section 4.3. All of these examples indicate the same effect as discussed here.

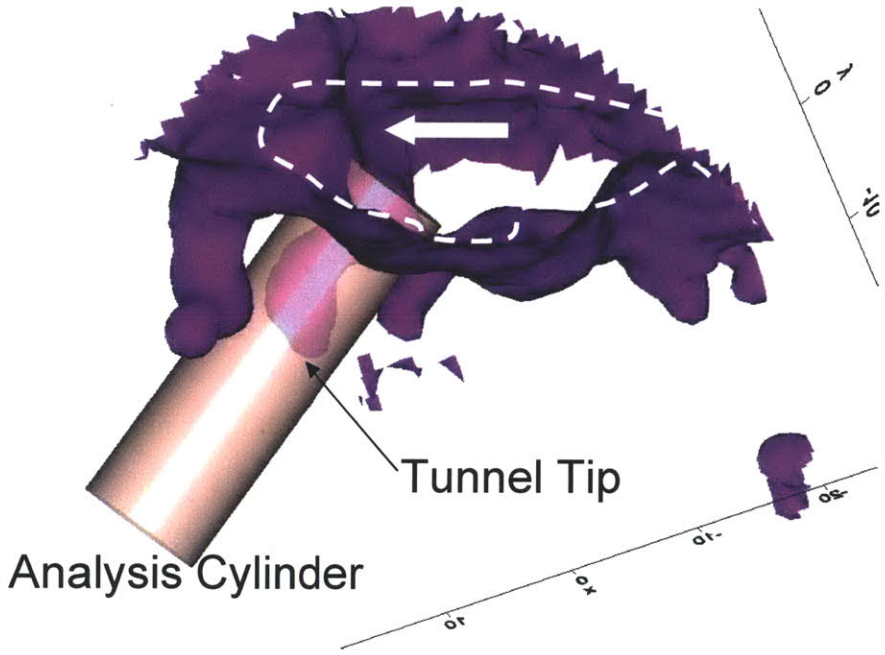

Figure 6-24: Analysis of bulk directly in front of selective corrosion pathway

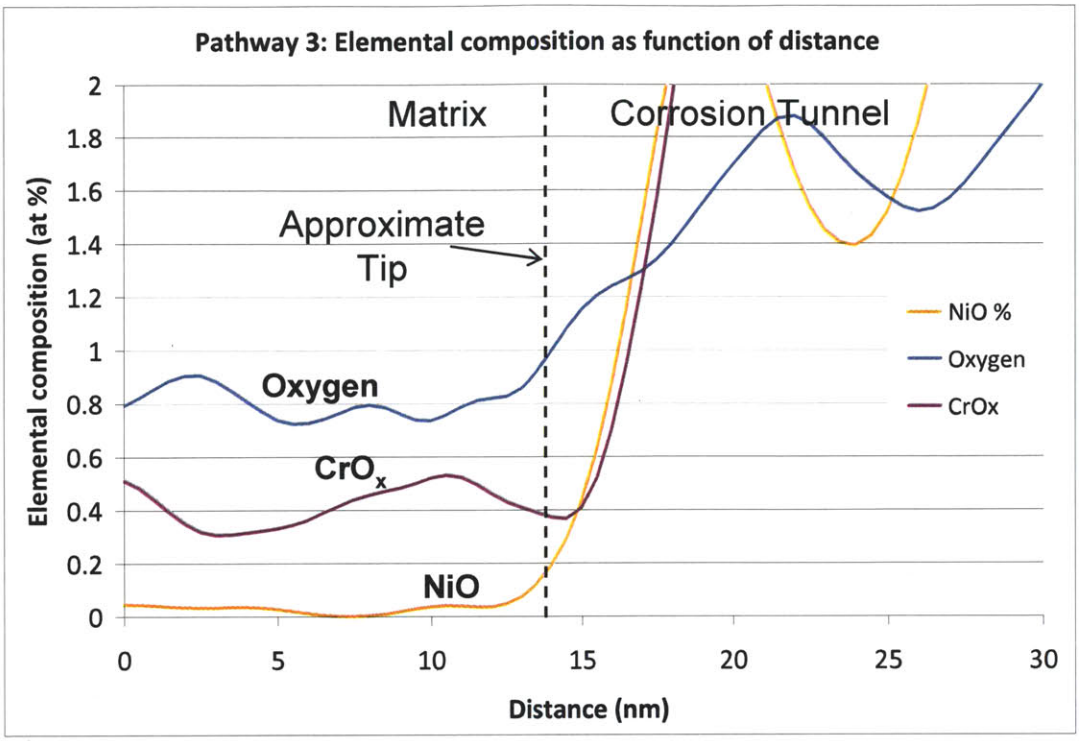

Figure 6-25: 1D Elemental concentration profile at and ahead of corrosion penetration

Corrosion penetrations or tunneling is not a new concept; however, this is the first instance where it has been able to be analyzed at such a high resolution with APT. An early reference to the corrosion tunneling concept was presented by Silcock and Swann.[47] They proposed that "corrosion tunneling" was incubated with a dislocation slip step rupturing the protective oxide film. Tunnel corrosion led to the formation of an oxidized corrosion sponge structure that ultimately ended in fracture of the material ligaments between each tunnel.

Oxygen penetration laterally from crack flanks

Oxygen diffusion/penetration into the bulk material laterally from the SCC crack flanks is another key indication that internal oxidation is active in the overall cracking mechanism. Lateral oxygen penetration is less likely to contribute to crack propagation (to be discussed shortly), but it clearly shows that oxygen transport into the bulk is occurring.

Figure 6-26 shows an APT reconstruction of a crack growing directly out of the page. The dotted lines indicate the approximate crack walls. The dark dashed ovals highlight that the

oxygen penetrations are numerous and occurring on both sides of the crack. Figure 6-27 shows a 2D concentration map of the oxygen penetrations highlighted in the lower image in Figure 6-26.

The lateral oxygen penetrations from the SCC crack flanks have a periodic spacing of approximately 4 nm and penetrate nearly 10 nm into the bulk material. These oxygen diffusion paths appear ordered which indicate that they are advancing along crystallographic features into the bulk material. The oxygen concentration at the tips of these penetrations (greater than 10 nm from crack wall) is only a fraction of an atomic percentage point, but it is clear that the diffusion pathways are ordered. The oxygen concentration directly exterior to the crack wall (in bulk, not inside crack) is between 1 and 1.5 at%.

The effect of internal oxidation is clearly contributing to the mode of crack propagation in alloy X-750; however, the exact mechanism is not specifically known. The internal oxidation model of Shen and Shewmon focused on internal methane or carbon dioxide bubble formation leading to internal stress is unlikely because the crack is not propagating directly on the grain boundary and the amount of carbon directly adjacent to the grain boundary is reduced due to carbide formation during the ageing treatment. Also, the high resolution SEM images of the fractography in this work do not show the presence of bubbles (which would be spherical). Moreover, it is calculated that these bubbles would have a diameter between 5 and 25 nm. No features resembling a bubble were detected with the atom probe analysis. Bubbles would escape the physical atom probe needles in the high vacuum atmosphere during the evaporation stage. When the bubble escaped the physical atom probe needle a voltage perturbation in the LEAP would occur. Additionally, the cavity left behind by the bubbles would be detected. Thus, it is unlikely that the bubble mechanism of the proposed internal oxidation is occurring.

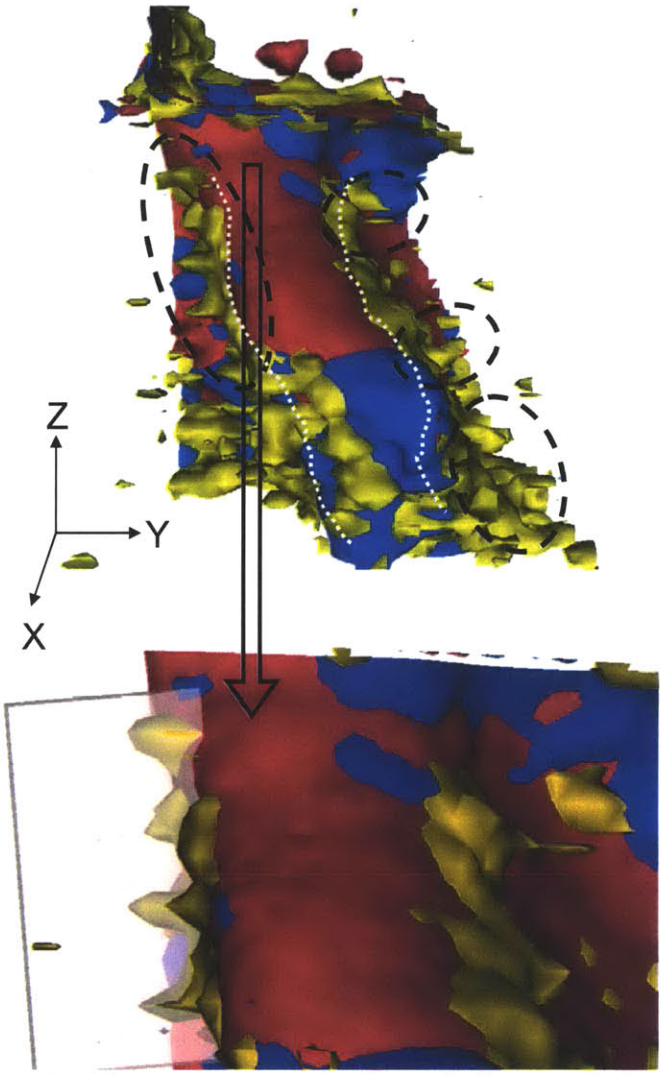

Figure 6-26: SCC crack with oxygen penetrating laterally from crack flanks. The isosurface elucidating the oxygen penetrations represents a 1.7 at% concentration of oxygen

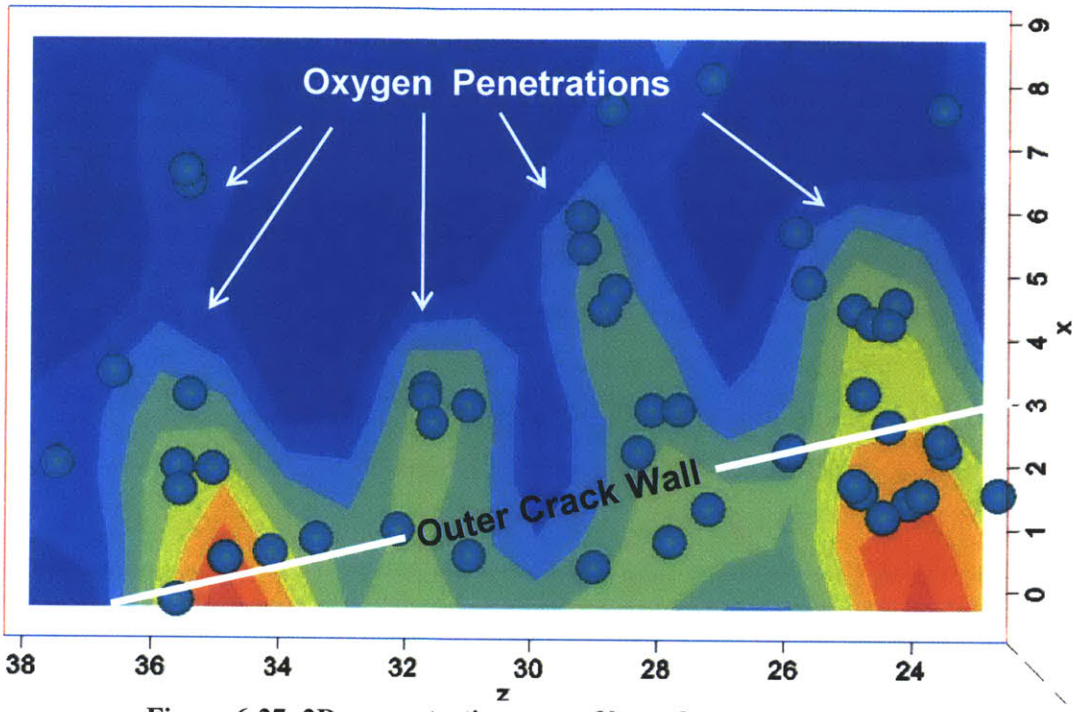

Figure 6-27: 2D concentration map of lateral oxygen penetrations

The internal oxidation mechanism proposed by Scott and LeCalvar [4] that focuses on internal oxidation of the solvent species (or the solute) more accurately fits with the observations in this work, at least in part. The oxide "fingers" present at the tip of the SCC crack clearly fall into this category. It was observed that oxide "fingers" penetrate into the bulk material at distances up to approximately 20 nm. These "fingers" may advance further than 20 nm, but were not detected in other APT reconstructions. Scott and LeCalvar identify that their model predicts crack growth rates two to three orders of magnitude too small, which is based on complete oxidation and brittle fracture. Another possibility, one which is likely in this alloy and environment, is that the oxide forms along ordered pathways, such as the oxide fingers identified in this work. The oxide "fingers" would decrease the strength of the alloy directly ahead of the crack and may serve as incubation sites for ductile fracture between the "fingers". This would result in higher crack growth rates for the documented values of oxygen diffusion coefficients. The actual degree of crack growth rate enhancement is unknown with the brittle-"finger" ductile-ligament rupture theory. However, this theory is difficult to prove without additional APT analysis. If mechanical fracture does occur between the oxide "fingers" it would be very difficult to detect on the fracture surface. The ligaments are only a few nanometers apart and once ductile rupture

occurs, and the fresh metal is exposed to the aqueous solution enabling oxidation, the fresh surface would oxidize and hide the fracture details.

It is clear that oxygen has been detected along grain boundaries and in the bulk ahead of cracks. This strongly suggests that internal oxidation is occurring. However, the inconsistencies with accurately predicting the crack growth rates are strongly suggesting that other mechanisms are simultaneously contributing to crack propagation. Much of the criticism of the internal oxidation theory is based on the observation that the measured diffusion coefficients are not sufficiently high to predict the reported crack growth rates. The crack growth rates in alloy X-750 are too high to be accurately predicted solely with the internal oxidation phenomenon. Moreover, the cracking in alloy X-750 follows several crack paths and different morphologies within the "same" crack path, which strongly suggests that multiple mechanisms are active. The fracture surface clearly shows that the crack path makes it extremely difficult to accurately predict the correct oxygen diffusion coefficient. These diffusion coefficients depend on diffusion paths, and the heterogeneity of the crack path (as discussed above) in alloy X-750 makes this task untenable. It is likely that additional mechanisms are active that assist internal oxidation, which result in an effect increase in oxygen diffusion. One of these mechanisms is vacancy diffusion, which is presented in the next section.

6.5 Vacancy-Creep Model

The premise behind the vacancy-creep (VC) model for environmentally assisted cracking of metallic materials is based on interactions of vacancies with dislocations to enhance slip concentration in the highly-stressed region ahead of the crack tip. This model was first presented in 1996 by Aaltonen, *et al.*[5] The VC theory argues that selective oxidation, and, thus, vacancy generation takes place at the same electrochemical potential where EAC cracking occurs for stainless steels, nickel-base alloys, and brass. Moreover, this model can be applied to IGSCC, TGSCC, and hydrogen embrittlement phenomena.

6.5.1 Migration of Vacancies Towards Maximum Stress Concentration

Vacancies will enrich near the metal-oxide interface due to lattice distortion. This phenomenon has been reported by Anthony.[48] The vacancy enrichment establishes a vacancy concentration gradient and gives rise to vacancy diffusion to lower concentration in the bulk metal. Aaltonen

demonstrated that the vacancies will migrate towards the maximum tensile stress because the equilibrium concentration of vacancies increases as a function of tensile stress, as shown in Figure 6-28.

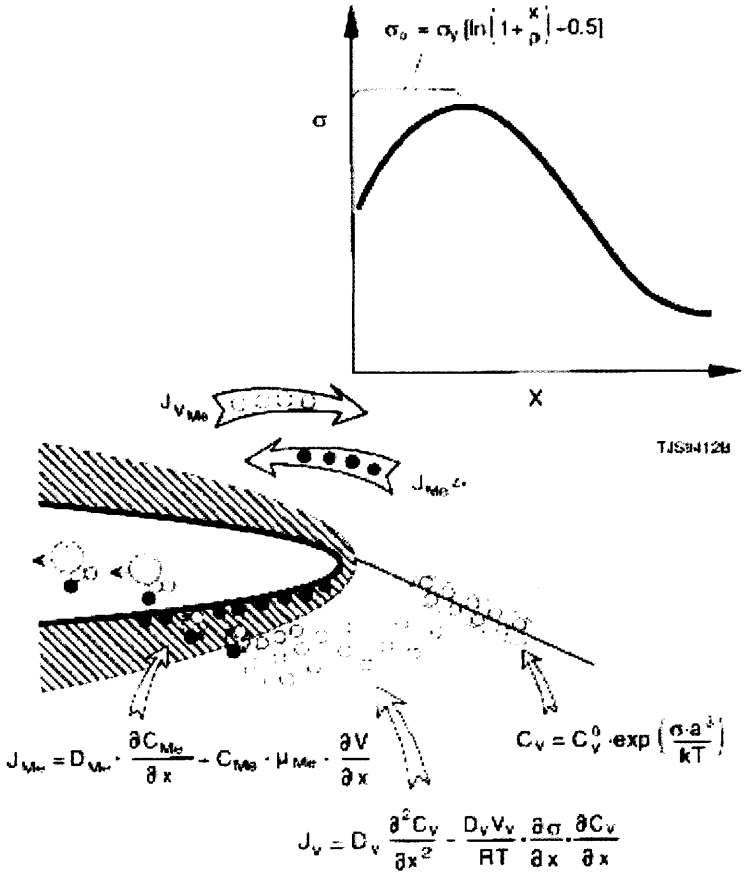

Figure 6-28: Schematic presentation of the principle of Vacancy-Creep model [5]

It is known that tensile stress reduces the free energy formation of vacancies. Equation (21) was derived by Hirth and Nix [49] that relates the equilibrium concentration of vacancies as a function of the tensile stress, σ:

$$C = C_0 \exp\left(\frac{\sigma V}{kT}\right), \tag{21}$$

where:

σ = tensile stress

V = atomic volume

T = temperature

K = Boltzmann constant

C = vacancy concentration

C_0 = temperature dependent equilibrium vacancy concentration in stress-free matrix

Thus, the net flow of vacancies is due to the opposite stress gradient and vacancy concentration between the crack tip (vacancy source) and the region of high stress. The maximum stress in the plastic zone ahead of a crack tip can be modeled by Equation (22) as a function of the crack tip radius, ρ:

$$\sigma = \sigma_y \left[\ln\left(1 + \frac{x}{\rho}\right) + \frac{1}{2} \right], \tag{22}$$

where:

σ_y = material's yield strength

ρ = crack tip radius

x = distance from crack tip

Materials with higher yield stress will exhibit a higher maximum stress ahead of the crack tip, and subsequently a higher vacancy concentration. Meletis *et al.* [50] modified Van Leeuwen's equation to account for vacancies. Equation (23) describes the vacancy flux in terms of a stress and concentration gradient:

$$J_V = \frac{\partial C_V}{\partial t} = D_V \frac{\partial^2 C_V}{\partial x^2} - \frac{D_V V_V}{RT} \frac{\partial \sigma}{\partial x} \frac{\partial C_V}{\partial x}, \tag{23}$$

where:

v = vacancy term

V_V = equivalent vacancy partial molar volume

Figure 6-29 shows the vacancy concentration profile ahead of the crack tip that has been calculated for alloy 600 at 300 °C.[5] In short time increments in a stress and concentration field, vacancies can migrate ahead of the crack tip in concentrations significant to assisting SCC.

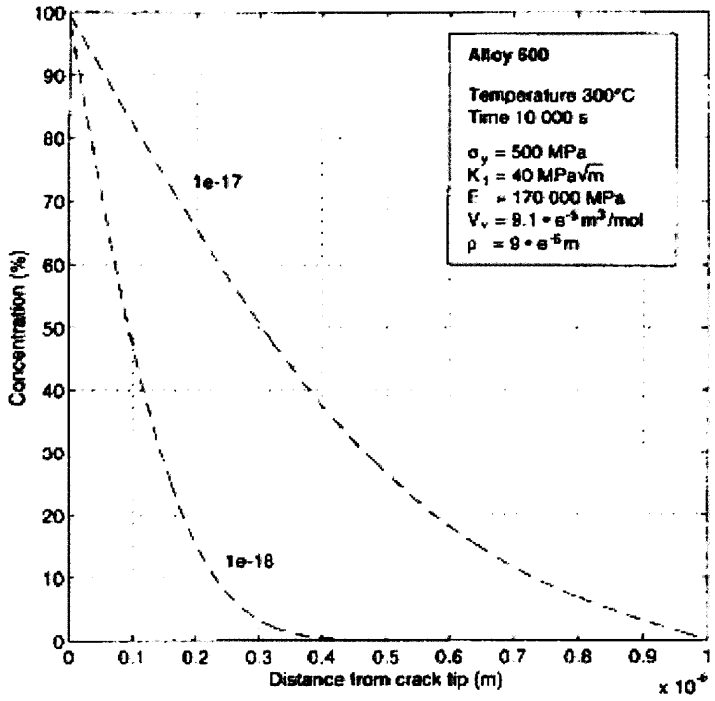

Figure 6-29: Calculated vacancy concentration profiles with two different diffusivities in alloy 600 at 300 °C [5]

The high vacancy density in front of the crack pathway contributes to fracture by several mechanisms: dislocation interaction and elemental (primarily oxygen) migration. The focus of this immediate discussion is focused on fracture, but the effect of oxygen migration will be presented shortly when it is combined with the internal oxidation model.

Vacancies are produced when the metal cations react with the oxidizing species at and in front of the crack tip. It has previously been shown that these vacancies migrate into the base metal, away from the high vacancy concentration and towards the high-stress region.[5] During migration these vacancies interact with dislocations, which have a large concentration in the highly strained/stressed region directly in front of the crack, and enhance dislocation climb. When dislocations reach a slip plane during climb, they induce slip and can further assist in

elemental migration. Numerous dislocations at and ahead of the crack tip can act as a preferential sink for the inward migrating vacancies. Agglomeration of vacancies simultaneously occurs with vacancy migration. The natural vacancy sink will be along the dislocations on the crack plane directly ahead of the crack tip. When the dislocation pile-ups and networks are at or very close to the grain boundary, intergranular fracture will occur.

Lattice point defects contribute to fracture by causing the stacking fault to spread in directions where these obstacles are present, as shown by Garner and Gelles.[51] A stacking fault can affect the crack tip deformation in two ways: first, local creep can be caused by crack tip dislocations interacting with the dislocation network ahead of the tip. Second, the stacking fault in FCC metals results in an HCP lattice and can provide a twinning mechanism for deformation.[51] This mechanism can explain the cleavage-like TGSCC fracture morphology in certain metals, such as in austenitic stainless steels. When vacancy concentration ahead of the crack tip increases to a sufficient level, the load bearing capacity of the ligament is exceeded, and the crack is extended as a jump.

6.5.2 Application of Vacancy-Creep Model to Alloy X-750

The VC model contributes to an understanding of the environmental cracking of alloy X-750 in this work by accounting for the effect of vacancy agglomeration ahead of the SCC crack tip. The VC model predicts vacancy diffusion to the peak stress location ahead of the crack tip. Agglomeration of vacancies directly ahead of the crack tip could serve as a crack embryo nucleation site, which has been documented in other SCC systems. Additionally, vacancy migration ahead of the crack and along grain boundaries can result in weakening grain boundaries to facilitate further fracture. Figure 6-30 shows evidence of grain boundary decohesion occurring about 8-10 μm ahead of the visible SCC crack, and Figure 6-31 shows evidence of decohesion 50-60 μm ahead the visible SCC crack tip. It is important to note here that the SCC crack may extend further beyond what is visible on the surface. This is especially true in Figure 6-31 because vacancy agglomeration would not occur at such long diffusion distances. Moreover, grain boundary decohesion may be assisted by shear loading which was commonly observed between grains.

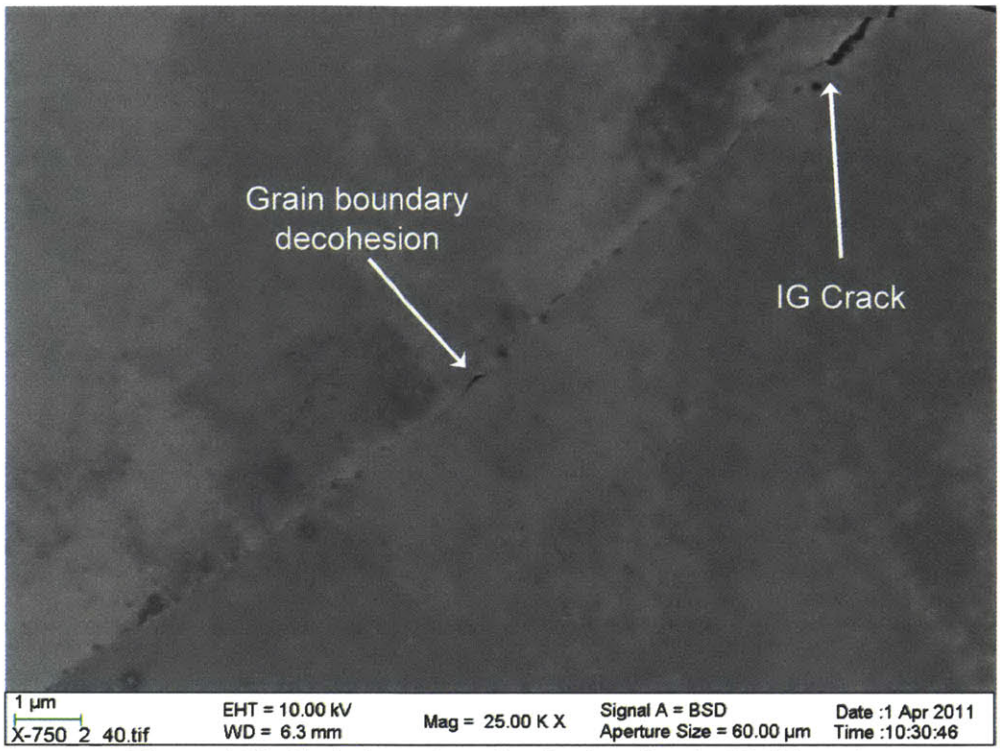

Figure 6-30: Grain boundary decohesion ahead of SCC crack

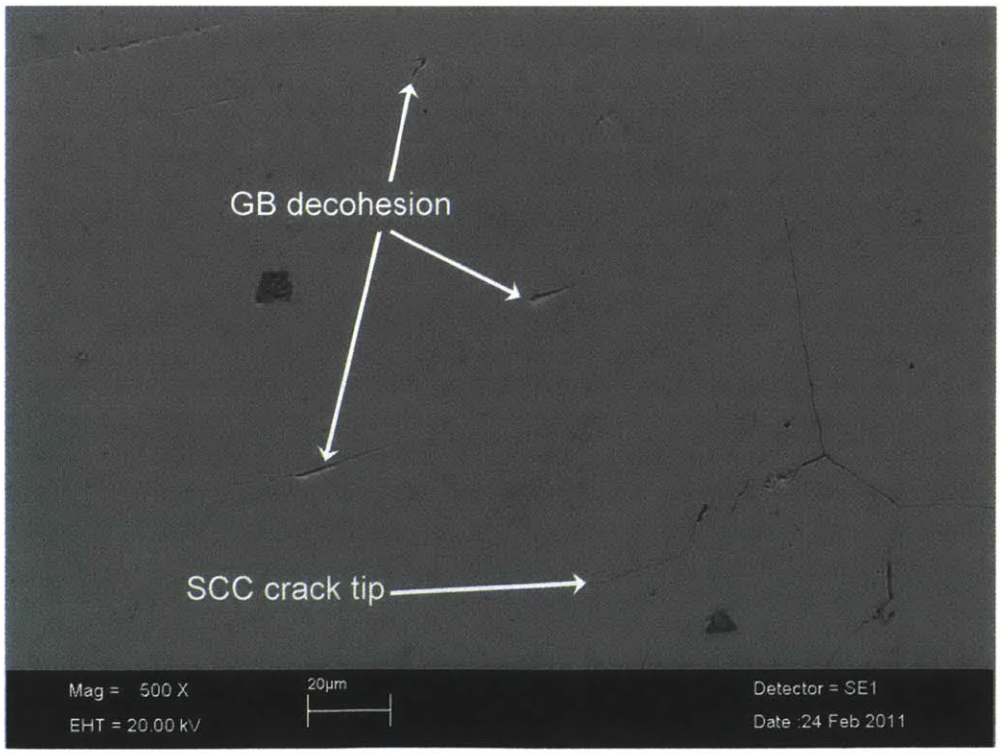

Figure 6-31: Grain boundary decohesion ahead of SCC crack

It was shown that by combining Equations (21) and (22) the vacancy concentration ahead of the crack tip is a strong function of the material's yield strength. Alloy X-750's yield strength is approximately three times higher than that of alloy 600, which will result in a more concentrated volume of vacancies within a shorter distance ahead of the crack tip. This will result in shorter fracture steps but brittle-like fracture nonetheless. Vacancy interaction with dislocations facilitates dislocation climb and subsequent slip. The high yield strength in alloy X-750 facilitates this effect because the increased vacancy concentration directly ahead of the crack tip assists dislocation climb and slip.

The VC model also couples nicely with the internal oxidation theory presented above. It was previously mentioned that the internal oxidation theory is reliant upon uncertainties in oxygen diffusion coefficients and largely underpredicts (by up to three orders of magnitude) the crack growth rate. Vacancy diffusion is driven by two factors: migration towards the region of higher stress and with a vacancy concentration gradient. The secondary effect of vacancy migration ahead of the crack tip is coupling with other elements, especially oxygen. Additionally, the vacancy migration is enhanced by the large dislocation network at and around the crack tip. These dislocations further serve as diffusion pathways, for both vacancies and oxygen (or any other element). These combined effects increase the effective oxygen diffusion rate, which will result in crack growth rate more representative to those experimentally measured.

6.5 SCC Model Integration Discussion

The discussion and analysis thus far suggests that no one known SCC model can completely describe and predict the crack growth morphology and failure mechanisms in alloy X-750 in this work. However, several models can accurately describe some of the features of the behavior observed in this work. It is clear that multiple synergistic cracking mechanisms are active at any given time and the degree of contribution to cracking varies with very specific parameters such as grain boundary structure, intragranular crystallographic features, and environment. These parameters and how they contribute to oxidization/dissolution and mechanics is outlined in Table 6-1 and have been adapted from the work by Rios *et al.* [52] on alloy 600 for the behavior observed in this work for alloy X-750.

Table 6-1: Interpretation of influence of various parameters on dissolution/oxidation and plasticity in alloy X-750 SCC

Parameters	Oxidation /dissolution	Mechanics
Hydrogen	Favors dissolution at low overpressures and can impede at high temperatures [53]	Enhances local plasticity and shearing. Decreases the local K_{IC} at the head of dislocation pile-ups [54]
Water chemistry NWC/HWC	Modifies the domains of oxide stability (e.g. NiO), controls electrochemical potential gradient between bulk and crack mouth	-
Chromium in solid solution	Favors passivity	Slows down dislocation motion (and creep rate) [55]
Carbon in solid solution	Increases oxidation/dissolution [56]	Slows down dislocation motion (and creep rate) [55]
Intergranular $M_{23}C_6$ carbides	Decreases intergranular (non-carbide/matrix) dissolution/oxidation (through a local decrease of soluble carbon) [56], chromium oxidizes and contributes to crack wall passivity	Relax stress at grain boundaries [57]; increase macroscopic creep rate and decrease intergranular creep rate [58]; increases locations for void initiation leading to shear fracture
Intergranular Nb-carbides	Oxidize and contribute to Nb content at crack tip	Reduces grain boundary shear motion, unless fractured
Intragranular and pseudo-intergranular γ'	Oxidize if exposed to water chemistry, contribute to aluminum oxide content at crack tip	Primary strengthening phase, constrain crack path along pseudo-intergranular grain boundaries
External load	Governs oxide fracture rate, depassivation/repassivation phenomena; increases oxygen, hydrogen, and vacancy transport ahead of crack tip	Governs dislocation emission at crack tip

It is possible that local differences in the interface between the aqueous environment on the metal and stress state at the crack tip account for different crack propagation mechanisms, which explains why some cracks propagate in a serpentine path around grain boundary carbides and other cracks advance in a slip-step fracture mode. Chromium present at the grain boundary results in the formation of stable, Cr-rich film at the crack tip. This chromium can come from bulk chromium content, albeit adjacent to the grain boundary, or from partial chromium carbide dissolution. The cracking advancing along pathways without grain boundary carbides (e.g. highly-coherent or twin grain boundaries) may have a Ni-rich film, which may become unstable due to the proximity to the Ni/NiO equilibrium at the crack tip conditions. As a result of these local differences, less-frequent film rupture would occur for the Cr-rich film locations (Cr_2O_3 is stable over a large potential range and is not affected by the Ni/NiO equilibrium). Moreover, if

the crack tip conditions correspond to stable NiO (not unstable NiO near the Ni/NiO equilibrium line), quicker film repair would result in lower corrosion rates and subsequently lower local hydrogen evolution rates. Support for this explanation is provided by Shei and Yang [59] who documented that Cr-rich oxides formed preferentially at the crack tips of several nickel-based alloys in high-temperature caustic solutions. Additionally, a considerable amount of the ATEM crack tips chemistry results have documented chromium oxide at crack tips in nickel-based alloys.[60] The crack tip analysis with APT performed in this work shows similar crack tip chemistry: Cr-rich oxide at and in front of the crack tip along with a smaller quantity of NiO. Cr-rich oxide has been proposed as the mechanism responsible for the SCC resistance of thermally treated alloy 600. Lozano-Perez and Titchmarsh [61] performed TEM work on crack tips in alloy 600 and reported that the crack growth rate depended upon oxygen diffusion ahead of the crack tip and that the diffusion was dislocation, vacancy, and stress enhanced.

The slip-dissolution/oxidation and vacancy-creep theories have regions of overlap that have a pronounced effect on the corrosion-deformation interaction and internal oxidation mechanisms. When lattice-slip occurs, fresh metal can be exposed to the aqueous solution and anodic dissolution occurs (fresh metal will only be exposed if the slip step is sufficiently large to allow water access to the bare metal). Anodic dissolution occurs until the passive film is reestablished and vacancies form at the rupture sites due to the dissolution. Film rupture is occurring over the full crack tip region and the dissolution produces a large quantity of vacancies. The dissolution process establishes the vacancy concentration gradient that drives vacancies into the material ahead of the crack. These vacancies subsequently assist in unfavorable (e.g. lead to fracture) dislocation dynamics and can partition with oxygen for internal oxidation.

Another corrosion process which is pertinent to the crack tip and local area is the migration of hydrogen into the metal surrounding the tip. Hydrogen is inevitably produced as a byproduct of corrosion and, at the temperature range of interest, will readily migrate into the matrix. This atomic hydrogen can either: 1). react with a solute species within the matrix (carbon to form methane gas, metal hydride, etc.), 2). react with other atomic hydrogen to form hydrogen gas, or 3). diffuse through the matrix and away from corrosion region. Hydrogen presence in the matrix also has a subsequent effect on lowering the energy barrier for dislocation movement. It has been shown that hydrogen greatly reduces the fracture toughness of alloy X-750.[62-63]

However, hydrogen agglomeration leading to substantial embrittlement is not likely in the high temperature test conditions in this work because of hydrogen's high lattice diffusion rate.

Hydrogen embrittlement effects at and in front of the crack tip are largely a function of the vacancy concentration. It was previously discussed that the void concentration in front of the crack in alloy X-750 will be large due to the high yield strength. This will have one of two possible (competing) effects for hydrogen diffusion or agglomeration (resulting in bubbles): the hydrogen diffusion away from the crack tip will be enhanced if the vacancies are unable to coalesce or hydrogen can form small high-pressure bubbles that aid in matrix decohesion. It is important to note here that hydrogen gas can form when two or more hydrogen atoms combine in a void. Hydrogen gas will not move interstitially. This suggests that the effect of hydrogen embrittlement on the host alloy is in direct relation to the vacancy concentration. The result of the vacancy/hydrogen system is most likely a competing mechanism between vacancy diffusion and hydrogen agglomeration. However, no evidence was observed on the fracture surface that could be directly attributed to hydrogen bubble and matrix decohesion. Lack of observable features on the fracture surface does not necessarily indicate that this effect is not happening because these details would be on the nano-scale and excessively difficult to detect.

The results of this work have shown that the crack surface is predominantly intergranular and pseudo-intergranular and has highly localized regions of transgranular cracking, which occurs between two intergranular fracture zones. The intergranular cracking (and pseudo-intergranular cracking) propagated differently along grain boundaries that had continuous $M_{23}C_6$ carbides compared to boundaries with either a twin or highly coherent, which were devoid of grain boundary carbides. The crack propagated adjacent to grain boundary carbides in a pseudo-intergranular mode. The cracking on the highly-coherent boundaries was not influenced by grain boundaries carbides and propagated intergranularly and followed crystallographic features, as observed in alloy 600 and described with the corrosion-deformation interaction model. Crack tips showed evidence of oxygen diffusion ahead of the SCC crack and into the bulk material. The maximum penetration depth documented in this work was up to approximately 20 nm ahead of the SCC tip. Oxygen also penetrated in a periodic and orderly manner lateral to the crack flanks, approximately 20-30 nm in the wake of the crack tip. The internal oxidation theory combined with vacancy-creep phenomenon was used to describe the oxygen-assisted cracking. The hydrogen embrittlement effects are strongly related to the vacancy concentration and

migration. Cracking along twin or highly-coherent boundaries was described with the corrosion-deformation interaction model, which also takes into account selective dissolution, vacancy-creep, and hydrogen embrittlement through its influence on dislocation dynamics.

While the discussion in this chapter does not include all SCC models in literature (there are numerous), it is focused on those models that most accurately describe the corrosion and fracture observed in this work. This work clearly shows that no specific SCC model is sufficient to model the crack growth rates and fracture specifics, but each model has merit in describing individual mechanisms. Moreover, the many of the proposed models share common features such as selective dissolution, dislocation interaction with vacancy gradients, and the vacancies can partition with and cause elemental segregation (primarily oxygen and hydrogen in this case). The overall SCC process in alloy X-750 is a combination of the aforementioned models.

Using a TEM to understand the fracture mechanism in alloy X-750, Raymond found that the HTH condition contains a high density of dislocation concentrations near the grain boundaries.[64] Additionally, Lozano-Perez and Titchmarsh [61] examined a SCC crack tip in alloy 600 with a TEM and noted that dislocation array determined the location of crack termination.

6.6 References

1. C.K. Elliott, "Effect of thermal treatment on the fracture properties of alloy X-750 in aqueous environments", Ph.D. Thesis, Massachusetts Institute of Technology, 1985.

2. F.P. Ford and P.L. Andresen, Corrosion Mechanisms in Theory and Practice, Chapter 14, P. Marcus and J. Oudar, Eds., Marcel Dekker, Inc., New York, 1995.

3. T. Magnin, J. M. Boursier, D. Noel, R. Rios and F. Valliant, "Corrosion deformation interaction during stress corrosion cracking of alloy 600 in primary water", Proceedings from the Sixth International Symposium on Environmental Degradation in Nuclear Power Systems – Water Reactors, TMS, 1993.

4. P.M. Scott, M. LeCalvar, "Some possible mechanisms of intergranular stress corrosion cracking of Alloy 600 in PWR primary water," Proceedings from the Sixth International Symposium on Environmental Degradation of Materials in Nuclear Power Systems – Water Reactors, TMS, pp. 657-665, 1993.

5. P. Aaltonen, T. Saario, P. Karjalainen-Roikonen, J Piillo, S. Tahtinen, M. Itaaho and H. Hänninen, "Vacancy-creep model for EAC of metallic materials in high temperature water", Corrosion/96, Paper 81, NACE, 1996.

6. G.P. Sabol and R. Stickler, "Microstructure of nickel-based superalloys," Physica Status Slidi, Vol. 35, pp. 11-52, 1969.

7. H.L. Logan, "Film-rupture mechanism of stress corrosion", Journal of Research of the National Bureau of Standards, Vol. 48, No. 2, pp. 99-105, 1952.

8. F.P. Ford, Stress corrosion cracking, *Corrosion Processes,* R.N. Parkins, Ed., Applied Science, 1982.

9. R.N. Parkins, "Environment sensitive fracture – controlling parameters," Proceedings of Third International Conference on Mechanical Behavior of Materials, K.J. Miller and R.F. Smith, Eds., Pergamon, New York, Vol. 1, pp. 139-164, 1980.

10. J.M. Kraft and J.H. Mulherin, Trans. ASM, Vol. 62, pg. 64, 1969.

11. T.P. Hoar, "Stress corrosion cracking", Corrosion 19: pp. 331-338, 1963.

12. P.R. Swann and H.W. Pickering, "Implications of the stress aging yield phenomenon with regard to stress corrosion cracking," Corrosion 19, Second International Congress on Metallic Corrosion, NACE, pp. 128-147, 1963.

13. F.P. Ford, "Mechanisms of environmental cracking peculiar to the power generation industry," EPRI Report NP2589, 1982.

14. F.P. Ford, The crack tip system and its relevance to the prediction of environmentally assisted cracking," Proceedings of the First International Conference on Environmentally Assisted Cracking of Metals, Kohler, Wisconsin, NACE, pp. 139-166, 1988.

15. E.M. Gutman, "An inconsistency in "film rupture model" of stress corrosion cracking", Corrosion Science, Vol. 29, pp. 2289-2302, 2007.

16. M.M. Hall Jr. "Critique of the Ford-Andresen film rupture model for aqueous stress corrosion cracking", Corrosion Science, Vol. 51, pp. 1103-1106, 2009.

17. D.A. Jones, "A unified mechanism of stress corrosion and corrosion fatigue cracking," Metallurgical and Materials Transactions A, Vol. 16, Issue 6, pp. 1133-1141, 1985.

18. M.F. Ashby, S.H. Gelles and L.E. Tanner, Philosophical Magazine, Vol. 19, p. 757, 1969.

19. P.L. Andresen and F.P. Ford, Life prediction by mechanistic modeling and system monitoring of environmental cracking of iron and nickel alloys in aqueous systems,", Materials Science and Engineering, Vol. 103, Issue 1, pp. 167-184, 1988.

20. J. Lepinoux and T. Magnin , "Stress Corrosion microcleavage in a ductile f.c.c. alloy", Materials Science and Engineering: A, Vol. 164, pp. 266-269, 1992.

21. P.B. Hirsch, S.G. Roberts and J. Samuels, "The dynamics of dislocation generation at crack tips and the brittle-ductile transition," Scripta Materialia, Vol. 21, pp. 1523-1528, 1987.

22. J.P. Hirth and J. Lothe, *Theory of Dislocations,* Krieger Publishing Co., Malabar, 1982.

23. M.T. Miglin and H.A. Domain, "Microstructure and stress corrosion resistance of alloys X750, 718, and A286 in light water reactor environments", Journal of Materials Engineering, Vol. 9, No. 2, pp. 113-132, 1987.

24. W.J. Mills "The deformation and fracture characteristics of Inconel X-750 at room temperature and elevated temperatures," Metallurgical Transactions A, Vol. 11, pp. 1039-1047, 1980.

25. T. Magnin, "A unified model for trans and intergranular stress corrosion cracking", Corrosion-deformation interactions CDI'92, pp. 27-41, 1992.

26. P.M. Scott, "An overview of internal oxidation as a possible explanation of intergranular stress corrosion cracking of alloy 600 in PWRs", Proceedings from the Ninth International Symposium on Environmental Degradation of Materials in Nuclear Power Systems – Water Reactors, TMS, pp. 3-14, 1999.

27. P. Kofstad, *High Temperature Corrosion*, Elsevier Applied Science, London/New York, pp. 324-341, 1998.

28. Y.M. Mishin and G.Borchardt, "Theory of oxygen tracer diffusion along grain boundaries in the bulk in two-stage oxidation experiments. Part II: analysis of the type B regime", J. Phys. III France, Vol. 3, pp. 945-960, 1993.

29. D.S. Morton, S.A. Attanasio, J.S. Fish and M.K. Schurman, "Influence of dissolved hydrogen on nickel alloy SCC in high temperature water", Corrosion/99, Paper 99447, NACE, 1999.

30. T.R. Lucas, "The effect of thermal aging and boiling water reactor environment on type 316L stainless steel welds", Ph.D. Thesis, Massachusetts Institute of Technology, 2011.

31. D.M. Symons and A.W. Thompson, "The effect of hydrogen on the fracture toughness of alloy X-750," Metallurgical and Materials Transactions A, Vol. 28, No. 13, pp. 817-823, 1997.

32. D.A. Woodford and R.H. Bricknell, "Embrittlement of high temperature alloys by oxygen" Treatise in Materials Science and Technology, Vol. 25, pp. 157-199, 1983.

33. C.H. Shen, P.G. Shewmon "A mechanism for hydrogen-induced intergranular stress corrosion cracking in alloy 600," Metallurgical Transactions A, Vol. 21, pp. 1261-1271, 1990.

34. Y. Shen and P.G. Shewmon, "IGSCC crack growth of alloy 600 and X 750 in steam" Corrosion/91, Vol. 47, pp. 712-718, 1991.

35. Y. Shen and P.G. Shewmon, "Intergranular stress corrosion cracking of alloy 600 and X 750 in high temperature deaerated water/steam," Metallurgical and Materials Transactions A, Vol. 22, pp. 1857-1864, 1991.

36. M.H. Wood and K.L. Kear "On the in-pile nucleation and growth of grain boundary bubbles," Journal of Nuclear Materials, Vol. 118, pp. 320-324, 1983.

37. G. Roberts "Diffusion with chemical reaction," Metal Science, Vol. 13, No. 2, pp. 94-97, 1979.

38. T. S. Gendron, P.M. Scott, S.M. Bruemmer, L.E. Thomas: "Internal oxidation as mechanism for steam generator tube degradation", Proceedings of the Third International Steam Generator and Heat Exchanger Conference, Canadian Nuclear Society, Vol. 2, pp. 5.18-5.35, 1998.

39. T.S. Gendron, "Intergranular oxidation as a mechanism of stress corrosion cracking of nickel base alloys in high temperature de-oxygenated water", Ph.D. thesis, University of Manchester, United Kingdom, 1999.

40. L.E. Thomas and S.M. Bruemmer, "High resolution characterization of intergranular attack and stress corrosion cracking of alloy 600 in high temperature primary water", Corrosion, NACE, Vol. 56, No. 6, pp. 572-587, 2000.

41. P. Laghoutaris, J. Chene, C. Guerre, O. Raquet, M. Sennour, R. Molins, F. Villiant and P. Scott, "Contribution to understanding of stress corrosion cracking of alloy 600 in PWR primary water", Energy Materials: Materials Science and Engineering for Energy Systems, Vol. 3, No. 2, pp. 119-125, 2008.

42. S. Lozano-Perez, M. Schroder, T. Yamada, t. Terachi, C.A. English, and C.R.M. Grovenor, "Using NanoSIMS to map trace elements in stainless steels from nuclear reactors", Applied Surface Science, Vol. 255, Issue 4, pp. 1541-1543, 2008.

43. G.C. Wood, F.H. Stott, D.P. Whittle, Y. Shida, and B.D. Bastow "The high temperature internal oxidation and intergranular oxidation of nickel-chromium alloys" Corrosion Science, Vol. 23, pp. 9-25, 1983.

44. D.P. Whittle, Y. Shida, G.C. Wood, F.H. Stott, and B.D. Bastow "Enhanced diffusion of oxygen during internal oxidation of nickel-base alloys" Philosophical Magazine A, Vol. 46, pp. 931-949, 1982.

45. T.B. Cassagne, P. Combrade, M.A. Foucault and A. Gelpi, "The influence of mechanical and environmental parameters on the crack growth behaviour of alloy 600 in PWR primary water," Proceedings of the Twelfth Scandinavian Corrosion Congress and Eurocorr '92, pp. 55-67, 1992.

46. S. M. Bruemmer and L. E. Thomas, "Mechanistic Insights on Environmental Degradation from Nanometer-scale Crack-tip Measurements," Proceedings from the Eleventh International Conference on Fracture, 2005.

47. J.M. Silcock and P.R. Swann, "Microstructural aspects of environment sensitive failure of austenitic stainless steels, International Conference on Mechanisms of Environment Sensitive Cracking of Materials, University of Surrey, England, pp. 66-82, 1977.

48. T.R. Anthony, "Atom currents generated by vacancy winds" In: *Diffusion in solids, recent developments*, A.S. Nowick and J.J. Burton, Eds., Academic Press, New York pp. 353-379, 1975.

49. J.P. Hirth and W.D. Nix, "Analysis of cavity nucleation in solids subjected to external and internal stresses," Acta Metallurgica, Vol. 33, pp. 359-368, 1985.

50. E.I. Meletis, K. Lian and W. Huang, "Vacancy-dislocation interactions and transgranular stress corrosion cracking," Proceedings from the International Conference on Corrosion-Deformation Interactions, CDI'92, Les Editions de Physique Les Ulis, pp. 69-81, 1993.

51. F. A. Garner and D. S. Gelles, "Irradiation creep mechanisms: an experimental perspective," Journal of Nuclear Materials, Vol. 159, pp. 286-309, 1988.

52. R. Rios, T. Magnin, D. Noel and O. deBouvier, "Critical analysis of alloy 600 stress corrosion cracking mechanisms in primary water," Metallurgical and Materials Transactions A, Vol. 26, pp. 925-939, 1995.

53. Z. Szklarska-Smialowska, "Factors Influencing IGSCC of Alloy 600 in. Primary and Secondary Waters of PWR Steam Generators," Proceedings from the Fourth International Symposium on Environmental Degradation of Materials in Nuclear Power Systems-Water Reactors, TMS, vol. 6, pp. 1-24, 1989.

54. T. Magnin, "Corrosion-Deformation Interaction," Solid State Phenomena, Vol. 35, pp. 319-33, 1994.

55. J.K. Sung, J.W. Jones and G.S. Was, "Effect of carbon on the low-temperature creep-behavior of Ni-16Cr-9Fe," Metallurgical and Materials Transactions A, Vol. 23, Issue 3, pp. 1033-1037, 1992.

56. W.K. Lai and Z. Szklarska-Smialowska, "Effect of heat treatment on the behavior of alloy 600 in lithiated water containing dissolved hydrogen at 25 to 350 °C," Corrosion/91, Vol. 47, pp. 40-47, 1991.

57. S.M. Bruemmer, L.A. Charlot, and C.H. Henager, Jr., "Microstructure and microdeformation effects on IGSCC of alloy 600 steam generator tubing,", Corrosion/88, Vol. 44, pp. 782-88, 1988.

58. J.M. Boursier, D. Desjardins and F. Vaillant, "The influence of the strain-rate on the stress corrosionc racking of alloy 600 in high temperature primary water", Corrosion Science, Vol. 37, Issue 3, pp. 493-508, 1995.

59. S.A. Shei and W.J. Yang, "Stress Corrosion Crack Tip Microstructure in Nickel-Base Alloys," Corrosion/94, NACE, Paper 154, pp. 1-19, 1994.

60. L.E. Thomas and S.M. Bruemmer, "Summary of analytical electron microscopy observations of intergranular attack on stress corrosion cracks in alloy 600 steam generator tubing," TR 1011683, EPRI, Palo Alto, CA, March 2005.

61. S. Lozano-Perez and J.M. Titchmarsh, "TEM investigations of intergranular stress corrosion cracking in austenitic allows in PWR environmental conditions", Materials at High Temperatures, Vol. 20, Issue 4, pp. 573-579, 2003.

62. D.M. Symons and A.W. Thompson, "The effect of hydrogen on the fracture toughness of alloy X-750," Metallurgical and Materials Transactions A, Vol. 28, pp. 817-823, 1997.

63. D.M. Symons, "The effect of hydrogen on the fracture toughness of alloy X-750 at elevated temperatures," Journal of Nuclear Materials, Vol. 265, Issue 3, pp. 225-231, 1999.

64. E.L. Raymond, "Effect of grain boundary denudation of gamma prime on notch-rupture ductility of Inconel nickel-chromium alloys X-750 and 718", Transactions of the Metallurgical Society of AIME, Vol. 239, pp.1415-1422, 1967.

Chapter 7 – Summary, Conclusions, and Future Work

7.1 Overview

The goals for this research project were to more thoroughly understand the fundamental mechanisms of crack growth for nickel-based superalloy X-750 in high temperature aqueous systems and to understand the interplay between the various phenomena and SCC. In order to accomplish this task, it was necessary to more completely characterize the crack tip and local microstructure at high resolution. The results from this work and how they met and exceeded the initial goals is discussed in this chapter. Areas for critical future work are also identified and presented in this chapter.

7.2 Summary and Conclusions

7.2.1 Crack Growth Testing

The crack growth rate response of alloy X-750 was determined in normal water chemistry (NWC) and hydrogen water chemistry (HWC). The crack growth rates were measured *in situ* with DCPD and the results for the constant stress intensity loading are recorded in Table 7-1.

Table 7-1: Summary of steady state SCC growth rates

SCC Crack Growth Rate	Stress Intensity (constant K)	Temperature	Water Chemistry
1.2×10^{-7} mm/s	27.7 MPa$\sqrt{m}$	288 °C	NWC
1.4×10^{-8} mm/s	27.7 MPa$\sqrt{m}$	288 °C	HWC
Not observed	30.0 MPa$\sqrt{m}$	93 °C	HWC

A crack growth rate of 3×10^{-7} mm/s was recorded by Shen [1], who used bolt-loaded U-bend specimens in similar aqueous conditions. Shen determined the growth rate by measuring the time to failure, which assumes that the crack tip is already conditioned to SCC conditions at the test beginning. Crack growth rates measured in this work agree nicely with the limited data available in literature. Other crack growth rate testing has been conducted on alloy X-750 in the HTH condition but not in the environment of interest in this work.

The corrosion potential was lowered by switching from NWC to HWC. This was an important step because alloy X-750 has been previously documented as being susceptible to hydrogen embrittlement, albeit for non-HTH heat treatments, as discussed in Chapter 1. When the environment was switched from NWC to HWC there was a clear change in crack growth rate,

which indicates that specimen (bulk) corrosion potential is extremely important to SCC susceptibility. Figure 7-1 shows that the resulting SCC induced fracture is predominantly intergranular and pseudo-intergranular (propagating directly adjacent to grain boundary $M_{23}C_6$ carbides) with small and localized regions of transgranular fracture. The SCC crack path in HWC is similar to that in NWC and is predominantly intergranular and pseudo-intergranular with localized regions of transgranular failure.

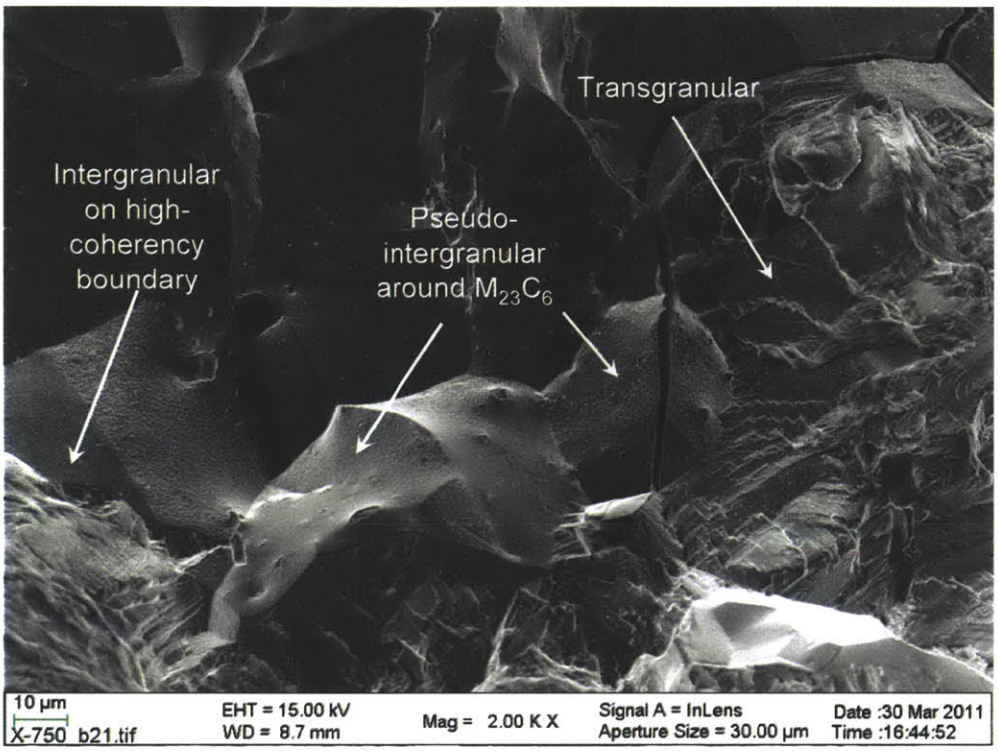

Figure 7-1: SCC and crack conditioning fracture morphology (NWC)

Cracking as a Function of Grain Boundary Type

Grain boundary structure appears to have the strongest internal influence on the mode of crack propagation (external influence would be load and environment). Figure 7-2 shows how grain boundary structure is dependent upon coherency of adjacent grains and the morphology can change abruptly between grains. The main crack was growing on a boundary with carbides, but cracking also started along a carbide-free boundary. Metal oxidation on both types of boundaries, but is more prevalent on boundaries with carbides. Cracking along a grain boundary with $M_{23}C_6$ carbides exhibits a less direct path than a coherent boundary and interaction with the

grain boundary structure, both electrochemically and mechanically, determines the SCC susceptibility.

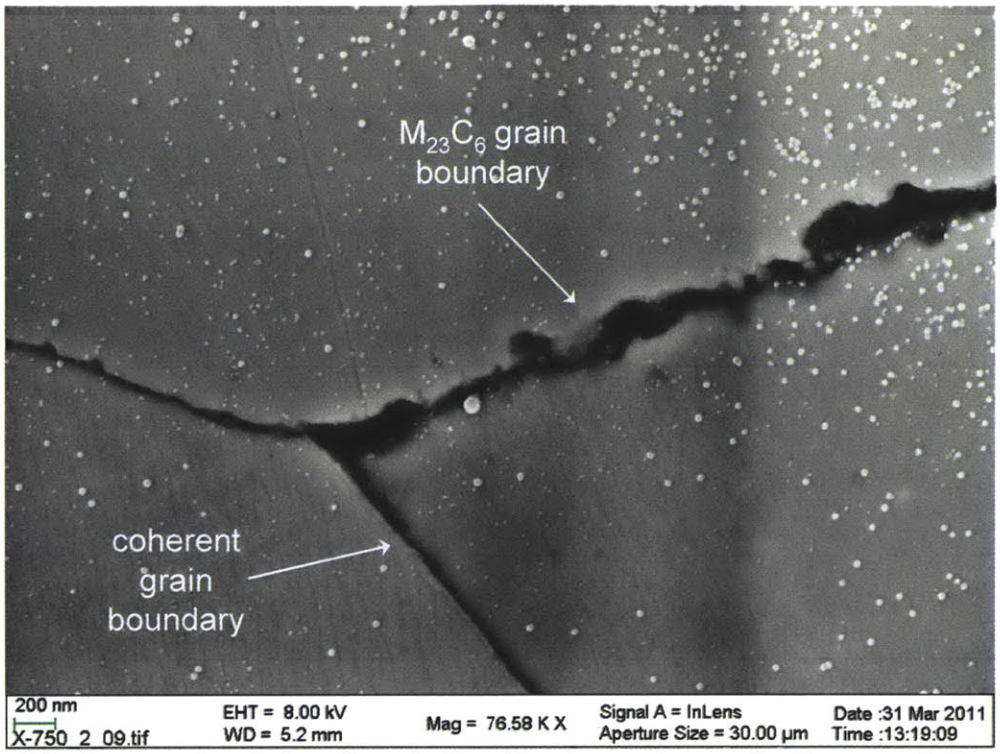

Figure 7-2: Cross-sectional view of crack changing propagation mechanism at grain boundary junction (transitioning from $M_{23}C_6$ to coherent boundary)

7.2.2 Crack Tip Characterization

High-resolution characterization of the crack tips was an extremely important step in developing more fundamental understanding operating mechanisms in the cracking process. Atom probe tomography (APT) greatly facilitated the crack tip characterization and provided outstanding and high-quality results.

The APT reconstructions identified several key features that impact/characterize the cracking process.

1. Finger-like "tunnels" are growing ahead of the main crack and are enriched in both oxygen and oxide. The tunnel structure is comprised of both metal atoms and oxide. The oxide is a chromium-nickel spinel type oxide.
2. The matrix directly ahead of each of the finger-like "tunnels" is also enriched in oxygen and predominantly chromium oxide. This indicates that oxygen is diffusing ahead of the

3. Oxygen penetrates directly into the base material from the crack walls in an ordered manner, which suggests that it is controlled by crystallographic features. The oxygen penetrations exhibit a spacing of approximately 4 nm and were documented to penetrate into the bulk up to approximately 10 nm.
4. The main SCC crack tip is full of predominantly oxide and, to a lesser extent, metal ions. The very crack tip forms a spinel of chromium and nickel oxide. Iron oxide begins to contribute to the oxide spinel approximately 25-30 nm from the actual tip.
5. The γ' precipitates directly adjacent to each crack tip and crack wall were deficient in aluminum content. The bulk γ' have an aluminum content of approximately 6.6 at% and the near-crack γ' had an aluminum content ranging from approximately between 2.5-3.5 at%.
6. No $M_{23}C_6$ carbides or any other grain boundary carbide have been located in an APT specimen in this project. Based on the evidence presented here and relating these results to literature results, the evidence supports the notion that the crack propagates adjacent to the grain boundary and not on the grain boundary. Furthermore, the $M_{23}C_6$ carbides on the grain boundary are too large to capture completely in an APT reconstruction. Small-sized grain boundary carbide is approximately the same size as the largest APT reconstruction presented in this work.

7.2.3 Application to SCC Models

The SCC crack path does not adhere to a specific morphology, and the overall propagation process does not admit to a single SCC model description. The SCC phenomena were categorized by identifying the morphology of the fracture surface and cross-sectional crack characteristics. The observed SCC phenomena observed in this work are as follows:

- Crack propagation is pseudo-intergranular, intergranular, and transgranular
- Metal dissolution occurs along the crack path and is more severe along boundaries with $M_{23}C_6$ carbides

- Crack propagation mode is dependent on the presence of $M_{23}C_6$ carbides on grain boundaries
    - Grain boundaries without $M_{23}C_6$ carbides are twins or highly coherent. Cracks propagate in a different mode on $M_{23}C_6$ boundaries vs. boundaries without carbides (coherent boundaries)
- Slip-step cracking can be main or secondary cracking
- Cracking on a twin or highly-coherent grain boundary results in a smooth fracture surface and indicates brittle-like fracture
- Cracking can occur ahead of active crack tip and appears as grain boundary decohesion
- Localized shear loading assists in grain boundary decohesion and separation of cracking surfaces
- The fracture surface undergoes localized regions of ductile fracture
- Microcracks nucleate and grow off main and secondary cracks in crystallographic order, which indicates that transgranular microcracking is occurring

Four of the many proposed models describe some of the features of the SCC and fracture process: (1) the slip-dissolution model developed by Ford and Andresen [2]. (2) corrosion-deformation interaction model developed by Mignin [3]. (3) internal oxidation and fracture model developed by Scott and LeCalvar [4]. (4) and the vacancy-creep model presented by Aaltonen [5]. Each of these models contains aspects that provide insight into specific features observed in alloy X-750 SCC under the environmental conditions in this work. The applicability of each model to alloy X-750 SCC was discussed. Each model presented can describe some of the individual features observed on the fracture surface and crack cross-section analysis; however, no one model can completely describe the environmental fracture process. All four models have been tied together here and a discussion has been presented how the models interact and contribute to a description of the overall SCC of alloy X-750.

7.3 Original Contributions

The original contributions in this thesis represent a significant contribution to the understanding of the fundamental SCC process at the crack tip in alloy X-750. The results from the crack growth rate response analysis allow prediction of component lifetime for specific conditions. The crack tip characterization has provided unique insight to the processes occurring at and

ahead of the crack tip, which was accomplished through high-resolution reconstruction and elemental analysis. This thesis was the first successful attempt to complete an atom probe reconstruction of a crack tip and established the methodology and procedures for atom probe abalysis of crack tips. This achievement will spurn additional attention to this characterization technique for further SCC analyses. Together these contributions will facilitate a greater undertstnading of the SCC processes and facilitate mitigation processes. The original contributions in this work are as follows:

- Determination and analyses of crack growth rates of alloy X-750 in 200 ppb dissolved oxygen at 288 °C.
- Determination and analyses of crack growth rates of alloy X-750 in 5-30 cc/kg hydrogen water chemistry at 93 and 288 °C.
- Determination of the crack path and role of grain structure in controlling environmental fracture.
- Critical analyses of crack tip properties by three dimensional crack tip reconstruction with atom probe tomography.
    - Determined crack tip and ahead of crack tip chemistry
- Substantially advanced the knowledge of fundamental SCC mechanisms active in alloy X-750 for NWC and HWC.

7.4 Future Work

The work completed in this research project made great strides to further understand the SCC mechanisms active in alloy X-750. However, further critical research is required.

- More crack growth rate response analysis needs to be completed. Much of the data in literature to date for alloy X-750 testing has been focused on conditions not representative of LWRs. Many of non-representative environments are chosen to simply speed-up the cracking process. However, it is important to use prototypic conditions if crack tip characterization is a subsequent step for the research. Also, *in situ* crack monitoring is preferential for reporting accurate crack growth rates, as opposed to simply measuring the time to failure. The SCC response analyzed in this work was focused on primarily one stress intensity in two environments. In order to more thoroughly

- The above mentioned task becomes daunting and unwieldy quickly due to the numerous parameters that will be varied. For this reason it is important to have wide collaboration with common test environments on a single alloy heat.

- A multi-scale characterization technique should be employed to more completely identify the SCC features. This process should include high-resolution scanning electron microscopy, nano secondary ion mass spectroscopy, orientation image mapping, transmission electron microscopy, and 3D atom probe tomography. Each of these listed techniques can offer unique results for SCC mechanism identification.

  The high resolution SEM work should be focused on fracture morphology and identifying whether cracking is more favored on a particular crystallographic orientation. An example would be how the crack advanced on a grain boundary with $M_{23}C_6$ carbides compared to a more-coherent boundary, as seen in this work. The OIM would be able to identify these crystallographic differences.

  NanoSIMS could be used to determine the extent of elemental enrichment/depletion at and ahead of the crack tip. This is most applicable if oxygen diffusion ahead of the crack is likely, but it can also be valuable if boron, sulfur, or phosphorus segregation is likely. The nanoSIMS can provide results from the nano- to micro-scales for elemental mapping.

  The TEM and ATEM can be used for two purposes: 1). analytical chemistry at the crack tip, and 2). identifying the dislocation network at and ahead of the tip. Recent work with ATEM on stainless steels has been promising and further work is warranted. Moreover, the TEM bridges the gap between the atom probe and SEM.

  3D APT is extremely valuable to provide sub-nanometer resolution of the crack tip chemistry and structure. This work showed that capturing a SCC crack tip in an APT reconstruction is possible, albeit extremely difficult! The APT technique will provide the highest-resolution results available for crack tips and should be pursued aggressively.

- More crack tips need to be reconstructed with APT and from more environments. The SCC crack tip reconstructions presented in this work were for a crack that ended in HWC. It would also be extremely valuable to perform an identical analysis for a crack tip from a NWC environment. Moreover, integrating APT work for crack tips from high-temperature gas cracking is extremely valuable. The merit for gas cracking is that the oxygen potential at the crack tip is explicitly known. These results would help pinpoint the effect of oxygen on and ahead of the crack tip.

- Further alloy characterization is necessary. This needs to be accomplished with both ATEM and APT. This characterization needs to occur on the specific heat of the alloy being tested and not just a generic alloy. The ATEM needs to be focused on more closely mapping the grain boundary $M_{23}C_6$ carbides and the width of the sensitized and γ' denuded zone.

  Additional APT work needs to be focused more on base-metal characterization to determine the chemistry differences between the γ' in the denuded zone and bulk γ'.

  APT samples should be reconstructed for material in close-proximity to the $M_{23}C_6$ carbides. Unfortunately, the grain boundary $M_{23}C_6$ carbides are too large to capture in an APT reconstruction.

- The effect on the aluminum-deficient γ' should be addressed. This may be an artifact that is easily addressed with the above listed points by examining the γ' near the grain boundaries. However, if the γ' within the denuded zone in an untested material is more representative of the bulk γ', then it is likely that there is an electrochemical effect that affects aluminum content in the γ' within close proximity to a SCC crack.

- The basis for this work was focused on establishing a foundation for further testing in the advanced test reactor at Idaho National Laboratory. To more accurately understand the SCC response in LWRs it is necessary to use materials that have undergone varying levels of irradiation damage. The crack characterization should be the same as the non-irradiated samples.

7.4 References

1. Y. Shen and P.G. Shewmon, "Intergranular stress corrosion cracking of alloy 600 and X 750 in high temperature deaerated water/steam," Metallurgical and Materials Transactions A, Vol. 22, pp. 1857-1864, 1991.

2. F.P. Ford and P.L. Andresen, *Corrosion Mechanisms in Theory and Practice*, Chapter 14, (P. Marcus and J. Oudar, Eds.) Marcel Dekker, Inc., New York, 1995.

3. T. Magnin, "A unified model for trans and intergranular stress corrosion cracking", Corrosion-deformation interactions CDI'92, pp. 27-41, 1992.

4. P.M. Scott, and M. LeCalvar, "Some possible mechanisms of intergranular stress corrosion cracking of Alloy 600 in PWR primary water", Sixth International Symposium on Environmental Degradation of Materials in Nuclear Power Systems – Water Reactors, Editors: R. E. Gold and E.P. Simonen, TMS, pp. 657-665, 1993.

5. P. Aaltonen, T. Saario, P. Karjalainen-Roikonen, J Piillo, S. Tahtinen, M. Itaaho, and H. Hänninen, "Vacancy-creep model for EAC of metallic materials in high temperature water", Corrosion 96, Paper 81, NACE, 1996.

Appendix A – Atom Probe Sample Prep

This appendix contains the step-by-step process to perform a site-specific lift-out with a dual-beam FIB and sharpen the atom probe tips.

A.1 Initial Surface Inspection

The initial surface inspection and sample procurement was performed on a small ingot removed from the interior of a 1TCT specimen. This ingot was polished to a mirror surface with the last step using 0.05 μm aluminum-oxide or silicon-oxide dispersion. The initial inspection of the polished surface revealed several crack tips, propagating primarily in an intergranular fashion normal to the load direction. The crack grew in a classical branched fashion indicative of SCC, and is shown in Figure 1. The four main crack tips were present on the sample and three are indicated by arrows in Figure 1. The crack tip used for these analyses was lifted from the path indicated by the middle arrow. Figure 2 shows a higher magnification image of the crack tip.

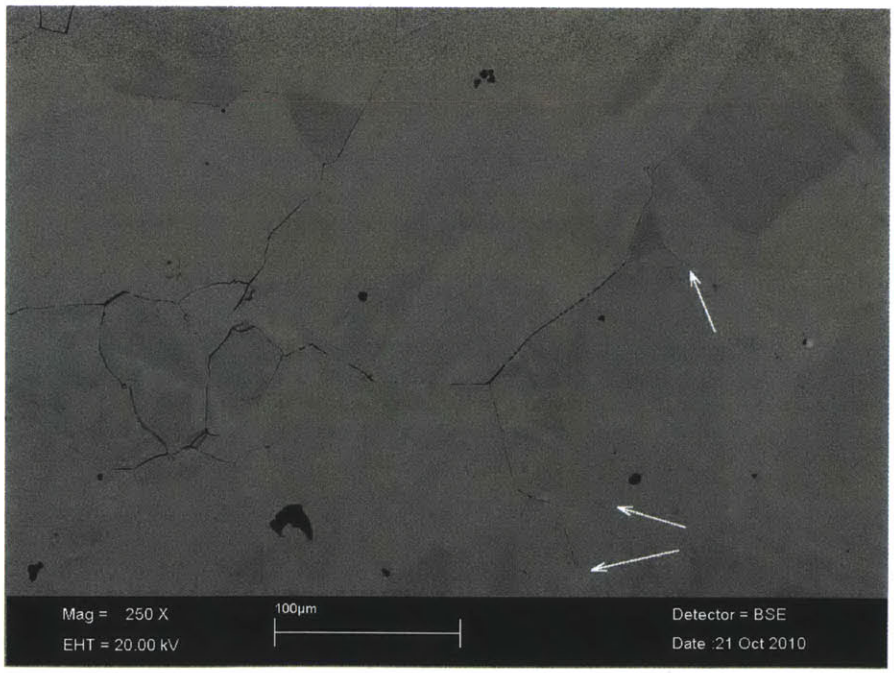

Figure 1: Crack Path with three branched crack tips

Figure 2: Crack tip used for APT (middle crack tip from Figure 1)

A.2 Atom probe tip blank removal and mounting

The angles and currents referenced in this section pertain to using a Helios NanoLab FIB manufactured by FEI. The Helios FIB has its ion column oriented 52° with respect to the horizontal axis. Many of the angled FIB cuts in this write-up occur at 22° with respect to the horizontal axis. If one were to use a microscope with an ion column oriented at an angle different than 52° the referenced angles in this appendix will need to be adjusted accordingly. For example, a Zeiss FIB microscope has the ion column oriented at a 54° angle and would require a 24° tilt. The beam currents would also need to be adjusted accordingly to the values similar to those referenced here. Ultimately, these parameters are only meant to provide a starting reference and the currents/tilt angles are user preference.

The microscope accelerating voltages and milling/deposition currents are recorded in Table 1.

Table 1 – Microscope Parameters

Step	Beam	Voltage	Current
Pt-deposition (line markers and protective cap for lift-out area)	SEM	5 kV	5.5 nA
Trench Cuts (regular and cleanup) (trenches 1-4)	FIB	30 kV	6.5 nA
Pt-deposition (attach Omniprobe)	FIB	30 kV	48 pA
Pt-deposition (attach blank to Si-micropost)	FIB	30 kV	48 pA
Trench Cut (cut APT blank from wedge)	FIB	30 kV	48 pA
Annular Mill Steps 1-3	FIB	30 kV	2.8 nA
Annular Mill Step 4	FIB	5 kV	48 pA

The lift-out procedure was a several step process and is outlined here:

1. The crack tip was marked by depositing two strips of platinum oriented normal to the growth direction (Figures 3a and 4a). One strip was downstream of the crack tip and the other was about 0.5 μm ahead of the crack tip. This was necessary to mark the location of the crack tip for later steps in the lift-out process. The platinum markers can be any shape or pattern that can assist the user in identifying the crack tip location.
2. Several "search" trenches were milled into the base material in front and behind the crack. This step was to identify a grain boundary through which the crack was advancing. These trenches are shown in Figure 3b and at the edges of 3d and 3e. A grain boundary was not identified ahead of the crack, but the growth angle was identified through a trench downstream of the crack. About 5μm downstream of the crack tip, the crack was oriented close to orthogonal with the surface.
3. A platinum strip was deposited on top of the crack path and along the projected crack direction (Figure 3c). Thus, the crack tip now was indicated as being between the two normal platinum strips and beneath the horizontal strip.
4. A platinum cap was deposited about 3 μm wide, along the crack path, and between the two exploratory trenches (Figure 3d). This step was necessary to shield the surface of the APT tips from gallium implantation during the milling process with the FIB. It the final

5. The sample stage was rotated to 22°, such that a trench was cut with the FIB at 60°. The trench was cut between the two exploratory trenches, at the periphery of the platinum deposition cap (Figures 3e and 4b).
6. The sample was rotated 180° and a second trench was milled along the periphery of the platinum cap (Figure 3f and 4c).
7. Keeping the sample at the same angle as in the previous step, a third removal trench was cut at the upstream end targeted lift-out volume (Figure 3g and 4c). This is the end of the lift out volume with which to connect the Omniprobe micro manipulator.
8. The stage was rotated 180° (return to 0° stage rotation) and the stage tilt was lowered to 0°. The Omniprobe micro-manipulator was inserted and attached to the lift-out section. (Figure 3h and 4d)
9. A final trench was cut to remove the remaining ligament, which connected the lift-out volume to the base sample. (Figure 3i)
10. The entire lift-out volume was removed and brought to the APT microarray for tip mounting (Figures 3j and 4e)

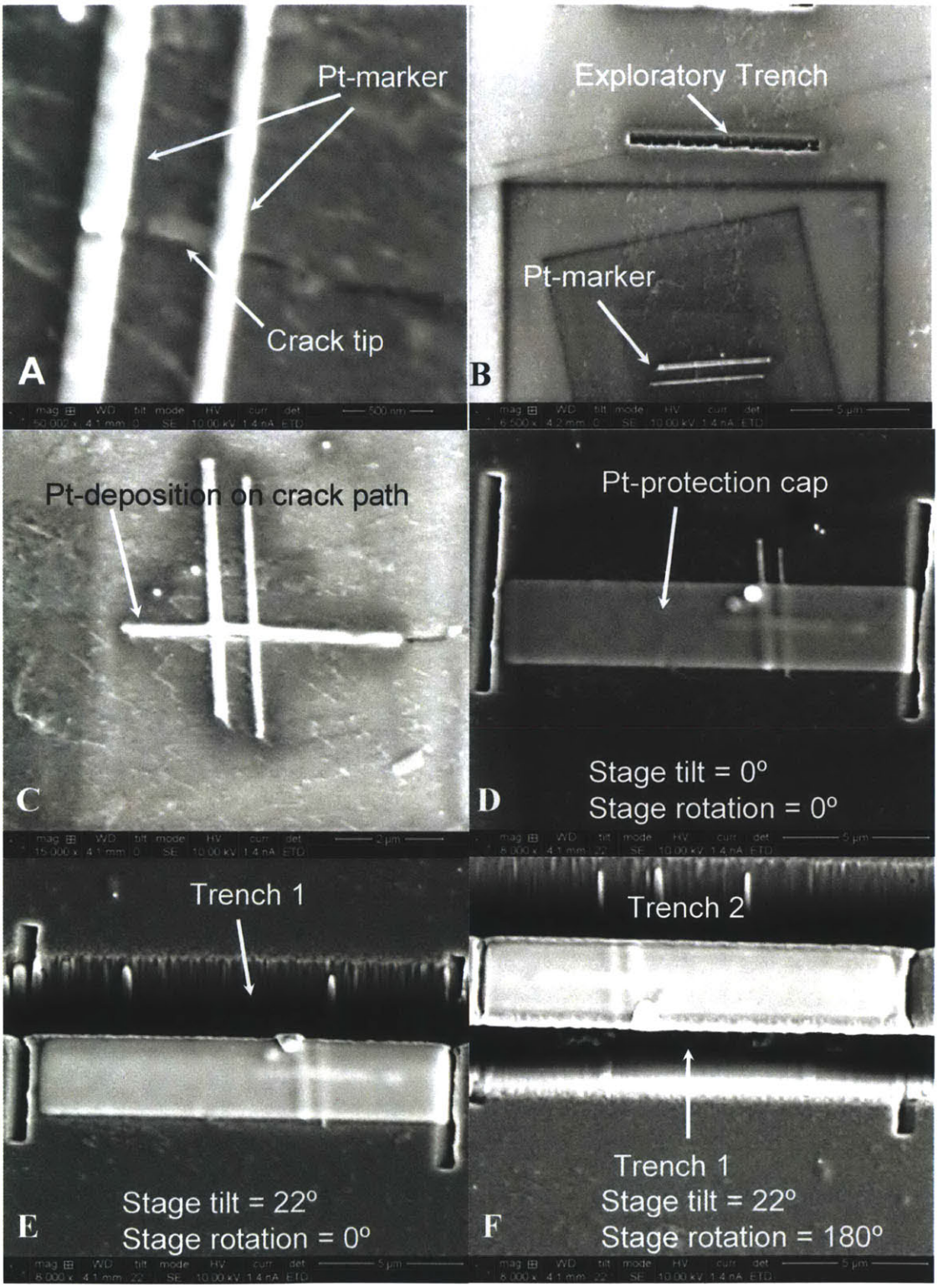

Figure 3: Site-specific lift-out sequence, part 1

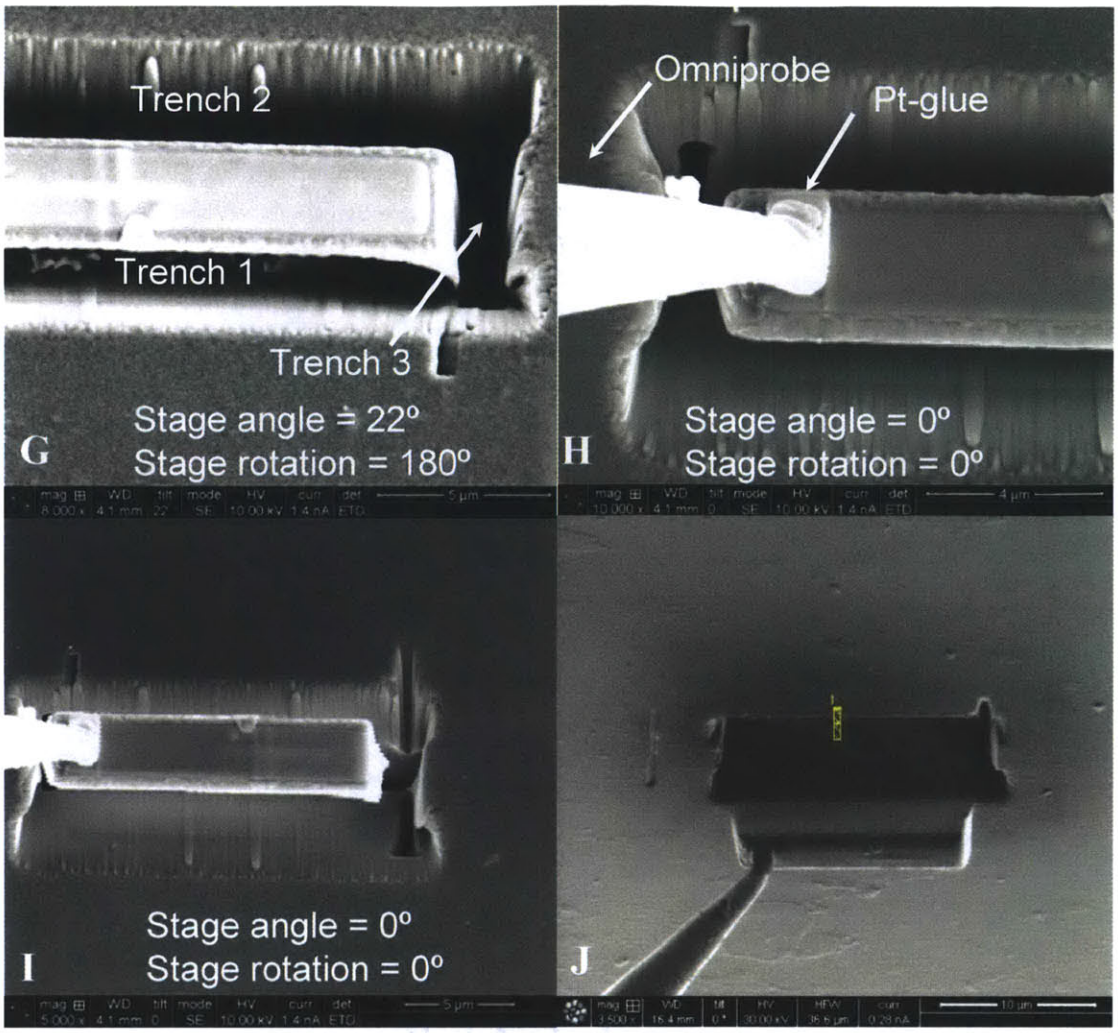

Figure 3: Site-specific lift-out sequence, part 2

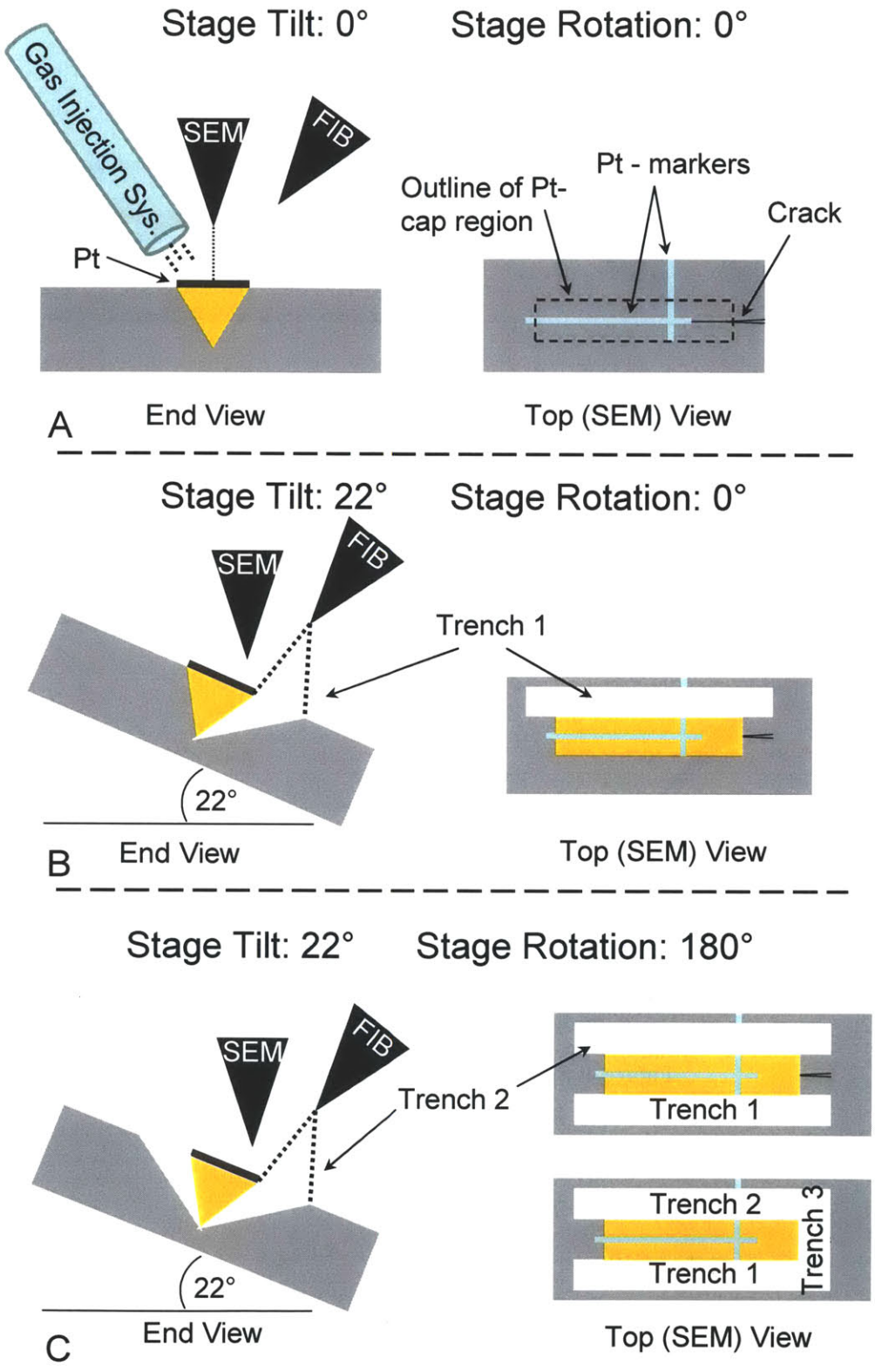

Figure 4: Site-specific lift-out, Part 1

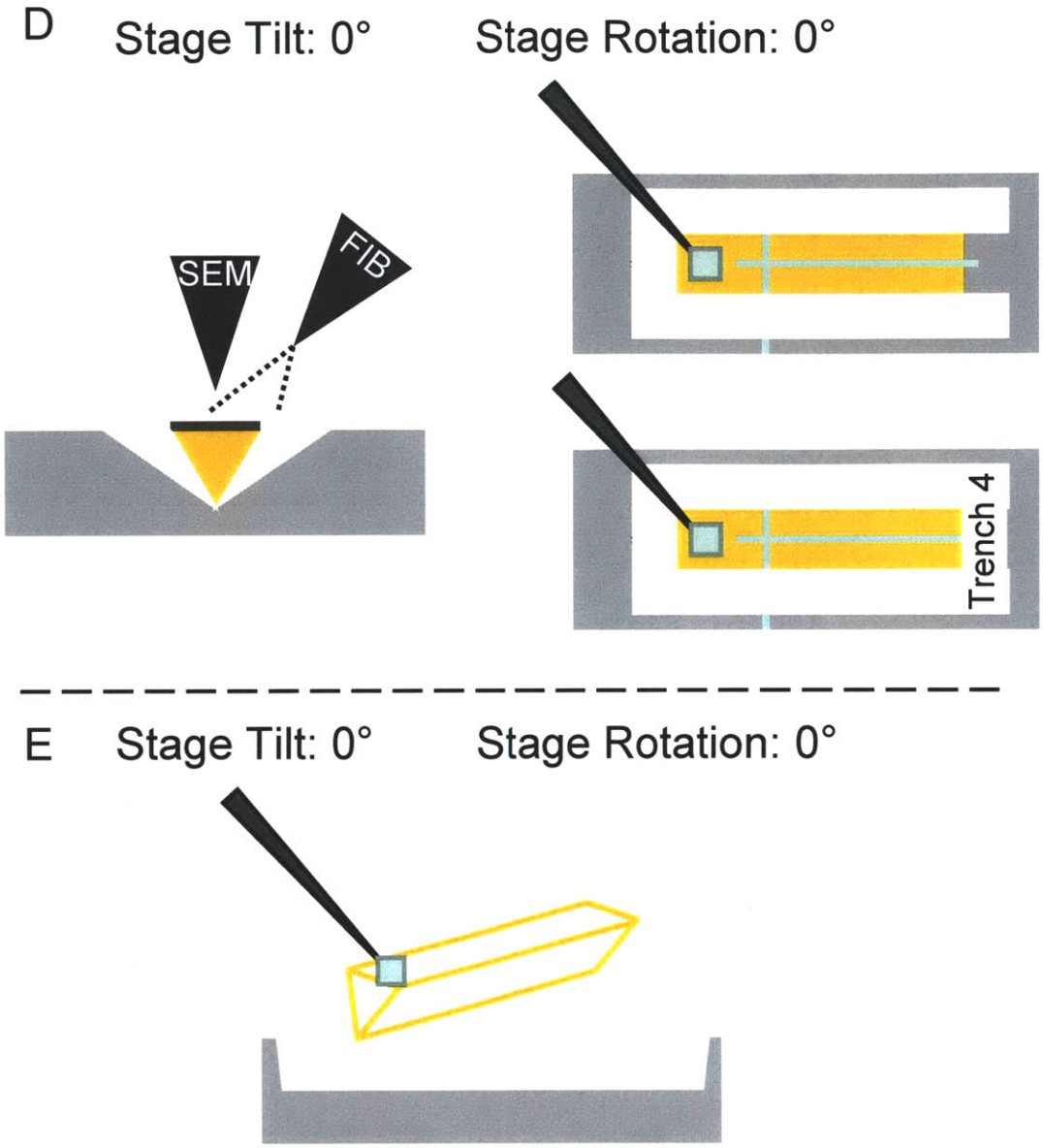

Figure 4: Site-specific lift-out, Part 2

A.3 Crack Sharpening Procedure

1. The "wedge" of lift-out material was moved to begin mounting APT blanks on the Si-micropost array (Figures 5a and 6).
2. The wedge was rested on a micropost and a platinum "weld" spot was deposited to connect the wedge, which is now connected to the Omniprobe and the micropost. (Figures 5b and 6).
3. A cut-off trench was milled into the wedge approximately 3-4 μm from the leading edge. The platinum deposition in the previous step held the APT blank to the micropost as the remaining wedge was backed away. (Figure 5c and 6)
4. The park, glue, and cut method was repeated until the desired number of APT blanks were mounted on microposts.
5. The micropost array was then rotated such that top surface of the APT blank was normal to the FIB column (Figures 7 and 8).
6. A series of annular masks were used to sharpen the APT blank into a sharp tip. The tip was sharpened through a series of decreasing internal diameter annular masks and subsequent lower milling current. The overall sharpening process is shown in Figure 8a-8h. The target diameter of the final tip was 80-100 nm.
7. The final APT tip mounted on a micropost is shown in Figure 8i.

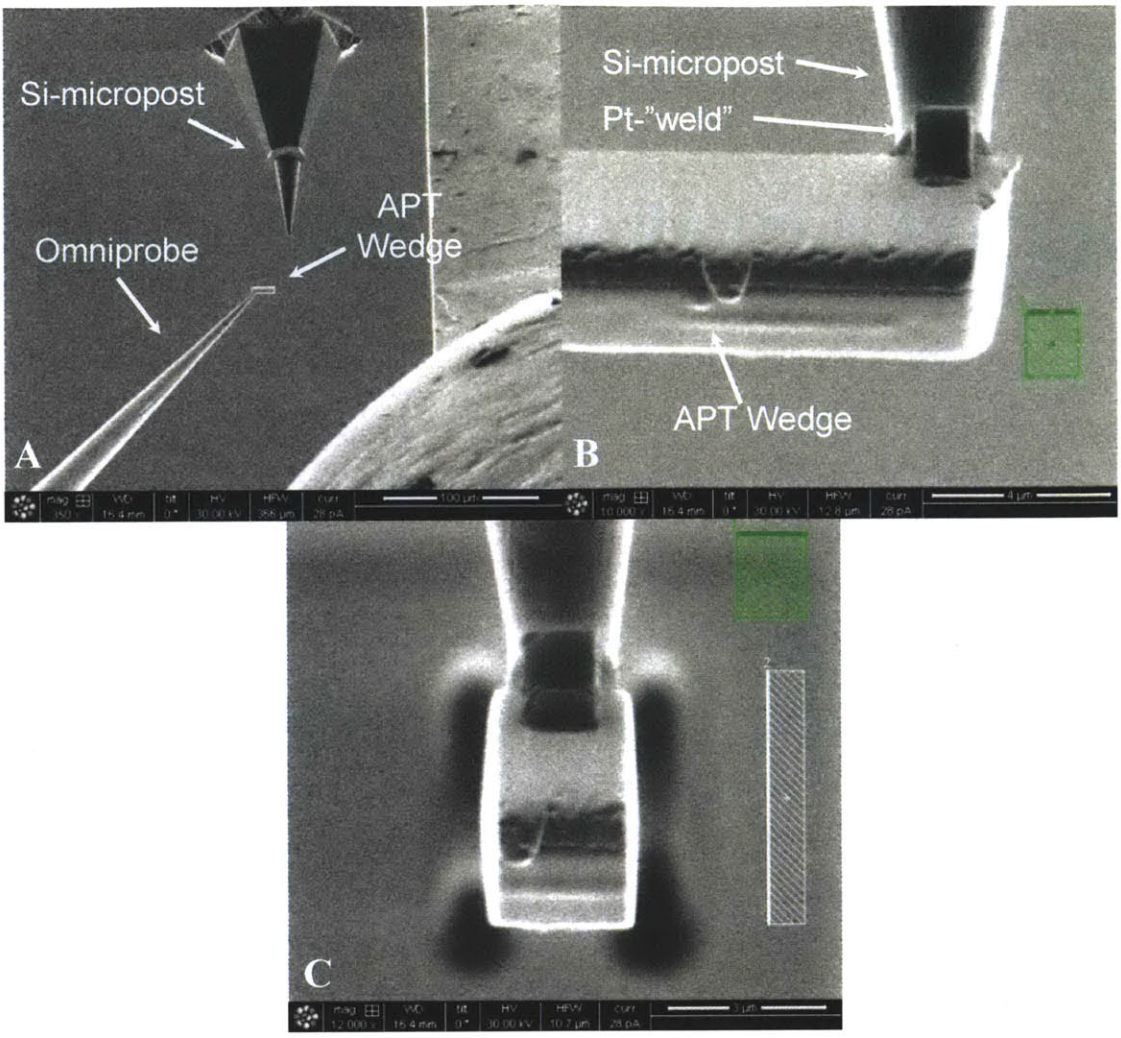

Figure 5: Mounting APT blanks to Si-micropost array

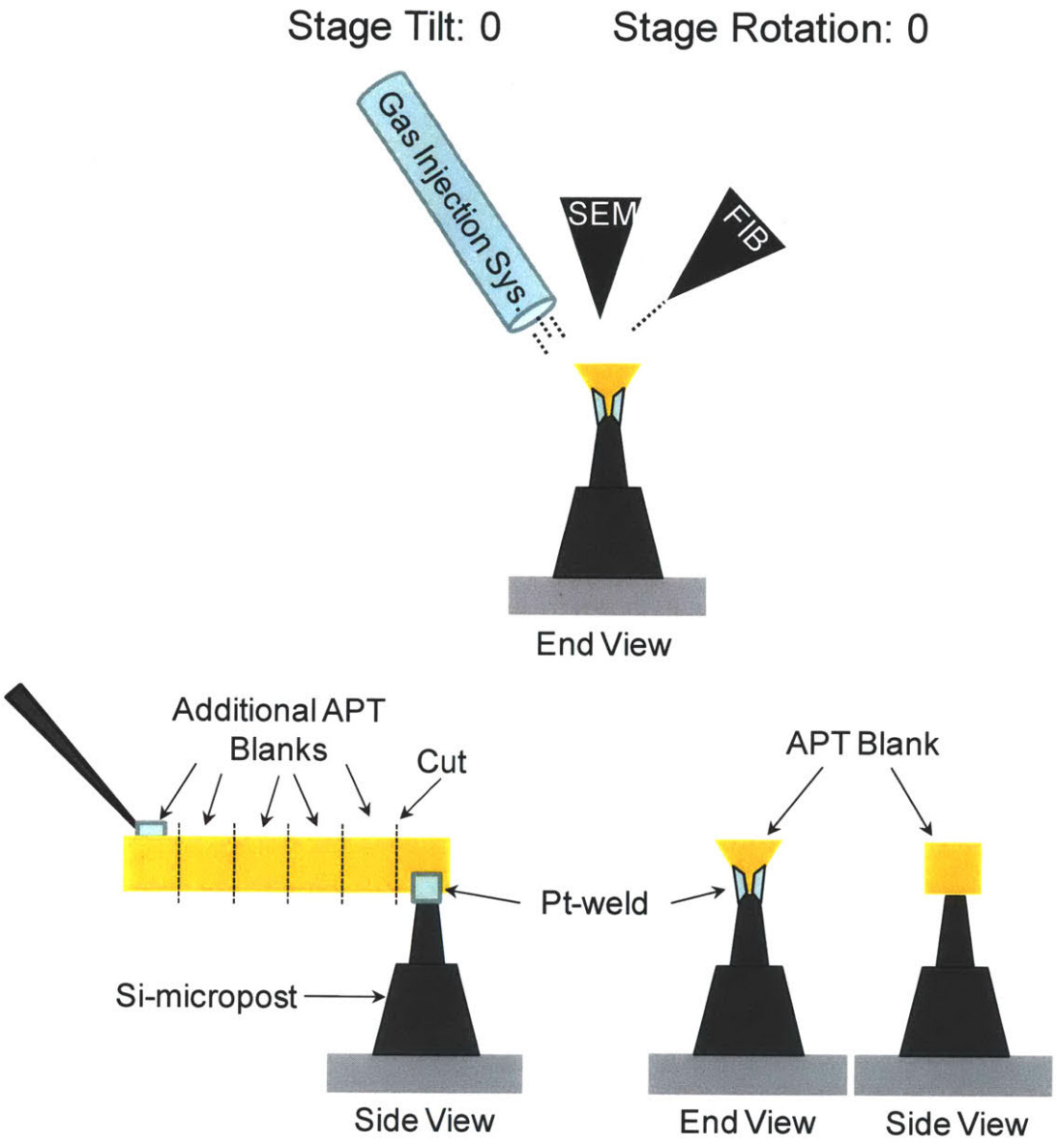

Figure 6 – Mounting lift-out blanks to Si-microposts

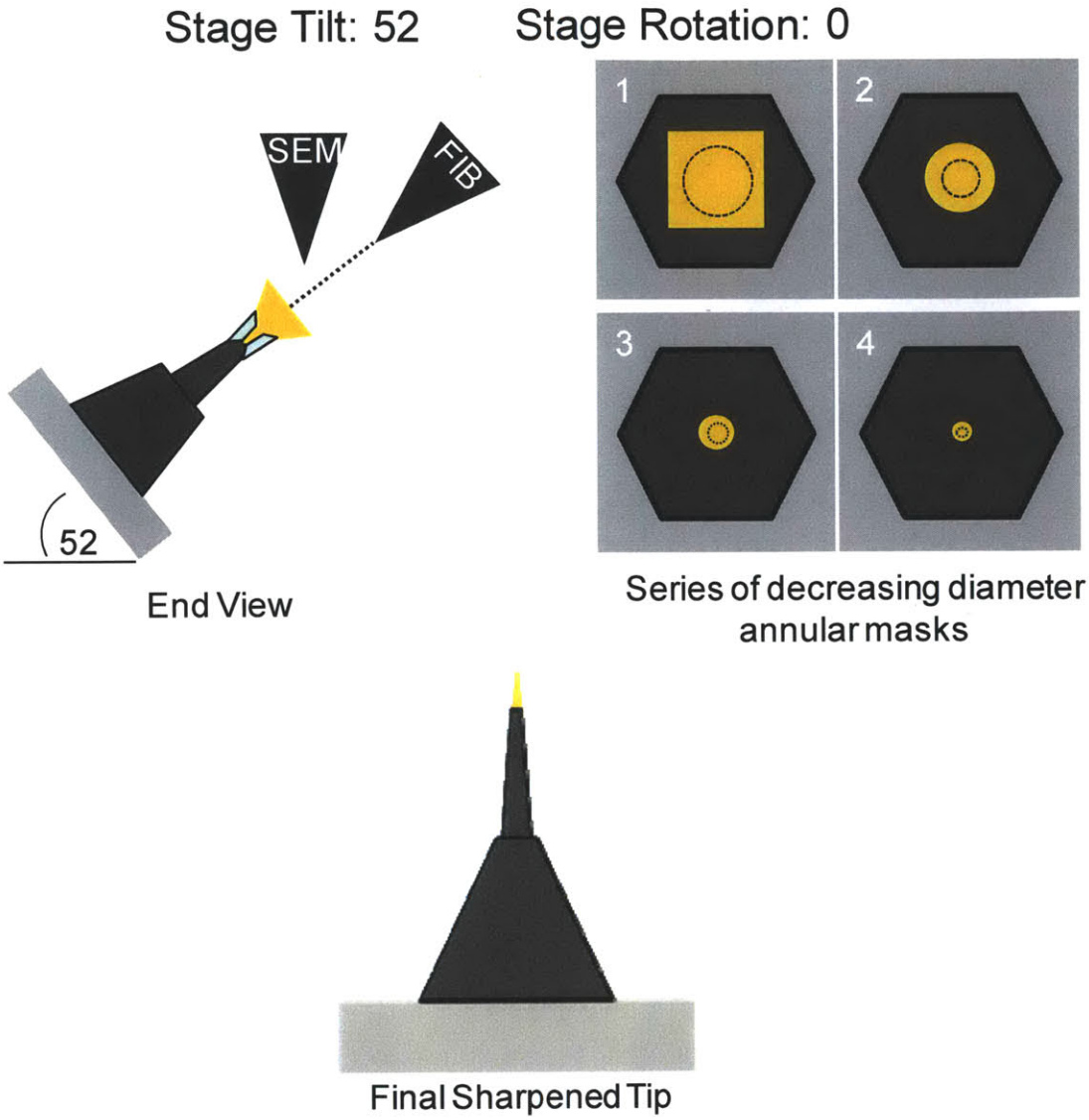

Figure 7 – APT tip sharpening schematic

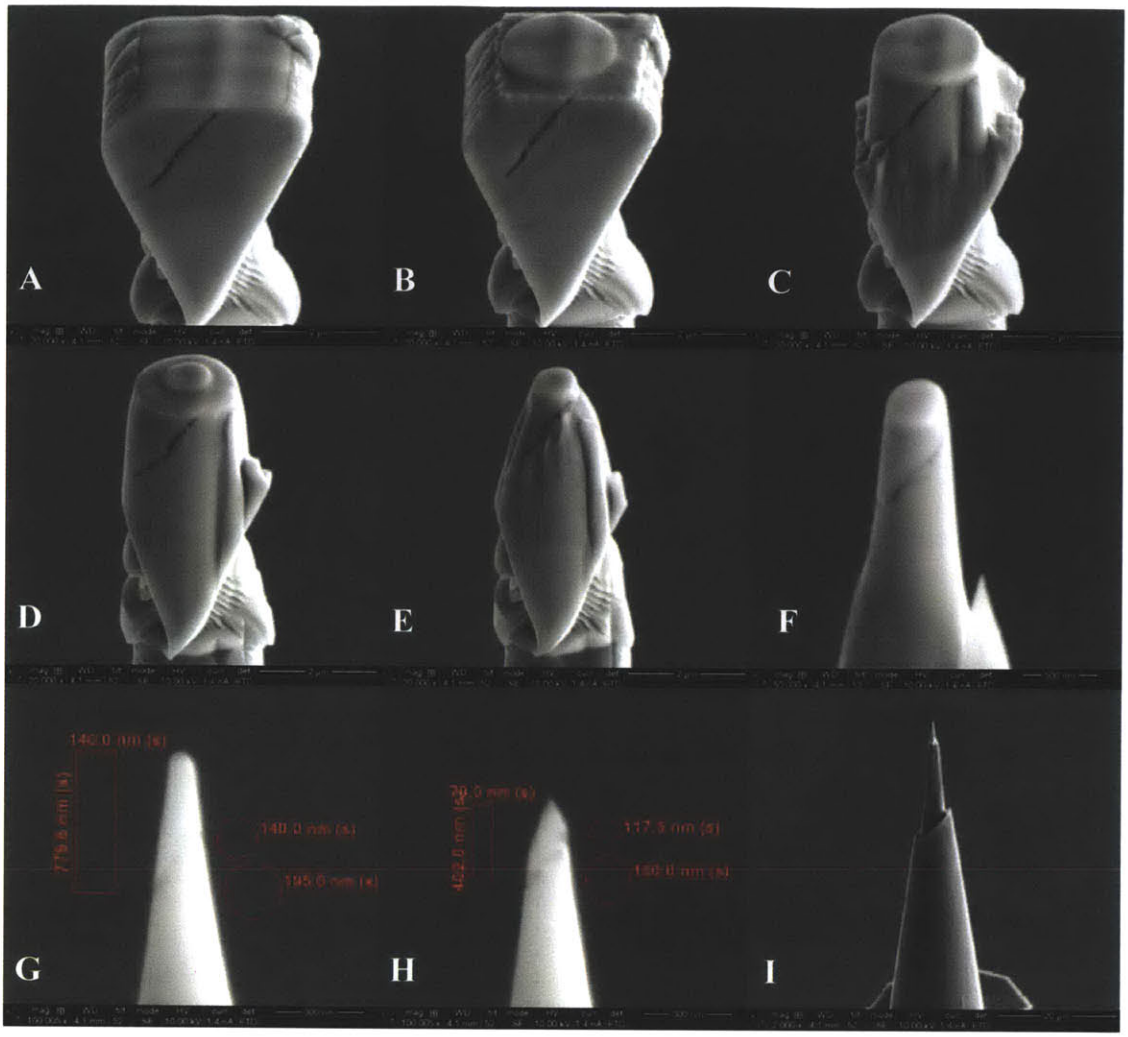

Figure 8: APT tip sharpening

Appendix B – Atom Probe Graphs with Error Bars

This appendix contains the graphs presented in the main text, but with error bars included. If the graph was generated as a byproduct of a proxigram analysis the error is reported in terms percentage. This is an absolute percentage, not a relative percentage based on each individual element. If a plot was generated as a byproduct of 1D concentration profile the error is presented in terms of percent sigma for a Gaussian distribution. This means that 100% sigma corresponds to an uncertainty of 34.1%, 10% sigma is 3.41% uncertainty, etc. The sigma uncertainty percentages reported here are absolute percentages, not elemental relative percentages. For example, a 2% uncertainty for an element that has a concentration of 10 at% corresponds to a 20% relative uncertainty.

Crack growth rate graphs from Chapter 3 are not included because the total error was small (≈ 4%).

B.1 Chapter 2 Graphs

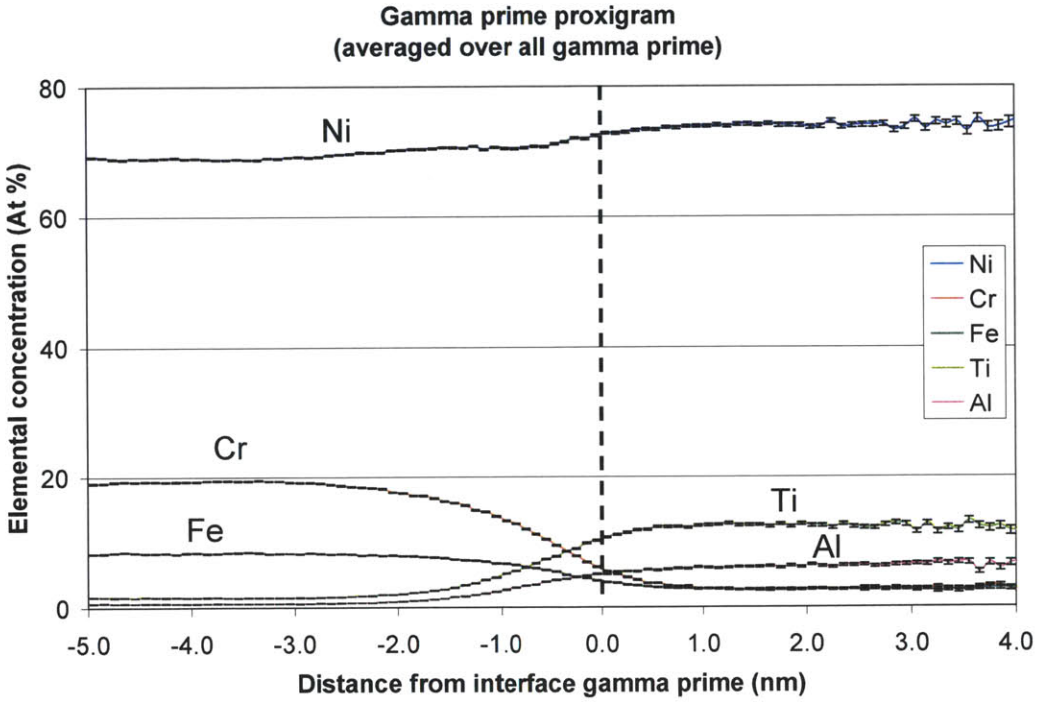

Figure 1: Compositional profiles in γ'

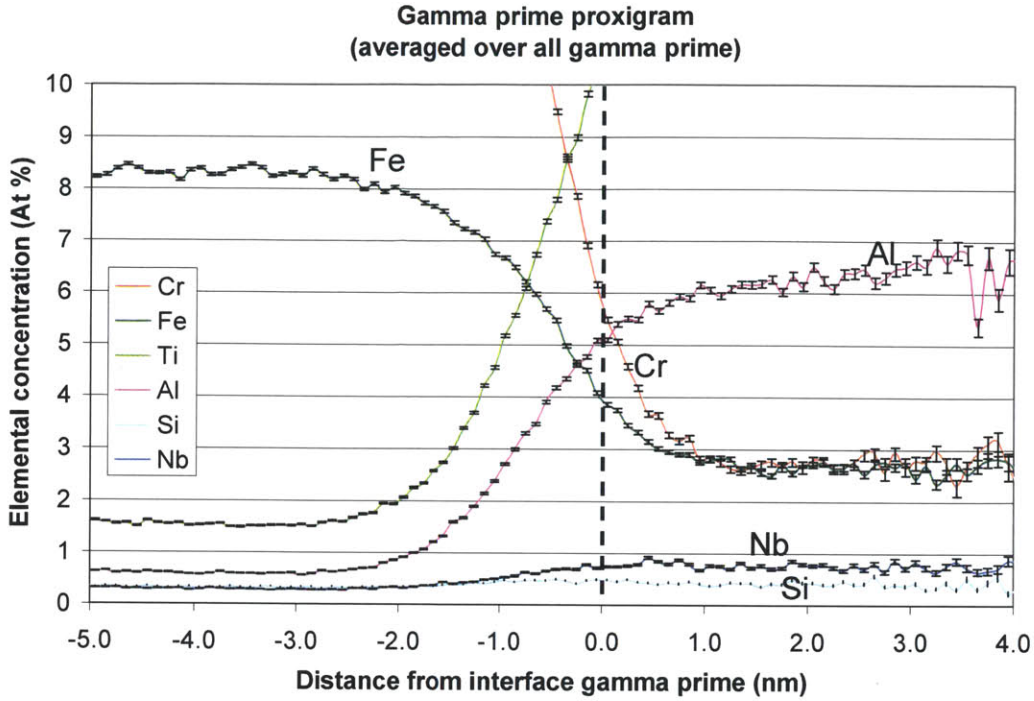

Figure 2: Compositional profiles in γ' (focused on 0-10 at% range)

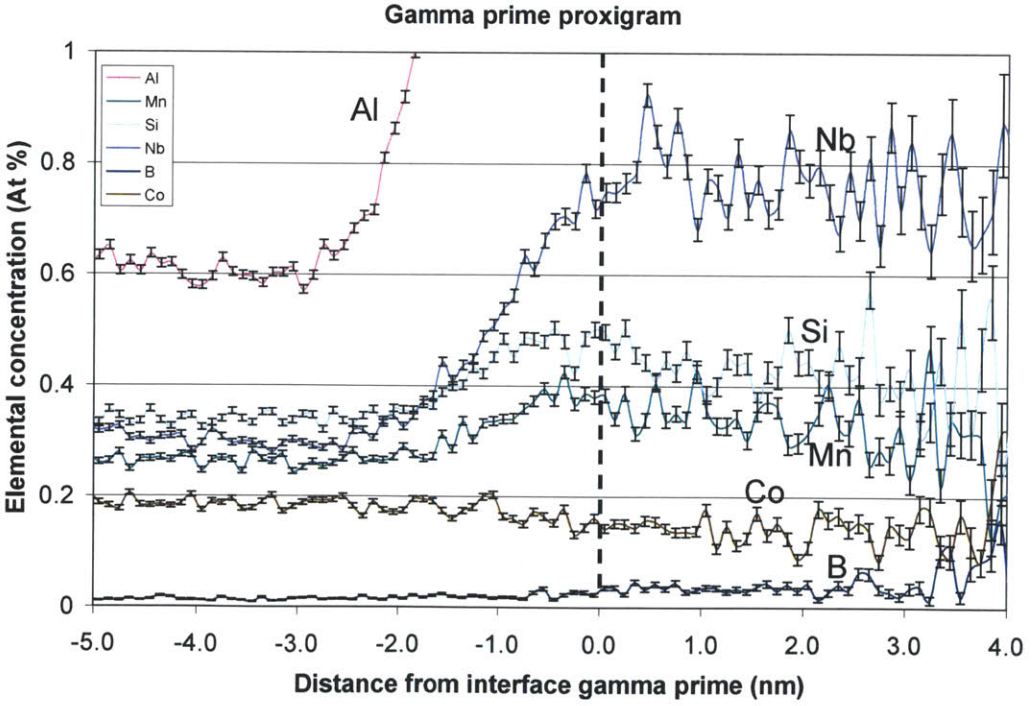

Figure 3: Compositional profiles in γ' (focused on 0-1 at% range)

B.2 Chapter 5 Graphs

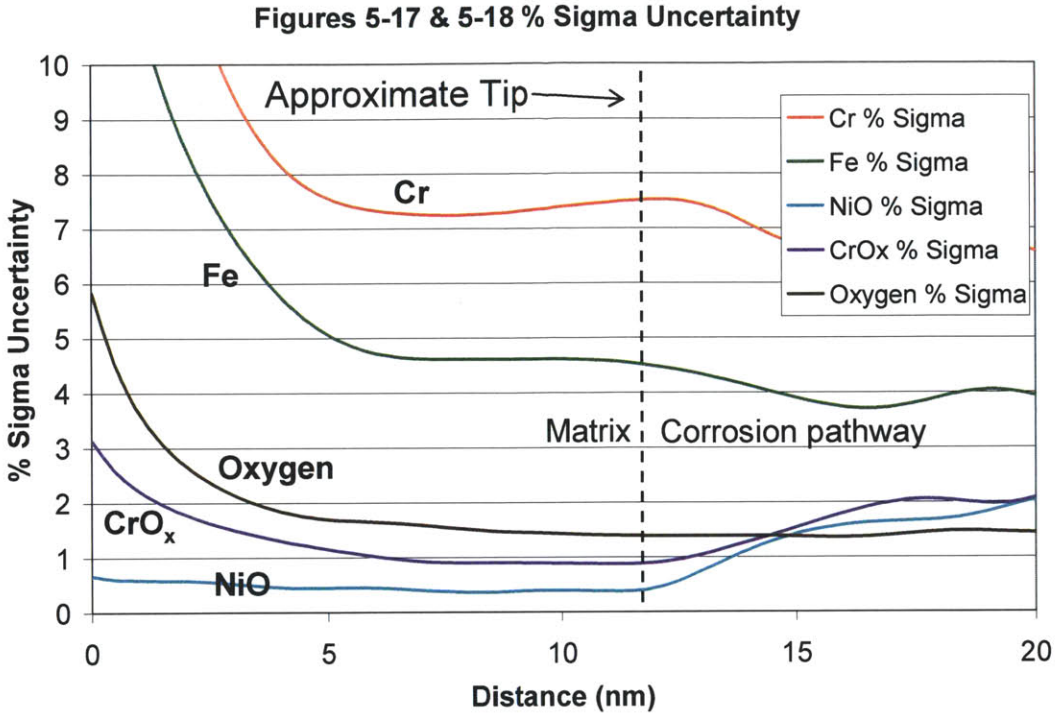

Figure 4: Percent sigma uncertainty for tunnel #1 composition measurements, focused on oxygen and oxides

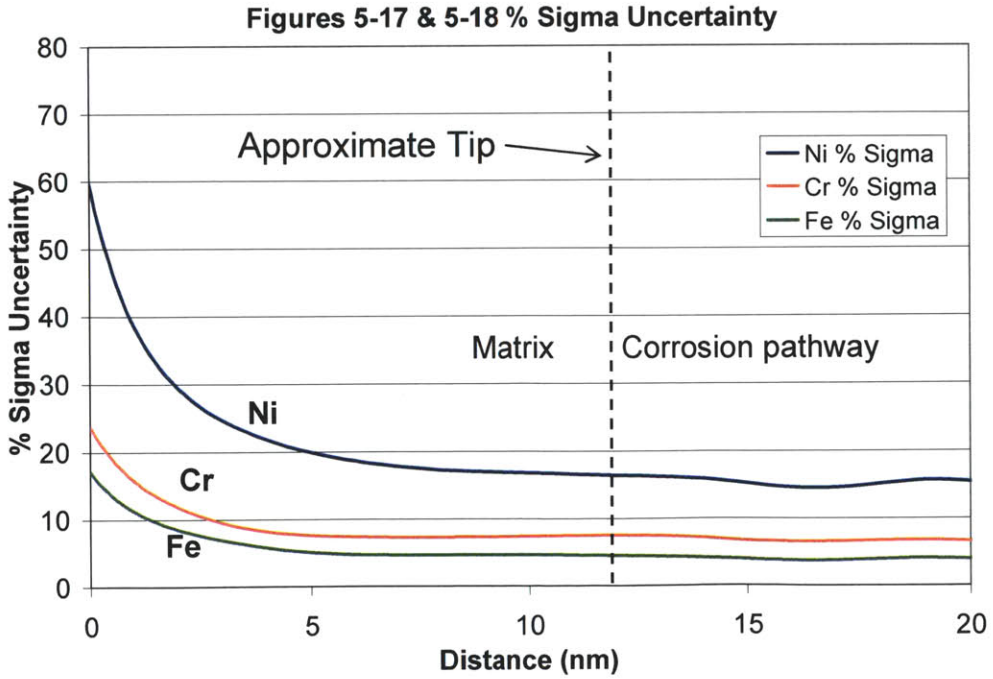

Figure 5: Percent sigma uncertainty for tunnel #1 composition measurements, focused on main alloying elements

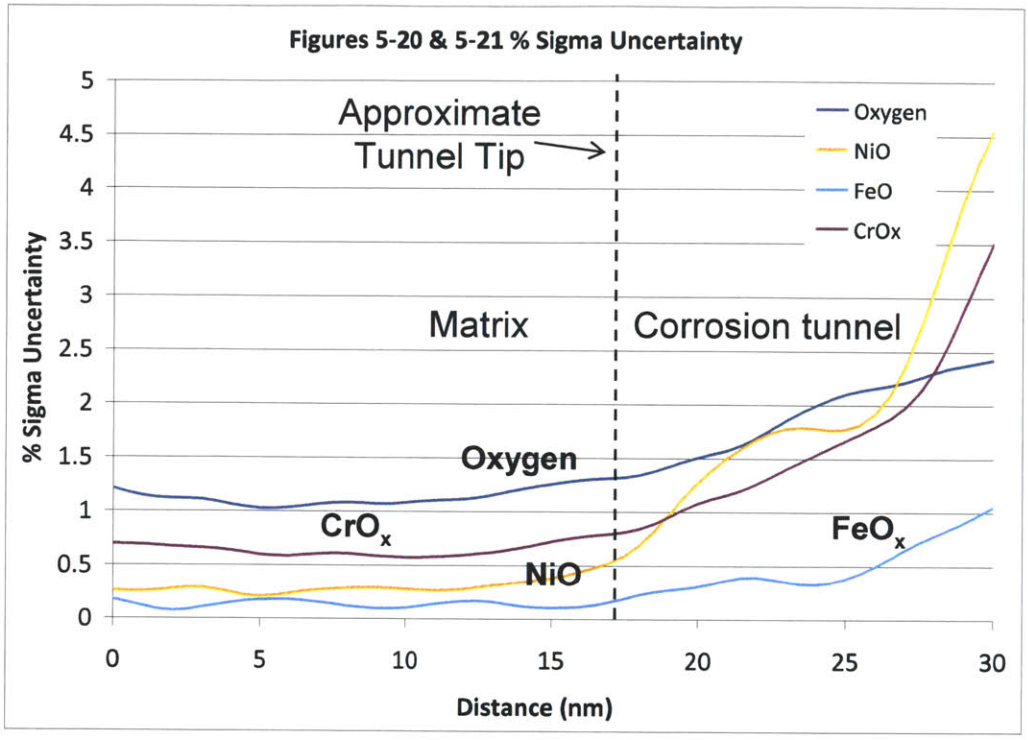

Figure 6: Percent sigma uncertainty for tunnel #2 composition measurements, focused on oxygen and oxides

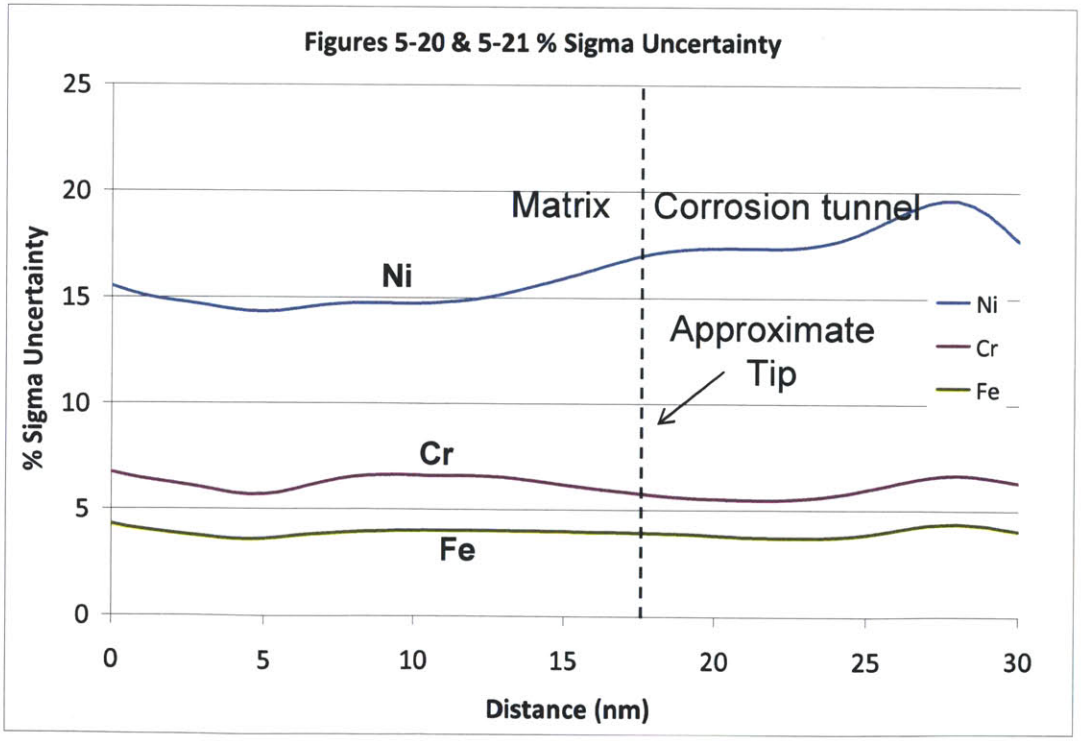

Figure 7: Percent sigma uncertainty for tunnel #2 composition measurements, focused on main alloying elements

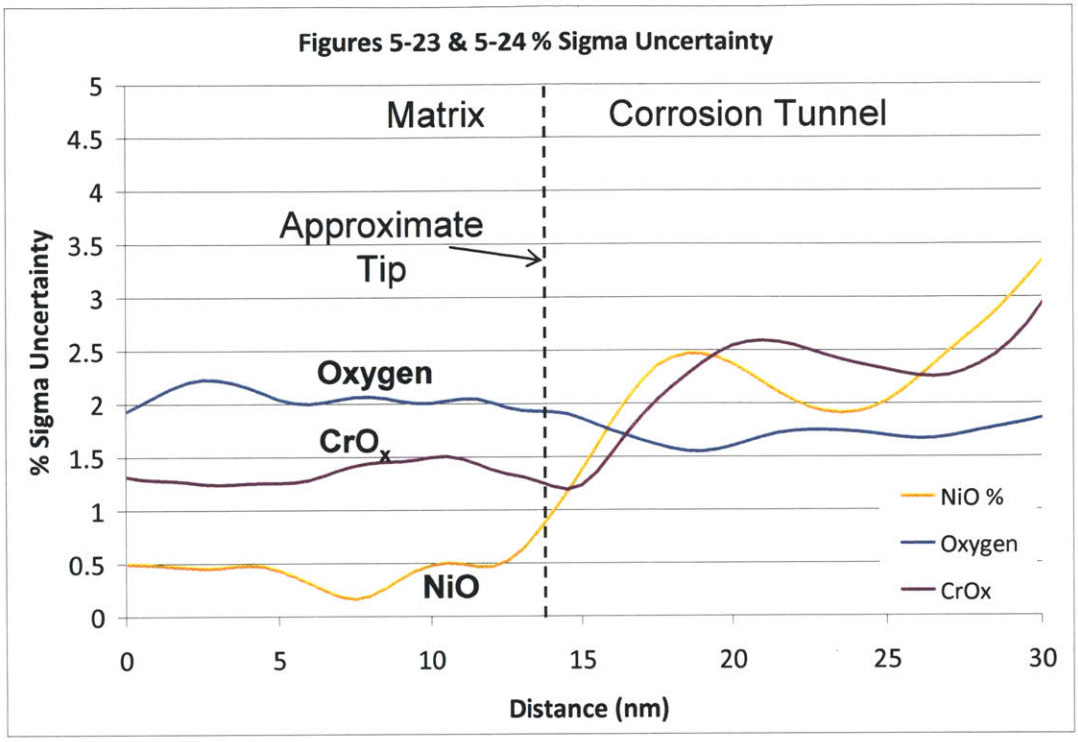

Figure 8: Percent sigma uncertainty for tunnel #3 composition measurements, focused on oxygen and oxides

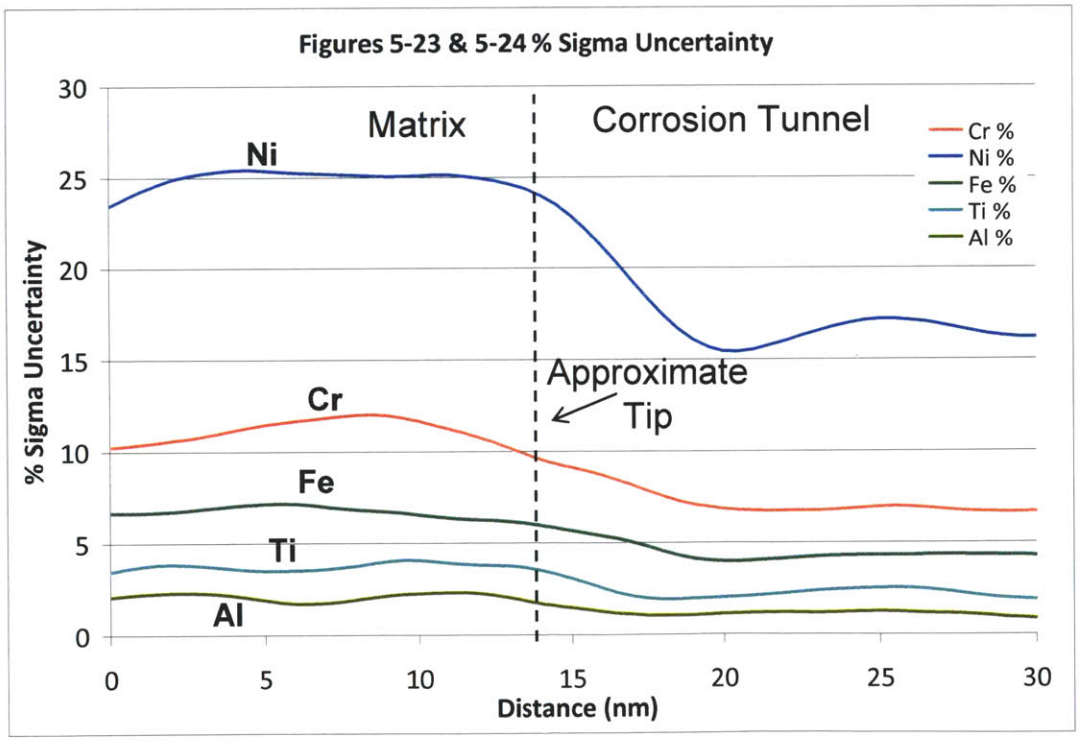

Figure 9: Percent sigma uncertainty for tunnel #3 composition measurements, focused on main alloying elements

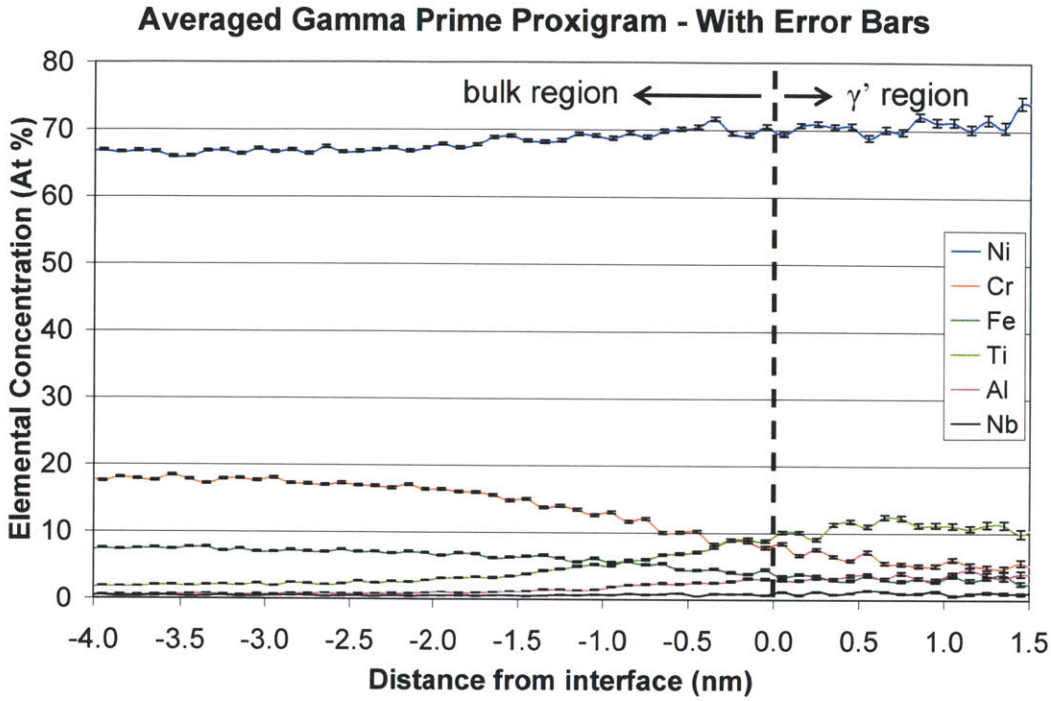

Figure 10: Proxigram of averaged γ' composition in Crack Tip 1, focused on main alloying elements

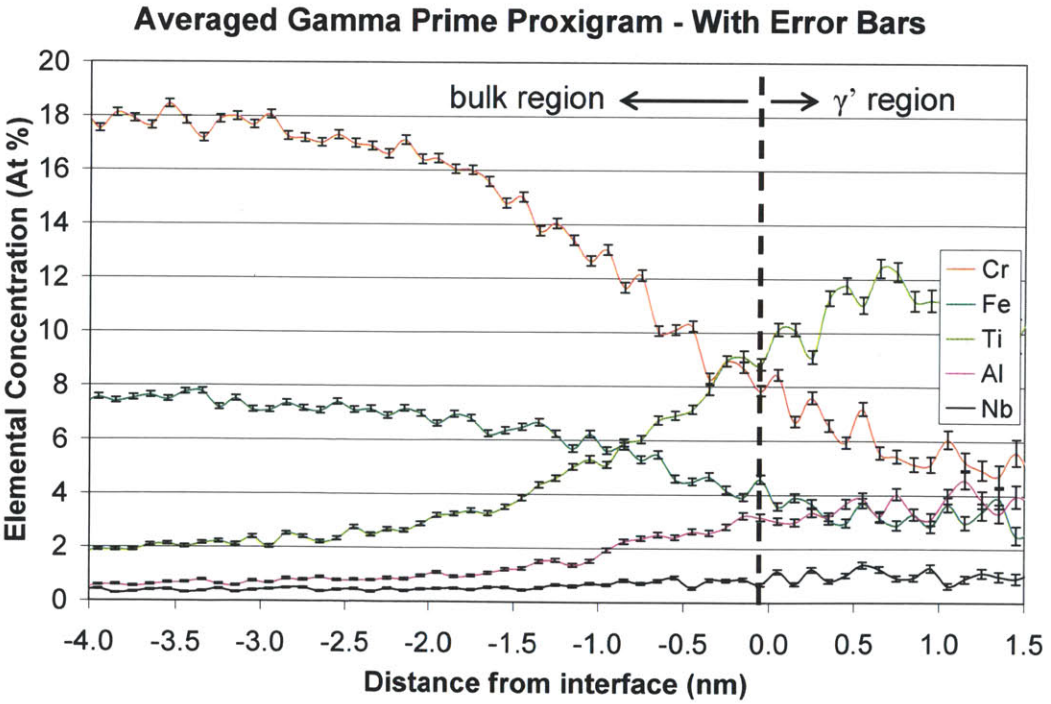

Figure 11: Proxigram of averaged γ' composition in Crack Tip 1, focused on mid-range alloying elements

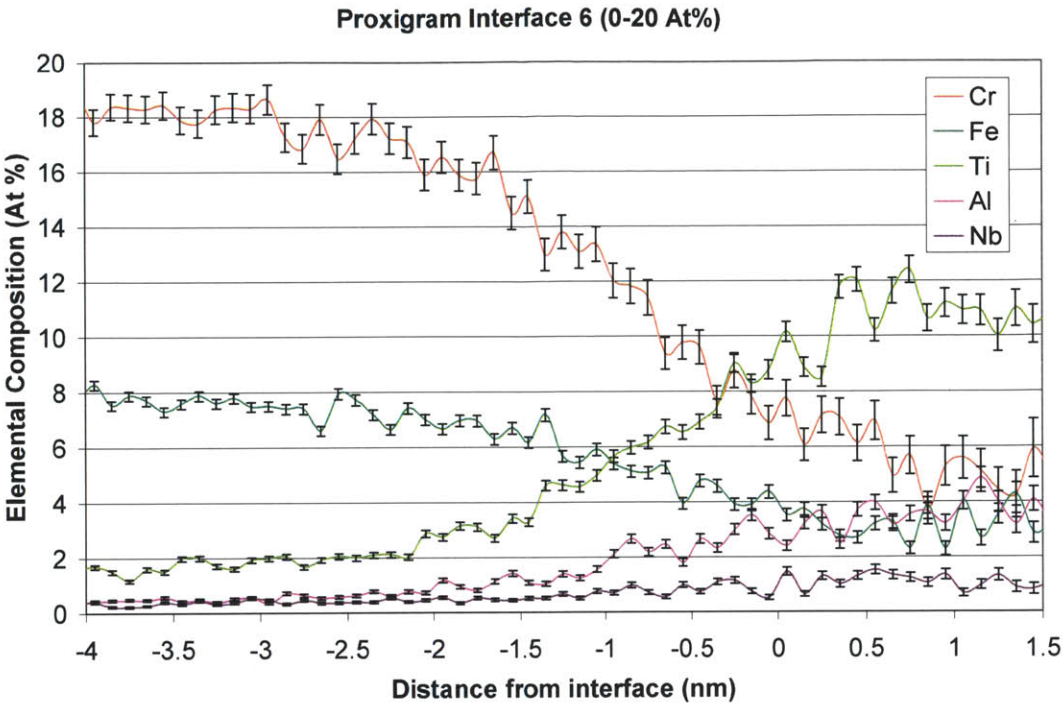

Figure 12: Proxigram for γ' located close to crack wall (γ' indicated by arrow in original figure)

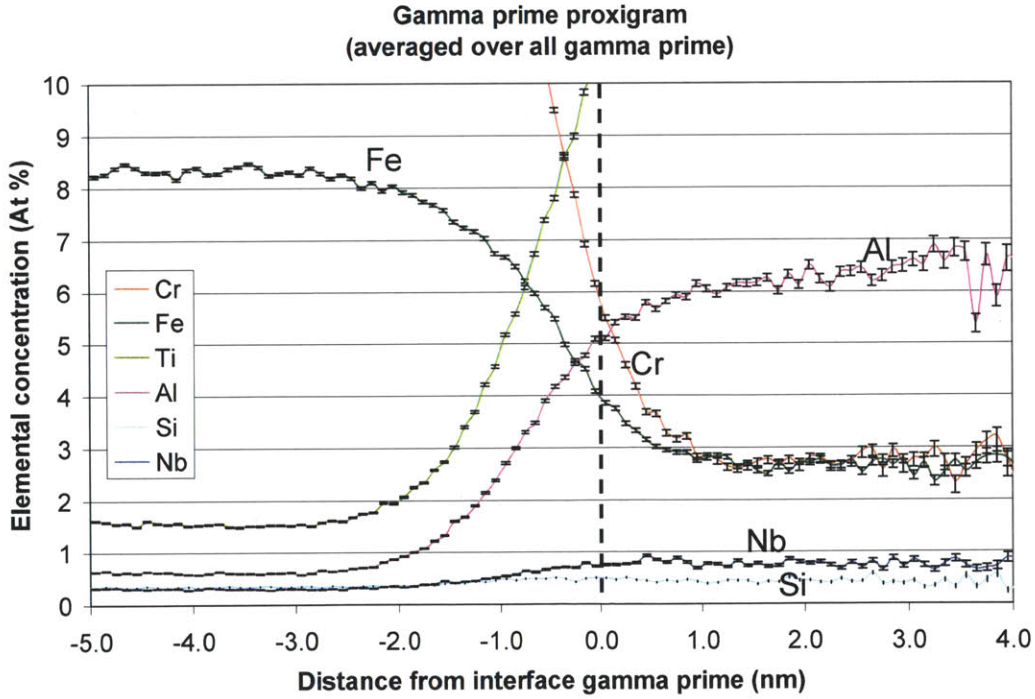

Figure 13: Proxigram of bulk γ' and surrounding base material

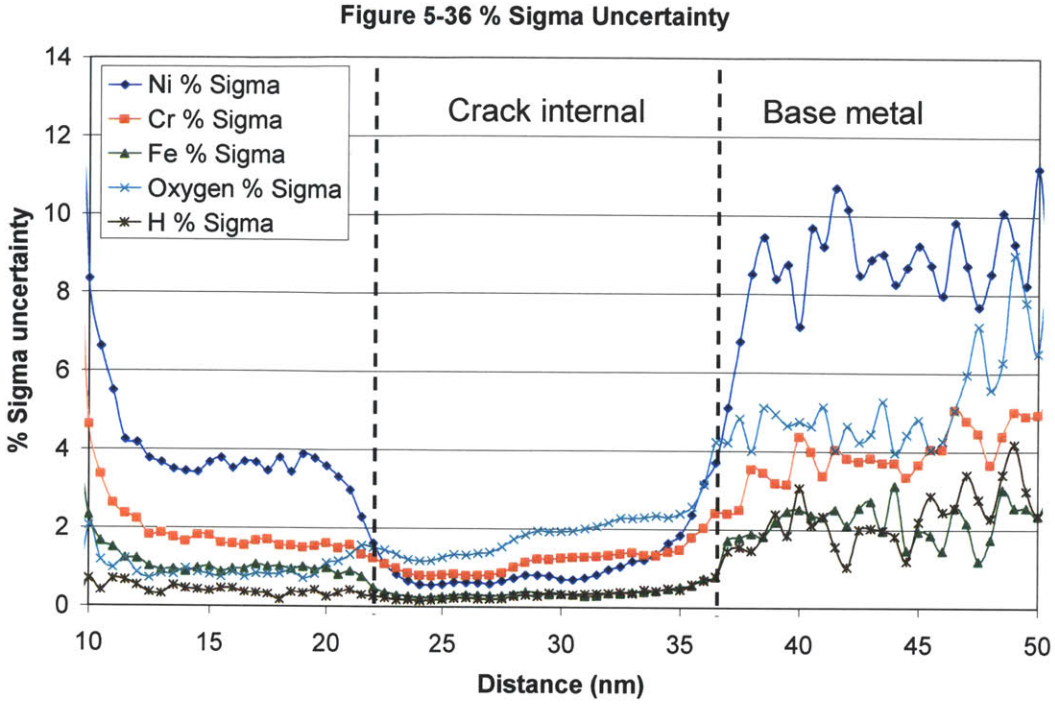

Figure 14: Percent sigma uncertainty of crack oxide elemental concentration profile

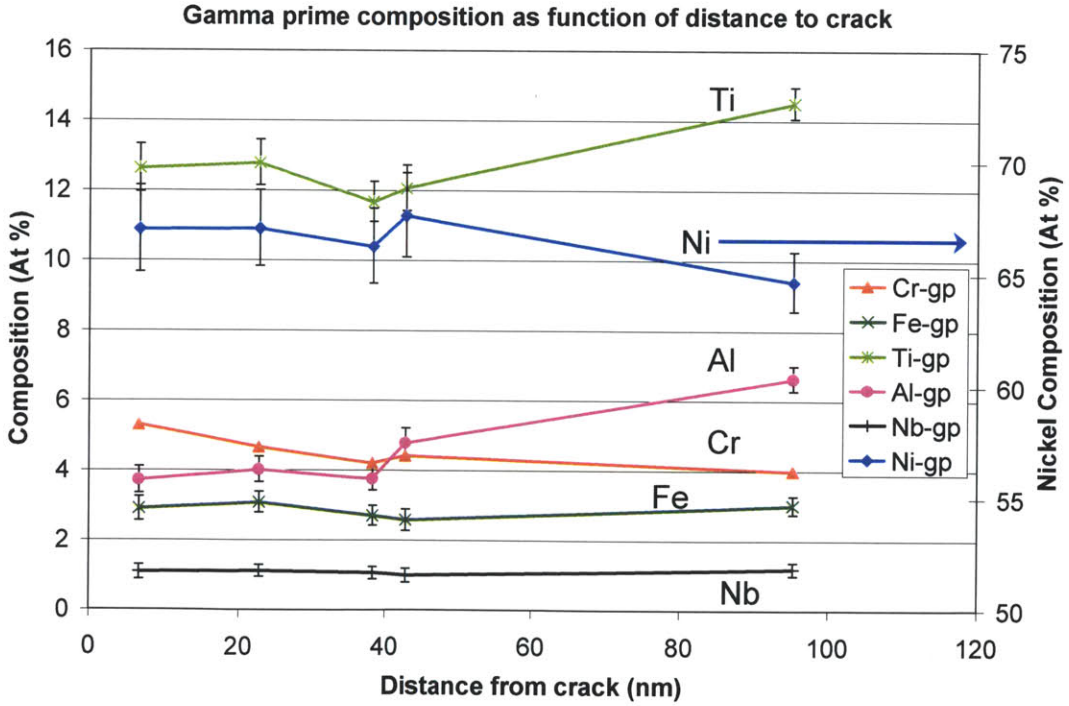

Figure 15: γ' composition as function of distance from crack wall

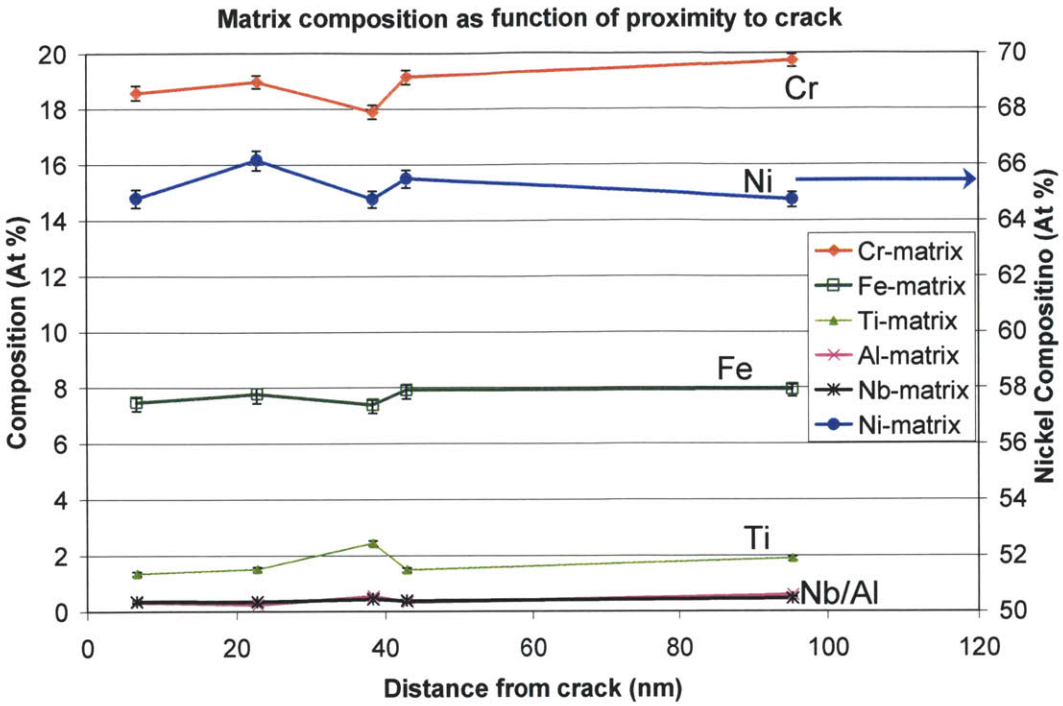

Figure 16: Matrix composition as function of distance from crack wall

Appendix C – Mechanical Testing: Tensile and Fracture Mechanics

C.1 Overview

Interior and surface flaws are found in all metal structures, which cannot be avoided as they arise from the manufacturing process. Fortunately, not all flaws are unstable under *in situ* service conditions. Fracture mechanics is the analysis of the stable vs. unstable cracks and crack propagation methods. Two of the original theories that addressed the issue of fracture mechanics are Griffith's theory of strain-energy release rate and Irwin's theory, which is a modification of Griffith's theory and addresses fracture toughness. The following information is needed for a fracture mechanics prediction of failure:

1. Applied stress
2. Residual stress
3. Size and shape of the component
4. Size, shape, location, and orientation of the crack

Usually, all of this information is available and conservative assumptions have to be made in engineering design. Occasionally, post-mortem fracture-mechanics analyses are carried out to determine failure modes and methods. In the absence of extreme overload, the causes are either insufficient toughness (K_{IC}) or an excessively large crack that was not detected during routine inspection. Insufficient fracture toughness is a highly important criterion for determination of impending failure in nuclear reactor components. The dose rate and accumulated dose are both important as they can influence the fracture toughness value; most notably, cause a reduction which may lead to a previous stable flaw becoming unstable. This thesis served as a baseline for eventual IASCC and environmental fracture testing. The irradiation and aqueous fracture tests will be an extension of this project and are outside the range of the material in this thesis.

Fracture toughness is measure of the amount of energy a structure containing an existing flaw can absorb before crack growth and is an important criterion for determining the susceptibility to failure of structural materials. For this project, mechanical characterization included tensile testing and fracture toughness testing, at room temperature and at 288 °C. The tensile testing was performed as per ASTM E8-04 on specimens machined from the same X-750 ingot as the compact tension specimens for the fracture toughness tests. The fracture toughness tests were

performed using an Instron 8500 servo-hydraulic load frame with temperauture control via an MTS box furnace. The fracture toughness evaluations followed ASTM E1820 using 1T compact tension (CT) specimens, which are illustrated in Figure 1. The room temperature tensile and all fracture toughness tests were completed at the Idaho National Laboratory and the 288 °C tensile tests were completed at the Massachusetts Institute of Technology. The experimental procedure for these tests is presented in the ASTM guidelines for fracture toughness testing.

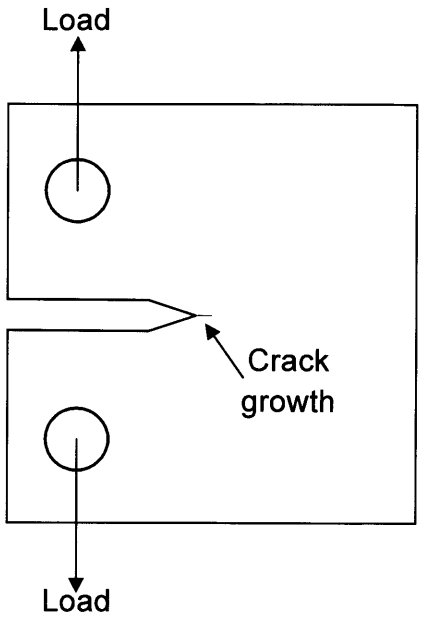

Figure 1: CT Specimen

J-integral vs. crack extension data was evaluated to estimate a crack growth resistance (J-R) curve. From this curve a value for J_{IC} was estimated and from this K_{IC} is calculated from Equation (1). K_{IC} is the plain strain fracture toughness for the material (estimated from the non-linear elastic fracture toughness, J in this case but strictly represents fracture toughness for a brittle material). The equation for K_{IC} is a function of Young's Modulus, *E*, and Poisson's ratio, ν. The J-intergral is the strain energy release rate for the material as a crack propagates; the linear elastic fracture toughness (K) may be calculated from the non-liner elastic fracture toughness (J) provided that no plastic unloading has occurred at the crack tip, i.e. prior to stable tearing. The point J_{IC} defines the point at which stable crack propagation beings under mode one loading. K_{IC} and J_{IC} are affected by many conditions; most important to this project are temperature and environment. The environment is namely high purity water with dissolved hydrogen or oxygen. The environment will eventually include radiation dose as the project evolves. K_{IC} values are used to determine the critical crack length when a given stress is applied to a component, above which will lead to unstable propagation. The two most common expressions for plane-strain fracture toughness are Equations (2) and (3):

$$K_{IC} = \sqrt{\frac{J_{IC} E}{1-\nu^2}} \tag{1}$$

$$\sigma_C \leq \frac{K_{IC}}{Y\sqrt{\pi a}} \tag{2}$$

$$a_C = \frac{1}{\pi}\left(\frac{K_{IC}}{\sigma Y}\right)^2 \quad (3)$$

In fracture mechanics, Equation (2) is used to determine the critical stress value when a crack of a given length, *a*, is found in a component and Equation (3) is used to determine the critical crack length when a given stress is applied to a component. These expressions for critical stress (and critical crack length) can be determined by rearranging the fracture toughness expression in ASTM E1820. The variable Y is a constant related to the sample's geometry, and can be taken as unity for the general case of an infinite plate containing a center crack of length 2a. Sigma, σ, is the stress applied to the component. It should be noted here that the above expressions of fracture toughness are provided for conceptual understanding and the methods used to determine the mechanical properties followed the guidelines in the ASTM standards.

The variability of the fracture toughness and J-integral values can be attributed to several reasons, such as different ingots within the same heat treatment, orientation of machined specimens, and experimental error. The fracture toughness of a material commonly varies with grain direction; therefore, it is conventional to specify specimen and crack orientations. The CT specimens used for all of the testing were machined from the same heat of metal in the same orientation. Therefore, orientation is not a variable in this set of mechanical tests. The results for the fracture toughness for this set of tests are consistent with the variability of the published mechanical properties for Inconel alloy X-750.

C.2 Tensile Testing

C.2.1 Overview

Tensile tests have been completed for room temperature testing and the results are used to determine yield strength (σ_Y), ultimate strength (σ_U), and percent elongation. Typical results for tensile tests are presented in terms of stress vs. strain, and are shown in Figures 2 and 3 for the room temperature tests. Figure 3 shows a complete stress-strain curve for an alloy X-750 sample with the yield, ultimate, and rupture stresses labeled. Figure 3 is focused on the location of the yield strength and has the yield strength and the 0.2% offset labeled. Two other alloy X-750 specimens were tested at 25 °C and the results for the three tensile tests are recorded in Table 1.

C.2.2 Room Temperature Test Procedure

The tensile specimens were machined from an 82.6 mm (3.25 in) diameter ingot of alloy X-750. The specimens had a nominal diameter of 8.9 mm (0.35 in) and a 35.6 mm (1.4 in) gage length. The crack plane was perpendicular to that of the compact tension specimens. The specimens were secured in the test frame with 5/8 inch threaded grips. The tensile test was run with a constant strain rate of 0.5 mm/min until rupture. The load, load frame load-line displacement, and extensometer readings were recorded.

C.2.3 288 °C Test Procedure

The tensile specimens were machined from the same ingot as the room temperature tests and their preparation is described above. The tensile specimens were tested with an Instron 8500 servo-hydraulic load frame in constant a constant displacement rate of 0.5 mm/min until rupture. The strain rate was measured with the internal Instron linear variable differential transformer (LVDT). A resistive heater was used to maintain the test specimen at 288 °C. Each specimen test temperature was verified with two type-K thermocouples attached to the surface. The specimens' surface temperature were maintained at 288 ± 3 °C for fifteen minutes to ensure homogeneous temperature. During heat-up, the Instron test frame was kept in force control with a small amount of preload (≈50 lbs) was maintained on each specimen during the short temperature equilibration period. The load and load frame load-line displacement were recorded.

C.2.3 Results and Discussion

Comparing the tensile test results to published mechanical data for Inconel alloy X-750 reveals some discrepancy in properties. The mechanical properties for the room temperature tensile tests in this work are recorded in Table 1. The published mechanical properties are recorded in Table 2. A rough approximation for the Young's Modulus was calculated using the elastic region from the tensile tests yields a value are within 5% of industry accepted values and are within acceptable experimental scatter. The yield and ultimate strength for this set of tests are considerably lower than the published values. The average yield strength is 565 MPa compared to the published value of 841 MPa. Similarly, the average ultimate strength is 998 MPa compared to the published value of 1240 MPa.

Table 1 - Room Temperature Tensile Data

Specimen	Young's Modulus, E, (GPa)	Yield Strength (MPa)	Ultimate Strength (MPa)	Rupture Strength (MPa)
I	210.7	557.0	988.6	835.3
II	207.3	582.5	1018.5	856.8
III	207.2	555.5	987.8	847.0
Average	208.4	565.0	998.3	846.4

Table 2 - Published Data [1]

Temperature (°C)	Young's Modulus, E GPa (Msi)	Yield Strength MPa (ksi)	Ultimate Strength MPa (ksi)
25	213.7 (31.0)	841.2 (122.0)	1241.1 (180.0)

Tensile specimens failed after approximately 44% engineering strain and the fracture surface exhibited predominately ductile fracture, as evident by the dimpled morphology and the "orange-peel" topography on the outer surface. It is important to note here that the stress-strain curves for samples II and III employed an extensometer with a one-inch gage length and only capable of approximately 10% strain. Therefore, the strain to failure was not recorded. The extensometer was removed after the yield strength was established, which is the most important engineering parameter for these tests. The stress-strain test for Specimen I employed a large-range extensometer with a 1.4 inch gage length. The large-range extensometer was kept on the tensile specimen through failure.

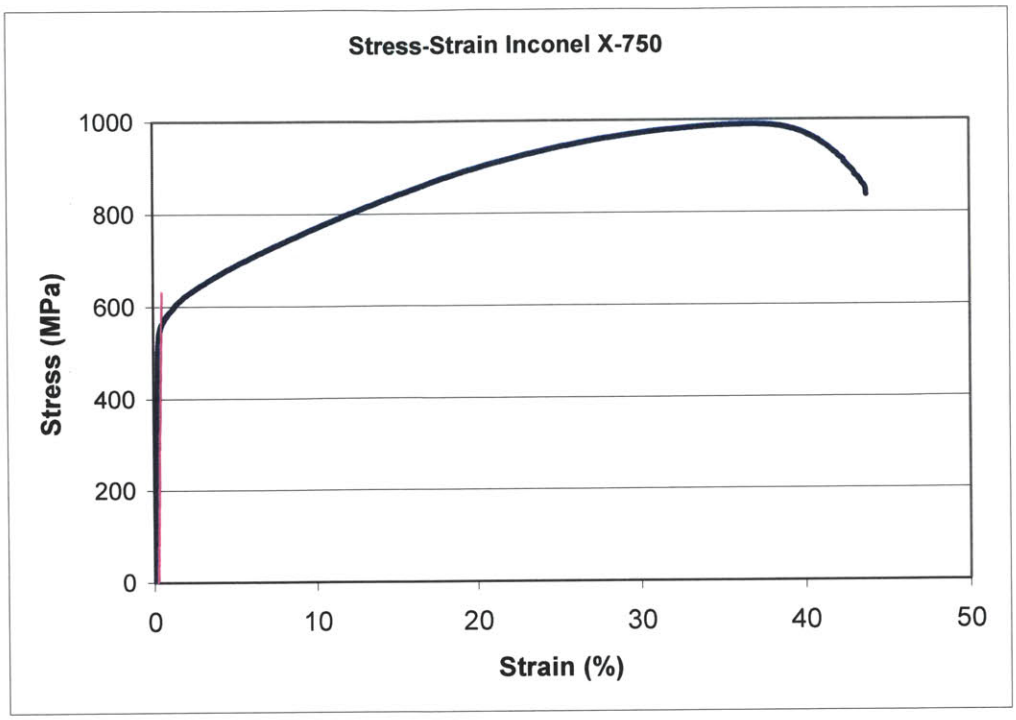

Figure 2: 288°C stress-strain curve: Inconel alloy X-750

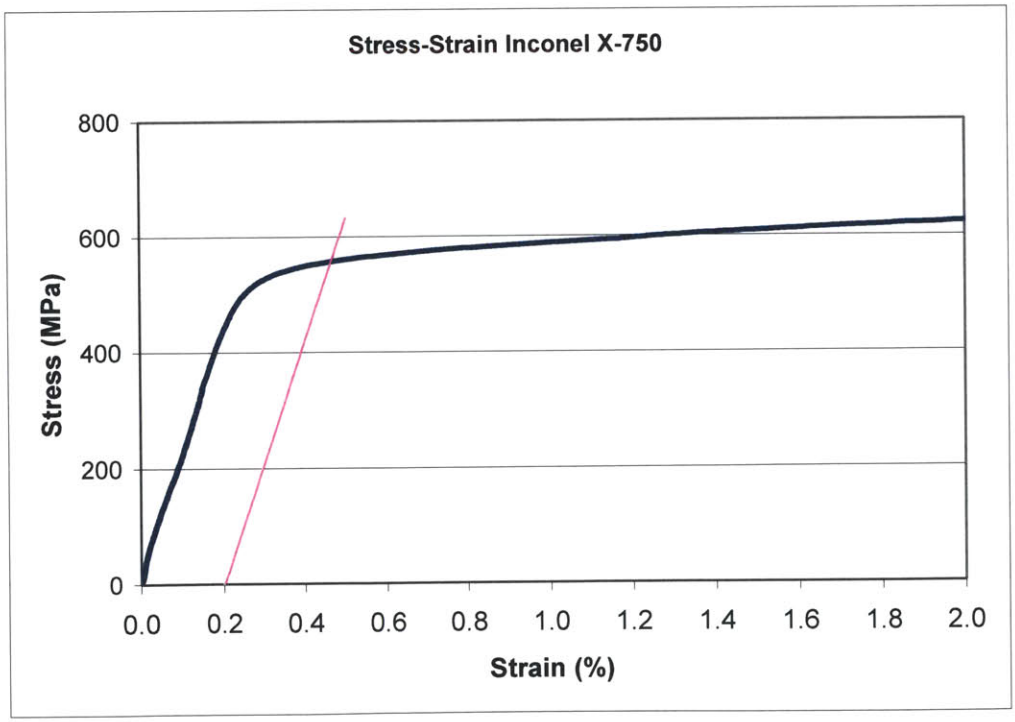

Figure 3: 288°C stress-strain curve: Inconel alloy X-750, reduced strain range

C.3 Fracture Toughness Testing

C.3.1 Test Procedure and Specimen Preparation

Fracture tests were performed at room temperature and 288 °C. The published mechanical properties (Poisson's ratio, Young's Modulus, and ultimate strength), provided in Table 2, were employed to calculate the K_{IC} and J_{IC} values. The precracking procedure was performed in air at room temperature and monitored with DCPD. The fatigue precrack extension was performed under constant amplitude (R = 0.1) at room temperature for the room temperature and 288 °C specimens. The 288 °C specimens were fatigued with a lower ΔK to compensate for the lower Young's Modulus at 288 °C. The precracking for the room temperature fracture toughness tests ended at $K \approx 60$ MPa$\sqrt{m}$ and at $K \approx 29$ MPa$\sqrt{m}$ for the 288 °C tests. The room temperature fracture tests employed a constant displacement rate of 0.2 mm/min. The displacement rate was slowed to 0.1 mm/min for the high temperature fracture tests until the specimen was undergoing steady, ductile tearing, at which point the rate was increased to 0.2 mm/min. The lower displacement rate for the 288 °C was used to record a greater amount of data during the early stage of the test. DCPD was utilized to measure incremental crack extension and was set to sample the voltage change at predesignated intervals of time, load, and displacement. The lower displacement rate was chosen for the 288 °C tests to record the fracture data with a smaller mesh space. The initial crack extension data points are especially important to determine accurate K_{IC} and J_{IC} values and the slower displacement rate provides higher accuracy results.

The 1TCT specimens were machined from the same ingot as the tensile specimens and the specimens used in this work for crack growth rate testing. The room temperature specimens were side-grooved with a 10% semicircle width reduction along the crack plane to provide a singularity to promote straighter crack growth. Specimens used for the 288 °C tests were initially side grooved in the same manner as the room temperature specimens, but experienced pronounced crack front tunneling. The side groove was increased to 25% width reduction with 60° grooves, which is the maximum allowed in the ASTM guidelines. The increased singularity resulted in slight reverse tunneling, but the overall crack extension fell within the ASTM limits addressing the required uniform crack front.

It is important to note here that the DCPD wire placement did not follow the ASTM guidelines and the arrangement for this set of tests is illustrated in Figure 4. Furthermore, the a/W formula

used to compute the incremental crack extension was developed by General Electric and corresponds to non-ASTM wire placement. The equations use to relate voltage changes to a/W is provided in Equation (4). The test assemblies are shown in Figures 5 and 6 for the 288 °C testing. The room temperature tests used the same setup minus the furnace and quartz clip gauge.

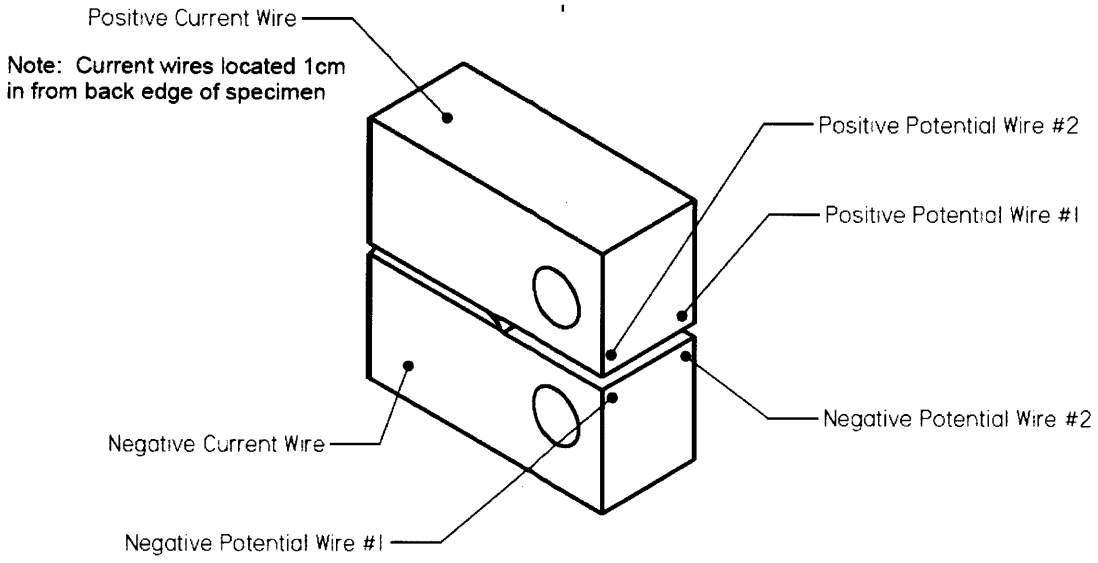

Figure 4: DCPD wire placement

$$a/W = \frac{-1}{2.43175 \ln\left(\frac{\frac{-10.7615}{V} - 1}{-29.1584}\right)}, \tag{4}$$

where:

a/W = the ratio of crack length divided by total specimen length

V = calibrated voltage

The test procedure for the room temperature and 288 °C specimens was identical, except that the 288 °C tests employed a quartz clip gauge and a resistive-heated furnace. The specimens for the 288 °C tests were brought to test temperature and maintained at a surface temperature of 288 ± 3 °C for a minimum of 30 minutes. The temperatures were verified by three type K

thermocouples: one thermocouple was placed across the crack plane on each side of the specimen and one was placed on the bottom, back corner near a current wire.

After sufficient ductile tearing was achieved each specimen was post J-test fatigue cracked to clearly delineate the end of the ductile tearing region. The test completed with tearing the specimen into two pieces. Optical measurements were taken at 9 locations widthwise to document crack extension and calculate the fracture toughness value. The voltage readings were calibrated to correspond to the initial crack length and then the incremental crack extensions were calculated using the physical crack length and the DCPD measurements. Next, the fracture data was processed using the relationships outlined in ASTM E1820 Section A2. The results for the room and 288 °C tests are shown in Figures 7 and 9, respectively, and are in the form of a set of J vs. Δa curves.

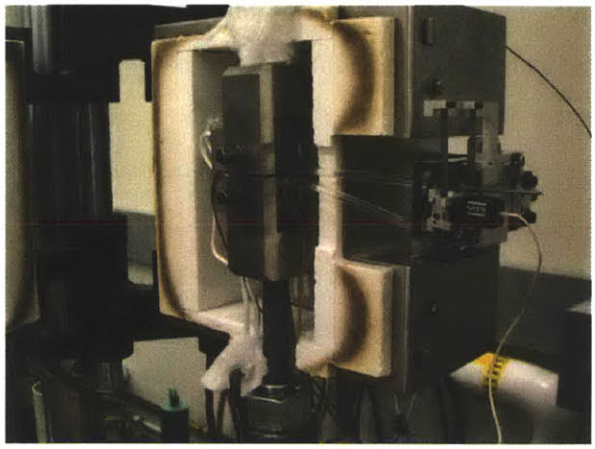

Figure 5: Furnace (open) test apparatus

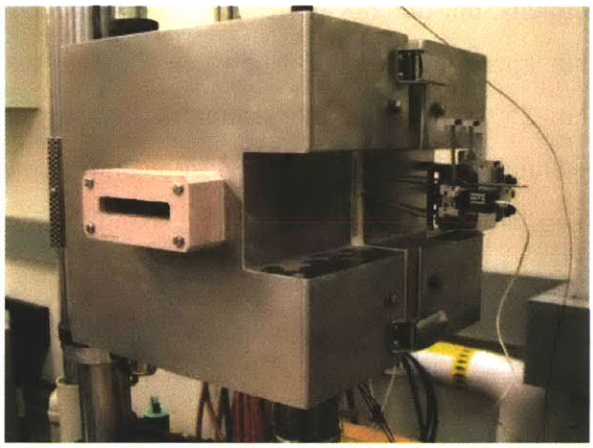

Figure 6: Furnace (closed) test apparatus

C.3.2 Data Handling and Results

The data collected in each test included load, crosshead displacement, and DCPD voltage at several probe distances. Clip gage displacement was also recorded for the 288 °C tests. The fracture data was recorded and then processed using the relationships outlined in ASTM E1820 for incremental crack extension measured with DCPD. The results for the room and 288 °C tests are shown in Figures 7 and 8 and are in the form of a set of J vs. Δa curves. The J-integral values were determined by calculating the J value with each incremental crack extension. The beginning of each test exhibited large crack extension with small J values. This is an artifact of the DCPD measurements and measure large voltage changes with initial crack opening. The K

and J values have a large degree of uncertainty, as evident in the results. Much of this uncertainty stems from the lack of distinctive boundary in the DCPD readings between the crack mouth opening and the beginning of the linear elastic region. Truncating the lower range data removes the ambiguity of the crack opening effects on the DCPD measurements. These DCPD readings registered voltage changes indicating large crack extensions at low loads. Truncation eliminates bogus readings when the test is within the initial crack mouth opening, but includes data that determine the J_{IC} values in the linear elastic region and track stable crack tearing. The J_{IC} values have close agreement among the room temperature specimens, but the 288 °C results exhibit larger scatter. The J_{IC} values at low temperature were within approximately 12% between the two extremes and the high temperature values were within 25%. Despite the scatter in the J_{IC} values for both sets of tests, the K_{IC} scatter is substantially lower. K_{IC} is the elastic component of J_{IC} and these contributions between samples are similar. The high temperature tests only have two data points for comparison and the degree of uncertainty is inconclusive with a sample size of two specimens. It is important to note here that the mechanical properties (Young's Modulus, yield strength, and ultimate strength) for the J-curve and the K_{IC} calculation were those listed in Table 2 and not the properties obtained through the tensile tests.

Table 3 -Air fracture data

Specimen	K (ksi$\sqrt{in}$)	J (psi-in)
RT1	123.8	1686
RT2	125.2	1900
RT3	128.9	1865
HT1	153.7	759
HT2	179.5	1035
RT Average	**126.0**	**1817**
HT Average	132.9	897

RT = room temperature, 25°C
HT = 288 °C

The truncated data required further data handling to obtain the J and K values. Before truncation each J-curve began at the origin; however, the invalid data due to the crack mouth opening effects resulted in false toughness values. Thus, after the invalid data was truncated each J-curve was linearly extrapolated to J=0 and then shifted so that this extrapolation passed through the origin. The J_{IC} value was determined from the J vs. Δa curves (intersection of construction line and J curve) and the K_{IC} value was calculated from the J_{IC} value. The relationship between K and J is provided in Equation 5.[2] The J_{IC} values are for the room temperature and 288 °C fracture tests are recorded in Table 3. The room temperature scatter is acceptable and the K_{IC} values are within 5% between the most extreme data points. Similarly, the 288 °C results are within 9%. The average room temperature fracture toughness is 126.0 ksi$\sqrt{in}$ (138.3 MPa$\sqrt{m}$). The average 288 °C fracture toughness is slightly higher than the room temperature toughness at

132.9 ksi√in (167.3 MPa√m) Symons, *et al.* documented K_{IC}=145 MPa√m for Inconel Alloy X-750, HTH heat treatment for the same room temperature testing conditions.[3] Thus, the results reported here are well within acceptable experimental scatter to accepted published properties.

$$J_{(i)} = \frac{K_{(i)}^2\left(1-\nu^2\right)}{E} + J_{pl(i)}\ , \tag{5}$$

where:

$J_{(i)}$	=	elastic component of J_{IC}
E	=	Young's Modulus
$K_{(i)}$	=	stress intensity
N	=	Poisson's ratio

Poisson's ratio was set at 0.3 for the room temperature and 288 °C tests, which is consistent with literature.

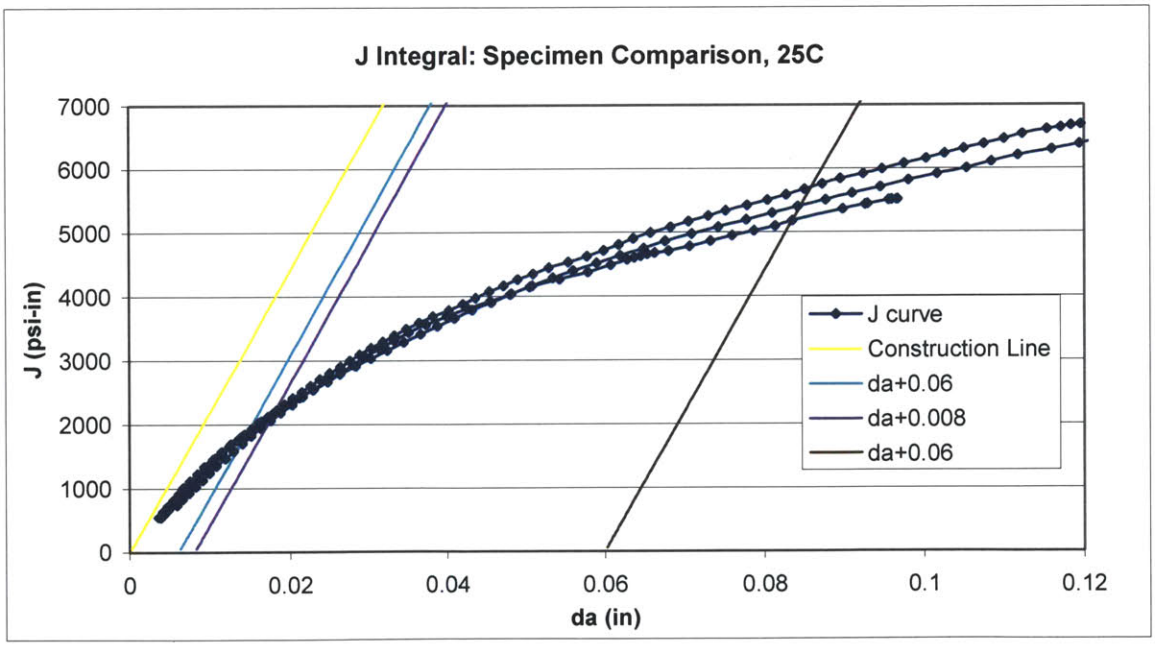

Figure 7: Room temperature J-integral fracture test

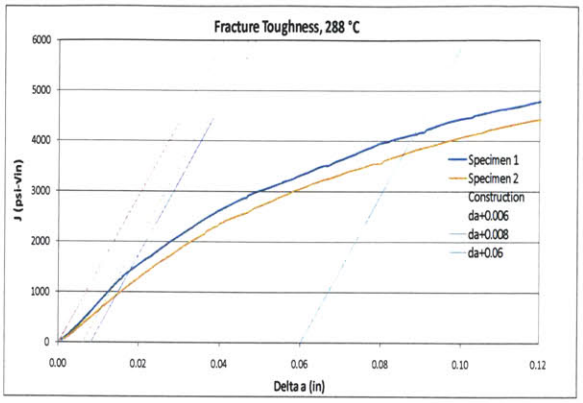

Figure 8: 288 °C J-integral fracture test

C.3.3 Fracture Discussion

The fatigue crack growth was predominately transgranular and the fracture surface consists of beachmarks perpendicular to the direction of crack extension along with ductile rupture stringers in the tension direction.

A micrograph of the alloy X-750 microstructure is shown in Figure 9. The specimen was cut from a room temperature tensile specimen, wet polished to a 1200 grit finish, and then immersion etched in a 2% bromine balance methanol solution. The microstructure exhibits an average grain size of approximately 120 to 150 μm. A prominent microstructural feature is the density and distribution of inclusions. The inclusions are predominately intragranular and consist of few large particles and a multitude of smaller particles. The average inclusion spacing is approximately 10 to 20 μm.

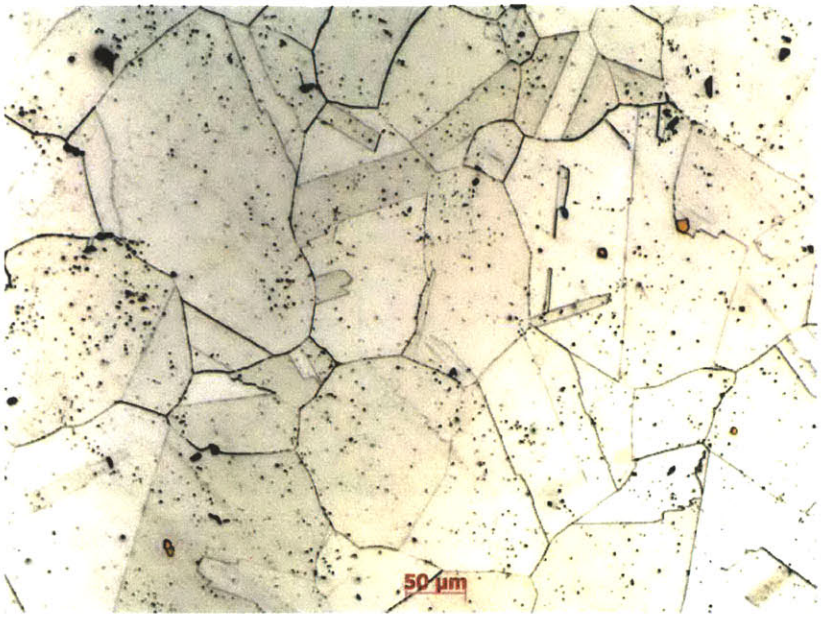

Figure 9: Alloy X-750 Microstructure

The stable crack extension propagates though ductile rupture as evident by the fracture morphology exhibiting a transgranular, ductile, dimple surface for both the 25 and 288 °C specimens. The large size and wide dispersion of the dimples on the fracture surface indicate large coalescence of microvoids before fracture. Intergranular dimple rupture was not observed and further indicates intragranular microvoid nucleation as the fracture mechanism. The distance between dimple sites is approximately the same as between inclusions, which is an indication as to the location of microvoid nucleation initiation sites. The interface between the precrack and ductile tearing surface for the 25 °C tests is shown in Figure 10. The precrack fracture surface for the 25 °C tests are shown in Figures 11-13 and the ductile tearing surfaces are shown in Figures 14-17. The precrack fracture surface for the 288 °C specimens is not shown here because it was prepared under the same external conditions as the room temperature test specimens. The only difference between the room temperature and 288 °C precrack procedure is the ending stress intensity value (K); thus, the fracture surfaces are essentially the same. The interface between the precrack fracture and ductile tearing zones for the 288 °C tests is shown in Figure 18 and clearly distinguishes the smooth fatigue crack extension from the rough ductile rupture morphology. The fracture surfaces for the ductile tearing zone are shown in Figures 19-20.

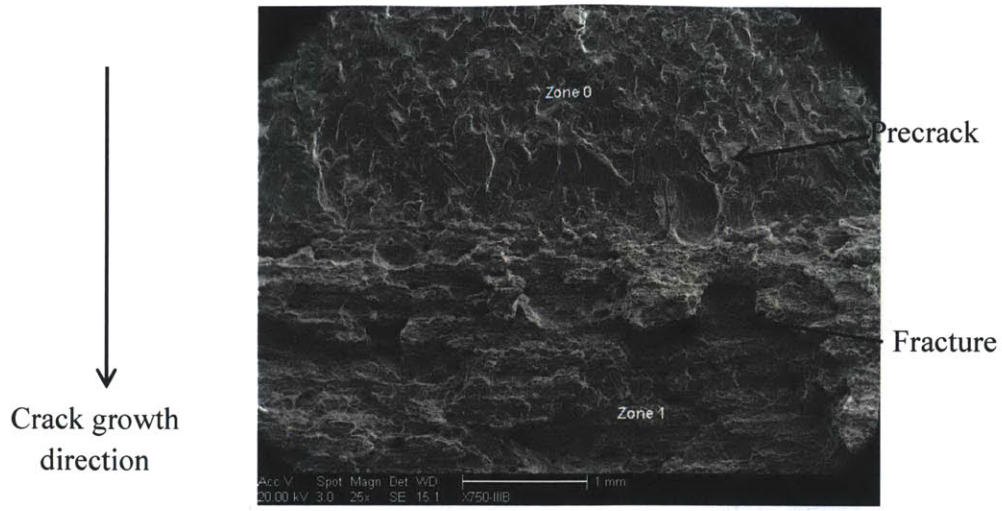

Figure 10: 25 °C, Precrack-fracture interface, 25X magnification

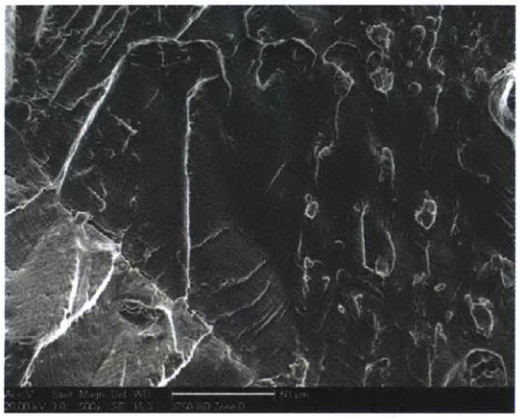

Figure 11: 25 °C, precrack zone, 500X

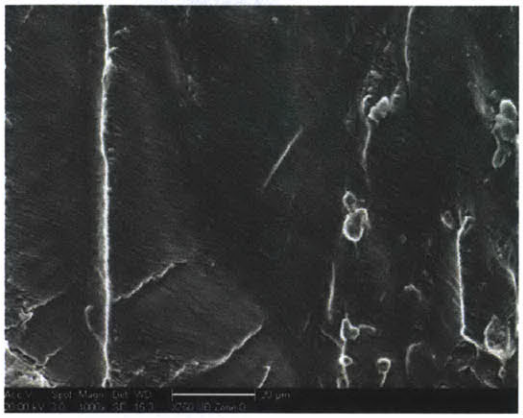

Figure 12: 25 °C, precrack zone, 1000X

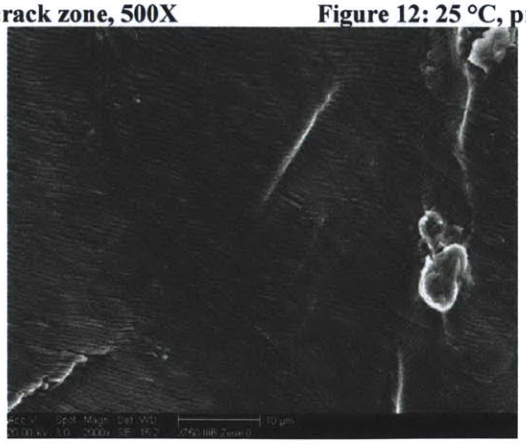

Figure 13: 25 °C, precrack zone, 2000X

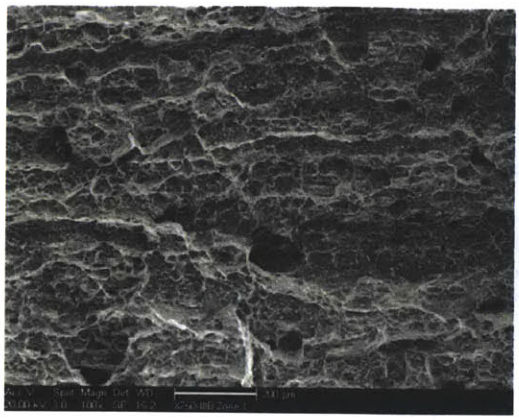

Figure 14: 25 °C, stable tearing, 100X

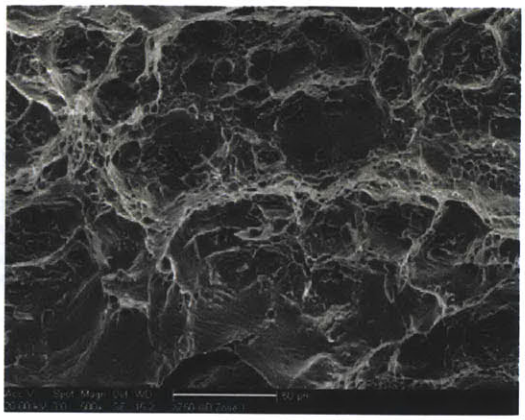

Figure 15: 25 °C, Stable tearing, 500X

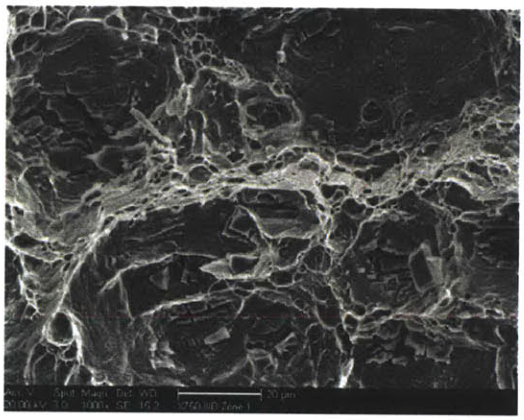

Figure 16: 25 °C, stable tearing, 1000X

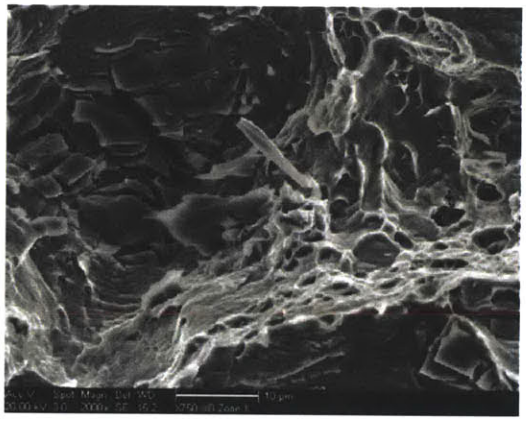

Figure 17: 25 °C, stable tearing, 2000X

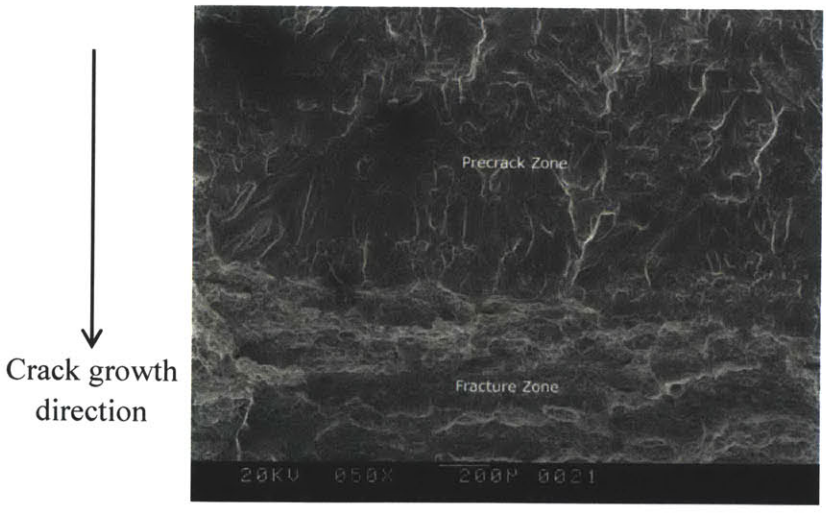

Figure 18: 288 °C, precrack-fracture interface, 50X magnification

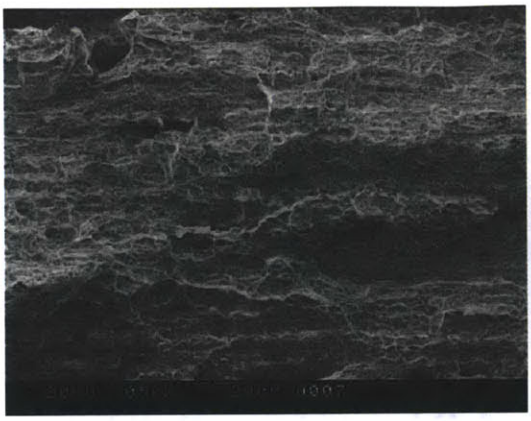

Figure 19: 288 °C, stable tearing, 50X

Figure 20: 288 °C, stable tearing, 100X

C.4 References

6. World wide web: http://www.specialmetals.com/documents/Inconel%20alloy%20X-750.pdf, Accessed 11 May 2011

7. ASTM E1820-08 Equation A2.7

8. D.M. Symons and A.W. Thompson, "The effect of hydrogen on the fracture toughness of alloy X-750," Metallurgical and Materials Transactions A, Vol. 28, pp. 817-823, 1997.

Appendix D – Cu/Cu_2O Reference Electrode Technical Information

This appendix contains technical information about the reference electrode used to measure the platinum potential and specimen ECP in this thesis. The Cu/Cu_2O reference electrode was provided by General Electric Corporate Research Center. The electrode was measured at +253 mV with respect to the standard hydrogen electrode (SHE). The technical paper that contains the discussion about the development, calibration, and limits of the Cu/Cu_2O is presented in its entirety here:

Use of a High Temperature pH Sensor as a "Pseudo-Reference Electrode" in the Monitoring of Corrosion and Redox Potentials at 285°C

Leonard W. Niedrach*

General Electric Corporate Research and Development, Schenectady, New York 12345

ABSTRACT

Corrosion and redox potentials measured at 285°C against a zirconium oxide, membrane-type pH sensor have been found to be more stable than similar measurements against more conventional reference electrodes. This is attributed to the excellent resistance of zirconium oxide to attack by high temperature water and to the absence of a liquid junction that permits exchange of an internal filling solution with the medium being monitored.

In monitoring corrosion and redox potentials in aqueous systems one ideally determines the pH as well, because the two parameters are intimately related. When the pH of the system is known to remain within narrow bounds, *e.g.*, as in the cooling water of nuclear reactors, measurement of only the corrosion or redox potential against a conventional reference electrode can be adequate (1-3). Under such conditions, however, it is equally possible to employ a pH sensor as a "pseudo-reference electrode." It has been our experience that at 285°C, corrosion and redox potentials measured against a zirconium oxide, membrane-type pH sensor (4) have been more stable than any we have achieved against more conventional reference electrodes. This is not surprising in view of the excellent resistance of zirconium oxide to attack by high temperature water. Further, there is no liquid junction to introduce an uncertain junction potential and to permit exchange of an internal filling solution with the medium being monitored and thereby cause drift. Because of the stability of zirconium oxide pH sensors we can visualize their being inserted at many critical monitoring sites in power plants, chemical processing plants, or other installations to provide useful corrosion potential measurements over extended periods with a minimum of maintenance. They could also be useful in laboratory tests, particularly with static autoclaves when consumption of oxygen deliberately added to the starting solution can be rapid, and when undetected changes of this type could lead to serious misinterpretation of data.

The use of a pH sensor in this proposed fashion is not of itself a new idea. Glass electrodes have been so employed in the past (5). The new, high temperature pH sensor merely facilitates extension of the idea to higher temperature systems. It is the purpose of the present paper to review some of the background on the zirconia sensor, indicate how its potential can be related to the standard hydrogen electrode (SHE) scale, and present data relating to corrosion and redox potential monitoring.

* Electrochemical Society Active Member.
Key words: cell, pH sensor, water, emf.

Background

Preferred form of the pH sensor.—The concept of the new, high temperature pH sensor and many of its properties have been discussed elsewhere (4). A

photograph of the device is shown in Fig. 1 and structural details are given in Fig. 2. The ceramic is a ¼ in. OD tube of yttria [8.0 weight percent (w/o)] stabilized zirconia (obtained from Corning Glass Works, Ceramics Products Division, Solon, Ohio, their composition 1372). It is retained in a Conax Type EG-125 Gland with a seal consisting of Teflon, Vespel, silver, and alumina elements as shown. On the basis of previous work we have selected the dry copper/cuprous oxide mixture as our preferred internal junction over the previously employed aqueous internal junctions. This has been done for several reasons: (*i*) we have found it to be readily prepared by simple mixing of the powders and packing into the tube; (*ii*) when prepared in this fashion it has been found to be extremely stable and reproducible; (*iii*) in contrast to aqueous internals it permits ready designation of the active region of the sensor because it does not wet the wall with a conducting film; and (*iv*) in the absence of an internal aqueous phase, seal fabrication is simplified. It also has the virtue of permitting a straightforward calculation of its standard potential against the SHE, a very desirable feature since it is common practice to normalize experimental data to the SHE scale.

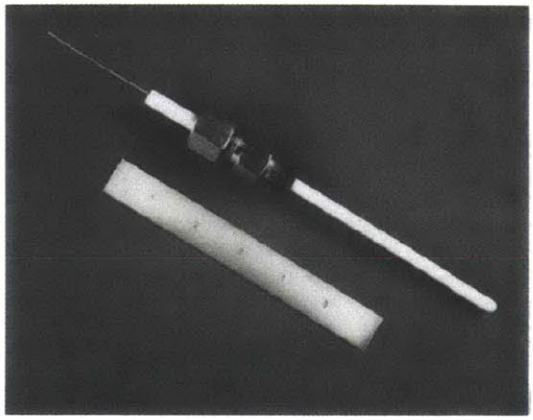

Fig. 1. Photograph of an assembled sensor

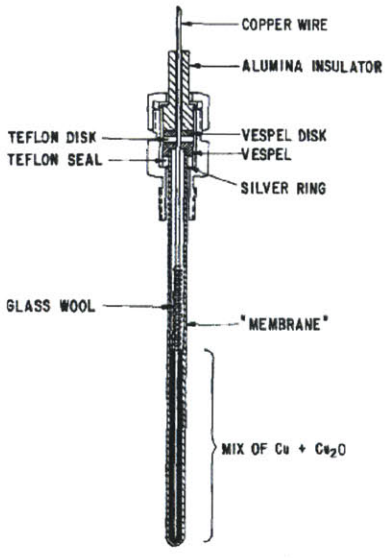

Fig. 2. Schematic diagram of sensor

For the junction we are employing a 1:1 (by weight) mixture of finely divided copper and cuprous oxide (Fisher Copper Metal-Electrolytic Dust, purified; Baker Cuprous Oxide Powder, Analyzed Reagent) to a depth of 2 in. A 30 mil copper wire serves as the contact and lead from the sensor.

Calculation of the standard potential of the sensor vs. the SHE.—For the sensor as shown in Fig. 2, several interphase potentials are involved in series between the external terminal (copper lead wire) and the solution being monitored. These and the thermodynamic balances involved in the potential determining reactions at the various interfaces are summarized in Fig. 3 after the approach of Vetter (6). The balances are derived from the fact that at equilibrium the algebraic sum of the electrochemical potentials, $_i\eta_s$, of the reacting species is zero

$$\Sigma_i \nu_s \cdot {}_i\eta_s = 0 \qquad [1]$$

where

$$_i\eta_s = {}_i\mu_s + {}_iz_s \cdot \mathbf{F} \cdot {}_i\phi \qquad [2]$$

and where $_i\mu_s$ is the chemical potential of reacting species s in phase i, $_iz_s$ is the charge on the species, $_i\phi$ is the Galvani (inner) potential in phase i, $_i\nu_s$ is the stoichiometric factor of the species involved in the potential determining reaction, and **F** is the faraday.

In summing up the interphase potentials between phases 1 and 4 it is seen in Fig. 3 that the net change is equivalent to that for the simple copper/cuprous oxide couple

$$2Cu + H_2O \rightleftarrows Cu_2O + 2H^+ + 2e^- \qquad [3]$$

the thermodynamics for which relative to the SHE are well established.[1]

This is turn means that to relate the standard potential of the sensor to the SHE, the half-reaction for which also involves two hydrogen ions

$$H_2 \rightleftarrows H^+ + 2e^- \qquad [4]$$

we require only the free energy of the reaction

$$2Cu + H_2O \rightleftarrows Cu_2O + H_2 \qquad [5]$$

which does not involve the hydrogen ion concentration. If the zirconia sensor is to be used as a reference in a solution other than one containing the hydrogen

[1] The membrane may therefore be looked upon as a protective sheath that prevents the metal and its oxide from interacting directly with the solution or redox active species in the solution. While a copper/cuprous oxide mix could be exposed to water and dilute acids and bases without significant attack, such would not be the case with strongly acid or basic solutions. Under any conditions use of the unsheathed metal/metal oxide mix would necessitate alternative protection from direct interaction with hydrogen or oxygen. This behavior suggests that the arrangement might be useful in studying the electrochemistry and thermodynamics of other metal/metal oxide or mixed metal oxide systems.

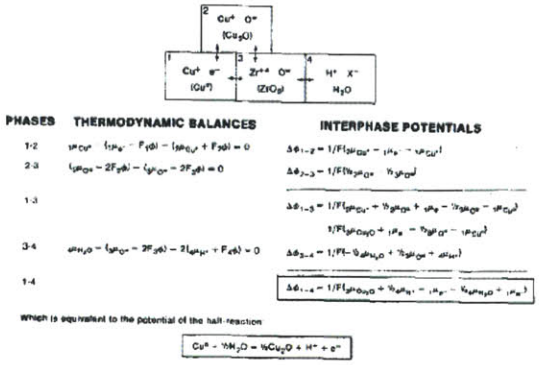

Fig. 3. Interphase potentials and related thermodynamic data for the sensor.

ion at unit activity, a pH correction must be applied in relating back to the SHE scale.

Relationship between the sensor potential and that of the oxygen electrode.—Also of interest in the monitoring of aqueous systems containing dissolved oxygen is the relationship between the sensor potential and that of the oxygen electrode. In this case the overall reaction is obtained from the sum of reaction [3] and the half-reaction for the oxygen electrode

$$\tfrac{1}{2}\,O_2 + 2H^+ + 2e^- \rightleftarrows H_2O \qquad [6]$$

to give

$$2Cu + \tfrac{1}{2}\,O_2 \rightleftarrows Cu_2O \qquad [7]$$

The potential of this cell can therefore be calculated directly from the free energy of formation of cuprous oxide from the elements.

Experimental

Determination of the standard potential of the sensor at 285°C.—Using equipment and procedures described in Ref. (4), the potential of the sensor has been measured against the hydrogen electrode. A well-passivated titanium autoclave was employed and the water entering the autoclave at a flow rate of approximately 15 ml/min was equilibrated with "forming gas" (10% hydrogen in nitrogen) at 25°C. A platinized platinum flag served as the sensing element of the hydrogen electrode. The results of three separate experiments, each yielding steady potentials for about 36 hr, are summarized in Table I.

In calculating the correction term for the hydrogen concentration in the water it was assumed that the concentration at 285°C was equal to that obtained in the equilibration at 25°C. This is reasonable since the test system was operated about 200 psi above the saturation pressure of water at 285°C and no gas phase was present in the autoclave. From data of Himmelblau (7) the hydrogen concentration in equilibrium with the 10% H_2-N_2 mixture at 25°C was estimated to be 0.152 ppm. At 285°C the concentration of hydrogen in equilibrium with 1 atm of hydrogen is 7.40 ppm. These concentrations coupled with the slope of 110.76/2 mV/decade at 285°C give the correction term of 93 mV. For the standard potential of reaction [5] data of Macdonald (8) were interpolated to 285°C. It is seen in Table I that the agreement between the measured and theoretical is very satisfactory.

Measurement of the potential of the sensor vs. the oxygen electrode.—Data for this combination were obtained over the pH range from 0.0005*m* sulfuric acid to 0.001*m* sodium hydroxide using aerated solutions containing about 8.2 ppm dissolved oxygen. In this case the agreement with theory was less satisfactory than in the case of hydrogen, and the value varied with pH as shown in Fig. 4. The theoretical potential of 635 mV was calculated from literature data for the free energy of formation of cuprous oxide (9) applying a correction term to allow for an oxygen concentration below that in equilibrium at 1 atm. The solubility of oxygen at 285°C at a pressure of 1 atm was taken as 110 ppm (7). The discrepancies are most likely associated with the oxygen electrode which is probably not yet sufficiently reversible even at 285°C.

Table I. Comparison of the measured value of the standard potential of the sensor with the calculated value at 285°C

Run	*E* of sensor *vs.* hydrogen electrode (mV)	ΔE for hydrogen activity* (mV)	E° (mV)	
A	274			
B	272			
C	280			
	Mean 275	93		368
			Calculated value	366**
			Difference	2

* $\Delta E = (2.303\,RT/nF)\log(C_1/C_s) = 55.38 \log(7.40/0.152) = 93$ mV, where C_1 is the solubility of hydrogen at 285°C and 1 atm pressure and C_s is the actual hydrogen concentration in water. [Solubility data from Ref. (7).]
** Based on data from Ref. (8).

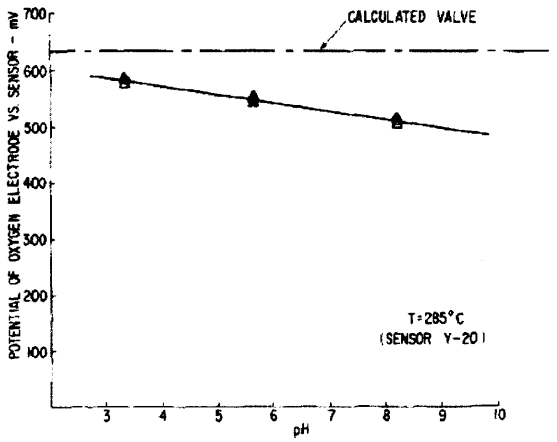

Fig. 4. Comparison of measured and calculated values of the potential of the oxygen electrode vs. the pH sensor. (Oxygen concentration in equilibrium with air at 25°C, *i.e.*, 8.2 ppm.)

Monitoring corrosion and redox potentials.—In the course of the development of the zirconia pH sensor two tests of about 40 days duration were performed to demonstrate long-term stability. During most of the period of these tests the system was exposed to aerated water at 285°C, but periodically excursions to 0.0005*m* H_2SO_4 and 0.001*m* NaOH were introduced. Potentials of the sensor (with Cu/Cu_2O internal), a platinum probe, and the 316 S.S. autoclave were monitored throughout using an Ag/AgCl reference electrode (10) initially charged with water and AgCl crystals, *i.e.*, no KCl was added. (This type of filling solution has proved to be more stable than those containing 0.01 or 0.1*m* KCl.) The potential of the zirconia sensor *vs.* the platinum probe was also followed directly throughout the tests. We have now reexamined the data as they bear upon the monitoring of corrosion and redox potentials with the autoclave serving as the corroding electrode.

The relative stabilities of the various electrodes against the reference electrode are shown in Fig. 5, and similar data for the corrosion and redox potentials against the pH sensor are shown in Fig. 6. In connection with the latter figure, it should be noted that, in contrast to the platinum probe, the potential of the autoclave was not monitored directly against the pH sensor during the tests. As a result, all of the corrosion potentials have been derived from independent measurements of the autoclave and the pH sensor against the Ag/AgCl reference. This may account in part for the greater scatter. Nevertheless, both sets of measurements indicate that the potentials measured against the pH sensor are at least as reliable as those measured against the more conventional reference electrode.

While the data in Fig. 5 and 6 pertain to the dilute acid solutions, similar results were obtained with water and the dilute base. This is evident from the clustering of the data points obtained throughout the tests and plotted for Run ZR02-19 in Fig. 7 and 8. Here we see additionally that the influence of pH on the corrosion potential essentially parallels that of the pH sensor. The slope of the redox probe response

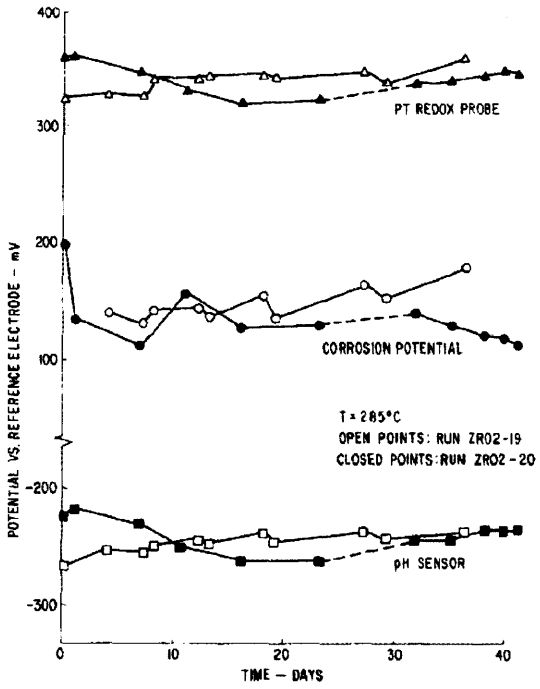

Fig. 5. Potentials measured against an Indig reference electrode. (0.0005*m* H_2SO_4 electrolyte; 8.2 ppm dissolved oxygen.)

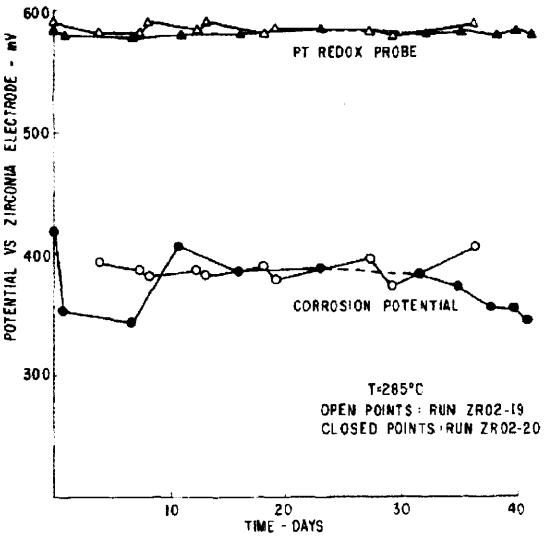

Fig. 6. Corrosion and redox potentials measured against the pH sensor. (0.0005*m* H_2SO_4 electrolyte; 8.2 ppm dissolved oxygen.)

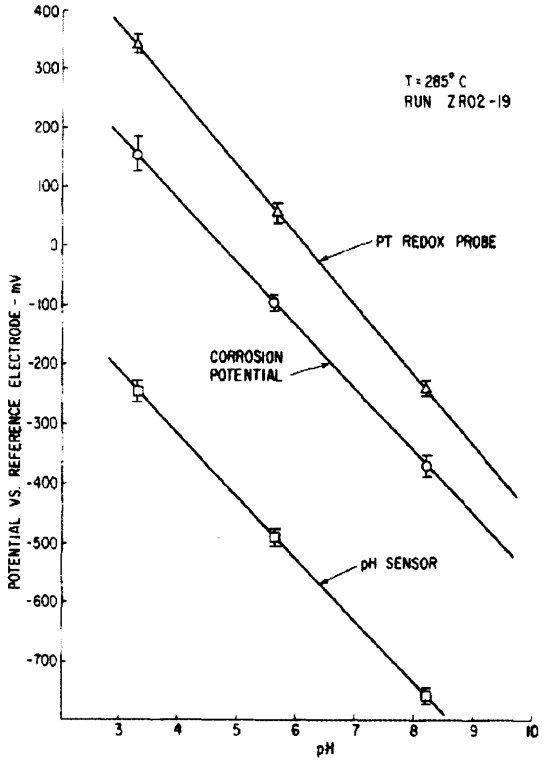

Fig. 7. Effect of pH on the potentials measured against the Indig reference electrode. (8.2 ppm dissolved oxygen.)

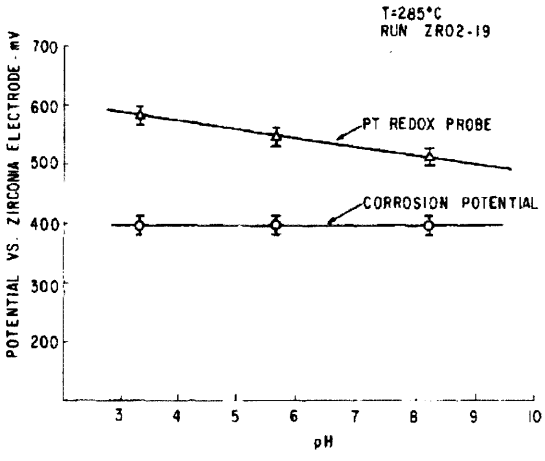

Fig. 8. Effect of pH on corrosion and redox potentials measured against the pH sensor. (8.2 ppm dissolved oxygen.)

(from the oxygen/water couple) is somewhat greater. As noted in the previous section this probably reflects remaining irreversibility in the oxygen reduction reaction at 285°C.

All of these data support the use of the pH sensor as an alternative reference electrode for the measurement of corrosion and redox potentials. They also indicate that using the pH sensor as a reference electrode automatically eliminates spurious pH change effects from the measurement of real interest, i.e., the shift in the relative oxidation level of the system through changes in concentration of redox active species *per se*.

In-Plant Applications

For in-plant applications we would envision the insertion of zirconia electrodes at a variety of locations where monitoring of corrosion and/or redox potential(s) were felt appropriate. In its simplest form the probe would be inserted through the wall of a pipe or flange. Only a female ¼ in. NPT is required for mounting. To monitor corrosion potentials a high impedance meter could be connected directly across the sensor and the pipe as indicated in Fig. 9. Because a small

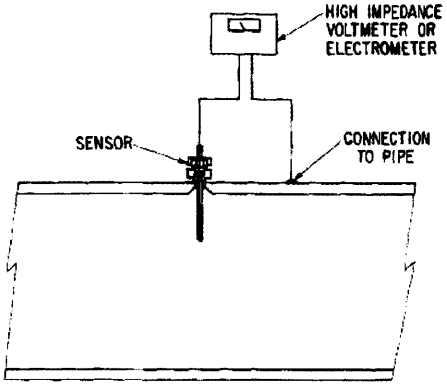

Fig. 9. Mounting of sensor for direct monitoring of the corrosion potential of a pipe.

platinum redox probe will respond more rapidly to changes in water chemistry than will the large area piping, it would generally be desirable to include such a probe in the monitoring system. This too can be inserted through a ¼ in. NPT, and it can be multiplexed to a common high impedance meter.

To allow for possible breakage of a zirconia tube, a slightly more sophisticated arrangement might be desired in which the zirconia sensor is surrounded by a screen or perforated shield that could retain any broken pieces. The screen or shield could be constructed of the same alloy as the piping and connected electrically to the piping. Under such conditions it would assume the corrosion potential of the more massive system and should not interfere with measurements.

It is conceivable that sensors would be desired at several sites around a plant as indicated in Fig. 10 where a boiling water reactor power plant is used as an example. In such a case it would probably be desirable to monitor potentials immediately after the demineralizers, farther along the feedwater train, and in the cooling water recirculation loop.

Acknowledgment

The author wishes to thank W. H. Stoddard for assistance with the fabrication of sensors and many of the measurements.

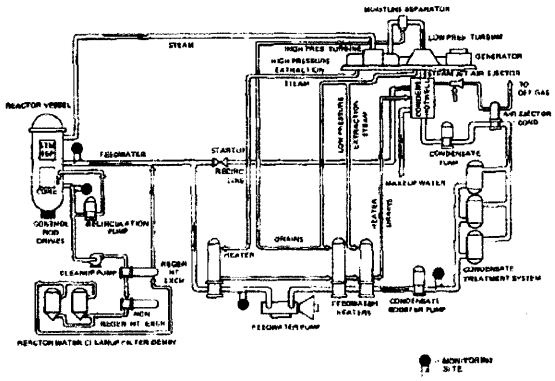

Fig. 10. Potential sites for monitoring corrosion potentials

Manuscript submitted Nov. 16, 1981; revised manuscript received Dec. 10, 1981. This was Paper 427 presented at the Denver, Colorado, Meeting of the Society, Oct. 11-16, 1981.

Any discussion of this paper will appear in a Discussion Section to be published in the June 1983 JOURNAL. All discussions for the June 1983 Discussion Section should be submitted by Feb. 1, 1983.

Publication costs of this article were assisted by General Electric Company.

REFERENCES

1. R. L. Cowan and A. I. Kaznoff, *Corrosion*, **29**, 123 (1973).
2. M. E. Indig, J. E. Weber, and A. D. Miller, *ibid.*, **34**, 3 (1978).
3. D. D. Macdonald, A. C. Scott, and P. Wentrcek, *This Journal*, **128**, 250 (1981).
4. L. W. Niedrach, *ibid.*, **127**, 2122 (1980).
5. D. J. G. Ives and G. J. Janz, Editors, pp. 261-263, "Reference Electrodes," Academic Press, New York (1961).
6. K. J. Vetter, "Electrochemical Kinetics," Translated by S. Bruckenstein and B. Howard, p. 17 ff, Academic Press, New York (1967).
7. D. M. Himmelblau, *J. Chem. Eng. Data*, **5**, 10 (1960).
8. D. D. Macdonald, G. R. Shierman, and P. Butler, AECL-4136, December 1972.
9. JANAF Supplement 54, December 1978.
10. M. E. Indig and A. R. McIlree, *Corrosion*, **35**, 288 (1979).